A description of the Bjønnes nepheline syenite intrusion, part of the Larvik plutonic complex, Norway

Niall Thomas Groome

Master Thesis in Geosciences

Study programme: Geology

60 credits

Department of Geosciences

Faculty of Mathematics and Natural Sciences

University of Oslo

01/06/2017

Supervisors: Henrik Friis (Natural History Museum, University of Oslo)
Tom Andersen (Department of Geosciences, University of Oslo).

This work is published digitally through DUO – Digitale Utgivelser ved UiO
http://www.duo.uio.no
It is also catalogued in BIBSYS (http://www.bibsys.no/english)

Acknowledgements

Firstly I would like to sincerely thank Henrik Friis and Tom Andersen for their dedicated supervision, guidance and support throughout this project.

Big thanks to Øyvind Sunde for sharing his knowledge of the LPC, particularly in the early stages of this project, for keeping me up to date with his current research in the area, and for his assistance and collaboration during fieldwork. Also thanks to Cassandra Ugland for her role in mapping the Bjønnes syenite and producing a digital geological map of the area.

Thanks to Alf Olav Larsen for taking myself and Øyvind to islands in the Langesundsfjord on his boat and for sharing his insight on the local geology. Also, thanks to Magnus Opsahl for kindly taking us out on his boat, to visit otherwise unreachable outcrops along the coast of the Bjønnes peninsula and the surrounding islands.

I would like to thank Muriel Erambert for her assistance in conducting electron microprobe analysis. I would also like to thank Berit Berg for her assistance in using the scanning electron microscope, and Salahalldin Akhavan for preparing thin sections.

Whole rock geochemical characterisation of samples was conducted by ACME Labs (Bureau Veritas Commodities Canada Ltd.) in Vancouver, Canada.

Abstract

The Larvik plutonic complex is an intrusive suite within the Palaeozoic Oslo Rift, Norway, consisting of ten individual ring sections of monzonite (larvikite) and lardalite. The Bjønnes nepheline syenite is a relatively small intrusive body within nepheline-normative larvikite and prior to this research, very little was known about the intrusion. The Bjønnes syenite is texturally and chemically heterogeneous, locally becoming mildly peralkaline ((Na+K)/Al = 0.91 – 1.06). These peralkaline nepheline syenites display agpaitic mineralogy, including minerals such as eudialyte and aenigmatite. The miaskitic-agpaitic transition is variable, most likely influenced by other factors beyond alkalinity. Agpaitic minerals were previously thought to be confined to nepheline syenite pegmatites in the Larvik plutonic complex.

Electron microprobe analysis of mafic minerals showed a compositional range from diopsidic to almost pure aegirine ($Ae_9Di_{59}Hd_{32}$ – $Ae_{99}Di_1Hd_0$). Clinopyroxenes produce a single evolutionary trend away from a primitive composition through zonation and increased alkalinity. Secondary clinopyroxene that replaced amphibole as a post-magmatic hydrothermal phase has the most evolved composition. Amphibole compositions show a similar increase in Na and Fe components as alkalinity increases.

Geochemical whole rock data shows that the Bjønnes syenite has been depleted in elements such as P, Sr and Eu, removed during extensive fractionation of plagioclase and apatite from a source melt. Incompatible trace element ratios suggest that the Bjønnes syenite originated from a homogeneous mantle source compatible with the source of the larvikites. Complex field relationships and major element comparisons suggest that the Bjønnes syenite intruded hot larvikite of ring section VI and most likely originated from the same, fractionated melt source. Widespread gneissic texture relates to syn-magmatic deformation, possibly indicating emplacement via faulting. Nepheline syenite dykes in the surrounding areas are likely related to the Bjønnes syenite based on similarities in texture, filed relationships and geochemistry.

Glossary

LPC	Larvik plutonic complex
RS I – X	Ring sections 1 – 10 of the LPC
Agpaitic	Nepheline syenite with an alkalinity index >1.2 and/or mineralogy that includes complex Ti- and Zr-silicate minerals.
Miaskitic	Non-agpaitic nepheline syenite
REE	Rare-earth elements (Lanthanides)
LREE	La – Eu
HREE	Gd – Lu
EGM	Eudialyte-group minerals
HFSE	High field-strength element
fO_2	Oxygen fugacity
a_x	Activity of X
Nds	Sodium disilicate component $Na_2Si_2O_5$
apfu	Atoms per formula unit
PPL	Plain polarised light
XPL	Cross polarised light

Table of selected minerals relevant in the text

Mineral	Abbreviation	Mineral formula
Aegirine	Aeg	$NaFe^{3+}Si_2O_6$
Aenigmatite	Aen	$Na_4Fe^{2+}{}_{10}Ti_2Si_{12}O_{40}$
Analcime	Anl	$NaAlSi_2O_6 \cdot H_2O$
Apatite	Ap	$Ca_5(PO_4)_3(F,Cl,OH)$
Arfvedsonite	Arf	$NaNa_2(Fe^{2+}{}_4Fe^{3+})Si_8O_{22}(OH)_2$
Catapleiite	Cat	$Na_2ZrSi_3O_9 \cdot 2(H_2O)$
Chamosite	Chm	$(Fe,Mg,Al)_6(Si,Al)_4O_{10}(OH,O)_8$
Eudialyte	Eud	$Na_{15}Ca_6(Fe,Mn,Na)_3(Zr,Ti)_3(Si,Nb)Si_{25}O_{73}(O,OH,H_2O)_3(Cl,OH)_2$
Natrolite	Ntr	$Na_2(Si_3Al_2)O_{10} \cdot 2(H_2O)$
Pyrochlore	Pcl	$(Na,Ca)_2Nb_2(O,OH,F)_7$
Rosenbuschite	Ros	$Ca_6Zr_2Na_6(Zr,Ti)_2(Si_2O_7)_4(OF)_2F_4$
Sodalite	Sdl	$Na_4Si_3Al_3O_{12}Cl$
Titanite	Ttn	$CaTiSiO_4(O,OH,F)$
Wöhlerite	Woh	$NaCa_2(Zr,Nb)(Si_2O_7)(O,F)_2$
Zircon	Zrn	$(Zr,REE)SiO_4$
Zirconolite	Zcl	$CaZrTi_2O_7$

Table of contents

1. Introduction 1
1.1 Regional geological setting 1
1.1.1 Larvik Plutonic Complex 3
1.1.2 Nepheline syenites in the LPC 5
1.2 Alkaline felsic systems 7
1.3 Methodology 9
1.3.1 Whole rock characterisation 9
1.3.2 Electron microprobe analysis 10
1.3.3 Scanning electron microscope 10
1.3.4 Data calculations & software 10
1.3.5 Mineral formulae and abbreviations 11
2. Description of the Bjønnes syenite and related rocks 12
2.1 Samples 12
2.2 Larvikite (RS VI) 13
2.3 Bjønnes syenite 14
2.3.1 Textural overview 14
2.3.2 Gneissic texture 16
2.3.3 Equigranular texture 17
2.3.4 Trachytoid texture 18
2.3.5 Porphyritic texture 18
2.3.6 Mineral banding 19
2.3.7 Eudialyte in syenite 21
2.3.8 Larvikite-syenite relationship 23
2.3.9 Pegmatites 25
2.3.10 Faulting 25
2.3.11 Other field relationships 26
2.4 Nepheline syenite dykes in Tvedalen and the Langesundsfjord 28
2.4.1 Langesundsfjord 31
2.5 Lågendalen 32
2.6 Mineral descriptions and relationships 34
2.6.1 Feldspar 34
2.6.2 Nepheline & sodalite 36
2.6.3 Olivine 37
2.6.4 Clinopyroxene 37
2.6.5 Amphibole 40
2.6.6 Biotite 42
2.6.7 Sulphides 43
2.6.8 Fe-Ti oxides 43
2.6.9 Titanite 45

2.6.10 Aenigmatite 46
2.6.11 Zirconolite 47
2.6.12 Baddeleyite 48
2.6.13 Zircon 48
2.6.14 Eudialyte 49
2.6.15 Catapleiite & rosenbuschite 50
2.6.16 Apatite 51
2.6.17 Britholite-(Ce) 51
2.6.18 Pyrochlore 51
2.6.19 REE carbonates 52
2.6.20 Thorite 52
2.6.21 Fluorite 52
2.6.22 UKM1 & UKM2 53
3. Results 54
3.1 Whole rock geochemistry 54
3.1.1 Major elements 54
3.1.2 Trace elements 60
3.1.3 Rare Earth elements 60
3.2 Mineral chemistry 62
3.2.1 Olivine 62
3.2.2 Clinopyroxene 63
3.2.3 Amphibole 71
3.2.4 Biotite 78
3.2.5 Titanite 79
3.2.6 Aenigmatite 80
3.2.7 Zirconolite 81
3.2.8 Eudialyte 82
3.2.9 Rosenbuschite 83
3.2.10 Catapleiite 83
3.2.11 Apatite 83
3.2.12 Monazite-(Ce) 84
3.2.13 Britholite-(Ce) 84
3.2.14 Pyrochlore 84
3.2.15 REE Carbonates 85
3.2.16 Thorite 85
3.2.17 UKM1 85
3.2.18 UKM2 86
4. Discussion 87
4.1 Timing of emplacement 87
4.2 Internal evolution of the Bjønnes syenite 88
4.2.1 Textural variations 88
4.2.2 Alkalinity and textural distribution 90
4.2.3 Evolution of paragenesis 90

4.2.4 Zr and Ti incorporation in mafic minerals *93*
4.2.5 Evolution of mafic mineral chemistry *94*
4.2.6 Eudialyte syenite *96*
4.2.7 Eudialyte alteration *98*
4.2.8 The roles of Cl and F *102*
4.2.9 Oxygen fugacity *102*
4.2.10 Porphyritic syenite (NTG17) *104*
4.3 Nepheline syenite dykes 106
4.3.1 Evidence for timing *107*
4.3.2 Source of the nepheline syenite pegmatites *107*
4.4 The Bjønnes syenite as part of the LPC 108
4.4.1 Comparing geochemistry *108*
4.4.2 Evolution of mineral chemistry *114*
4.4.3 Emplacement of the Bjønnes syenite *117*
4.5 Comparisons to other alkaline complexes 120
4.6 Resource potential 123
5. Conclusions 125
5.1 Further research 126
References 127
Web references 134

Appendix

Appendix 1: thin section descriptions
Appendix 2: geochemical data
Appendix 3: ASI (aluminium saturation index)
Appendix 4: electron microprobe data
Appendix 5: Figure 51 data

1. Introduction

The Oslo Rift in Southeast Norway is well known for its diverse range of alkaline igneous rocks, of which the Larvik plutonic complex (LPC) is a part of. The LPC consists of predominantly of monzonites (larvikite), along with lardalite (nepheline syenite) and other nepheline syenite bodies, such as the Bjønnes nepheline syenite pluton towards the western margin of the complex. It is thought to relate to a series of nepheline syenite dykes in the larvikites of the surrounding areas, which in turn are thought to be associated with mildly agpaitic nepheline syenite pegmatites (*Dahlgren, 2010*). Foyaitic nepheline syenite intrusions exist in the Northern part of the complex and their relationship with the Bjønnes syenite has not been studied in detail, although they are treated as separate units in literature (*Raade, 1973; Neumann, 1980*).

The purpose of this study is to provide the first detailed description of the Bjønnes syenite and to examine its relationship to other units of the LPC. The pluton was mapped and field observations were made about the textural variations throughout the pluton, as well as its interaction with its surrounding rocks. Geochemical whole rock analyses of major elements were used to characterise the rocks.

Whole rock major and trace element data were compared to similar analyses from other parts of the LPC in an attempt to determine the genesis of the Bjønnes syenite. These analyses, along with textural observations from the Tvedalen and Lågendalen areas, were used to speculate on the relationship between the Bjønnes syenite and other nepheline syenites in the complex. Whole rock geochemical data was used to explore similarities and differences between units. Detailed petrographic and mineralogical study was used to explore crystallisation conditions.

1.1 Regional geological setting

The Oslo Rift is a high-volcanicity continental rift system that was active from the Late Carboniferous to Permian as a product of lithospheric stretching to the North of the Tornquist fault line. The rifting was part of an Upper Palaeozoic to Mesozoic continental extensional regime across Northern Europe relating to the Variscan orogeny (*Larsen et al., 2008*). Close comparisons to the Oslo Rift have been made from present-day examples in the East African rift complex such as in Kenya and Ethiopia (*Larsen & Sundvoll, 1984*). The Oslo Rift spans approximately 500 km in length along a N-S axis, comprised of four polarity-offset half-grabens (*Larsen et al., 2008*). A simplified

geological map of the rift can be seen in Figure 1.

Magmatic rocks related to rifting show great compositional variety, ranging from alkaline olivine basalts to granites and syenites. Intermediate intrusive monzonites (larvikites and kjelsåsites) and compositionally equivalent latitic lavas, known as rhomb porphyries, comprise a significant volume of the Oslo rift, making up approximately 40% of exposed surface and sub-surface rocks (*Ramberg, 1976; Neumann et al., 2004*).

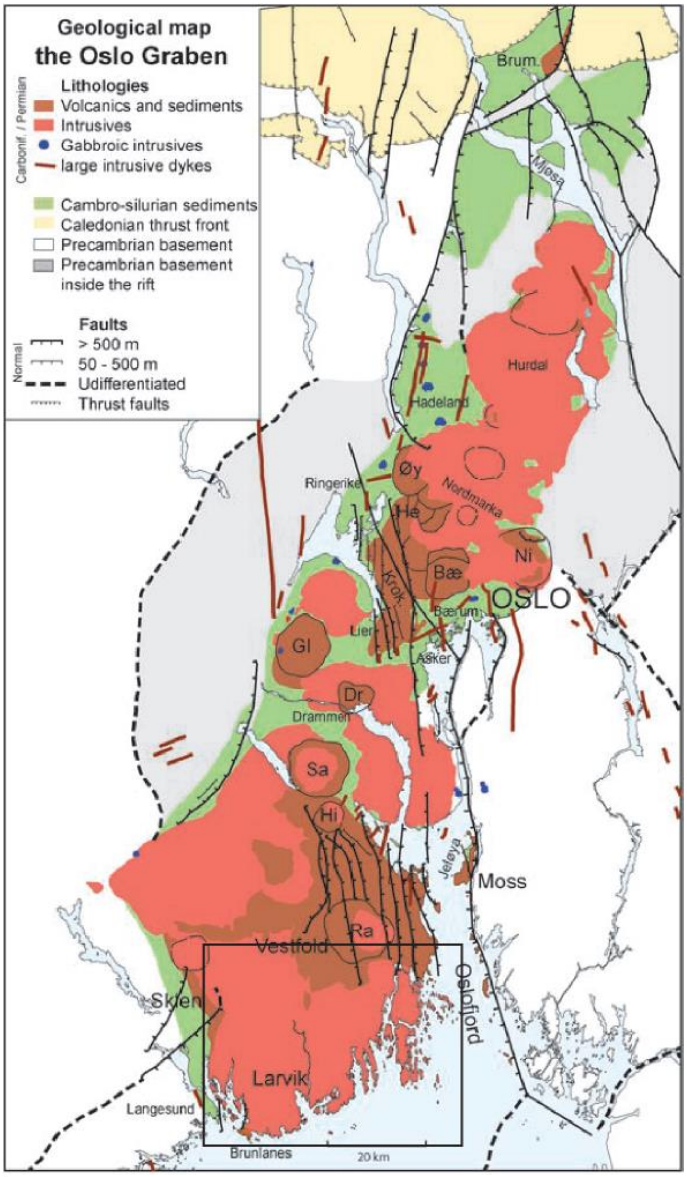

Figure 1: Simplified geological map of the Oslo Rift (*Larsen et al, 2008*). The highlighted area shows the location of the LPC (see Figure 2).

Rifting and magmatic activity is thought to have lasted a total of 65 million years based on Rb-Sr dating of some of the youngest plutons in the complex, however more recent unpublished data does not confirm this (*Corfu, unpublished*). Rifting can be divided into six stages of evolution, as described by *Larsen et al. (2008)*. The bulk of magmatism took place across stages II, III and IV, climaxing in stage III. Stage III was marked by the eruption of rhomb porphyry lavas in great volume along large fissure volcanoes, whilst basaltic lavas continued to be produced. Rhomb porphyry lava flows are found extensively throughout the Oslo Rift but production rate of lavas varied greatly. In Vestfold, a stratigraphic thickness of around 3 km (75% rhomb porphyry) can be observed as opposed to 900 m (80% rhomb porphyry) northwards in Krokskogen. The shallow emplacement of larvikitic plutons (intrusive equivalents to rhomb porphyries), including the Larvik Plutonic Complex, marked the end of stage III (*Neumann, 1976; Larsen et al., 2008*). Later emplacement of larvikite intrusions would continue to take place beyond this point, however, forming the Siljan-Mykle complex for example, situated immediately North of the LPC (*Andersen & Sørensen, 1993; Pedersen et al., 1995*).

It is currently unclear whether rifting was caused by the upwelling of a mantle plume, or by passive lithospheric stretching (*Pedersen & van der Beek, 1994; Larsen et al., 2008*). The formation of the intermediate lavas and plutons is thought to be a result of fractionation of basaltic melts rising from a mantle source. The basaltic melts sat at the mantle-crust boundary or lower mantle, trapped by relatively light crust. The crust acted as a density filter, meaning fractionation occurred until an intermediate residual melt with sufficient buoyancy and viscosity was produced and able to ascend (*Neumann, 1980; Neumann et al., 2004; Larsen et al., 2008*).

1.1.1 Larvik Plutonic Complex

The southernmost onshore part of the Oslo Rift is the LPC, in the central part of the Vestfold graben. The classical model for the internal model of the LPC shows a complex consisting of 10 distinguished ring sections (RS I – X), as shown in Figure 2 (*Petersen, 1978*). Geochemical data suggest that each ring section represents a separate intrusion, or series of intrusions, as observed in RS V (*Neumann, 1980; Rämö & Andersen, 2011*). U-Pb dating of magmatic zircons has shown that emplacement of all ten ring sections took place 299-289 Ma (*Rämö & Andersen, 2011*).

The complex consists predominantly of silica-oversaturated (quartz-bearing) to silica-undersaturated (nepheline-bearing) monzonites known as larvikite, along with lardalites (nepheline syenites; *Le Maitre, 2002*) and a variety of smaller syenite bodies (*Raade, 1973*). Figure 2 displays the compositional changes evolving through ring sections, from quartz-monzonitic in the oldest rocks of the complex (RS I – II), to monzonitic (III, V), to nepheline-monzonitic (RS IV – VIII), and finally to lardalites making up the youngest ring intrusions (RS IX – X) (*Raade, 1973; Neumann, 1980; Dahlgren, 2010*). This shows a systematic and almost continuous evolution from weakly silica-oversaturated to silica-undersaturated, a process thought to mostly be a result of fractional crystallisation of the source in the lower crust (*Neumann, 1980*). Crustal contamination during emplacement is not considered a significant factor in the evolution of the LPC (*Corfu & Dahlgren, 2007; Rämö & Andersen, 2011*).

Beyond variations from quartz-bearing to nepheline-bearing, the larvikites of the complex remain mineralogically similar, dominated by hypersolvous ternary alkali feldspars (An_{5-15}). Mafic minerals include olivine (Fo_{17-35}), augite, calcic amphiboles, biotite and Fe-Ti oxides. Common accessory minerals include zircon, titanite and apatite (*Raade, 1973; Piilonen et al., 2012*). The cryptoperthitic nature of the feldspars in larvikite create a schiller effect, a characterising feature that makes the larvikite a

popular building stone, known in construction as pubstone. As a result, extensive quarrying takes place in the area.

The lardalites that make up the youngest ring sections (RS IX – X) however do not conform to the theory of continuous fractionation from the larvikites. Geochemical analysis suggests that they were not a product of further fractionation of the same source, or by the partial melting of crystallised larvikites. They appear to be a separate, low a_{SiO2} trend of evolution. *Neumann (1980)* concluded that they were most likely the product of a complex accumulation process.

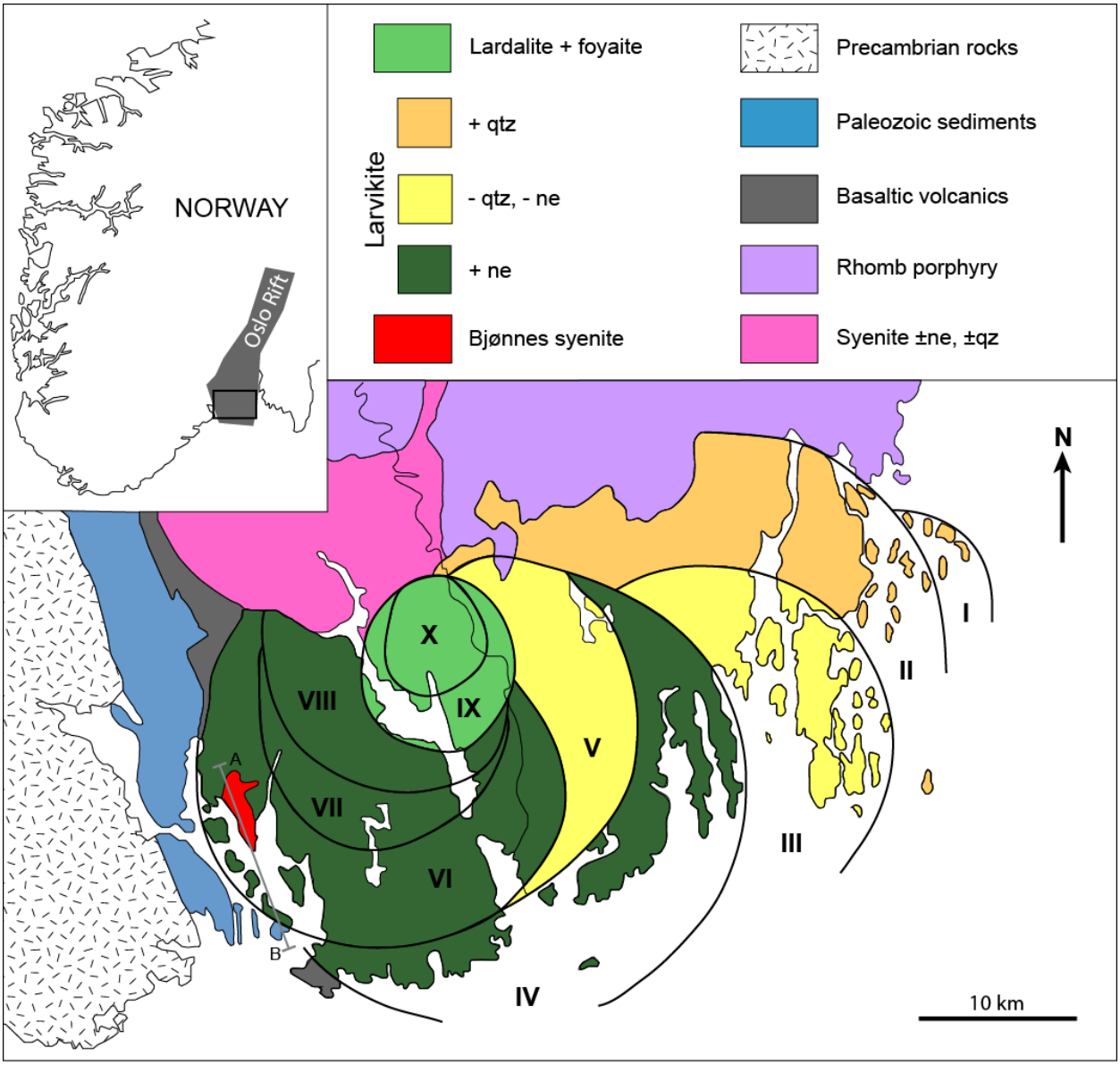

Figure 2: Simplified geological map of the Larvik Plutonic Complex and its ring sections, including the Bjønnes syenite towards the Western margin (modified from *Petersen, 1978; Dahlgren, 2010*). See Figure 3 for line A – B cross-section.

The geographical placement of the ring sections shows a general migration of activity from East to West, and also to the North in the later stages of emplacement, shown in Figure 2 (*Petersen, 1978*). This suggests a shift in the centre of magmatic activity over time, probably related to movement of the rifting lithosphere over a more stationary magma source.

1.1.2 Nepheline syenites in the LPC

Aside from the lardalites, two key types of nepheline syenites have been identified in the LPC, often referred to in past literature as foyaite/hedrumite, associated with lardalites in the Lågendalen area, and 'ditroite-schist', associated with the Langesundsfjord area, both first described by *Brøgger (1890)*. Neither was emplaced as ring sections in the manner of the larvikites and lardalites.

In Lågendalen, the Northern part of the complex, foyaites and hedrumites intrude the lardalites of RS IX and X in the form of both dykes and larger masses. These are described as the 'ordinary' nepheline syenites of the LPC, characterised by platy feldspars that create a trachytiod texture. Hedrumite is used to describe the nepheline-poor to nepheline-absent variations of foyaite of the area (*Brøgger, 1898; Raade, 1973*). Geochemical analysis suggests that the foyaites and hedrumites are probably related through fractionation of feldspars and mafic minerals but are not strictly cogenetic (*Neumann, 1980*). Sodalite foyaite can also be found within the foyaite-hedrumite suite (*Petersen, 1978*). The foyaite/hedrumites are unlikely to be directly related to the lardalites because they are younger and crystallised under more oxidising conditions (*Neumann, 1976; Petersen, 1978*).

'Ditroite schist' was used to describe nepheline syenite with a gneissic texture by *Brøgger (1890)*, and the term 'ditroite' has been used as a general term in past literature to describe the nepheline syenites of the Langesundsfjord. However, *Dahlgren (2010)* mentions several textures attributed to these nepheline syenites, including gneissic, equigranular, porphyritic and trachytoid. Ditroite is officially classified as a nepheline syenite containing biotite, cancrinite, primary calcite and intergranular sodalite (*Le Maitre, 2002*). This concludes that 'ditroite' is not suitable as a general term for all nepheline syenites in the Langesundsfjord. Gneissic texture is a common feature of nepheline syenites in the area however, described by *Brøgger (1890)* as a fluidal structure. It was suggested that the syenites intruded partly crystallised larvikite and the two were subject to deformation during crystallisation. It has also been argued that the texture was a product of sodic metasomatism (fenitisation) of larvikite (*Oftedahl, 1960*).

The Bjønnes syenite represents the largest known body of nepheline syenite in the Langesundsfjord area, found as a pluton exposed on the Bjønnes peninsula near the western margin of the LPC (*Dahlgren, 2010*). Nepheline syenite dykes are also found commonly on islands in the Langesundsfjord as well as in the Tvedalen area to the East of the Langesundsfjord, typically associated with mildly agpaitic nepheline syenite pegmatites. Little is known about their complex relationship, with examples of pegmatites crystallising inside nepheline syenite dykes and other examples of nepheline syenites found occupying pegmatite cores (*Dahlgren, 2010*).

Nepheline syenite pegmatites are generally associated with the Western LPC and RS VI, but are known to occur as far East as RS III in quartz-bearing larvikite. They are also known to intrude beyond the western contact of the LPC into metamorphosed gneisses, basanites and nephelinites (*Brøgger 1890; Larsen, 2010*). The mineralogy of the pegmatites is diverse but they are generally described as mildly agpaitic (*Andersen et al., 2010*). It is unclear whether the pegmatites originate from the host larvikite or the nepheline syenites that they are often associated with (*Dahlgren, 2010*). Corresponding miaskitic quartz syenite pegmatites are associated to the eastern LPC. In the Lågendalen area, truly agpaitic Bratthagen-type pegmatites are found associated to foyaites (Sæbø, 1965; *Neumann, 1980; Andersen et al., 2010*).

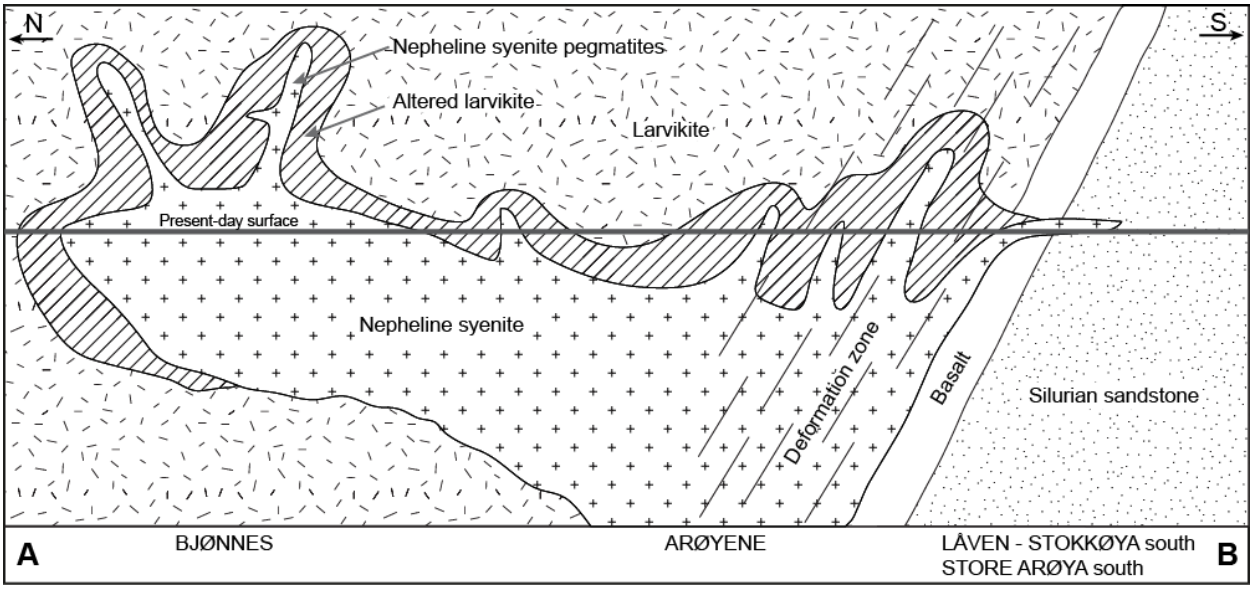

Figure 3: An interpretation of the Bjønnes syenite and its extent beneath the Langesundsfjord, showing how nepheline syenite pegmatites originate from the pluton, radiating outward into surrounding larvikite. The model shows a schematic cross-section from A – B, shown in Figure 2 (modified from *Dahlgren, 2010*).

A model produced by *Dahlgren (2010*), as seen in Figure 3, suggests that the Bjønnes syenite and other intrusive nepheline syenites may be part of a larger nepheline syenite system across the Langesundsfjord area. The model also suggests

that the mildly agpaitic nepheline syenite pegmatites in the LPC originate from residual melts from the Bjønnes syenite pluton, which intruded into surrounding larvikite. In reality, little is known about the relationship between the nepheline syenites of the Bjønnes pluton and the smaller nepheline syenite bodies in the Langesundsfjord and Tvedalen.

1.2 Alkaline felsic systems

In most alkaline systems, mafic silicate minerals, notably pyroxene and amphibole, are significant components that are involved in all stages of evolution. Their extensive variability in composition makes them ideal for tracking the evolution of magmatic evolution and analysing the effects of mineral fractionation and contamination (*Marks et al, 2004; Reguir et al., 2012*). In the LPC, major and trace element analytical studies of pyroxenes and amphiboles have been previously conducted by *Neumann (1976)*, *Murad et al. (2006)* and *Piilonen et al. (2013)*, whilst major element analytical studies are also available from *Larsen (1995)* and *Larsen & Raade (1997)*. *Larsen (1998)* also provides geochemical data from micas in the LPC.

The major elemental trends of clinopyroxenes tend to evolve from diopsidic with low Na content towards sodic, ferric compositions through fractionation, with the degree and timing of this change related to oxygen fugacity. Amphiboles follow similar trends, evolving from calcic to sodic through fractionation (*Marks et al., 2004*). In the LPC, clinopyroxenes in mildly agpaitic pegmatites are rich in Na and Fe^{3+} towards an aegirine composition whilst miaskitic pegmatites have more diopsidic clinopyroxene compositions (*Piilonen et al., 2013*). Amphiboles in the LPC also show a similar evolutionary trend to corresponding pyroxenes (*Neumann, 1976; Piilonen et al., 2013*) This fractionation trend is often considered to be a result of the fractional crystallisation of plagioclase, altering Na/Ca ratios and Al content in the melt (*Neumann, 1976*).

The composition of trace elements in alkaline rocks is less dependent on the host minerals and partitioning is controlled more by the melt composition, so better reflects magmatic processes. An important trace element in alkaline rocks is zirconium, which becomes enriched in the most sodic mafic minerals increasing in content concordantly with Na/Ca ratios, as they are more easily incorporated into the mineral structure (*Marks et al., 2004*). In contrast, Ti decreases as Na increases (*Piilonen et al., 2013*).

Zirconium also shows a slight partitioning preference towards clinopyroxenes over amphiboles (*Marks et al., 2004*). The partitioning of Zr into clinopyroxene and amphibole is dependent on a complex interplay of alkalinity, silica activity and oxygen

fugacity. Under the right conditions clinopyroxene and amphibole can act as a Zr sink, preventing the formation of more typical Zr-bearing minerals (*Andersen et al., 2011*). The atomic radius of Zr^{4+} is also identical to that of Mg^{2+}, which makes it an ideal occupant of the M1-site in clinopyroxene, assuming that a suitable charge-balancing mechanism can be found.

Zircon is a common accessory mineral in most igneous rocks, particularly in felsic rocks. It is the principal host mineral for Zr, whilst other trace elements such as Hf, U, Th and heavy rare earth elements (HREE's) also have strong partitions to zircon. Crystallisation of zircon is dependent on factors such as temperature, volatile content, Zr content, silica saturation, alkalinity and halogen activities (*Watson & Harrison, 1983; Andersen et al., 2010*). The presence of zircon, and subsequent distribution of Zr, can therefore be used as a decent petrogenetic indicator for highly evolved felsic rocks such as nepheline syenites.

Agpaitic rocks were originally defined by *Ussing (1912)* as rocks with a molecular ratio (alkalinity index) of ((Na + K) / Al) > 1.2. Under modern nomenclature, they are now described as peralkaline nepheline syenites with an alkalinity index of > 1.0 and the presence of complex Zr- and Ti-silicate minerals as opposed to zircon, titanite and ilmenite (*Sørensen 1992; Khomyakov, 1995; Le Maitre, 2002*). Agpaitic Zr-silicate minerals found in the Oslo Rift include catapleiite and members of the rosenbuschite-group, wöhlerite-group and eudialyte-group minerals in assemblages that are dependent on a number of factors such as peralkalinity, water activity and fluorine activity, discussed in *Andersen et al. (2010).* Zircon can occasionally coexist in some assemblages. More complex Zr-silicate mineral assemblages exist in more highly agpaitic complexes (*Sørensen, 1997*). Rocks with an alkalinity index of < 1.0 or that contain zircon, ilmenite and titanite as characteristic minerals are defined as miaskitic. Peralkaline nepheline syenites (alkalinity index > 1.0) can therefore be classified as either agpaitic or miaskitic depending on their mineral assemblages (Khomyakov, 1995; *Le Maitre, 2002*).

Agpaitic nepheline syenites require extensive differentiation from a mafic parental source at low oxygen fugacity. This important factor allows the presence of a CH_4 fluid phase as opposed to CO_2-H_2O, which causes a fractionating melt to become rich in sodium, fluorine, chlorine and other volatiles. This enrichment is necessary for the formation of characteristic complex zirconium and titanium silicate minerals as N-, Cl- and F-enriched melts increase the solubility of HFSE (high field-strength elements) such as Zr and Ti (*Marks et al., 2011 and references within*).

1.3 Methodology

Samples were collected from Bjønnes, Tvedalen and from Lågendalen (RS IX and X), and were chosen based on geological significance and geographical distribution. The samples were labelled and GPS coordinates were recorded. Most samples were collected with the intention to use for whole rock characterisation so were large enough to be representative of the whole rock that accurately represented the sample area. Other samples were collected to display textural features and were not used for whole rock characterisation. Due to the heterogeneous nature of the Bjønnes syenite, representative whole rock samples could not be collected and these samples were not selected for whole rock analysis. Other hand specimen samples were collected from the three study areas but were not analysed and were used mainly as reference materials.

Samples were cleaned after collection and surface alteration and irregularities were removed using a circular saw if necessary. The circular saw was also used to reduce the size of large blocks to be crushed and to cut thin section blocks. A total of 21 thin sections were prepared at the Department of Geosciences, University of Oslo. All thin sections were polished, uncovered and were 30 μm thick. Thin sections were taken from the same material as their corresponding whole rock samples.

1.3.1 Whole rock characterisation

Eighteen samples were selected for whole rock characterisation. The samples were cleaned using a sonic bath and dried in an oven before crushing. A jaw crusher was used to crush samples into an aggregate of <10 mm in diameter. The crusher and equipment were cleaned thoroughly between uses to avoid contamination. A representative 20g of material from sample was then extracted for milling. A Cr-V steel cross mill was used to further reduce the grain size to <125 μm. The mill and equipment were also cleaned between uses.

The milled samples were sent to ACME Labs (Bureau Veritas Commodities Canada Ltd.) in Vancouver, Canada for analysis. Total whole rock characterisation (package LF200) was performed by ICP-ES for major elements and ICP-MS for trace elements, analysing a suite of 44 elements. Minimum detection limits and upper resolution limits for each element can be found in the whole rock raw geochemical data table (see Appendix 2). Iron analyses were determined as Fe_2O_3 only, which also represents ΣFe.

1.3.2 Electron microprobe analysis

Electron microprobe analysis was conducted at the Department of Geosciences, University of Oslo, using a Cameca SX100 instrument fitted with five wavelength-dispersive (WDS) spectrometers. An accelerating voltage of 15kV and current of 15nA were used, giving a beam diameter of approximately 0.1 μm and an excitation volume of 1-2 μm^3. Counting time was 10 seconds.

A total of 10 elements were sought after. Calibration standards and X-ray lines used were wollastonite (Si Kα, Ca Kα), Al_2O_3 (Al Kα), pyrophanite (Ti Kα, Mn Kα), Fe metal (Fe Kα), MgO (Mg Kα), orthoclase (K Kα), albite (Na Kα) and Monastery Mine zircon (Zr Lα). Matrix effects and elemental overlaps were corrected with the Cameca PAP procedure (*Pouchou and Pichoir, 1984*). The first analysed elements were Na and K since they were most susceptible to dissipation. SEM EDS analysis was used to check minerals to ensure that they did not contain significant amounts of other elements that were not sought after by EMP analysis.

Before analysis, selected thin section samples were coated in a carbon film. A total of ten samples were analysed by EMP. The analysis was focused on collecting compositional data for mafic minerals (clinopyroxene and amphibole). Additional data was also collected on other minerals such as biotite, olivine and aenigmatite. Each area of interest was analysed with two to three analytical points in close proximity to avoid anomalous data and increase precision.

1.3.3 Scanning electron microscope

Energy-dispersive X-ray spectrometry (EDS) was conducted at the Department of Geosciences, University of Oslo, using a Hitachi SU5000 scanning electron microscope (SEM) equipped with a Bruker XFlash 6|30 detector. It was used to identify accessory minerals within samples. Backscatter electron (BSE) imaging was done using both SEM and EMP.

1.3.4 Data calculations & software

Raw data for whole rock characterisation and EMP analysis can be found in Appendix 2 and Appendix 4 respectively. All presented whole rock data is within the range of the minimum detection limit and maximum resolution limit for its corresponding element. Nickel and chromium data were ignored from analysis because their enrichment is a product of the crushing equipment used in sample preparation.

Rare-Earth element data from the lanthanide series (REE) were normalised to C-1 chondrite values (*McDonough & Sun, 1995*) and plotted on a logarithmic scale using ioGas software.

The EMP data were grouped with similar data from the same samples, which were deemed to be slight variations of the same compositions. An uncertainty of 2 standard deviations (2σ) has been applied and presented with data consisting of analyses from more than one point. Anomalous data were removed if deemed unreliable, for example an apparent mixture of two mineral compositions at a grain boundary.

Pyroxene mineral formulae were calculated from EMP data using a spreadsheet constructed by *Brady & Perkins (2015)*. Since EMP analysis cannot distinguish Fe^{3+} from Fe^{2+}, the data for FeO represents FeO_{total} and therefore ΣFe atoms per formula unit. The spreadsheet recalculates the $Fe^{3+}/\Sigma Fe$ ratio based on stoichiometry and charge balance. Pyroxene end-member proportions for the aegirine-diopside-hedenbergite (Ae-Di-Hd) ternary system were calculated manually. The lack or absence of aluminium calculated in the octahedral sites implied that a jadeite (Jd) end-member component would be relatively insignificant. Biotite mineral formulae were calculated using the same method.

Amphibole mineral formulae were calculated using a spreadsheet presented by *Locock (2014)*, which uses a set of assumptions for each analysis that can be determined manually. The $Fe^{3+}/\Sigma Fe$ ratio is estimated based on charge balance and assumptions on site occupancy. The spreadsheet also determines the name of each analysis according to amphibole nomenclature recommended by the International Mineralogical Association (*Hawthorne et al., 2012*).

1.3.5 Mineral formulae and abbreviations

Ideal mineral formulae used within this text and for identification and calculation purposes are from *Strunz & Nickel (2001)*, and supplemented by data from *https://www.mindat.org/*. Mineral abbreviations used in figures throughout this text are in accordance with *Whitney & Evans (2010)*, and supplemented by *Marks et al. (2011)*. A selection of minerals relevant to this text and their abbreviations and ideal formulae can be found in the glossary.

2. Description of the Bjønnes syenite and related rocks

Fieldwork and sample acquisition was undertaken in three areas of the LPC; Bjønnes, Tvedalen and Lågendalen. The broad locations of these areas are indicated in Figure 4 in relation to the ring sections of the LPC. As can be seen, Bjønnes and Tvedalen sit within RS VI and Lågendalen covers an area across RS IX and X. Geographically, Bjønnes and Tvedalen are much closer together than Lågendalen.

The following chapter gives detailed descriptions on field relationships and textural variations of the nepheline syenites from each of the three study areas, as well as mineralogy and petrography of the collected samples.

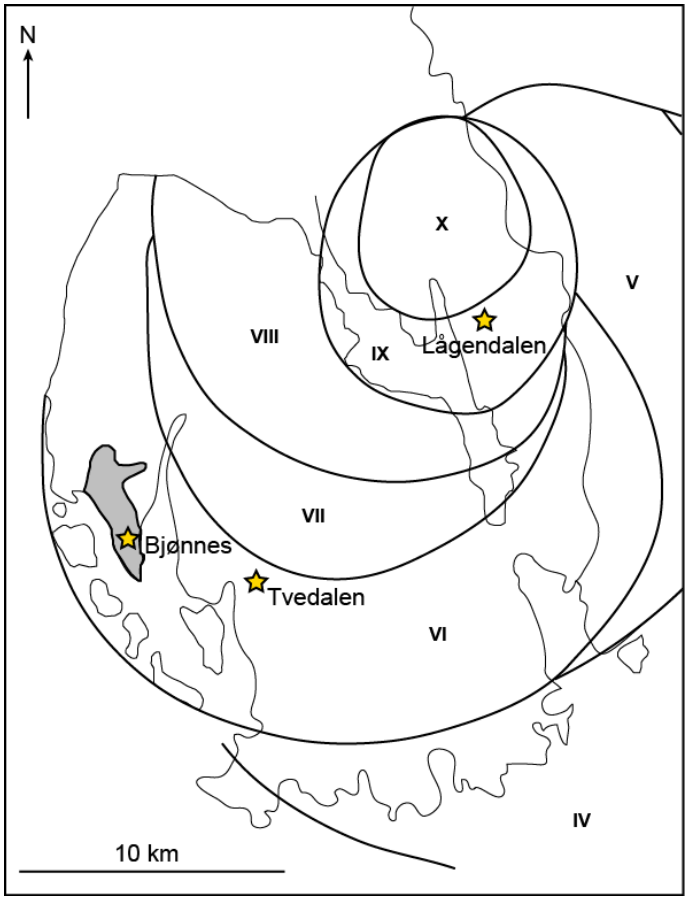

Figure 4: Map of the Western LPC including ring sections, showing the broad location of the three main study areas (modified from *Dahlgren, 2010*; see Figure 2 for full LPC).

2.1 Samples

Table 1 shows the samples collected from the three study areas and used for analysis, giving details about the samples themselves and what analytical techniques were performed on them. GPS coordinates provided are easting and northing coordinates for UTM projection at 32N. Many other samples were also collected as reference materials but were not used for analysis. Supplementary thin sections of samples collected by *Raade (1973)* were used, particularly to describe larvikite and samples from Lågendalen.

Table 1: A list of samples collected and used for analysis. Rock types for Bjønnes samples include texture classification.

Sample	Rock type	Location		Analysis			
		Study area	GPS coordinates	WR	Optical	WDS	EDS
NTG6	Nep. Sy. (equigranular)	Bjønnes	054418 654664	✓	✓	✓	✓
NTG7	Nep. Sy. (trachytoid)	Bjønnes	054446 654529		✓		
NTG8	Nep. Sy. (trachytoid)	Bjønnes	054442 654560	✓	✓	✓	✓
NTG12	Foyaite	Lågendalen	055613 655833	✓	*		
NTG14	Foyaite	Lågendalen	055811 655830	✓	*		
NTG15	Nep. Sy. (gneissic)	Bjønnes	054365 654689	✓	✓	✓	✓
NTG16a	Nep. Sy. dyke	Tvedalen	054773 654546		✓		
NTG16b	Nep. Sy. dyke	Tvedalen	054773 654546	✓	✓		
NTG17	Nep. Sy. (porphyritic)	Bjønnes	054402 654547	✓	✓	✓	✓
NTG18	Nep. Sy. (gneissic)	Bjønnes	054379 654577	✓	✓	✓	
NTG19	Nep. Sy. (gneissic)	Bjønnes	054386 654556		✓	✓	✓
NTG20	Nep. Sy. (equigranular)	Bjønnes	054448 654490	✓	✓	✓	
NTG21	Nep. Sy. (gneissic)	Bjønnes	054386 654671	✓	✓	✓	
NTG22	Nep. Sy. dyke	Bjønnes	054498 654741	✓	✓		✓
NTG23	Nep. Sy. (gneissic)	Bjønnes	054369 654682	✓	✓		✓
NTG24	Nep. Sy. (gneissic)	Bjønnes	054358 654706	✓	✓		
NTG25	Nep. Sy. (gneissic)	Bjønnes	054365 654696	✓	✓	✓	✓
NTG26a	Nep. Sy. dyke	Tvedalen	055046 654368	✓	✓		
NTG26b	Nep. Sy. dyke	Tvedalen	055046 654368	✓	✓		
NTG29	Nep. Sy. dyke	Tvedalen	054868 654529	✓	✓		
NTG30	Nep. Sy. (gneissic)	Bjønnes	054394 654528	✓	✓	✓	✓
NTG33	Nep. Sy. (gneissic)	Bjønnes	054332 654710		✓		

* Supplemented by samples collected by *Raade (1973)*.
WR – whole rock geochemical analysis
WDS – analysis using electron microprobe
EDS – analysis using scanning electron microscope

2.2 Larvikite (RS VI)

The Bjønnes syenite and the syenite dykes in Tvedalen, both within RS VI of the LPC, are surrounded by nepheline-bearing larvikite, which shows very little textural variation between the two areas. The larvikite is coarse-grained and homogeneous, dominated by euhedral, perthitic feldspars up to 2 cm in length. The feldspars give the larvikite its characteristic blue Schiller effect and blue/light grey appearance, however in the Bjønnes area feldspars are often bleached white as a product of weathering. Dark minerals including olivine, clinopyroxene, amphibole, biotite and Fe-Ti oxides are found interstitially. Larvikite also contains zircon and apatite as accessory minerals.

Rhythmic, sub-horizontal magmatic layering can be seen in both areas, best observed in the quarry faces of Tvedalen. The layers comprise of a higher relative proportion of mafic minerals towards the base, probably a result of gravitational settling.

2.3 Bjønnes syenite

The Bjønnes syenite outcrops mainly across the South and West of the Bjønnes peninsula, as well as several small islands in the surrounding area. The main outcrop spans approximately 6 km^2, showing an irregular and N-S elongated shape. The syenite was observed to be very heterogeneous, particularly towards the pluton boundary. Because of this, the syenite has been divided into four units based on textural variations. Figure 5 shows a geological map of the Bjønnes syenite, displaying the extent of the pluton as observed from the surface and the distribution of these textures and also the locations of collected samples listed in Table 1. The Bjønnes peninsula is largely covered by woodland and is the site of many holiday cabins, making systematic sampling impossible.

2.3.1 Textural overview

The Bjønnes syenite is medium to coarse grained and generally light coloured, dominated by perthitic feldspars, which made up approximately 60 – 80 % of the rock volume (excluding extreme local compositional variations). Feldspar habit ranges from equigranular to tabular lathes.

The abundance of nepheline ranges from approximately 2 – 25 % average whole rock volume. Generally as modal volume of nepheline increases, nepheline crystals tend to be larger and more euhedral. Abundance can vary greatly over small distances. In some places nepheline crystals could be found grouped together as 'nepheline roses', as seen in Figure 6, taken from the location of NTG7. Nepheline content was not used as an influential component in categorising different units of the Bjønnes syenite in the field due to common, significant local concentration variations and its diverse weathering profiles, making it much more visible in some areas than others.

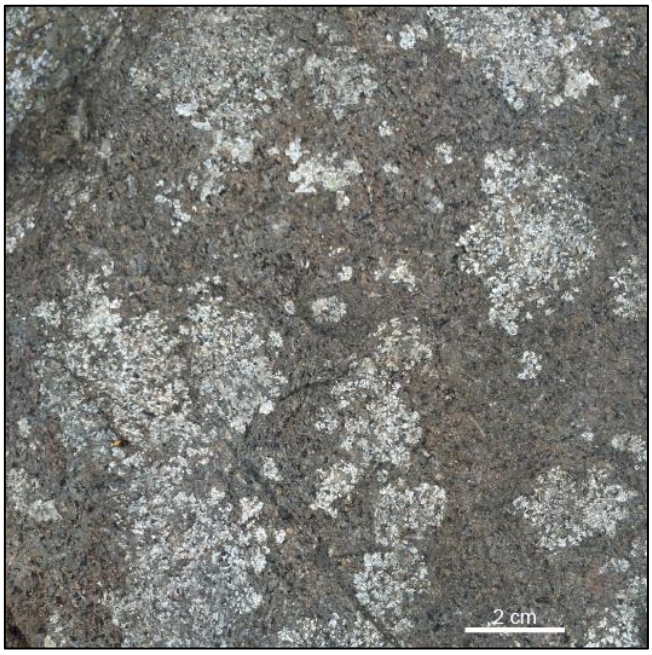

Figure 6: Nepheline 'roses' in trachytoid syenite at location of NTG7, where the weathering profile highlights the distribution of nepheline (white) as being confined in concentrated patches or 'roses'.

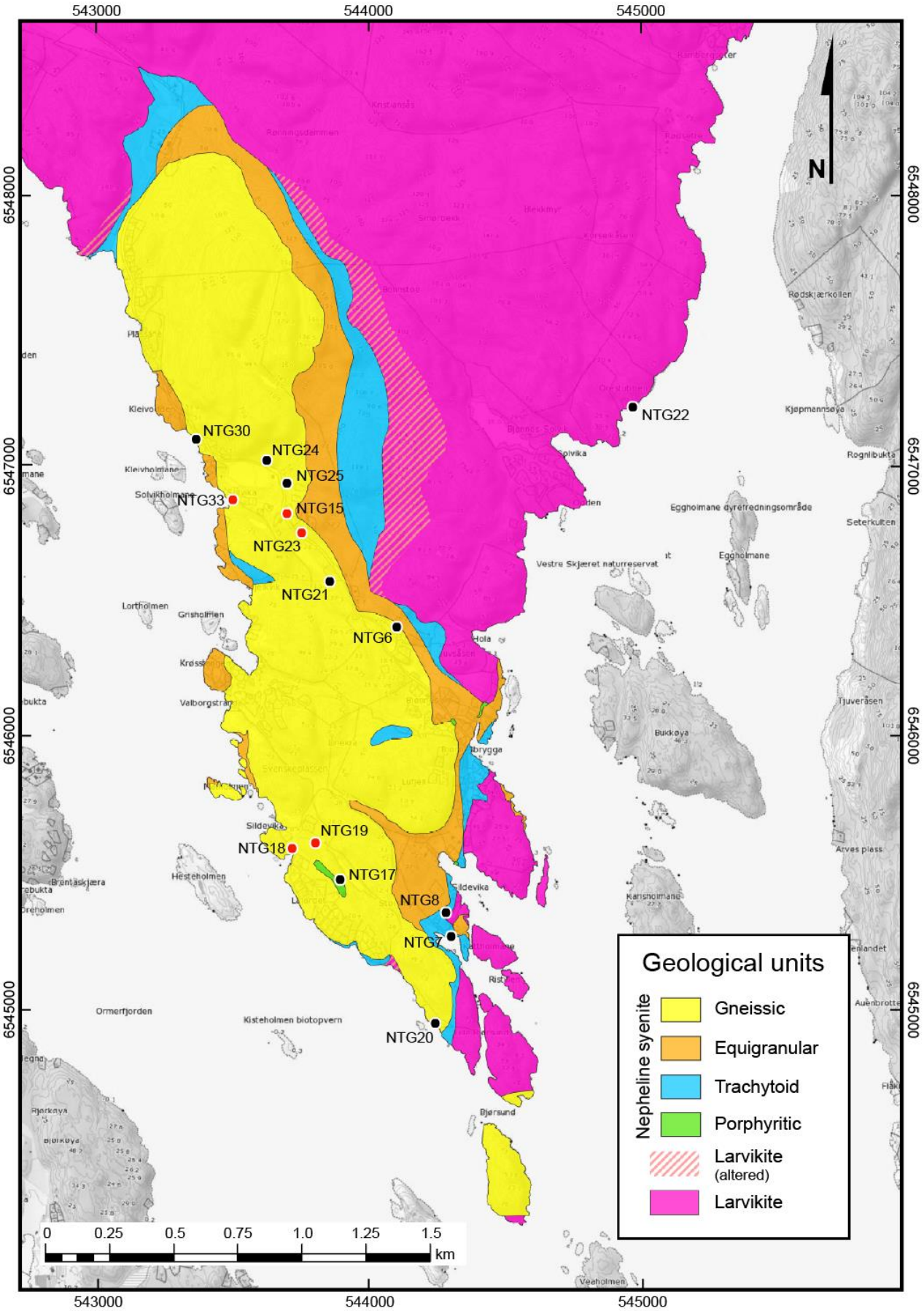

Figure 5: Geological map of Bjønnes showing textural variation of the Bjønnes nepheline syenite (produced by Cassandra Ugland) and sample locations (see Table 1). Samples with red points contain eudialyte.

Dark minerals, mostly consisting of pyroxene, amphibole, biotite and Fe-Ti oxides, often create a spotty appearance to the syenite, either as large single grains or as polymineralic aggregates. These spots can reach sizes of up to 2 cm in diameter. Their shapes vary from tight, round spots, to poikilitic, branching and irregular spots. A key factor in categorising syenite textures in the field was whether the texture was defined by these mafic spots or by the feldspars.

The Bjønnes syenite was divided into four textural categories; gneissic, trachytoid, equigranular and porphyritic. These four textures are described below. It must be emphasised that the Bjønnes syenite is very texturally heterogeneous and transitional. Consequently, the nepheline syenite will always contain elements of gneissic, trachytoid and equigranular textures, despite its classification. This does not apply to porphyritic texture, which is distinct, as discussed below.

2.3.2 Gneissic texture

The gneissic texture of nepheline syenites from the Langesundsfjord was originally described as ‘ditroite schist’ by *Brøgger (1890)* and refers to the magmatic foliation produced in the rock, often resulting in a gneissic appearance. The foliation, or as is more commonly observed, lineation of the syenite creates a banded appearance. As shown by Figure 5, gneissic syenite is the most widespread texture observed in the Bjønnes syenite. The intensity of this gneissic texture is variable. Around the location of NTG15 for example, mafic and felsic minerals are separated into individual bands.

The gneissic texture refers mostly to the differentiation of mafic minerals. In gneissic syenite it is common that bands rich in large mafic spots, often rich in amphibole and biotite, would alternate with mafic-poor bands containing relatively small mafic minerals, mostly pyroxene, elongated parallel to banding. This is shown in Figure 7. Feldspars in gneissic syenite also show a primary alignment in the direction of banding, at least to some extent. Modal nepheline content was observed to fluctuate between these bands in some places. In eudialyte-bearing gneissic syenite, eudialyte is also typically found concentrated in certain bands.

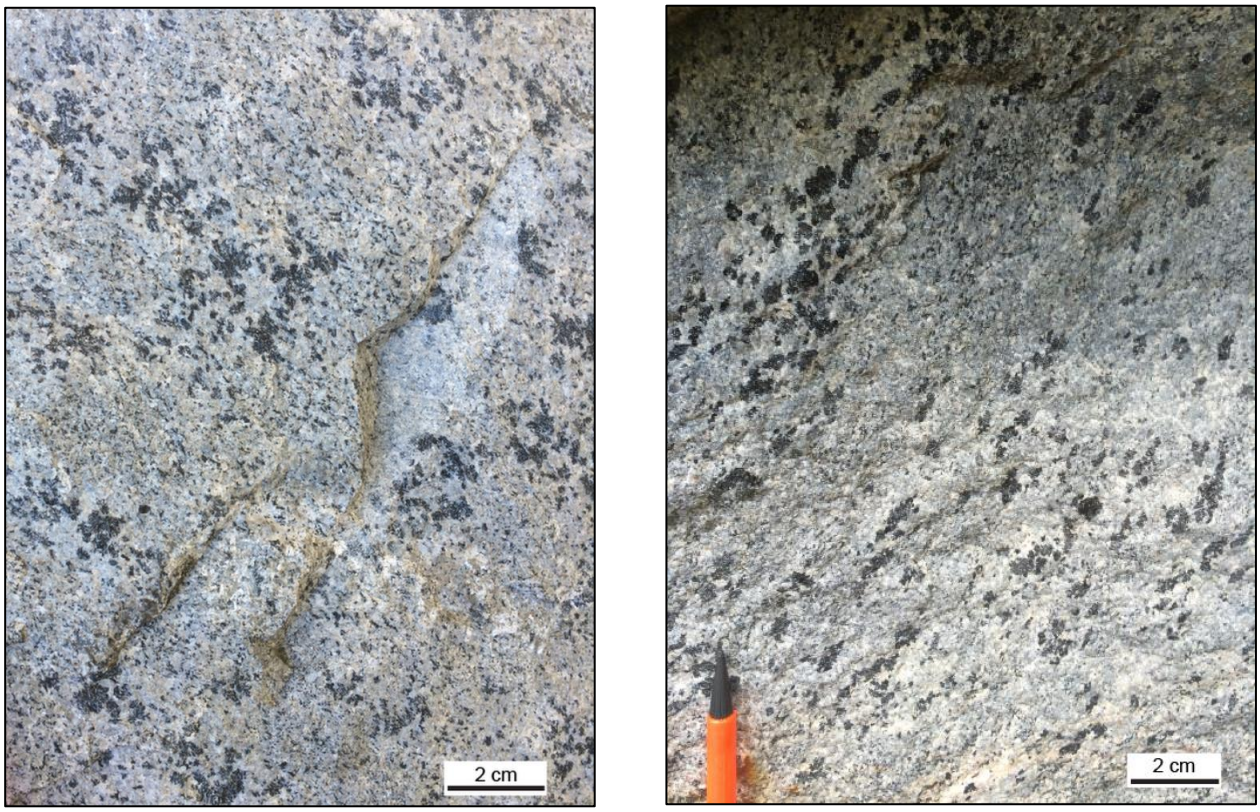

Figure 7: Nepheline syenite with gneissic texture, showing alternating bands of syenite with large, rounded mafic mineral clusters, and more felsic bands with small elongated mafic minerals. Images were taken from the localities of samples NTG26b (left) and NTG15 (right) respectively.

2.3.3 Equigranular texture

Equigranular texture is defined by the less dominant appearance of feldspars and lack of gneissic banding. Feldspars are tabular to equigranular and have less textural control, allowing the formation of mafic spots, although they often show an alignment. The equigranular syenite is the non-banded equivalent of the gneissic syenite. It seemingly represents a variety of nepheline syenite which has not undergone the deformation process that defines the gneissic syenite. It is likely that there is a gradational transformation from equigranular to gneissic through increased deformation. This leaves mafic minerals unsorted, resulting in a

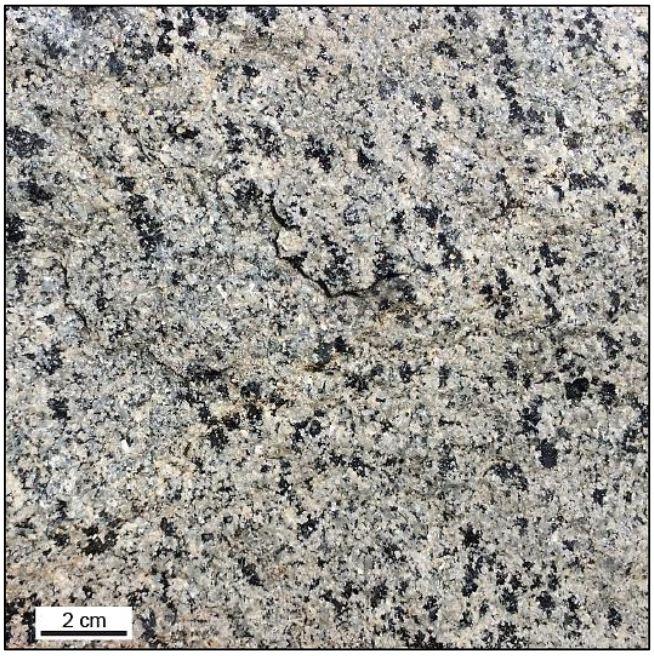

Figure 8: Equigranular syenite texture showing unsorted mafic spots and less dominant feldspar lathes mixed with euhedral nepheline. The photograph does not represent a named sample but provides a good representation of the texture.

more random distribution. Figure 8 shows an example of equigranular syenite. It may show some alignment of mafic minerals in places but unlike the examples shown in Figure 7, they are not differentiated into bands. An unusual equigranular syenite is represented by NTG20, which is fine grained and relatively dark in colour. It has low nepheline content and patches of larger mafic minerals, mostly biotite, scattered throughout.

2.3.4 Trachytoid texture

Trachytoid texture is defined by platy feldspars, often aligned to form flow textures. The example in Figure 9 shows a trachytoid syenite with poorly developed flow textures. The trachytoid syenite shares a similar appearance to foyaites in Lågendalen (see Figure 29). Mafic minerals and, to an extent nepheline, fill interstitial spaces between feldspar lathes. Nepheline content is generally lower than gneissic and equigranular syenites. Mafic content is more scattered and evenly distributed than in gneissic syenite and the rock loses its 'spotty' appearance that is characteristic of the gneissic and equigranular syenites. The grain sizes of mafic minerals often depend on the size of feldspars, where porphyritic syenites containing larger feldspars result in larger mafic minerals since there are larger interstitial spaces to accommodate. Two samples, NTG7 and NTG8, represent the area containing 'nepheline roses', seen in Figure 6. The syenites themselves are relatively dark in colour and often show a rusted surface. Nepheline content in NTG7 is mostly confined to these roses and is very low outside of them.

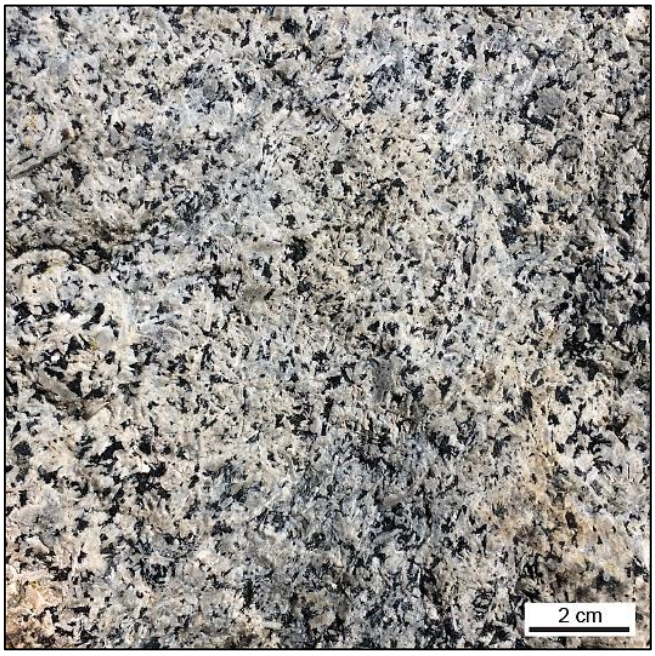

Figure 9: Trachytoid syenite texture, with white tabular feldspars dominating the appearance, with dark minerals infilling interstitial space. The photograph does not represent a named sample but provides a good representation of the texture.

2.3.5 Porphyritic texture

Porphyritic texture is defined by the presence of large, randomly-orientated and fairly evenly-distributed feldspar lathes in varying concentrations. These feldspars are approximately 2 cm in length and have a very similar appearance to those found in surrounding larvikite, yet are much larger to those in any observed nepheline syenite in

the LPC, excluding lardalites. The feldspars maintain a good elongated tabular shape but tend to display slightly rounded edges. The surrounding nepheline syenite remains consistent with others in the Bjønnes syenite, with a gneissic, trachytoid or equigranular texture. However these feldspar megacrysts result in a unique texture. Occurrences of this texture are rare in the Bjønnes syenite and appear to be confined to small areas. An example of porphyritic syenite is represented by NTG17, taken from the largest found continuous outcrop (see Figure 10). The syenite itself has an equigranular texture and is rich in mafic minerals, with feldspar megacrysts occupying approximately 30 % of its volume.

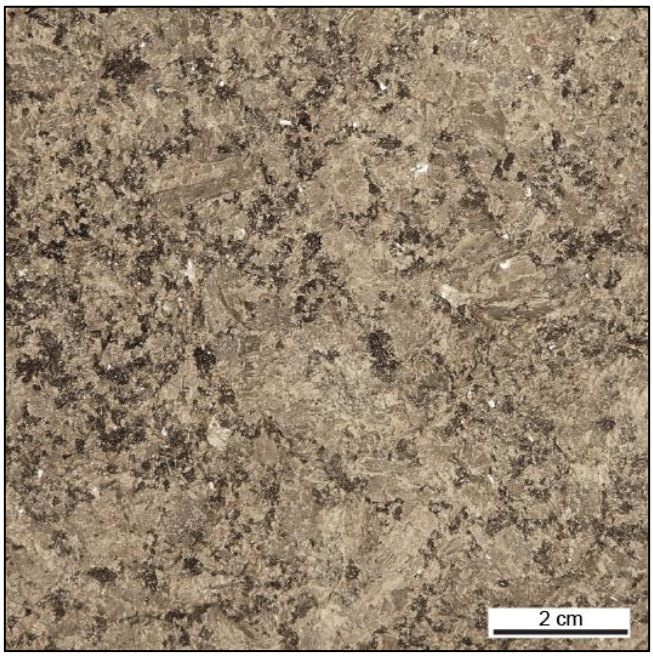

Figure 10: porphyritic syenite texture showing randomly orientated feldspar megacrysts up to 2 cm in length within a finer grained equigranular syenite. Taken from locality of NTG17.

As can be seen from Figure 5, there appears to be a general zonation of the exposed Bjønnes syenite, with a gneissic core. The syenite towards the edge of the pluton grades into equigranular and then trachytoid. This suggests that the factors creating the gneissic texture are more prevalent in the core, since the equigranular syenite is similar but without banding. The feldspars at the rim of the pluton are relatively well-formed and create the trachytoid texture. Flow textures are more likely the result of a different process than those that produced gneissic banding, since the syenite interacts strongly with surrounding larvikite, as discussed below, and the trachytoid texture is generally confined to the outer parts of the Bjønnes syenite. There are no evident constraints on the location of the porphyritic syenite.

2.3.6 Mineral banding

A smaller-scale factor in the heterogeneity of the Bjønnes syenite is mineral banding, particularly relevant for the local distribution of mafic minerals and nepheline. Mafic banding mainly affects exposures of trachytoid syenites in the outer regions of the pluton. Irregular bands of mafic-rich material run through the syenite, both concordant and discordant with flow textures or banding. Some bands have clear controls, such as being confined along a boundary between two different syenite bodies, as seen in

Figure 11, whereas others show no clear constraints, such as Figure 12, where bands curve against flow direction and appear very discontinuous. Irregular, rounded enclaves dominated by mafic minerals were also found and were up to 50 cm in diameter, occasionally deformed by the direction of flow of the surrounding nepheline syenite (see Figure 13).

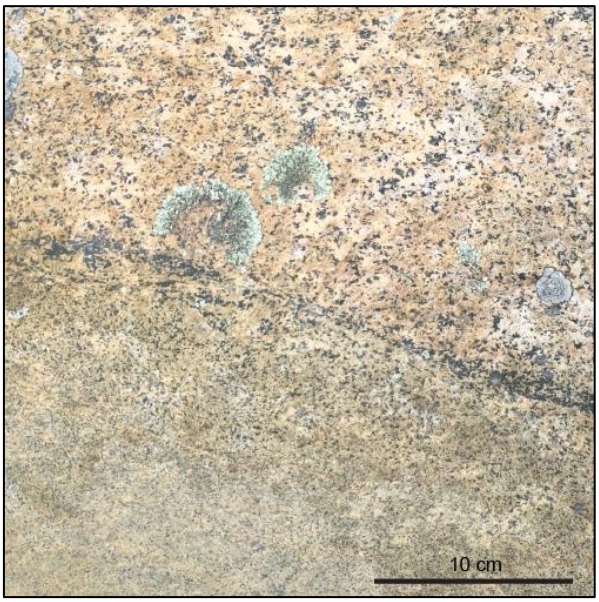

Figure 11: Two bodies of trachytoid syenite (coarse above, fine below) divided by a linear band of mafic material along the contact.

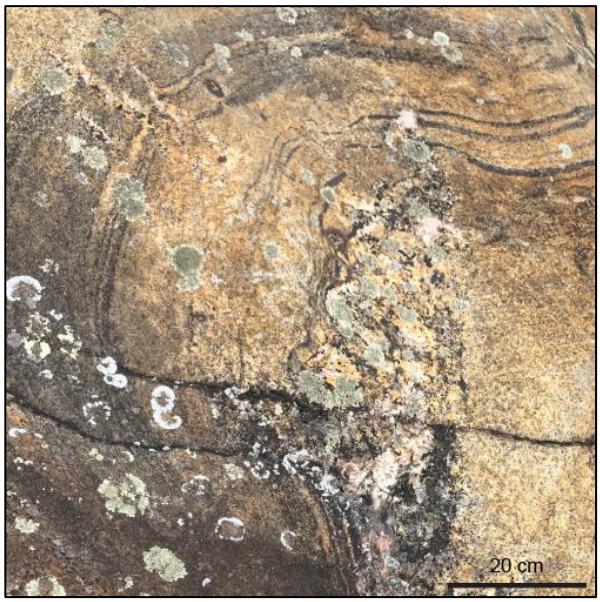

Figure 12: A series of meandering, irregular and discontinuous bands rich in mafic material within syenite, running parallel to flow textures. The bands stretch for approximately 5 m before gradually dissipating.

Figure 13: An enclave of highly concentrated mafic material sits within a trachytoid syenite. The light material above is fresh exposure of the syenite, and the termination of a mafic band can be seen to the right.

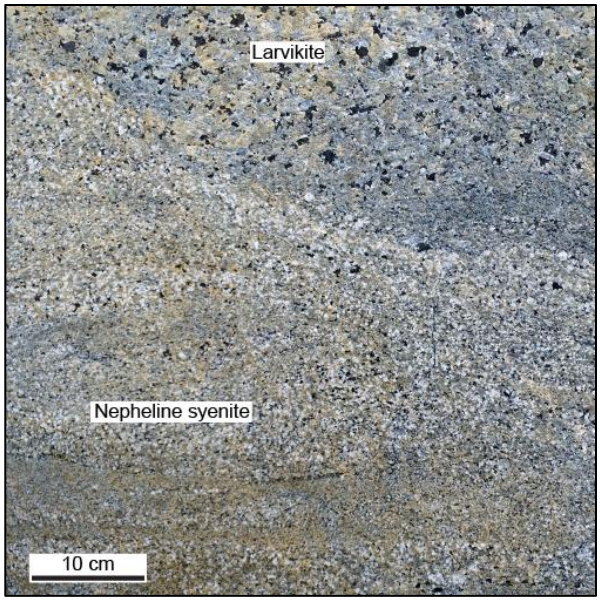

Figure 14: Nepheline banding within the flow textures of a syenite. Nepheline is the white mineral, and concentration varies greatly between bands. Towards the top right is part of a rounded larvikite block, most likely a xenolith.

The banding of nepheline is more widespread throughout the Bjønnes syenite, often concordant to general flow textures. An example of this can be seen in Figure 14, where the weathered surface gives nepheline a white appearance, allowing it to stand out and display its relative differences in concentration.

2.3.7 Eudialyte in syenite

Eudialyte is a complex Zr-silicate mineral commonly found in low to highly apgaitic associations (*Khomyakov, 1995*). In the LPC, eudialyte has previously been found only as a late-magmatic constituent of nepheline syenite pegmatites (*Bollingberg et al. 1983; Schilling et al., 2011*). At Bjønnes, eudialyte was discovered as a primary phase in the syenite, occurring mainly as an early magmatic mineral and also interstitially as a late magmatic mineral. Its presence is indicative of agpaitic mineral assemblages existing within the Bjønnes syenite.

Eudialyte distribution in the Bjønnes syenite is highly irregular, with substantial amounts observed at only a small number of locations. These locations are not expansive, with eudialyte occurring in high concentrations over small, isolated areas of just tens of square metres within the syenite. Five analysed samples from Bjønnes are eudialyte-bearing and they seem to collectively represent three eudialyte syenite areas. NTG15 and NTG23 appear to be parts of the same eudialyte syenite, whilst NTG18 and NTG 19 are probably also related to each other. NTG33 represents a third eudialyte syenite occurrence. The expanse of eudialyte-bearing syenite can be seen from Figure 5, where NTG15 and NTG23 are flanked by NTG25 to the North-West and NTG21 to the South-East, both absent in eudialyte, but containing zircon.

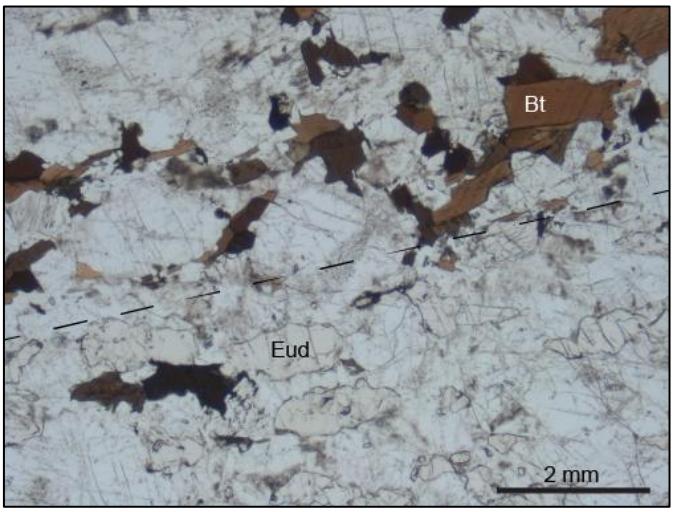

Figure 15: PPL image of gneissic syenite showing primary eudialyte (Eud) mostly confined to the lower band and separated from a biotite-rich (Bt) band directly above. Taken from NTG15b.

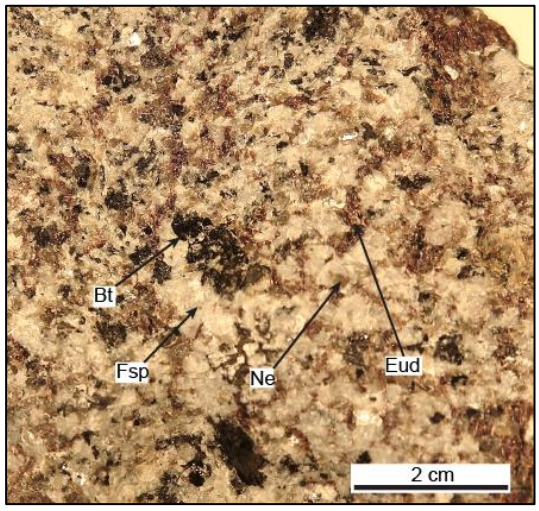

Figure 16: Eudialyte-rich syenite represented by NTG18 showing interstitial eudialyte (Eud), and also relatively large eudialyte (top right) and biotite (centre, low centre) crystals within a medium-grained syenite.

Eudialyte was found in gneissic syenite with high nepheline content. Typically, the gneissic texture of the syenites concentrates eudialyte into bands of felsic material, separating it somewhat from bands of dark minerals, as seen in Figure 15. The concentrations of eudialyte in these bands vary massively from 0 – 50 % and concentrations also change laterally throughout bands. In some cases, eudialyte is present in high concentrations in one band and absent in those directly above and below. Another feature of eudialyte-bearing syenite is the occasional presence of abnormally large eudialyte and biotite crystals within the syenite, like in Figure 16.

Eudialyte was also found infrequently outside of these three main, eudialyte-rich zones within the Bjønnes syenite. It primarily exists in small, isolated eudialyte-rich pockets within syenite, found particularly along the West coast of Bjønnes. They typically include euhedral nepheline and biotite surrounded by interstitial eudialyte, or primary eudialyte and biotite surrounded by nepheline and feldspar. Nepheline often shows evidence of hydrothermal alteration into an assortment zeolites, most commonly natrolite and analcime. This alteration process is seen throughout the LPC and is known locally as spreustein (*Brøgger, 1890; Dahlgren, 2010*). Eudialyte in some pockets also showed alteration in the form of green secondary aegirine rims. The pockets are typically surrounded by eudialyte-absent syenite. However many of these pockets grade into the surrounding syenite and small amounts of eudialyte are often found within a small radius around the pockets. Grain size is very variable, with large eudialyte and biotite crystals being common, often producing a pegmatitic texture. They

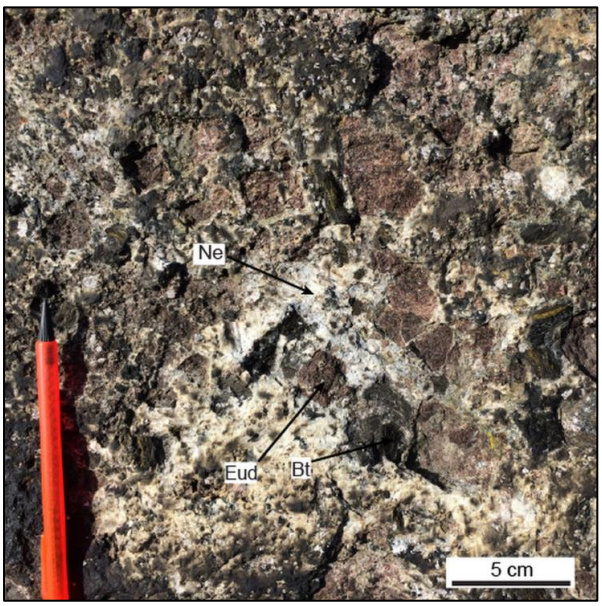

Figure 17: Pegmatite pocket containing primary eudialyte (Eud) and biotite (Bt). There are several similar pockets in close proximity that account for all eudialyte content in the local area. The pockets show a distinct contact with the surrounding syenite.

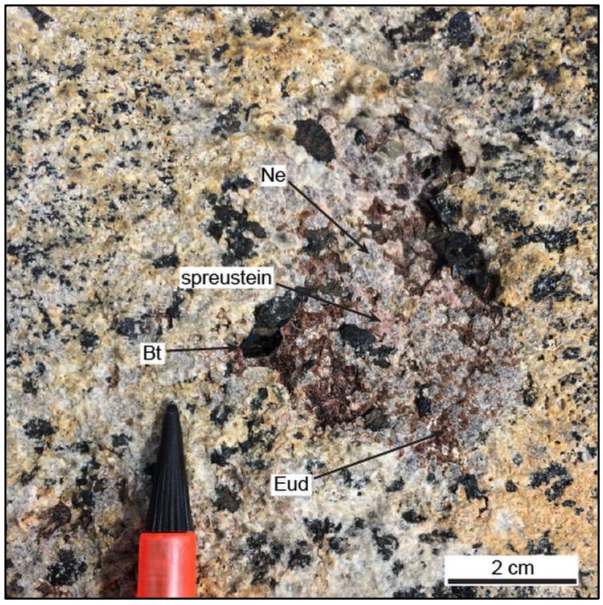

Figure 18: Eudialyte-rich pocket of material with interstitial eudialyte (Eud) between primary biotite (Bt) and nepheline (Ne). Small amounts of eudialyte are present in the surrounding syenite. The pocket grades into the surrounding syenite.

appear to represent small pegmatite-like pockets of material, as shown in Figures 17 and 18.

2.3.8 Larvikite-syenite relationship

There are two types of contact between the Bjønnes syenite and the surrounding larvikite. Observed contacts to the North-West and East of the pluton were typically sharp, presumably occurring along fault planes. The non-faulted contact between syenite and larvikite is typically much more transitional. In Figure 5, larvikite that has seemingly been affected by the Bjønnes syenite has been labelled as altered larvikite.

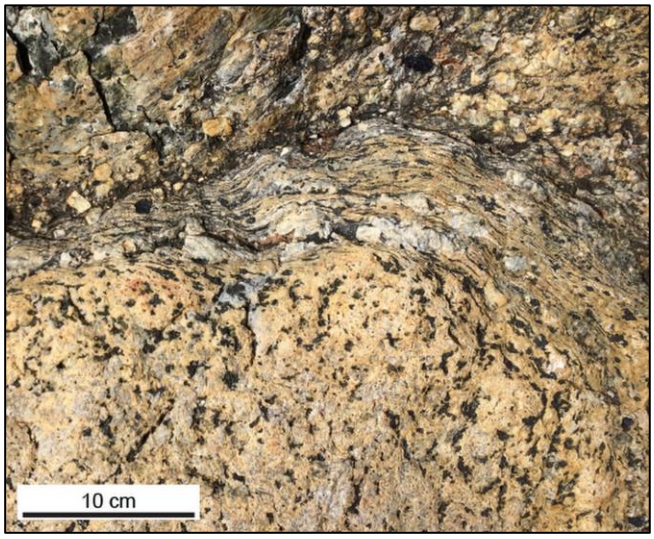

Figure 19: Deformation of larvikite towards the edge of a block, producing an almost mylonitic texture. The central area of the larvikite block (lower left) remains undeformed. The block is in contact with a poorly exposed pegmatite (top).

The transitional zones between syenite and larvikite are highly irregular and complex. They are characterised by features such as locally extremely heterogeneous syenite with intense flow textures, larvikite blocks encapsulated by syenite, deformation of larvikite, syenite dykes intruding larvikite, and highly irregular pegmatites interacting with both rock types.

Larvikite blocks isolated within syenite are common features of these transitional zones and ranged greatly in size from as little as 10 cm to around 50 m. The blocks typically have smooth, rounded edges. Towards the edge of these blocks, larvikite often shows intense plastic deformation where it appears to have been stretched into a locally gneissic texture, as seen in Figures 19 and 20. This feature is usually confined to the edges of blocks (<10 cm) and does not tend to affect their central area. Stretching is most intense at the boundary, decreasing inwards. This gives the appearance of one half of a shear zone, with the block edge acting as the shear centre, accommodating the most strain. The

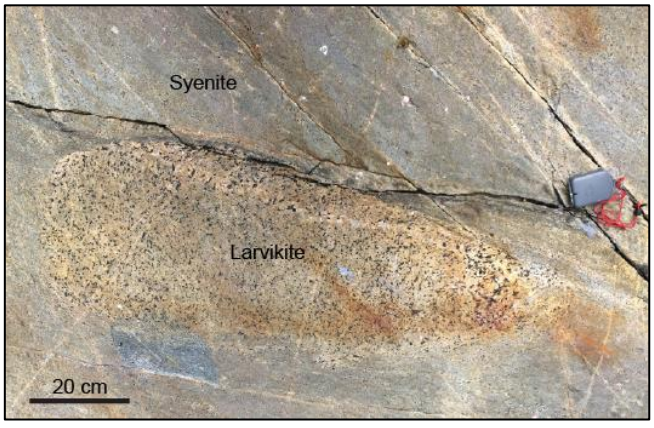

Figure 21: Larvikite block enclosed in nepheline syenite. Strands of larvikite have been pulled away from the block and into the syenite, particularly evident to the right of the block.

surrounding syenite does not mimic this feature and is dominated by characteristic flow textures flowing around the larvikite blocks.

Examples of larvikite being assimilated into the surrounding syenite are common, with an example shown in Figure 21. In this example a thin fragment has partially become separated from a larger block and the tail of the fragment, where the surface area to volume ratio is greatest, is being pulled away and assimilated in the direction of the syenite flow texture. This assimilation of larvikite probably contributes to the heterogeneity of the surrounding syenite, where thin, relatively coarse bands may represent remnants of larvikite.

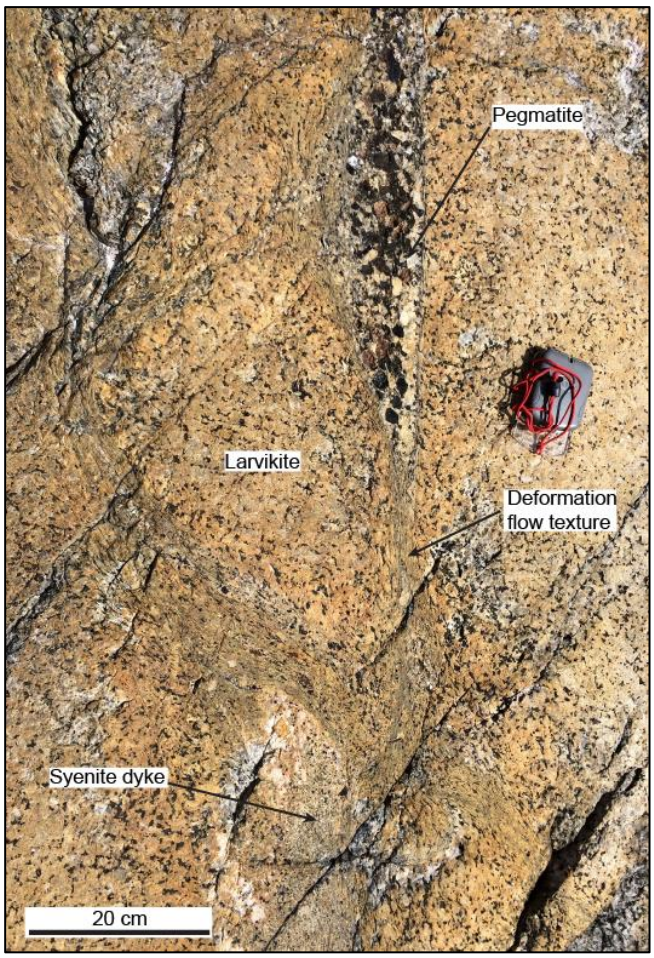

Figure 20: A larvikite domain in the larvikite-syenite transition zone intruded by a pegmatite and nepheline syenite dyke. Internal plastic deformation of larvikite causes the formation of larvikite blocks. The pegmatite appears to influence this deformation, particularly along the left-hand margin.

Syenite dykes often intrude into larvikite around transition zones, as seen in Figure 20. The syenites are usually fine-grained and some dykes show mildly-developed flow textures. Contacts are sharp with no margins or transitional zones. The syenites are not closely associated to deformation of the larvikite host as they are with larvikite blocks.

Pegmatites in the larvikite-syenite transitional zone are very commonly observed. In addition to the typical larger sheet pegmatites described below, smaller finer-grained and highly irregular pegmatites were also occurring within deformed larvikite. They have sharp contacts and occurred as veins that often disperse over short distances. They appear to be significant contributing factors to the deformation of larvikite locally, with an example shown in Figure 20. Within syenite however, pegmatite material tends to have much less structure and was incorporated more as transitional patches of coarse material, rather than defined pegmatites.

2.3.9 Pegmatites

Pegmatites are hosted by both syenite and larvikite and occur as highly irregular veins. The syenite-pegmatite contact is typically sharp to gradational (<1 cm wide). The larvikite-pegmatite boundary is sharp but often invokes deformation flow textures in larvikite to various extents. Small syenite dykes sometimes enclose pegmatites, acting as a barrier between larvikite and pegmatite, a feature commonly seen in Tvedalen. Patches of nepheline syenite were also found within pegmatites, showing a gradational contact and appearing to be mixing with the pegmatites. Based on field observations, there appears to be no mineralogical distinction between pegmatites hosted by syenite by larvikite. They appear to have the same genetic origin.

Mineralogically, pegmatites range from miaskitic to mildly agpaitic assemblages, and are more commonly mildly agpaitic. Pegmatites are mineralogically similar to those in Tvedalen and the Langesundsfjord (*Andersen et al., 2010; Dahlgren, 2010*), consisting of mostly white microcline with euhedral nepheline and biotite, along with other dark minerals (pyroxenes, Fe-Ti oxides etc.), titanite and sulphides. Spreustein alteration of nepheline and possibly sodalite is common in both types. In mildly agpaitic pegmatites, secondary aegirine, zoned pyroxenes and poikiloblastic pyrochlore were also commonly observed.

Interstitial eudialyte and primary, euhedral wöhlerite and zircon are the most common Zr-bearing minerals found in mildly agpaitic pegmatites, although zircon does not coexist with eudialyte. Eudialyte and wöhlerite were rarely observed in the same pegmatites, but could be found coexisting. Pegmatites typically showed a zonation with these Zr-bearing minerals being most common in outer zones. Primary, elongated zircon is the most common Zr-bearing minerals in miaskitic pegmatites.

One large, individual pegmatite, found within nepheline syenite on the West coast of Bjønnes shows a composition similar to pegmatites observed on Låven (*Øyvind Sunde, pers. comm.*), an island in the Langesundsfjord. It contains lots of astrophyllite, altered mossandrite and an outer zone rich in altered eudialyte and secondary aegirine occurring only on one side of the pegmatite.

2.3.10 Faulting

Evidence of faulting is rarely preserved at Bjønnes although it appears to have been a prominent feature in shaping the exposed surface of the Bjønnes syenite. Several examples of slickenlines were found within the syenite, suggesting that faulting occurred in cold conditions. Slickenlines were not found with fault rocks suggesting that

the pluton was still under moderate pressure during faulting. The post-magmatic structural geology of the LPC has not been studied in detail but faulting is most likely related to the Oslo Rift, which remained active long after the emplacement of the LPC (*Petersen, 1978; Larsen et al., 2008*).

Towards the North-West contact of the Bjønnes syenite, an outcrop of highly weathered syenite was observed trending N-S. The outcrop runs alongside a small valley, with unaltered syenites and larvikites exposed in the surrounding areas. Within larvikite to the West of the contact, a linear zone of red, altered larvikite was observed with small calcite veins running parallel. The zone runs almost parallel to the syenite-larvikite contact outcropping approximately 20 m to the West. These features may indicate parts of fault zones in the area.

2.3.11 Other field relationships

The Bjønnes syenite and surrounding larvikite is intruded by a number of doleritic dykes, a common feature across the LPC (*Dahlgren, 2010*). The dykes are large uniform sheets typically up to 5 m thick and primarily striking N-S with a subhorizontal to steep Westward dip. The dykes usually show a small chilled margin and a sharp cross-cutting contact with both syenite and larvikite. There is evidence to suggest the occurrence of multiple generations of dolerite intrusion in some cases.

Across the Bjønnes peninsula, numerous bodies of what appear to be rhomb porphyries can be found in syenite or larvikite. They are dark in colour with a fine-grained matrix and a varying proportion of feldspar rhombs (0.5 – 5 cm in diameter) that appear to be deformed in some cases. Rhombs typically made up <5 % of the total volume and concentrations showed small and seemingly unconstrained internal variations, excluding contact margins around 5 cm wide. The rhomb porphyry bodies have an irregular shape and a sharp contact, but may mingle with the host rock in some places (Figure 22). The internal fabric of the rhomb porphyry bodies becomes more fluid towards contacts. In one example, shown in Figure 22, a small vein appearing to be of syenite origin crosscuts both the rhomb porphyry and the syenite. The bodies are usually up to several metres wide and sheet-like.

One unique rhomb porphyry body to this was found near the Eastern coast of Bjønnes, North of the Bjønnes syenite, where a relatively large yet poorly-exposed rhomb porphyry body was found within larvikite. It shows a dense packing of rhombs, comprising approximately 50 % of the total volume. No rhombs were present within 10 – 15 cm of the contact (Figure 23). There appeared to be some recrystallised larvikite

material within this margin.

This contact relationship would suggest that the rhomb porphyry body had intruded into the larvikite. Other rhomb porphyry bodies give more contradictory evidence about whether they represent intrusions or xenoliths within the host larvikites or nepheline syenites. The relationship between these rhomb porphyries and their host rocks is unclear. It must also be remembered that the rhomb porphyries most likely represent multiple generations, some of which may precede their hosts and others which may intrude the same host rocks.

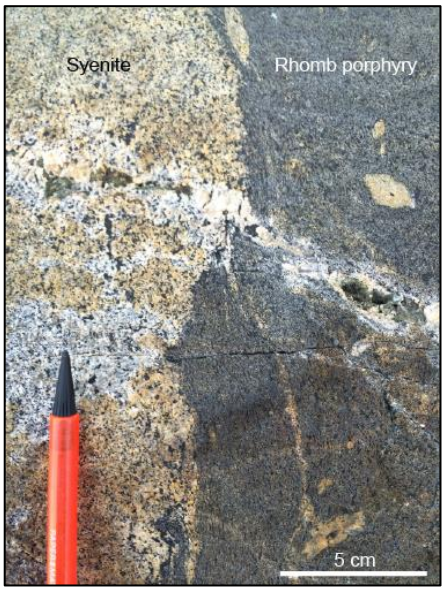

Figure 22: Contact of rhomb porphyry and nepheline syenite, where the two bodies appear to mingle and flow texture develops in the rhomb porphyry. A small vein of syenite material crosscuts the rhomb porphyry.

Figure 23: Rhomb porphyry in contact with heavily weathered larvikite. Rhombs are densely packed in the rhomb porphyry but are absent in the margin along the contact, interpreted as a chilled margin.

Within the Bjønnes syenite, very rare occurrences of baked limestone xenoliths were observed, not exceeding 10 cm in size. These most likely originate from the Silurian sediments along the Western contact of the LPC, which presumably has been intruded by the source of the nepheline syenites. The incorporation of xenoliths also suggests that contamination of the source occurred, although it is not clear as to what extent.

2.4 Nepheline syenite dykes in Tvedalen and the Langesundsfjord

Figure 24 is a map of the Tvedalen area showing the location of samples collected. Since the geology of the area is largely homogeneous (RS VI larvikite), the map used is a Google Earth image, displaying the scale of quarrying in the area. The quarries all take out larvikite for sale as building stone. No detailed geological maps showing pegmatite or nepheline syenite distribution, for example, are currently available.

Figure 24: Map of Tvedalen area showing sample locations. The vast extent of quarrying for larvikite in the area provides excellent fresh exposures to observe profiles of pegmatites and nepheline syenite dykes. Image from Google Earth, date taken 19/08/2015.

Nepheline syenites are common in the larvikite quarries of Tvedalen. They always occur as intrusive dykes, displaying very short gradational contacts with larvikite wall rocks. Unlike at Bjønnes, interaction between the rock types is uncommon or minor. An example of this minor interaction is the relatively mild deformation of larvikite around the contact of some nepheline syenite dykes. Most nepheline syenite dykes are associated with nepheline syenite pegmatites, with which they show a complex relationship. It is not clear if these pegmatites developed from a larvikite or nepheline syenite source (*Dahlgren, 2010*). No conclusive mineralogical differences were found between pegmatites with or without an association to nepheline syenite, based on field observations from Tvedalen and the Langesundsfjord (*Øyvind Sunde, pers. comm.*).

In many cases, nepheline syenites in Tvedalen closely resembles those

observed at Bjønnes, although they are typically coarser grained. However, textures observed in the Tvedalen syenites varied greatly between dykes and many show little textural similarity to Bjønnes syenite or other observed units.

There are petrographical differences between NTG16a and NTG16b (see Appendix 1) that suggest that the dykes in Tvedalen may be heterogeneous over short distances. NTG16 represents a vertical syenite dyke at Sagåsen, with NTG16a sampled from the base of a quarry bench, whilst NTG16b was sampled from the top of that quarry bench, with just approximately 10 m vertical distance between them. The differences may be due to gravitational fractionation or other more complex factors.

There is evidence to suggest that nepheline syenite emplacement occurred over multiple generations in some intrusions. An example can be seen from Østskogen quarry, where a nepheline syenite dyke sharply crosscuts larvikite and shows no internal flow textures. It shows two generations of nepheline syenites. The outer syenite (NTG26a) is medium grained with well-distributed, tight, round mafic spots around 5 mm in diameter. The spots are smaller at the contact margin and may represent a chilled zone against the larvikite host. The inner syenite (NTG26b) is coarser and has a more angular texture. It contains large, irregularly-shaped, poikilitic mafic clusters between 20 – 40 mm wide. This unit also has a reduced mafic spot size towards the margin of the outer syenite, interpreted as a chilled margin.

Both nepheline syenite dykes in this example have gneissic textures very comparable to those observed in the Bjønnes syenite. Many nepheline syenite dykes share similar textures to those of the Bjønnes syenite, ranging from gneissic to equigranular. Despite this, numerous nepheline syenite dykes do not accurately resemble the Bjønnes syenite. For example, NTG29 has an equigranular texture and aligned feldspars but mafic minerals are comparatively rare. Nepheline syenite dykes from Tvedalen appear to be systematically coarser than the Bjønnes syenite.

Most nepheline syenite dykes in Tvedalen were associated with nepheline syenite pegmatites and shared their characteristics of being highly irregular and inconsistent in both orientation and width. The relationship between the nepheline syenites and pegmatites was complex, with examples of pegmatites confined within nepheline syenite dykes, and others of pegmatites crystallising from the walls of larvikite with a core zone infilled by nepheline syenite.

Figure 25 shows an example of a nepheline syenite dyke intruding larvikite. It shows multiple layers of crystallised wall-rock zone pegmatite minerals (most visible are dark radiating aegirine, and other mafic minerals) followed by layers of nepheline syenite, and a relatively small, fully-developed pegmatite at the centre. The layers of pegmatite have been disturbed by the turbulent flow of the nepheline syenites, which preserve these flow textures. It appears that the introduction of nepheline syenite has occurred in pulses, with pegmatites crystallising in between. This implies that the fluids acting as a source for the pegmatites are remaining in the system, probably immiscible from the nepheline syenite. Alternatively, the nepheline syenites could have flushed away these fluids, only for them to be replenished between nepheline syenite injections. Interestingly, the upper pegmatite layers show comparatively less evidence of turbulence. Many similar examples of this complex dynamic between intrusive nepheline syenite and pegmatites can be observed throughout Tvedalen.

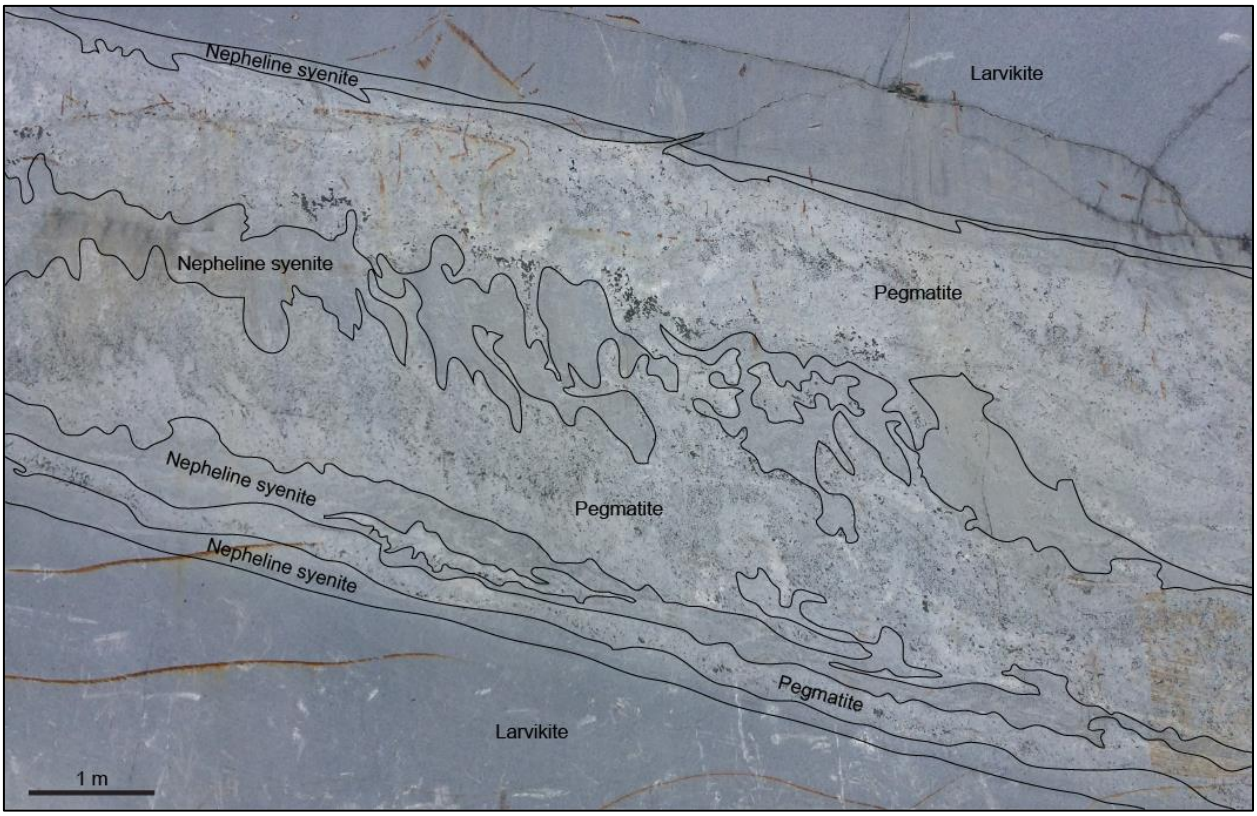

Figure 25: The complex interaction of pegmatite and nepheline syenite seen within a larvikite host in AS Granit quarry, Tvedalen. The broad interaction has been marked onto the figure, although is more complex on a smaller scale. It shows a turbulent alternation between layers of nepheline syenite and pegmatite.

2.4.1 Langesundsfjord

The islands of the Langesundsfjord, South of Bjønnes and West of Tvedalen, display the same features as both areas. They have larger nepheline syenite bodies that show a complex relationship to surrounding larvikite, such as compositional banding, intense local deformation and mingling of the two rock types, very similar to Bjønnes (Figure 26). Also on some of these islands, there are nepheline syenite dykes that interact with pegmatites in a similar manner to those in Tvedalen.

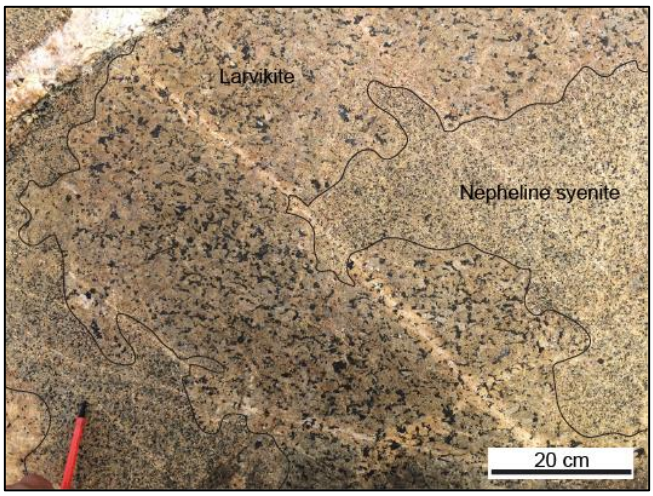

Figure 26: Mixing and mingling of larvikite and nepheline syenite on Håøya, Langesundsfjord, producing similar field relationships to those in syenite-larvikite transition zones around the Bjønnes syenite.

Figure 27 shows an example from Håøya of a nepheline syenite dyke confined within a pegmatite. The syenite has a turbulent flow texture and has broken alkali feldspars that grew upwards from the base wall of the pegmatite (Figure 27b). The equivalent feldspar crystals on the roof wall (Figure 27a) remain unbroken and the nepheline syenite has infilled spaces between them, also showing less developed flow textures. The crystals show no evidence of interaction with the nepheline syenite. This suggests that the pegmatite began crystallising from the wall of the larvikite and was then interrupted by a flow of nepheline syenite, which broke the base crystals and gently filled the space, probably pushing away the fluids that acted as the source of the pegmatite.

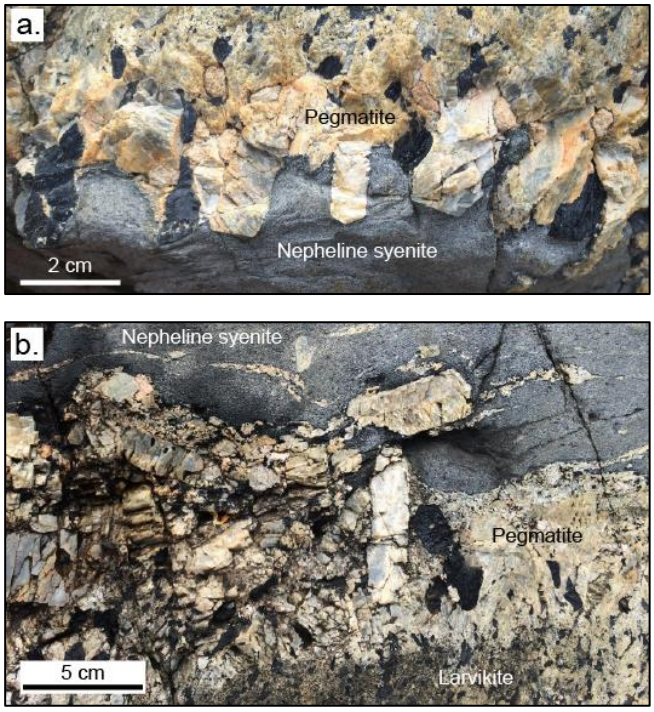

Figure 27: Nepheline syenite within the core a pegmatite at Håøya. The upper wall (a.) is gently infilled by nepheline syenite whereas the base wall (b.) shows broken pegmatite crystals, turbulent flow and pegmatite material suspended in nepheline syenite. The system is enclosed by larvikite host rock.

Nepheline syenite dykes were also found on occasion to the North of the Bjønnes syenite, on the Northeast of the Bjønnes peninsula. Like in Tvedalen and the Langesundsfjord, they

have very short gradational contacts with surrounding larvikite and vary in texture between intrusions. Many of these show similar textures to the Bjønnes syenite and some are less familiar. NTG22 is a relatively dark, very fine grained nepheline syenite dyke with no large mafic spots. Like many of these nepheline syenite dykes, they also commonly show association with pegmatites. In this case both a sheet-like pegmatites and pegmatite pockets within the nepheline syenite dyke were observed.

2.5 Lågendalen

The distribution of rock types in Lågendalen can be seen in Figure 28, from *Oftedahl & Petersen (1978)*. It shows the lardalites that define RS IX and X divided into separate units. Lardalite is coarse to very coarse grained and dominated by feldspar lathes often up to 5 cm in length. In many places, feldspars show magmatic orientation. Its appearance is similar to larvikite, but does not display the prominent schiller effect. Feldspars tend to have a slightly orange/brown appearance compared to other rocks of the LPC. Nepheline was observed to be mostly interstitial but also exists in euhedral form and constitutes 20 – 25 % volume of lardalite. Dark minerals such as biotite, clinopyroxene, amphibole and Fe-Ti oxides are all interstitial. Olivine is also a primary mineral. Coarse biotites are often poikilitic or possess cores of magnetite. Baddeleyite was also observed.

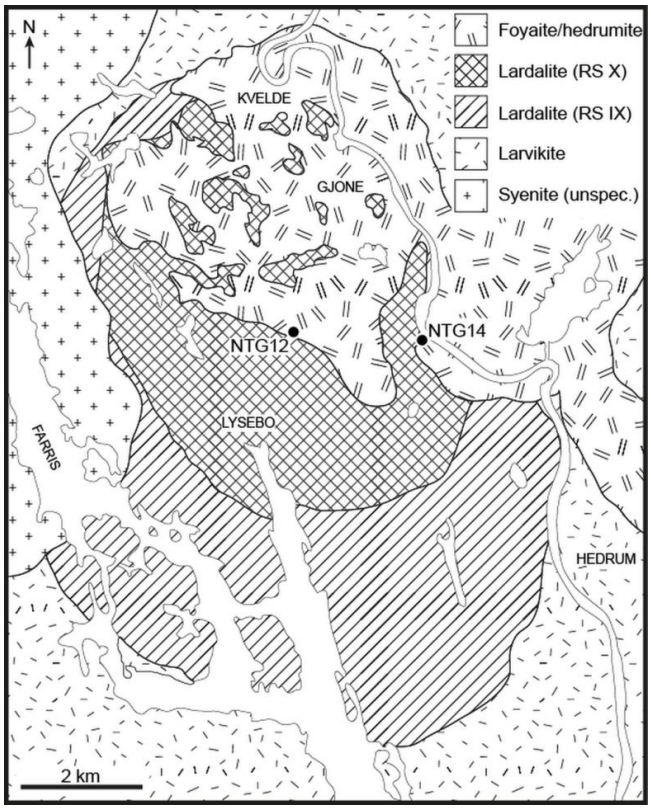

Figure 28: Geological map of the Lågendalen area showing sample locations (modified from *Oftedahl & Petersen, 1978*).

Foyaite is texturally more diverse, with a coarse grained texture and nepheline content observed to be up to approximately 20 %. Nepheline-absent hedrumite was not observed in the field. Foyaite typically has a light appearance, dominated by platy white feldspars up to 2 cm in length that often create a characteristic trachytoid texture. Spaces between feldspars are mostly filled by interstitial nepheline. The abundance of dark minerals is generally low compared to other observed units in the LPC. They consist mostly of biotite with some clinopyroxene. Clinopyroxene ranges from black (diopside) to green (aegirine).

Around Lysebo, a sodalite-bearing foyaite (NTG12) was found, and can be seen in Figure 29. It has a very light colour and feldspars aligned tightly to create a magmatic foliation. Feldspars comprised approximately 80 % of the rock's volume, more than the typical foyaites. The rock has relatively low nepheline content and contained lots of poorly-shaped zircons and interstitial titanite. Near Gjone, another similarly light-coloured, sodalite-bearing foyaite was found. In comparison it contains more nepheline and spreustein alteration is common but irregular. Feldspar alignment is less pronounced and shows random alignment in many places. Foyaites in Lågendalen are known to commonly contain sodalite and locally range into sodalite foyaite (*Oftedahl and Petersen, 1978*). These light foyaites differ from NTG14 for example, and including the hedrumites, which were not observed, the foyaite suite in Lågendalen appears to be quite diverse, despite being treated largely as a single undifferentiated lithological unit in past literature.

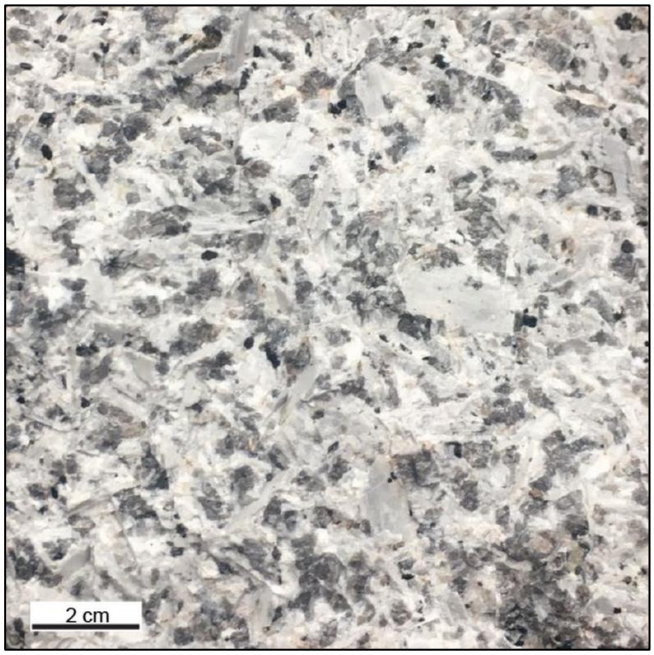

Figure 29: Sodalite-bearing foyaite represented by NTG12. It has a very light colour and is characterised by large, white platy feldspars. Nepheline, zircon and mafic minerals such as biotite lie mostly interstitially between the feldspars.

Lardalites are intruded by highly irregular bodies of foyaite (*Raade, 1973*), particularly in RS X. In the North of the area, near Kvelde, nepheline syenite (foyaite) can be seen in contact with larvikite, presumably from a neighbouring ring section (see Figure 2). The contact is gradational with small blocks of syenites within larvikite close to the boundary. The foyaite has a chilled margin, suggesting that it intruded into relatively cold larvikite, which is likely significantly older than the lardalites or foyaites.

Around Lysebo, nepheline syenite dykes up to 10 m wide intrude lardalite with a sharp contact. The syenite is divided into mixed domains of coarser and finer material, with these boundaries occasionally separated by pegmatites. The finer material may represent chilled zones, where material has been mixed back into central parts of dykes by magmatic pulses or via stoping. This would suggest that the nepheline syenites are notably younger than the lardalites, which must have had time to cool before being intruded.

2.6 Mineral descriptions and relationships

Table 2 shows the mineral assemblages of all analysed samples using the corresponding analytical techniques listed in Table 1. It must be considered that many accessory minerals were identified using EDS, but this analysis was not done on all samples. Minerals in some samples were also identified in hand specimen, despite not being found during analysis. Table 2 outlines the petrogenesis of each sample by determining if a mineral was found to be of primary magmatic origin or a product of secondary late- to post-magmatic alteration. As noted in Table 1, optical microscopy of samples from Lågendalen was done using thin sections of samples from roughly the same locations, collected by *Raade (1973)*. Samples NTG12 and NTG14 were analysed optically using thin sections from samples 14 and 19 respectively from *Raade (1973)*. Individual thin section descriptions can be found in appendix 1.

2.6.1 Feldspar

Feldspars dominate each sample, accounting for 60 – 80 vol.% of analysed thin sections. They typically occur as microperthitic microcline laths showing simple twinning with exsolved albite lamellae running perpendicular to the *c*-axis. Feldspar compositions vary between grains and modally between samples. Modal compositions range from $Or_{60}Ab_{40}$ – $Or_{40}Ab_{60}$. Albite is expected to have a small anorthite component. Alkali feldspar laths often show magmatic alignment parallel to their *c*-axis.

In some samples from Bjønnes, for example NTG18, perthitic feldspar laths are bordered by interstitial aggregates of homogeneous albite, displaying polysynthetic twinning, and microcline. Where this occurs, albite lamellae are often found to be more confined to the cores of the microcline-dominated feldspar laths, meaning towards the outer rim feldspars are more almost entirely of microcline composition. The extent of this feature is variable. In NTG24 for example, these aggregates of homogeneous feldspars fill consistently spaced interstitial gaps between perthitic feldspar laths (Figure 30), and are not found at the grain boundaries of other primary minerals such as nepheline. In other samples, such as NTG33, randomly orientated and poorly shaped plagioclase and microcline occur around larger perthitic feldspar laths and nepheline. In samples such as NTG19 and NTG33, the presence of homogeneous feldspars appears to affect the rims of mafic minerals, which become slightly poikilitic by seemingly intergrowing with aggregate of albite and microcline. These homogeneous feldspar aggregates likely represent late crystallising stages of feldspar (*Andersen et al., 2016*).

Table 2. Comprehensive table of minerals observed from each analysed sample.

	Bjønnes															Tvedalen					Lågendalen	
	NTG6	NTG7	NTG8	NTG15	NTG17	NTG18	NTG19	NTG20	NTG21	NTG22	NTG23	NTG24	NTG25	NTG30	NTG33	NTG16a	NTG16b	NTG26a	NTG26b	NTG29	NTG12	NTG14
Primary minerals																						
Feldspar	✓	✓	✓	✓	✓	✓	✓	✓	✓	✓	✓	✓	✓	✓	✓	✓	✓	✓	✓	✓	✓	✓
Nepheline	✓	✓	✓	✓	✓	✓	✓	✓	✓	✓	✓	✓	✓	✓	✓	✓	✓	✓	✓	✓	✓	✓
Sodalite	✓	✓		✓	✓	✓		✓	✓		✓	✓	✓	✓	✓		✓	✓	✓	✓	✓	✓
Olivine	✓	✓	✓					✓														
Clinopyroxene	✓	✓	✓	✓	✓	✓	✓	✓	✓	✓	✓	✓	✓	✓	✓	✓	✓	✓	✓	✓	✓	✓
Amphibole	✓	✓	✓	✓	✓	✓	✓	✓	✓	✓	✓	✓	✓	✓	✓	✓	✓	✓	✓	✓		
Biotite	✓	✓	✓	✓	✓	✓	✓	✓	✓	✓	✓	✓	✓	✓	✓	✓	✓	✓	✓	✓	✓	✓
Sulphides	✓	✓	✓	✓	✓	✓	✓	✓	✓	✓	✓	✓	✓	✓	✓	✓	✓	✓	✓	✓	✓	✓
Fe-Ti oxides	✓	✓	✓	✓	✓	✓	✓	✓	✓	✓	✓	✓	✓	✓	✓	✓	✓	✓	✓	✓	✓	✓
Titanite				✓		✓	✓				✓				✓	✓	✓	✓	✓		✓	✓
Aenigmatite				✓							✓			✓								
Zirconolite	✓	✓	✓							✓												
Baddeleyite	✓									✓												
Zircon	✓	✓	✓					✓	✓			✓	✓	✓		✓			✓	✓	✓	✓
Eudialyte				✓		✓	✓				✓				✓							
Rosenbuschite							✓															
Catapleiite				✓		✓	✓															
Apatite	✓	✓	✓	✓	✓	✓	✓	✓	✓	✓	✓	✓	✓	✓	✓	✓	✓	✓	✓	✓	✓	✓
Britholite													✓	✓								
Pyrochlore	✓	✓	✓		✓		✓			✓	✓			✓								
Thorite											✓											
UKM1							✓															
UKM2							✓															
Secondary minerals																						
Spreustein	✓			✓	✓	✓	✓					✓	✓				✓	✓		✓	✓	
K-feldspar				✓			✓				✓											
Sodalite				✓			✓				✓											
Clinopyroxene					✓	✓	✓						✓									
Biotite					✓	✓	✓															
Titanite				✓	✓	✓	✓				✓	✓	✓	✓			✓	✓	✓		✓	✓
Zircon				✓			✓				✓											
Rosenbuschite						✓	✓															
Catapleiite				✓			✓															
Pyrochlore				✓			✓				✓											
REE carbonates				✓	✓		✓				✓		✓	✓								
Thorite							✓				✓		✓									
Fluorite				✓		✓	✓				✓											
Calcite				✓	✓		✓				✓											
Chamosite			✓		✓																	
Quartz			✓																			

The feldspar megacrysts in NTG17 are microcline with perthitic lamellae of albite, and contain inclusions of nepheline and mafic minerals throughout. This texture was similarly observed in larvikite samples from the Langesundsfjord area. The grain boundaries of feldspar megacrysts are locally dictated by primary minerals such as nepheline and biotite, which suggests that the megacrysts may have still been growing after the crystallisation of other early-magmatic minerals. They also contain mafic minerals which appear to behave differently to those in the surrounding nepheline syenite.

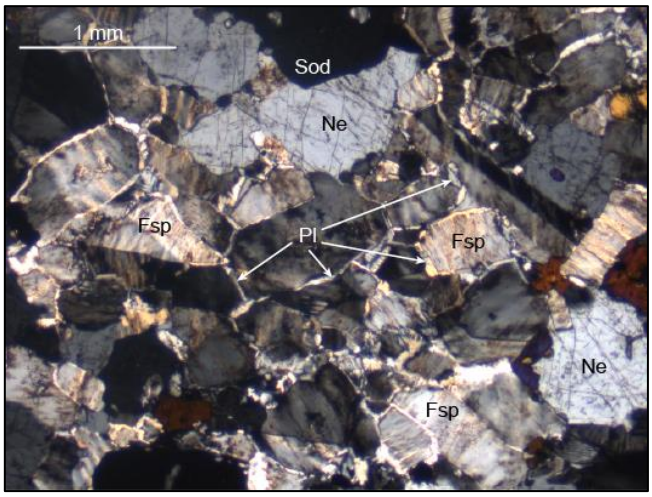

Figure 30: XPL image from NTG24 showing perthitic microcline-dominated feldspars (Fsp) enclosed by thin borders of interstitial albite/plagioclase (Pl). No albite/ plagioclase is found around the grain boundaries of other minerals such as nepheline (Ne) or sodalite (Sod).

Feldspars in all samples were quite heavily altered and would not have yielded useful results from chemical analysis. This is a problem that affects feldspars throughout the LPC (*Neumann 1980*).

2.6.2 Nepheline & sodalite

Nepheline is the dominant feldspathoid and was present in all analysed samples and content varies greatly, estimated between 5 – 25 vol.%. Primary sodalite displays very similar behaviour to nepheline and was generally rare. Although content varies between samples (0 – 2 %) it always occurs in fewer amounts than nepheline. NTG12 has relatively high sodalite content (approx. 4 %) but nepheline is more abundant, meaning that this is not one of the sodalite foyaites mentioned by *Oftedahl & Petersen (1978)*.

Nepheline and sodalite occur as primary minerals, most commonly in euhedral form, although early-forming feldspars and occasionally mafic minerals may limit crystal form to subhedral. An exception to this is NTG12 (foyaite), where nepheline and sodalite are anhedral to subhedral, confined to infilling interstitial space between early magmatic minerals. Samples from Bjønnes such as NTG19 contain nepheline that appears both interstitial in places and euhedral in others.

At the interface between nepheline and eudialyte, secondary sodalite and k-feldspar replace nepheline locally as part of a complex late- to post-magmatic alteration assemblage. Sodalite appears to be confined within the spaces of the original

nepheline grains.

In many samples from Bjønnes and Tvedalen, patches of acicular, radiating natrolite cover areas of felsic minerals, replacing feldspathoids and to a lesser extent feldspars. Patches appear like a groundmass around unaltered or partially altered mineral, typically spanning from several feldspathoids grains (a few mm) to larger domains (several cm or greater). From appearance, some feldspathoids have been completely replaced whilst others sit surrounded by natrolite, partially replaced, as shown in Figure 31. From these partially replaced feldspathoids, natrolite can be seen radiating outwards perpendicular to the grain boundary. Small, rounded analcime may occasionally be present (figure 31). Zeolite alteration in foyaites, seen in NTG12, is confined within single feldspathoids grains, where needles of natrolite radiate inwards. Minerals occupying the core are less acicular and low birefringence, most likely a combination of natrolite and analcime. This alteration of feldspathoids to zeolites is known as spreustein alteration.

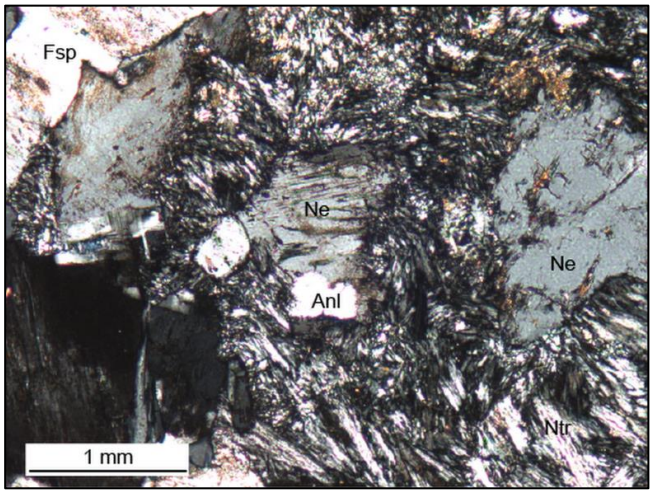

Figure 31: XPL image from NTG25 showing spreustein alteration of nepheline (Ne), where natrolite (Ntr) and some analcime (Anl) have formed as a low-temperature alteration assemblage.

In NTG26a, a colourless isotropic, low relief interstitial mineral appears to partially replace primary nepheline, occurring in small interstitial patches and showing no internal features. It could be spreustein alteration, or possibly secondary sodalite.

2.6.3 Olivine

Olivine occurs as a fairly common early magmatic primary mineral in several samples from Bjønnes. Grains are homogeneous and often heavily fractured. They tend to be overgrown by primary clinopyroxene, biotite, or both existing coevally. Heavy fracturing and complete absence in more evolved samples suggest that olivine is not very stable in such conditions.

2.6.4 Clinopyroxene

Clinopyroxene is most common as an early-magmatic primary mineral (Cpx I), found to some extent in all samples. It often shows zonation and is pleochroic, mostly

pale green in PPL, becoming deeper green towards the rim. Birefringence was variable, up to 0.045 and twinning was seen rarely in paler clinopyroxenes. Optical axes are biaxial (+,-), most commonly (+), suggesting species ranging from augite to aegirine-augite. Clinopyroxene in foyaite typically has a much richer, almost yellowish green colour in PPL and are pleochroic with a low extinction angle. They are optically (+,-), most likely aegirine-augites. Crystal shape is typically more slender, as opposed to clinopyroxene in nepheline syenites, which are wider when elongated but often lack decent shape and has a more round appearance. Clinopyroxene and biotite are contemporaneous and occasionally show small amounts of intergrowth at grain boundaries.

The abundance of primary clinopyroxene in a sample correlates with the abundance of amphibole. Amphibole overgrows primary clinopyroxene, a feature seen in all samples from Bjønnes and Tvedalen to various extents. In most cases there is evidence of replacement of clinopyroxene. Primary clinopyroxene is uncommon in more evolved samples, such as NTG18, where amphibole is the dominant mafic mineral and only small partially replaced clinopyroxene remains in their cores.

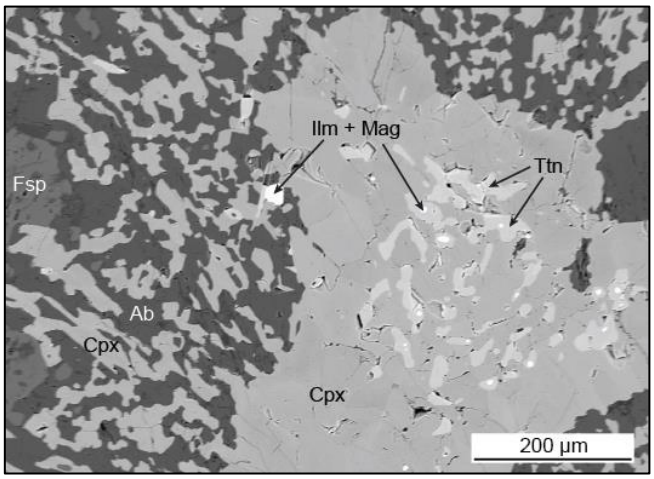

Figure 32: BSE image of a clinopyroxene (Cpx) inclusion within a perthitic feldspar (Fsp) megacryst from NTG17 showing anhedral titanite (Tt) inclusions in the core and intergrowth of clinopyroxene and albite (Ab) bordering the body.

In gneissic nepheline syenite, mafic minerals are divided between clinopyroxene-dominated and amphibole-dominated domains. Clinopyroxene-dominated domains, usually linear bands, consist of smaller grained mafic minerals, mostly clinopyroxene, Fe-Ti oxides and biotite. Biotite and elongated, well-formed clinopyroxene often show alignment concordant with feldspars. Amphibole is uncommon and only small amounts are seen partially overgrowing clinopyroxene. In amphibole-dominated domains however, clinopyroxene is very uncommon, having been mostly replaced by large poikilitic amphibole grains and observed only as small remnant cores.

Within megacrystic feldspars in NTG17, clinopyroxene acts differently. Large grains of clinopyroxene contain numerous inclusions of anhedral titanite within cores. Intricate intergrowths of clinopyroxene with albite radiate outwards around larger grains of clinopyroxene and Fe-Ti oxide, as shown in Figure 32. These assemblages are

confined within perthitic feldspar megacrysts as large, rounded inclusions. Outside of these porphyritic feldspars, clinopyroxene exists in the same form as is observed from other nepheline syenite samples from Bjønnes and Tvedalen, and is often extensively replaced by overgrowths of amphibole, with small amounts of secondary clinopyroxene and biotite intergrowths also occurring.

Secondary clinopyroxene (Cpx II) occurs in several samples from Bjønnes, and is also present in small amounts in one sample from Tvedalen, NTG26b. It is interpreted as secondary because it is only found within primary amphiboles but unlike primary clinopyroxene, it is not confined to amphibole cores and is often seen at grain boundaries or penetrating along fractures. Also, secondary clinopyroxene shows no evidence of zonation or defined crystal shape unlike primary clinopyroxene. It has a rich green colour in PPL, more so than primary clinopyroxene, and a generally higher birefringence. Optical signs could not be determined due to its lack of shape and intricate intergrowths, meaning that it could not be determined optically if the secondary clinopyroxenes were aegirine-augite or aegirine.

Samples containing secondary clinopyroxene are amphibole-rich, where amphibole has replaced most primary clinopyroxene. In NTG19, almost all clinopyroxene is secondary. Secondary clinopyroxene is found intergrown with biotite, replacing primary amphibole. In NTG18 and NTG19, fluorite accumulates along grain boundaries between clinopyroxene and biotite.

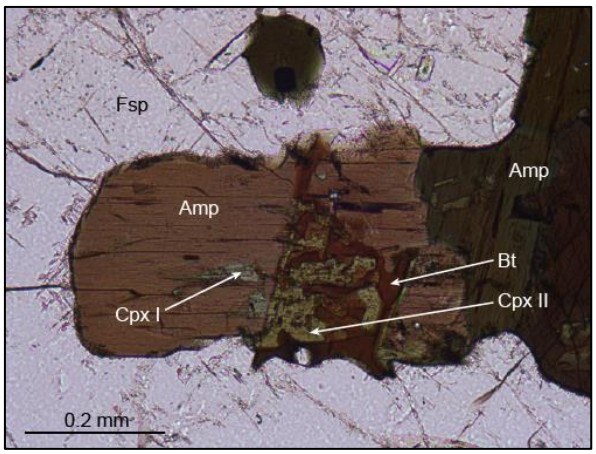

Figure 33: PPL image from NTG18 showing magmatic amphibole (Amp) with remnant primary clinopyroxene (Cpx I) in the core. Biotite (Bt) appears intergrown with amphibole, and secondary clinopyroxene (Cpx II) has developed within the biotite, seemingly replacing amphibole.

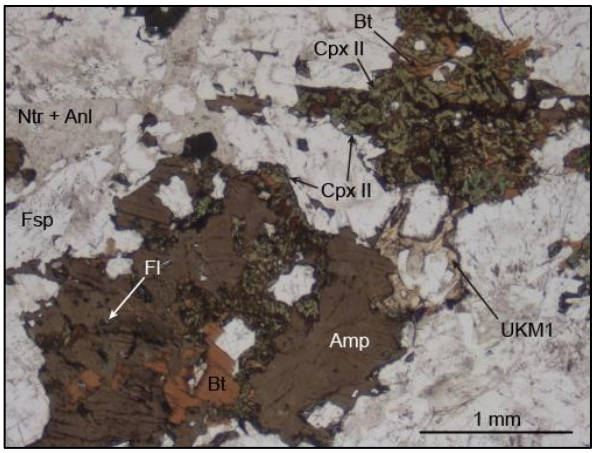

Figure 34: PPL image from NTG19 showing secondary clinopyroxene (Cpx II) and biotite (Bt) extensively replacing amphibole (Amp) whilst fluorite (Fl) has developed in small amounts within the secondary assemblage.

Secondary clinopyroxene replacement of amphibole is less extensive in NTG18 than in NTG19. In NTG18, secondary clinopyroxene is more confined by its association with biotite, and only forms in areas where biotite and amphibole intergrow, seen in Figure 33. Biotite is often seen intergrowing in accordance with amphibole cleavage planes due to similarities in their crystal structures, where there appears to be a structural constraint on orientation. In NTG19, secondary clinopyroxene is mixed randomly with small anhedral biotite. It is unclear whether biotite is primary or secondary in this case. Secondary clinopyroxene is more extensive and fully replaces some smaller amphiboles, as shown in Figure 34, where the original shape of the amphibole grain is maintained.

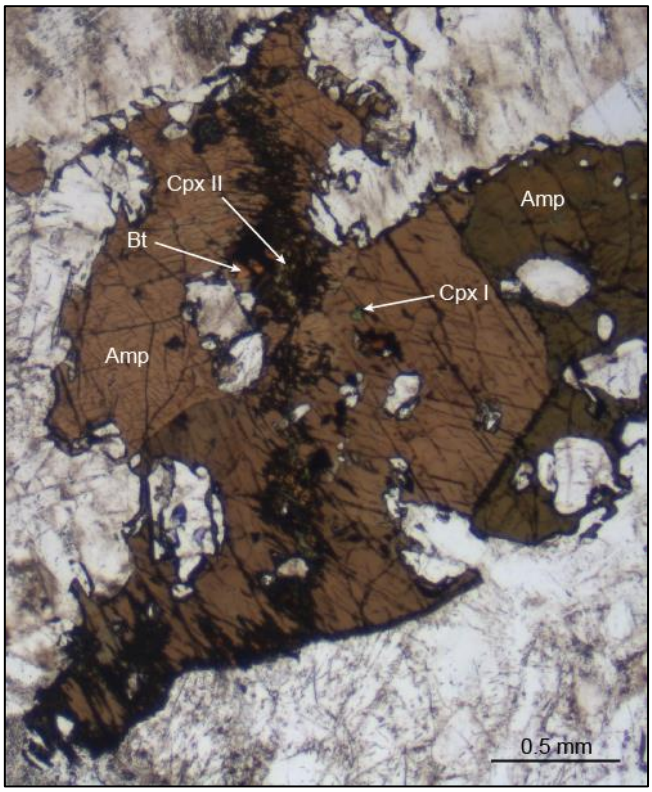

Figure 35: PPL image from NTG19 showing secondary clinopyroxene (Cpx II) and biotite (Bt) formation along a fracture through an amphibole (Amp) grain.

In Figure 35, secondary clinopyroxene and biotite formation spans laterally through an amphibole grain despite not reacting much with the amphibole rim. Alteration has presumably occurred along a fracture through the grain, where fluids have been able to percolate at a late- or post-magmatic stage. This suggests that secondary clinopyroxene formation is fluid related.

Secondary aegirine is a ubiquitous product of eudialyte alteration. It is the most abundant product in the alteration assemblage. Secondary aegirine was also found in small amounts in the alteration of magnetite to mostly what is believed to be chamosite.

2.6.5 Amphibole

One major mineralogical difference between Lågendalen foyaites and nepheline syenites in Bjønnes and Tvedalen is the presence of amphibole. In all samples from Bjønnes and Tvedalen (1 – 8 %), amphibole was found to some extent, but in foyaites, it was entirely absent from both analysed samples.

Amphibole is a magmatic rock-forming mineral that epitaxially overgrows primary clinopyroxene. It often has a partly interstitial, semi-poikilitic appearance, suggesting

that it formed at a relatively late magmatic stage. Amphibole is most abundant in more evolved samples and often becomes the dominant mafic phase, with NTG18 being a good example. In these more evolved samples amphibole typically becomes dark brown/green in PPL (Figure 35) and has a generally higher birefringence. In most samples amphibole is brown to dark brown in PPL. Amphiboles are typically biaxial (+,-) and have a birefringence of 0.010 – 0.060.

Amphibole overgrowths of clinopyroxene sometimes appear to be purely magmatic coronas but in most cases there is evidence of amphibole replacing clinopyroxene. Clinopyroxene systematically shows a decrease in size as overgrowing amphibole size increases. Clinopyroxene loses shape and grain boundaries become transitional, whilst zonation is lost. Figure 36 shows a primary clinopyroxene being replaced by amphibole, where magmatic zonation is less apparent along the contact with amphibole, with small remnants of clinopyroxene in the amphibole matrix. The cleavage orientation of the surrounding amphibole suggests that amphibole is made up of several grains in this case.

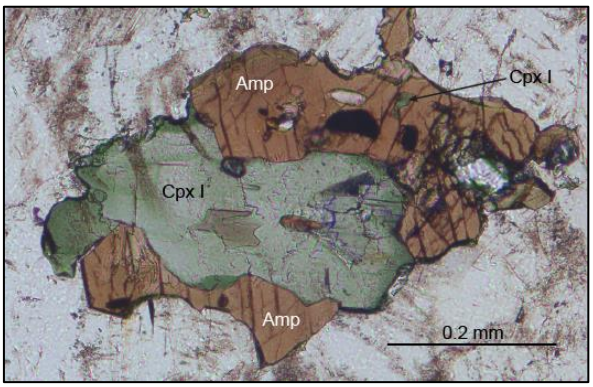

Figure 36: PPL image from NTG25 showing amphibole (Amp) overgrowing and replacing primary clinopyroxene (Cpx I). Magmatic zoning of clinopyroxene is less apparent along the contact with amphibole.

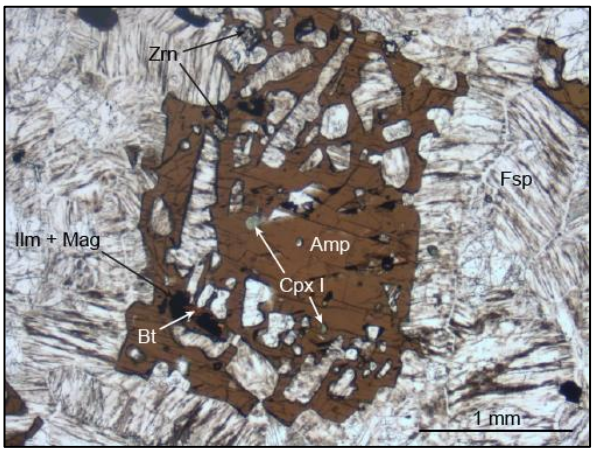

Figure 37: PPL image of NTG26a showing poikilitic amphibole (Amp) having extensively replaced primary clinopyroxene (Cpx I), leaving only small rounded remnants.

In gneissic nepheline syenite such as NTG25 and NTG26, amphibole grows into large poikilitic grains up to 2 cm in diameter. In some of these poikilitic grains, very small remnant clinopyroxene grains are seen occasionally towards the centre (Figure 37), where clinopyroxene has been almost comprehensively replaced by amphibole. Despite this, in intermittent zones of much smaller, aligned mafic minerals, amphibole is uncommon and primary clinopyroxene is left largely unaltered. Figure 36 represents the greatest extent of amphibole overgrowth of clinopyroxene in a clinopyroxene-dominated zone. There must be controls on the gneissic syenite causing amphibole to be confined to particular domains or bands.

2.6.6 Biotite

Biotite is a ubiquitous mineral in all three study areas and was typically associated with clinopyroxene and amphibole to form clusters of mafic minerals. Biotite exists coevally with both minerals. Biotite and primary clinopyroxene occasionally show small patches of intricate intergrowths. In gneissic samples such as NTG25, early-magmatic biotite can become partially overgrown by large poikilitic amphiboles, which have presumably grown continuously until a late-magmatic stage. Biotite is abundant in all samples and is the dominant mafic mineral in some highly evolved samples such as NTG15.

Biotite regularly overgrows Fe-Ti oxides (and sulphides), which is a common feature throughout the LPC and the Oslo rift. It is a feature observed from all samples in each study area. Multiple grains of biotite typically engulf single Fe-Ti oxides, suggesting that biotite actively nucleates from the Fe-Ti oxide surface. This is particularly evident with larger Fe-Ti oxides, or where biotite has a low abundance and can produce an almost radial appearance, as commonly seen in larvikites. Nepheline syenites from Bjønnes and Tvedalen generally have a smaller modal grain size of all grains including Fe-Ti oxides, allowing single biotite crystals to cover Fe-Ti oxides (Figure 38).

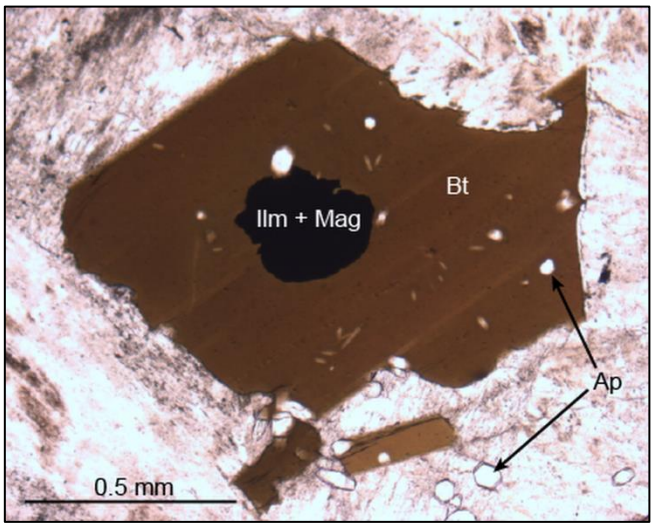

Figure 38: PPL image from NTG14 showing biotite (Bt) overgrowing and presumably replacing an anhedral Fe-Ti oxide (Ilm + Mag). Biotite has crystallised from a number of points around the surface of the oxide. Biotite has also overgrown some small, early-magmatic apatite (Ap) grains.

In gneissic samples, biotite grows into large poikilitic grains like amphibole. To create this texture, the grains must fill interstitial space in a mostly crystallised environment. In finer-grained clinopyroxene dominated domains, biotite acts as an early-magmatic mineral, mantling Fe-Ti oxides and growing contemporaneously with clinopyroxene. This suggests that biotite growth must have continued throughout most of the crystallisation period.

Biotite intergrows with secondary clinopyroxene within amphibole in some of the more evolved samples from Bjønnes and Tvedalen. Larger, more intact biotite maintains its good crystal form whilst pyroxene displays less shape and often grows along biotite cleavage planes. Biotite grows beyond amphiboles and into bordering felsic content, often by up to 0.2 mm. Although a reaction with amphibole may result in

a volume change, the similar crystallographic structures of the three mafic minerals means that expected volume change would be small. It would not account for biotite grains growing so far into felsic material. Also there is no evidence of secondary pyroxene occupying more volume than the replaced amphibole. Therefore the larger biotite must have crystallised from primary melt. Biotite is commonly overgrown partially by amphibole in many samples. It could be that fluids exploited the cleavage of biotite as an entry point for alteration of clinopyroxene. Small, anhedral biotite grains show an apparent symplectic intergrowth with secondary clinopyroxene (Figure 34) so may have been mobilised and recrystallised along with secondary clinopyroxene.

2.6.7 Sulphides

Sulphides were determined using EDS analysis and included pyrite, pyrrhotite, arsenopyrite, chalcopyrite, sphalerite, galena and molybdenite. Sulphides of non-specific species are present in all samples, often only as small individual grains that make up a very minor rock component. Fe-sulphides (pyrite and pyrrhotite) are most common and rarer species such as chalcopyrite and arsenopryite are typically found in association with them. Pyrite was often overgrown by primary biotite, much like the Fe-Ti oxides.

2.6.8 Fe-Ti oxides

Fe-Ti oxides exist as relatively small, round masses. They were also determined using EDS analysis and consist of exsolved magnetite and ilmenite of various proportions that show intricate exsolution lamellae in BSE imaging. Fe-oxide components are assumed to be magnetite based on the optically isotropic appearance of grains and the mineralogy of nepheline syenite pegmatites. However, deep orange/red, high relief material observed optically in NTG17 for example, is believed to be haematite, and was found in association with opaque Fe-Ti oxides. It was seldom possible to accurately distinguish between magnetite and haematite from semi-quantitative data since they have such similar Fe proportions.

Fe-Ti oxides were ubiquitous in all samples, but their distribution varied between samples, showing some possible correlation to mineralogy. They were seen to be less abundant in samples containing agpaitic minerals such as eudialyte and aenigmatite. They are also less abundant in amphibole-rich samples, seen more commonly in samples or domains rich in primary clinopyroxene. Fe-Ti oxides are often overgrown by biotite, which appears to be a replacement reaction.

In titanite-bearing samples, titanite rims often exist around Fe-Ti oxides with high Ti content. Homogeneous ilmenite is always observed to be overgrown by a titanite rim and some examples were also found around ilmenite-magnetite exsolutions. Pyrochlore was also commonly seen accumulated on the grain boundaries of oxides.

In NTG30, homogeneous ilmenite appears to encircle an exsolved grain of magnetite and ilmenite, all overgrown by biotite (Figure 39). Such high Ti content in the grain would typically result in the overgrowth of a titanite rim but NTG30 contains very little titanite, with aenigmatite as the main Ti-bearing mineral. It may be possible that the high proportion of an ilmenite component was too great to be fully exsolved and components needed for the production of titanite were unavailable, leaving excess ilmenite to be pushed out towards the grain boundary.

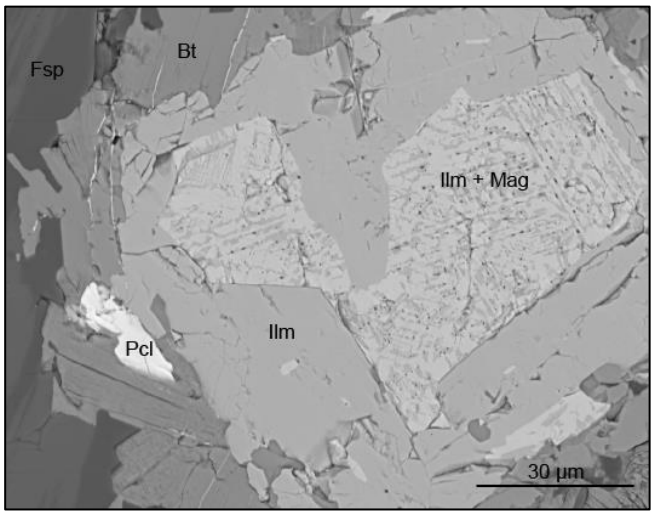

Figure 39: BSE image from NTG30 showing a Fe-Ti oxide (Ilm + Mag) overgrown by biotite (Bt). The oxide core shows exsolution of ilmenite and magnetite with trellis lamellae. The outer parts of the oxide consist of homogeneous ilmenite (Ilm) that appears to replace the exsolved core. Pyrochlore (Pcl) has nucleated in the surface of the oxide.

One example of magnetite and haematite being potentially distinguished from one another is seen in NTG17, where homogeneous magnetite has undergone replacement and a rim of oxidised haematite has formed around the remaining magnetite. Magnetite and haematite were distinguished based on differences in peak heights from EDS spectra of clean, uncontaminated analyses and confirmed using optical and reflective microscopy. The haematite rim is not present at the grain boundary between magnetite and surrounding amphibole. The alteration product is believed to be chamosite [$(Fe,Mg,Al)_6(Si,Al)_4O_{10}(OH,O)_8$], which is known as a late- to post-magmatic alteration product often associated with zeolites in the LPC. It shows excellent cleavage in one direction indicating that it is a phyllosilicate. This mineral was seen rarely as a product of internal alteration within Fe-Ti oxides, particularly in NTG17. Another example in NTG17 (Figure 40) shows ilmenite being internally replaced by chamosite and a minor amount of secondary aegirine, with a secondary rim of bladed Fe-oxide (possibly haematite) having formed around the remnant ilmenite. The presence of aegirine, even in small quantities, implies an oxidised environment.

In NTG8, an anhedral magnetite grain enclosed by biotite and zircon has undergone replacement to secondary quartz. The grain has been heavily fractured so replacement most likely involved infiltrating fluids. This must have been post-magmatic due to the magma being silica-undersaturated. Primary apatite has been unaffected.

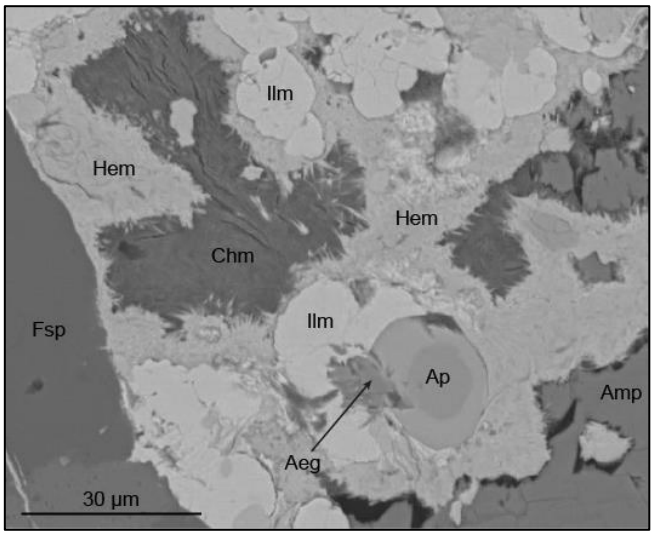

Figure 40: BSE image from NTG17 showing internal alteration of ilmenite (Ilm) into a Fe-oxide believed to be haematite (Hem) and a mineral believed to be chamosite (Chm), which shows one plane of excellent cleavage. Aegirine (Aeg) is also present and appears to be a secondary product.

2.6.9 Titanite

Titanite is a common accessory mineral in many samples from the three study areas, both as a primary and secondary mineral. Primary titanite in foyaite is very common, both euhedral and interstitial in nature. In NTG12 titanite is often very large, seen occupying interstitial spaces in excess of 4 mm in size, whilst euhedral crystals can reach similar sizes. In NTG14, titanite is common but smaller in size. Titanite is often associated with mafic minerals and forms contemporaneously with early-magmatic clinopyroxene.

In nepheline syenites from Bjønnes and Tvedalen, titanite also occurs in euhedral and interstitial form but typically much smaller and less abundant. Euhedral crystals also display a relatively poor shape and prisms are often skeletal, probably not formed as early as those in foyaite. Interstitial titanite fills small residual spaces as a late-magmatic phase.

NTG16 and NTG26 from Tvedalen have very high concentrations of titanite relative to samples from Bjønnes. Titanite is found both interstitially and as rims around Fe-Ti oxides. NTG29, also from Tvedalen, does not contain titanite and Ti is mostly confined in ilmenite.

Another common, more widespread occurrence of titanite is the formation of rims mantling Fe-Ti oxides. This can be seen on Fe-Ti oxides with and without a biotite overgrowth, suggesting that the titanite may have formed later as a secondary product. Titanite rims were mostly found around ilmenite, although they were also seen to occur around exsolved ilmenite-magnetite. Titanite did not appear to form around magnetite. This implies that ilmenite underwent partial replacement by titanite, which incorporated Ti from the ilmenite. The ulvöspinel content of magnetite is unknown but appears to be

low based on EDS analyses. Therefore, content is probably too low to allow the formation of titanite.

In NTG22, whole grains of ilmenite composition, identified using EDS analysis, were found unaccompanied by a titanite rim. The sample does not contain any titanite. One possible explanation is the presence of zirconolite, which would occupy a significant amount of Ti and Ca relative to other samples that do not contain zirconolite.

Primary titanite in the Bjønnes syenite occurs in only eudialyte-bearing samples. Despite this, primary titanite is common in Tvedalen nepheline syenites and Lågendalen foyaites, where there are no eudialyte occurrences. Titanite is found in all eudialyte-bearing and aenigmatite-bearing samples from the Bjønnes syenite. In NTG15 titanite appears to coexist with aenigmatite in some occurrences but seemingly partially replaced in others. In NTG19, titanite also appears to coexist with UKM1, an unidentified complex Ti-bearing silicate. The presence of titanite in samples containing agpaitic minerals is unusual since it is considered to be a non-agpaitic mineral under current definition (*Sørensen, 1997*).

2.6.10 Aenigmatite

Aenigmatite is a complex Na-rich Ti-silicate mineral that is associated with agpaitic systems (*Larsen 1977; Marks et al. 2011*). It was found only in several samples from Bjønnes but was a common mineral in those samples. It often occurs as large, poorly shaped primary magmatic grains. In NTG30, aenigmatite tends to be most abundant in the outer parts of mafic mineral clusters, perhaps implying that it began to form at a later magmatic stage relative to other primary mafic minerals.

NTG15 and NTG23 contained both aenigmatite and titanite, considered to be a miaskitic Ti-silicate mineral (*Andersen et al., 2010; Marks et al., 2011*). In NTG15, aenigmatite can be seen intergrowing with biotite and seemingly overgrowing and partially replacing titanite, which had formed groups of small subhedral crystals with Fe-Ti oxides in cores, as seen in Figure 41. Titanite coverage of oxides is not evenly distributed as observed elsewhere and aenigmatite makes contact with oxides in places, implying replacement of titanite. If this is the case, it may provide evidence that titanite overgrowth and replacement of oxides is a magmatic replacement feature, rather than post-magmatic. Aenigmatite seems to interact with biotite and can be seen along cleavage planes, suggesting that it may be partially replacing biotite also. Another example shows a primary titanite prism slightly overgrown by aenigmatite, where they appear to have crystallised together.

Aenigmatite often overgrows and presumably replaces Fe-Ti oxides. In NTG30, aenigmatite appears to replace primary clinopyroxene when in close proximity to Fe-Ti oxides. In one example, aenigmatite forms along the contact between clinopyroxene and Fe-Ti oxides. Clinopyroxene shows a slightly transitional boundary into aenigmatite in places. Aenigmatite replacement of clinopyroxene is not as extensive as amphibole replacing clinopyroxene, for example. Amphibole and aenigmatite appear to coexist.

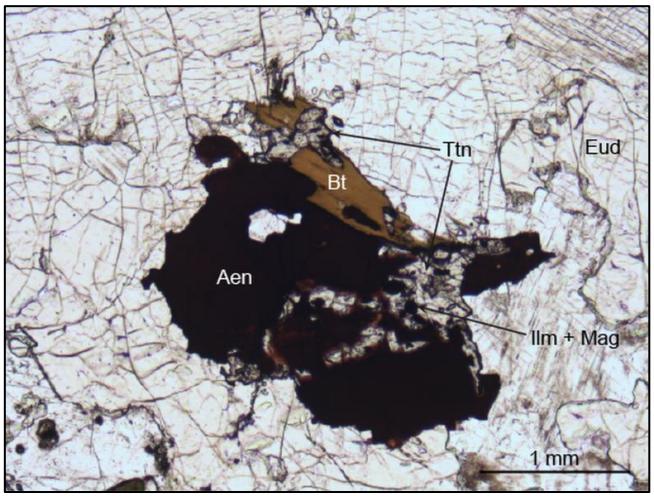

Figure 41: PPL image from NTG15b showing aenigmatite (Aen) seemingly overgrowing and partially replacing titanite (Ttn) and maybe biotite (Bt). Titanite has initially formed around Fe-Ti oxides (Ilm + Mag).

The occurrence of aenigmatite in NTG15 and NTG23 suggesting a more agpaitic nature of these rocks is supported by the presence of eudialyte, an agpaitic Zr-silicate mineral. Despite this, aenigmatite was not found in other eudialyte-bearing samples from Bjønnes. The highest concentration of aenigmatite was observed in NTG30, which contains zircon as opposed to eudialyte. This observation means that NTG30 simultaneously has an agpaitic Ti-bearing mineralogy and miaskitic Zr-bearing mineralogy. Aenigmatite and zircon were not observed in direct contact.

2.6.11 Zirconolite

Zirconolite was found in several samples from Bjønnes as a common accessory mineral. In NTG22 zirconolite is the dominant Zr-bearing mineral, with no zircon or eudialyte present. Examples of zirconolite being mantled by early magmatic clinopyroxene suggest that it crystallised early as a primary mineral. Grains reach up to 0.2 mm in diameter, relatively large in a fine-grained sample and similar in size to many mafic minerals and oxides. They are typically well formed subhedral grains, often coeval with pyroxene.

In NTG 8, and to a lesser extent NTG7, zirconolite is much more deteriorated, often intensely fractured to the extent that some grains have been structurally dismembered and grains appear to be undergoing replacement. One notable difference is that in NTG7 and NTG8, zircon is present and is the dominant Zr-bearing mineral. Small amounts of interstitial zirconolite (<50 μm diameter) were also found in NTG6, another zircon-bearing sample.

Zirconolite is also a Ti-bearing mineral. It was not observed in any samples that also contained titanite or aenigmatite.

2.6.12 Baddeleyite

Small amounts of baddeleyite were found in NTG22 using EDS. These grains tend to be very small (<50 μm) and partially overgrown by the more common zirconolite, another Zr-bearing oxide. Baddeleyite was also found in NTG6, intergrown with pyrochlore within a larger biotite grain overgrowing sulphides.

2.6.13 Zircon

Zircon was a common accessory mineral found in many samples from all three study areas. It was commonly found as stubby prisms, often near to mafic mineral assemblages as seen in Figure 37. Zircon was also found interstitially with anhedral form in some samples such as NTG8. In NTG8 zircon can be found both as a euhedral and an interstitial mineral. Zircon is often intensively fractured and inclusions of anhedral Fe-Ti oxides are common.

Primary magmatic zircon was not found in any eudialyte-bearing samples, with one exception, shown in Figure 42. A single elongated zircon grain estimated to have been up to 100 μm was found in eudialyte-bearing NTG19. The unstable zircon had undergone extensive replacement by a mineral assemblage of catapleiite, rosenbuschite, calcite and UKM3 leaving only a small remnant zircon core. UKM3 is an unidentified Al-silicate mineral containing a roughly equal proportion of Al and Si, with small quantities of Na and Ca. It is found interstitially between other minerals in the secondary assemblage and was not observed anywhere else. This provides evidence for zircon not being a stable mineral in an agpaitic eudialyte-bearing nepheline syenite, as suggested by *Andersen et al. (2010)*. Alteration of the zircon probably took place in relatively early stages of magmatic evolution.

Secondary zircon is a key component in eudialyte alteration assemblages, and the only major Zr-bearing mineral found in the secondary assemblages.

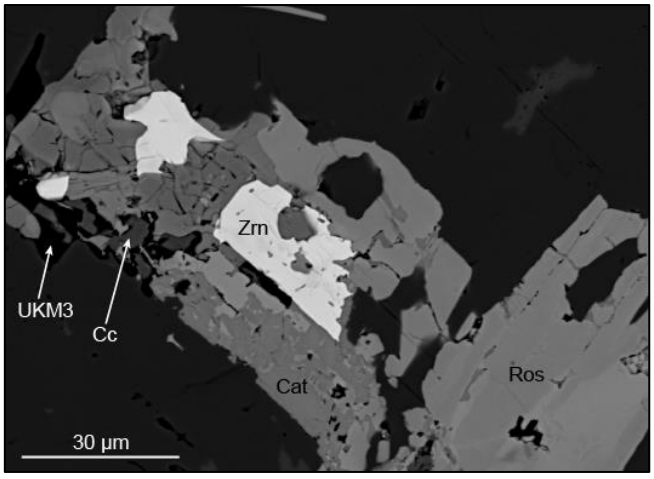

Figure 42: BSE image from NTG19 showing a remnant zircon (Zrn) that has been replaced by rosenbuschite (Ros), catapleiite (Cat), calcite (Cc) and an unidentified aluminoslicate (UKM3).

2.6.14 Eudialyte

Eudialyte occurs as an abundant primary mineral in some samples from Bjønnes, but is completely absent from other samples. No eudialyte was found in nepheline syenites from Tvedalen or foyaites from Lågendalen. Grains are typically large (up to 2 mm) and rounded, early magmatic but no euhedral crystal forms were found.

In all eudialyte-bearing samples, eudialyte is concentrated into zones, either in the form of bands or patches. In NTG18, small amounts of eudialyte outside of these zones are commonly interstitial, whilst primary eudialyte is dominant in these concentrated zones. Areas in NTG18 display predominantly interstitial eudialyte, whereas other areas show more primary eudialyte. Generally, eudialyte occurs as a primary, early-magmatic mineral. Eudialyte in NTG33 appears to be interstitially confined by only perthitic feldspars and nepheline, with some examples of eudialyte mantling feldspar. This suggests that eudialyte may have crystallised later than some of the earliest forming minerals, but still within relatively early magmatic conditions.

Late magmatic alteration of eudialyte rims occur in all eudialyte bearing samples, most notably when in contact with biotite or nepheline. It breaks down into an assemblage typically comprised of altered primary eudialyte + aegirine + zircon + pyrochlore ± fluorite ± calcite ± REE carbonates ± thorite ± britholite ± sulphides. Catapleiite was also found within some alteration zones in NTG15 although its role is unclear. These alteration rims consist mostly of anhedral aegirine with patches of remnant, partially altered eudialyte (low contents of Na, Fe, Cl). Anhedral zircon, pyrochlore and other products sit within aegirine as isolated singular grains. An example is shown in Figure 43.

Alteration appears to be a result of mineral interface rather than the presence of fluids, also suggesting that the process occurred during the magmatic stage. However differences in extent of alteration may be due to the ability for fluids to percolate through different minerals and mineral interfaces. The extent and components of alteration of eudialyte appears to be dependent on the neighbouring mineral. Eudialyte in contact with feldspars, for example, rarely shows signs of alteration. However alteration fringes develop along grain contacts between eudialyte and nepheline. In this case, an intergrowth of sodalite and K-feldspar forms as a secondary product of nepheline around the eudialyte grain, as shown by the example in Figure 43. When in contact with a biotite grain, eudialyte alteration is usually more pervasive, with examples of eudialyte grains being completely replaced by secondary assemblages. What appears to be secondary titanite is often found at the grain boundary of eudialyte and biotite.

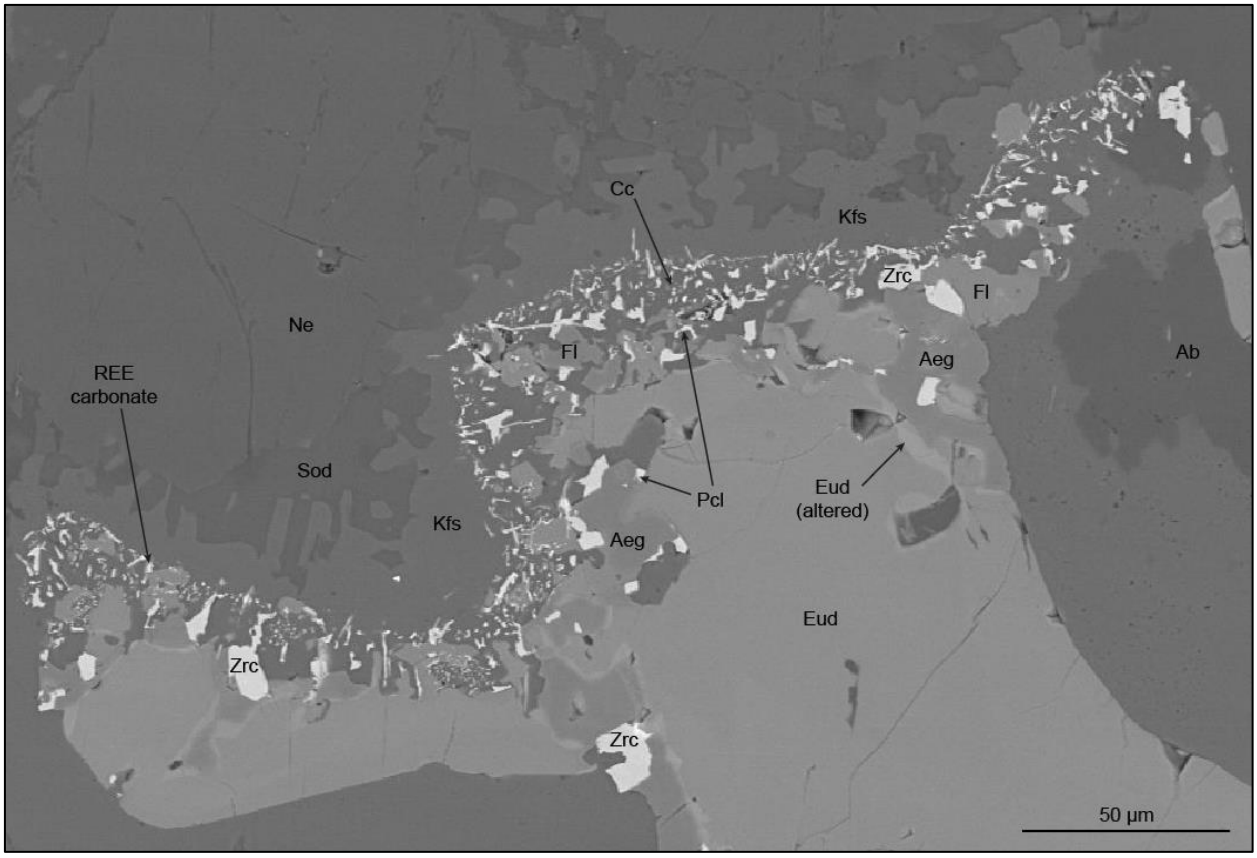

Figure 43: BSE image from NTG19 showing the alteration of eudialyte (Eud) in contact with nepheline (Ne). A thin rim of altered eudialyte, which appears slightly lighter, creates a rim around unaltered eudialyte from the alteration zone. An assemblage of aegirine (Aeg), zircon (Zrn), fluorite (Fl), pyrochlore (Pcl) and REE carbonates has formed a fringe as alteration products of eudialyte at the interface of eudialyte and nepheline. This alteration is not seen at the interface of eudialyte and albite (Ab). Nepheline has been altered to intergrowing sodalite (Sod) and K-feldspar (Kfs).

2.6.15 Catapleiite & rosenbuschite

Catapleiite was found in NTG15b as a coexisting phase with eudialyte and pyrochlore, all enclosed together within a sulphide crystal approximately 100 µm in diameter. It also occurs within alteration assemblages of eudialyte in NTG15b, although its relationship with eudialyte appears unclear. It appears to exist as a minor phase within eudialyte and appears to be a primary mineral. It was found only in an extensively altered eudialyte with no remaining fresh eudialyte to compare directly.

In NTG19, catapleiite occurs alongside rosenbuschite as part of a secondary mineral assemblage replacing unstable zircon. Rosenbuschite is the dominant phase and the two minerals are contemporaneously intergrown. Catapleiite and rosenbuschite also coexist as larger grains up to 200 µm with no evidence of having replaced another mineral.

2.6.16 Apatite

Apatite is a ubiquitous accessory mineral that was found in all samples, typically as small euhedral prisms. The presence of apatite embedded in early magmatic minerals such as clinopyroxene and Fe-Ti oxides suggest that apatite was one of the earliest minerals to crystallise. Apatite is often found in higher concentrations around mafic assemblages. Having crystallised early, this may be due to having more available space to grow away from early-magmatic felsic minerals. Apatites are often chemically zoned (Figure 40) showing an increase in Si and REE content towards the rim and a progression towards britholite composition.

2.6.17 Britholite-(Ce)

Britholite was found as a rare primary mineral in NTG25, usually found in very small amounts around the grain boundaries of euhedral apatite crystals, not as a direct result zonation of apatite. One grain shows primary zoned britholite breaking down into REE carbonates, thorite and aegirine. Due to the small size of these minerals, this relationship was difficult to determine for other grains, although a minor carbonate phase was often detected with britholite in NTG25 using EDS. Primary britholite up to 50 μm in diameter was also detected in NTG30, partially overgrowing euhedral apatite. It showed a sharp zonation and REE carbonates were found within internal fractures.

A REE-silicate mineral believed to be britholite was also found occasionally as a secondary mineral within eudialyte alteration assemblages, found in NTG23 for example. It was commonly found alongside thorite and REE carbonate minerals.

2.6.18 Pyrochlore

Pyrochlore was found in a variety of samples and it is most widespread as a minor accessory mineral, typically accumulated as small masses up to approximately 50 μm around grain boundaries of Fe-Ti oxides (Figure 39). These Fe-Ti oxides are overgrown by biotite. It is possible that the formation of pyrochlore was the result of alteration in a similar way to how titanite rims appear to have formed, however there is little definitive evidence to prove this. Titanite rims typically show even distribution around Fe-Ti oxides whereas pyrochlore accumulates in small, concentrated areas.

Pyrochlore can occur occasionally as equally small masses on the grain boundaries of euhedral apatite. Pyrochlore occasionally occurs intergrowing with other accessory minerals, such as baddeleyite in NTG6 and thorite in NTG23.

A red/orange isotropic mineral with high relief and weak anomalous anisotropism

along internal fractures is believed to be pyrochlore and was observed in both NTG7 and NTG8. In NTG7, they are fairly common and occur as small, fractured, subhedral granular crystals up to 0.1 mm in size. Some contain inclusions of rounded opaque minerals believed to be Fe-Ti oxides and they are often partially overgrown by clinopyroxene, although there is no clear evidence of replacement.

Secondary pyrochlore is a ubiquitous phase in eudialyte alteration assemblages. It is the only Nb-bearing mineral in these assemblages.

2.6.19 REE carbonates

REE carbonates occurred most commonly within eudialyte alteration assemblages. In NTG19, REE carbonates, along with other minerals such as thorite and fluorite were found as inclusions or within fractures in euhedral prisms of UKM1 and UKM2, as seen in Figure 44. They also occur as a secondary product of britholite in NTG25. In the same sample, they occur as primary minerals bordering apatite grains alongside Fe-Ti oxides. In NTG30, REE carbonates were found as inclusions in strongly zoned apatites.

2.6.20 Thorite

Thorite was found as a primary mineral in NTG23, both intergrown with pyrochlore and between strands of molybdenite, representing a very minor phase. Thorite also occurs as a secondary mineral and was observed in some eudialyte alteration assemblages. It was also found as a secondary replacement of primary britholite in NTG25, intergrowing with secondary aegirine and REE carbonates.

2.6.21 Fluorite

Fluorite was found as a secondary mineral in two situations. It is most common as an alteration product of eudialyte. In this assemblage, fluorite and calcite are the two main Ca-bearing secondary minerals and can coexist in the same assemblage. Fluorite is generally the dominant Ca-bearing mineral in NTG19 but is less common in NTG15 and NTG23, where assemblages often contain more calcite.

Fluorite was also found as part of a secondary assemblage with sodic pyroxene and biotite in NTG18 and NTG19. It concentrates along biotite cleavage planes. The presence of secondary fluorite in these samples suggests that they have a relatively high F content.

2.6.22 UKM1 & UKM2

UKM1 is a significant unidentified mineral that was found in NTG19 and possibly also seen in NTG33. It is a Ti-bearing silicate mineral containing Ca and a high REE content. The mineral is believed to be yellow. In PPL it is colourless, often with a yellow tint, isotropic and high relief (Figure 34). As a common accessory mineral, occurs typically as euhedral skeletal prisms up to 1 mm in length, often extensively fractured. Pyrochlore, thorite, Fe-Ti oxides and REE-carbonates were identified within the fractures. UKM1 appears to have an affiliation with amphibole, often seen alongside one another, with amphibole partially overgrowing UKM1, suggesting that it crystallised early. Amphibole may be partially replacing UKM1, as shown in Figure 44, where prisms of UKM1 appear to be infiltrated by amphibole. In Figure 34, amphibole creates a thin discontinuous rim around UKM1 extending outside of its grain boundary.

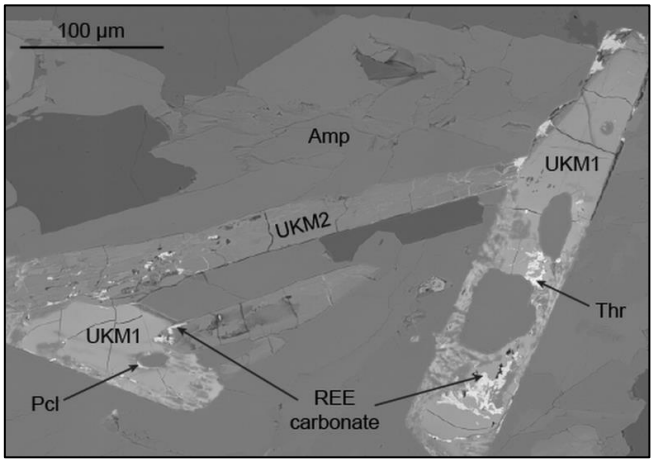

Figure 44: BSE image from NTG19 showing prisms of UKM1 and UKM2 with amphibole (Amp). Thorite (Th), pyrochlore (Pcl) and REE carbonates have been identified along surfaces and fractures.

UKM2 is also prismatic and exclusive to NTG19, typically found alongside UKM1, as in Figure 44. It is a F-bearing, Ca-rich Zr-Ti-silicate also containing Na, Al, and small amounts of Mn and Fe. It was not possible to accurately determine elemental proportions from semi-quantitative EDS data alone in order to positively identify this mineral. Its small size and numerous inclusions make it difficult to analyse optically also.

3. Results

The following chapter outlines findings from the analysis of samples outlined in Table 1. Whole rock geochemistry is used to classify rock types and provide insight into compositional variations of the Bjønnes syenite, both internally and relative to samples from Tvedalen and Lågendalen. The chemical compositions of minerals were analysed using EMP (electron microprobe) and SEM (scanning electron microscope) and show evolutionary trends and compositional variations of analysed minerals.

3.1 Whole rock geochemistry

Table 3 contains whole rock major and trace element data for a total of 18 samples taken from Bjønnes, Tvedalen and Lågendalen. It also includes calculated molar atomic ratios for alkalinity index AI ((Na + K) / Al) and Mg# ((Mg / (Mg + Fe_{tot})), both as decimal fractions.

3.1.1 Major elements

The (Na_2O + K_2O / SiO_2) ratios were used to chemically classify the samples using a TAS diagram (*Middlemost, 1994*), illustrated in Figure 45. With the exception of three samples, all fall into the classification of a foid-syenite, all since nepheline is the dominant feldspathoid mineral in all samples, they can be classified as nepheline syenites. Samples NTG8 and NTG17 are classified as nepheline monzosyenites. NTG22 sits in the syenite classification field, very close to the boundary of nepheline syenite. Petrographically, NTG22 does contain small amounts of nepheline so it is nepheline syenite. Sericite alteration, mostly of feldspars, can be seen optically. Sericite is a fine white mica produced from the hydrothermal alteration of K-bearing felsic minerals such as feldspars and feldspathoids (*Winter, 2010*). This most likely caused a reduction of Na_2O+K_2O content of NTG22, causing it to fall below the nepheline syenite field in the TAS diagram (Figure 45). NTG8 also shows sericite alteration of nepheline and feldspars. In feldspars, alteration is often confined along exsolved plagioclase lamellae. These three samples contain the highest TiO_2 contents of analysed samples.

Table 3: Total whole rock characterisation results including calculated alkalinity indexes and Mg#'s.

Sample	NTG6	NTG8	NTG12	NTG14	NTG15	NTG16b
Rock type	Nep. Sy.	Nep. Sy.	Foyaite	Foyaite	Nep. Sy.	Nep. Sy dyke
Location	Bjønnes	Bjønnes	Lågendalen	Lågendalen	Bjønnes	Tvedalen
Weight percent oxides						
SiO_2	56.59	57.25	57.12	57.28	56.08	57.30
TiO_2	0.99	1.59	1.30	0.56	0.86	0.93
Al_2O_3	19.93	17.13	17.97	22.27	18.90	18.87
Fe_2O_3	5.00	6.67	5.18	1.97	5.32	5.28
MnO	0.18	0.22	0.22	0.11	0.20	0.16
MgO	0.75	1.20	1.57	0.26	0.59	1.07
CaO	1.78	2.58	2.16	0.62	1.70	2.08
Na_2O	7.59	5.34	6.73	10.06	8.23	7.15
K_2O	6.15	6.30	5.40	5.76	5.98	5.69
P_2O_5	0.20	0.39	0.57	0.06	0.16	0.24
Total	99.16	98.67	98.22	98.95	98.02	98.77
Atomic ratios						
AI	0.96	0.91	0.94	1.02	1.06	0.95
Mg#	0.23	0.26	0.37	0.21	0.18	0.29
Trace elements, parts per million						
Ba	150	345	928	29	75	293
Sc	7	10	11	5	4	6
Be	4	4	5	3	12	6
Co	3	4	3	1	3	3
Cs	1	5	2	2	6	1
Ga	33	30	22	23	38	32
Hf	25	40	16	9	148	62
Nb	166	197	161	144	920	312
Rb	271	224	128	190	370	218
Sn	2	2	11	3	9	4
Sr	109	248	314	28	91	225
Ta	8	10	9	13	58	15
Th	9	12	20	8	37	14
U	3	3	5	9	10	5
W	1	1	3	1	25	1
Zr	1326	2137	722	325	5447	3208
Y	35	50	40	17	198	52
La	102	141	122	68	315	143
Ce	228	307	235	156	601	312
Pr	25	35	26	18	62	36
Nd	90	123	87	61	192	128
Sm	14	19	13	9	32	21
Eu	2	2	4	1	2	2
Gd	10	14	10	6	28	15
Tb	1	2	1	1	5	2
Dy	8	11	8	4	34	12
Ho	1	2	1	1	7	2
Er	4	5	4	2	24	6
Tm	1	1	1	0	4	1
Yb	4	5	4	2	27	6
Lu	1	1	1	0	4	1
ΣREE	492	669	516	330	1337	688

Table 3 continued.

Sample	NTG17	NTG18	NTG20	NTG21	NTG22	NTG23
Rock type	Nep. Sy.	Nep. Sy.	Nep. Sy.	Nep. Sy.	Nep. Sy dyke	Nep. Sy.
Location	Bjønnes	Bjønnes	Bjønnes	Bjønnes	Bjønnes	Bjønnes
Weight percent oxides						
SiO_2	56.58	56.33	56.85	56.11	58.31	55.63
TiO_2	1.28	0.94	1.19	0.83	1.49	0.87
Al_2O_3	17.60	19.15	18.98	20.96	17.06	19.03
Fe_2O_3	6.64	5.98	5.28	3.98	6.60	5.66
MnO	0.24	0.20	0.17	0.13	0.23	0.22
MgO	1.18	0.78	0.92	0.70	1.02	0.58
CaO	2.63	1.53	2.04	1.45	2.01	1.97
Na_2O	6.06	7.98	6.89	8.15	6.10	8.14
K_2O	5.69	5.87	6.41	6.41	5.92	5.92
P_2O_5	0.46	0.21	0.25	0.17	0.31	0.16
Total	98.36	98.97	98.98	98.89	99.05	98.18
Atomic ratios						
AI	0.92	1.02	0.96	0.97	0.96	1.04
Mg#	0.26	0.20	0.26	0.26	0.23	0.17
Trace elements, parts per million						
Ba	499	108	159	103	93	73
Sc	10	6	7	5	14	5
Be	8	17	5	7	4	14
Co	4	3	4	2	3	2
Cs	3	4	1	2	2	4
Ga	30	35	29	34	27	36
Hf	34	18	43	39	10	131
Nb	257	149	144	184	87	659
Rb	226	265	232	276	176	303
Sn	4	10	1	2	1	8
Sr	270	94	131	87	79	132
Ta	14	6	8	9	5	45
Th	20	48	12	11	4	41
U	6	9	4	3	1	9
W	3		1	1	1	26
Zr	1470	781	2428	2070	325	5115
Y	60	22	43	33	35	169
La	173	115	112	103	124	275
Ce	376	248	252	229	272	552
Pr	41	28	28	26	32	55
Nd	143	93	100	89	113	178
Sm	22	13	16	14	17	30
Eu	3	1	2	1	2	2
Gd	16	9	12	10	12	25
Tb	2	1	2	1	2	4
Dy	13	6	9	7	8	29
Ho	2	1	2	1	1	6
Er	6	2	5	4	4	19
Tm	1	0	1	1	0	3
Yb	7	3	5	4	4	22
Lu	1	1	1	1	1	3
ΣREE	806	519	544.98	490.31	592.35	1206

Table 3 continued.

Sample	NTG24	NTG25	NTG26a	NTG26b	NTG29	NTG30
Rock type	Nep. Sy.	Nep. Sy.	Nep. Sy dyke	Nep. Sy dyke	Nep. Sy dyke	Nep. Sy.
Location	Bjønnes	Bjønnes	Tvedalen	Tvedalen	Tvedalen	Bjønnes
Weight percent oxides						
SiO_2	55.76	56.00	56.53	56.56	58.77	56.77
TiO_2	0.92	0.86	0.88	0.91	0.61	1.12
Al_2O_3	20.01	20.07	20.20	19.56	20.72	18.96
Fe_2O_3	5.20	4.84	4.59	5.19	3.10	5.29
MnO	0.16	0.15	0.15	0.18	0.09	0.18
MgO	0.81	0.80	0.71	0.77	0.47	0.83
CaO	1.72	1.55	1.55	1.55	1.25	1.85
Na_2O	7.74	7.95	8.05	7.97	7.67	7.39
K_2O	6.40	6.29	6.28	6.13	6.43	6.31
P_2O_5	0.19	0.19	0.17	0.19	0.11	0.23
Total	98.91	98.70	99.11	99.01	99.22	98.93
Atomic ratios						
Al	0.98	0.99	0.99	1.01	0.95	1.00
Mg#	0.24	0.25	0.23	0.23	0.23	0.24
Trace elements, parts per million						
Ba	86	77	132	128	242	150
Sc	6	5	6	5	3	7
Be	6	9	8	10	2	12
Co	2	3	3	2	2	3
Cs	2	3	2	3	1	3
Ga	36	36	33	32	29	31
Hf	42	70	50	53	23	48
Nb	224	239	261	321	119	229
Rb	325	318	270	270	229	263
Sn	3	4	5	7	2	6
Sr	86	94	96	91	193	110
Ta	10	10	14	18	6	12
Th	13	18	27	33	6	32
U	3	4	8	13	2	6
W	1		3	2		4
Zr	2064	3861	2477	2518	1149	2364
Y	34	34	50	52	24	53
La	120	114	125	140	61	128
Ce	271	255	272	305	134	276
Pr	31	29	30	34	15	30
Nd	104	97	103	112	53	103
Sm	15	15	16	18	9	16
Eu	1	1	2	2	2	2
Gd	11	10	12	13	6	12
Tb	1	1	2	2	1	2
Dy	8	8	10	11	5	10
Ho	1	1	2	2	1	2
Er	4	4	6	6	2	6
Tm	1	1	1	1	0	1
Yb	5	5	6	7	3	6
Lu	1	1	1	1	0	1
ΣREE	573	541	588	652	293	596

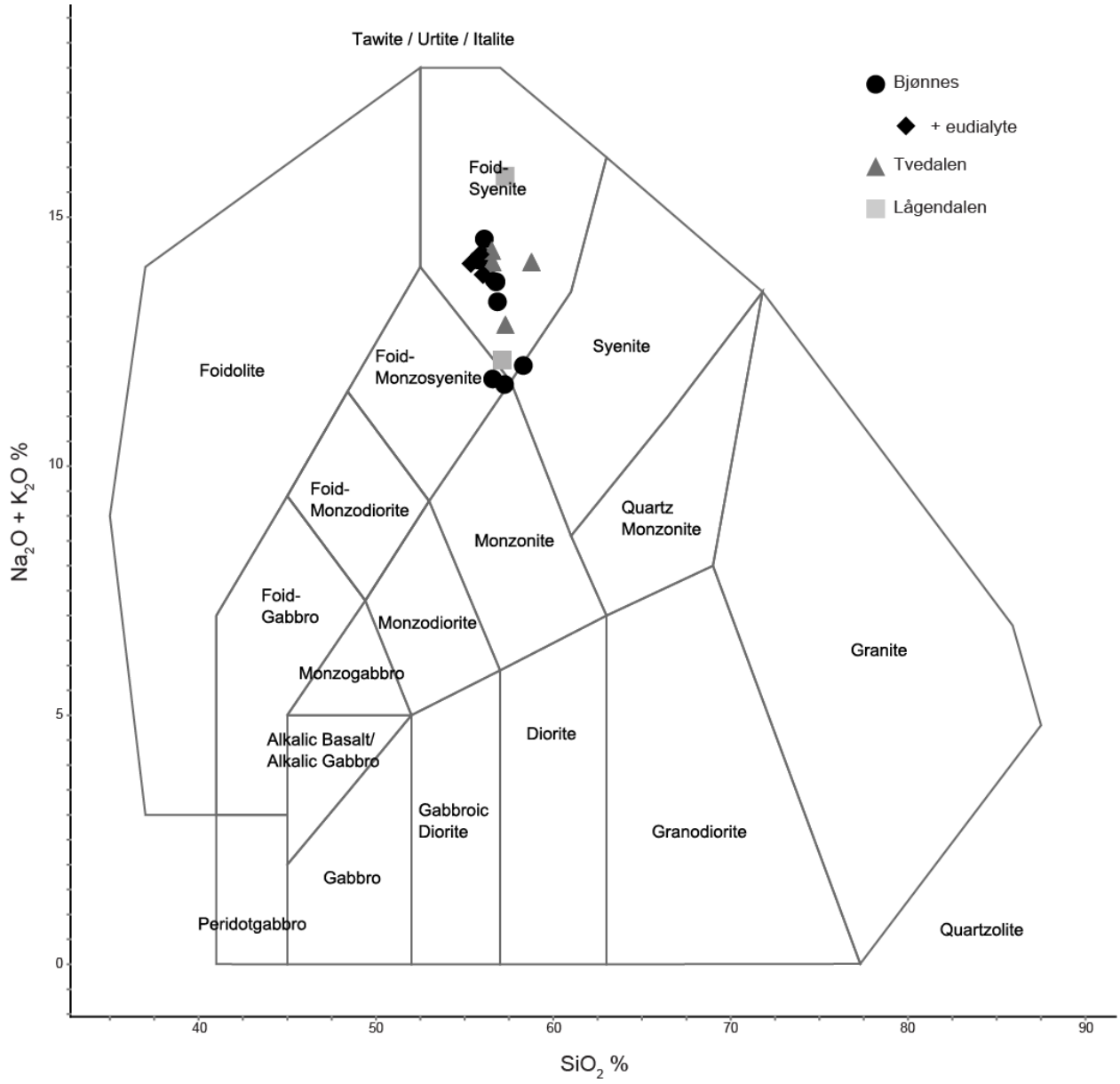

Figure 45: TAS plutonic diagram (*Middlemost, 1994*) used to chemically classify samples from Table 3. Most samples plot as nepheline syenites whilst three remaining samples plot marginally outside of the nepheline syenite field.

These three samples were collected from Bjønnes and show similarly low Na_2O+K_2O contents of 11.5 – 12 wt. %, also showing generally high SiO_2 contents. All other samples from Bjønnes are well grouped, ranging from 13.3 – 14.6 wt. % Na_2O+K_2O and 55.6 – 56.9 wt. % SiO_2. The main clustering of Bjønnes syenites has relatively low SiO_2 contents.

The four samples from Tvedalen show significant diversity. Samples NTG26a and NTG26b have very similar compositions and also fit well with the main cluster of Bjønnes syenites. However NTG16b has significantly lower Na_2O+K_2O in comparison and NTG29 has the highest SiO_2 content of all samples, around 2 wt. % higher than NTG26a and NTG26b. It also has an anomalously low mafic content, with a total (MgO

+ Fe_2O_3 + MnO) of 3.66 wt. %, compared to an average total of 6.03 wt. % in the other Tvedalen samples.

The two foyaite samples from Lågendalen have very similar SiO_2 contents, but NTG14 has a much higher Na_2O+K_2O content than all samples including NTG12 with a total of 15.82 wt.%, which is 1.26 wt.% higher than the next highest total (NTG21). It also has significantly less mafic content than any other analysed samples, totalling 2.34 wt. %. The overall average mafic content is 6.11 wt. %.

In all samples, Fe is the dominant mafic component, with molar Mg# ranging from 0.16 – 0.36 (see Table 3). The sample with the highest Mg# is NTG12, whilst the other sample from Lågendalen, NTG14 has a lower Mg# than the total average, 0.23. Along with NTG14, three other samples, NTG15, NTG18 and NTG23, have Mg# below 0.2, all from Bjønnes. The remaining samples from Bjønnes and Tvedalen have similar mafic compositions, ranging from 0.22 – 0.26.

Molar alkalinity indexes range from 0.91 to 1.06 (see Table 3), averaging 0.98. This is represented in Figure 46, where alkalinity index is plotted against SiO_2. There appears to be a broadly negative correlation between alkalinity index and SiO_2 content. Two horizontal boundaries are shown in Figure 46, at an alkalinity index of 1.0 and 1.2. The boundary at AI = 1.2 represent the original limit between agpaitic (>1.2) and non-agpaitic (<1.2) rocks defined by *Ussing (1912)*. Nepheline syenites with AI < 1.2 were later termed miaskitic (*Khomyakov 1995*). The boundary at AI = 1.0 indicates the limit of peralkalinity (*Frost & Frost, 2008*). Below this limit, rocks are classified as metaluminous (*Frost & Frost, 2008*).

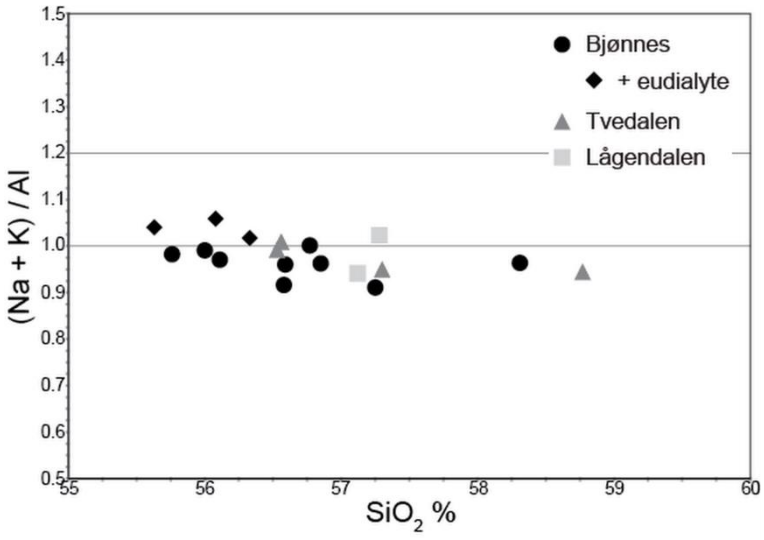

Figure 46: Alkalinity index plotted against SiO_2 content to categorise samples as agpaitic (AI>1.2) or non-agpaitic (AI<1.2) according to definition by *Ussing (1912)*, and as peralkaline (AI>1.0) or metaluminous (AI<1.0) from *Frost & Frost (2008)*.

According to limits defined by *Ussing (1912)*, no samples would be classified as agpaitic. However, six samples have an alkalinity index of above 1.0, so would be termed peralkaline, with their classification of miaskitic or agpaitic determined by their mineralogy (*Khomyakov, 1995; Marks et al., 2011*). The remaining samples with an alkalinity index below 1.0 are miaskitic. They are also metaluminous,

with the exception of NTG29, which is slightly peraluminous (see Appendix 3) (*Frost & Frost, 2008*).

From Bjønnes, three of four peralkaline samples, NTG15, NTG18 and NTG23, also had a relatively low Mg#, whilst from Lågendalen, NTG14 also had a low Mg# and alkalinity index above 1.0. From Tvedalen, NTG26a and NTG26b are higher than NTG16b and NTG29 in alkalinity, with NTG26b having an alkalinity index of 1.01. Two samples from Bjønnes, NTG8 and NTG17, show much lower alkalinity indexes than other samples, and both classified as nepheline monzosyenites on a TAS diagram (Figure 45). In general, alkalinity indexes in samples from Bjønnes and Tvedalen are very similar, with average alkalinity indexes of 0.98 in Bjønnes and 0.97 in Tvedalen.

3.1.2 Trace elements

Two samples from Bjønnes, NTG15 and NTG23, show similarly high concentrations of Zr, Nb, Hf, Ta, Rb, Th, U, Y, Be, Sn, W and REE's relative to other analyses. Of these, Zr is particularly high, with both containing over 5000 ppm, much greater than the overall average of 2210 ppm, whilst Nb and Hf are also greatly enriched. Another sample, NTG18, also has high similarly concentrations of Be, Sn, Th and U but has relatively low concentrations of Zr, Hf, Ta and Y. NTG22 also has relatively low concentrations of Zr, Hf and Ta, but also has low Th and U and relatively enriched in only Sc.

In general, samples from Bjønnes and Tvedalen show similar trace element concentrations. Perhaps an exception to this is NTG29, which is depleted in Hf, Nb, Th and U, similar to NTG22. However NTG29 is also enriched in Sr and heavily depleted in REE's with a sum of 293 ppm, much lower than the average across Bjønnes and Tvedalen, 662 ppm.

From Lågendalen, NTG14 is also heavily depleted in REE's, whilst NTG12 is below average but still has significantly higher REE content. Both samples show low Zr and Hf concentrations relative to those from Bjønnes and Tvedalen. Whereas NTG14 is heavily depleted in Sr, with just 28.4 ppm, NTG12 has the highest concentration of Sr, with 314.3, compared to the overall average of 137.7.

3.1.3 Rare Earth elements

Figure 47 shows the distribution of REE's between samples normalised to C1 Chondrite (*McDonough & Sun, 1995*). The general distribution pattern shows a moderately steep, LREE-enriched slope. All samples with the exception of NTG12

show a strong negative Eu anomaly. Within the LREE's (La – Eu), the gradient of the slope becomes greater towards Eu. Within the HREE's (Eu – Lu), the slope becomes curved and inverted, showing a relative increase in Yb and Lu.

Both NTG15 and NTG23 have relatively high concentrations of all REE's, excluding the Eu anomaly. The relative difference compared to the total average is generally greater for HREE's, although similar differences are observed in La concentrations. They also follow a much less curved path through the HREE's than is observed from other samples. Another sample from Bjønnes that does not fit the general trend neatly is NTG18, where LREE concentrations are consistent with other samples but it contains significantly lower HREE's relative to other samples from Bjønnes, also showing a more exaggerated curve resulting in a particularly low Er content.

Similar to trace elements, samples from Tvedalen and Bjønnes show very similar REE distributions. They make up the majority of samples and all show very consistent REE distributions, producing a very clear pattern, seen in Figure 47. An exception to this from Tvedalen is NTG29, which has much lower overall REE content and is particularly low in LREE's. Another feature of NTG29 is that it has a significantly weaker Eu anomaly than any other sample from Bjønnes or Tvedalen.

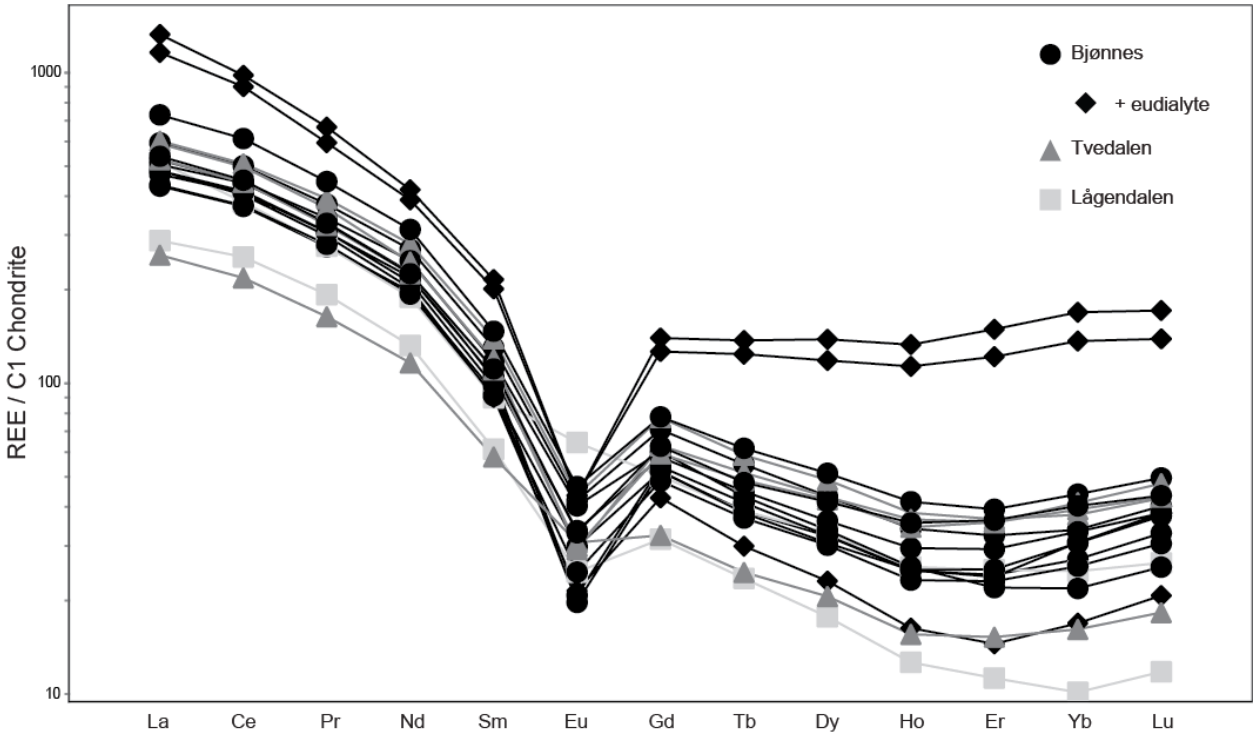

Figure 47: Rare Earth element spider diagram normalised to C1 Chondrite (*McDonough & Sun, 1995*) showing the abundance and distribution of REE's from whole rock geochemical data (Table 3).

Neither sample from Lågendalen conforms strongly with general REE distributions from Bjønnes or Tvedalen. Despite its REE pattern and content fitting well with the bulk of other samples, NTG12 shows no Eu anomaly, a prime feature of all analysed samples. Although very different to NTG12, NTG14 also does not fit the prevailing pattern. It does have an Eu anomaly, however it also has very low REE contents, particularly HREE's, where it shows less of a curved pattern than most samples, meaning that the heaviest HREE's are even lower in concentration. More analysis is clearly needed to properly constrain the REE distributions of foyaites in Lågendalen but this data at least suggests that they do not share a relatable REE pattern with the nepheline syenites of Bjønnes or Tvedalen.

3.2 Mineral chemistry

Quantitative element compositional data collected from EMP analysis of selected samples from the Bjønnes syenite are displayed for olivine, clinopyroxene, amphibole, biotite, aenigmatite and titanite. Data for single point analyses of clinopyroxene, amphibole and biotite is presented in Appendix 4. Semi-quantitative geochemical data for other accessory minerals, acquired from EDS analysis using SEM, are also discussed.

3.2.1 Olivine

Olivine (Fo-Fa solid solution) is reasonably common in samples such as NTG6, NTG8 and NTG20, but was not found at all in other samples from Bjønnes. Compositions of analysed olivine are displayed in Table 4. Olivine shows a consistently Fe-rich composition, ranging from $Fo_{13}Fa_{87}$ – $Fo_{14}Fa_{86}$ and also shows a notable Mn component. Other mafic minerals surrounding the olivine grains, notably clinopyroxene and biotite, show no clear distinction in chemical composition from others that are not in contact with olivine.

Table 4: Composition (weight percent oxides) and formula calculations of olivine from Bjønnes.

Sample	NTG6	NTG6	NTG6	NTG20	NTG20	NTG20	NTG20
Analysis	78/3	79/3	80/3	81/3	82/3	85/3	86/3
SiO_2	29.70	29.74	29.77	29.96	30.39	29.75	29.71
TiO_2	0.04	0.04	0.05	0.03	0.02	0.03	0.02
ZrO_2	0.02	0.01	0.01	-	-	-	0.01
Al_2O_3	-	0.01	-	-	-	0.03	-
FeO	59.63	59.37	60.01	59.19	59.34	59.37	59.07
MnO	4.02	4.12	3.95	4.21	4.07	4.25	4.06
MgO	5.11	5.42	5.05	5.40	4.91	5.20	5.29
CaO	0.27	0.25	0.22	0.34	0.36	0.27	0.32
Total	98.78	98.95	99.07	99.00	98.97	98.76	98.38
Mg#	0.13	0.14	0.13	0.14	0.13	0.14	0.14

Mg# (Mg/(Mg+Fe)) calculated as molar ratio and expresses as decimal fraction.
- : below detection limit

3.2.2 Clinopyroxene

Clinopyroxene compositions range from 9 – 99% (molar) of non-quadrilateral (En-Fs-Di-Hd) components. This is due to substantial Na content and also minor Al content. Therefore the commonly used Mg-Fe-Ca ternary diagram cannot be used to adequately depict the observed variations in chemical composition and an aegirine component must be considered. The low Al-content relative to Na implies that jadeite and NATAL components are insignificant.

Clinopyroxene compositions are therefore expressed in terms of three end-member components, aegirine ($NaFe^{3+}Si_2O_6$), diopside ($CaMgSi_2O_6$) and hedenbergite ($CaFe^{2+}Si_2O_6$) and all compositions plot within an aegirine-diopside-hedenbergite ternary diagram (Figure 48). The compositions range from $Ae_9Di_{59}Hd_{32}$ to $Ae_{99}Di_1Hd_0$, generally trending from a diopside-dominant composition towards increasing hedenbergite and aegirine components. Clinopyroxene compositions are presented in Table 5.

NTG19 consistently shows the most evolved compositions of any sample, hosting exclusively aegirine-dominated clinopyroxene ranging from $Ae_{79}Di_{10}Hd_{11}$ to $Ae_{99}Di_1Hd_0$. Clinopyroxene in this sample are almost all secondary and tend to have a much richer green colour than is typical in other samples. Ca^{2+}_{M2} + (Mg, Fe^{2+})$_{M1}$ → Na^{+}_{M2} + Fe^{3+}_{M1} is the primary substitution mechanism for increasing an aegirine component from a diopside-hedenbergite dominated composition, as demonstrated by Figure 49.

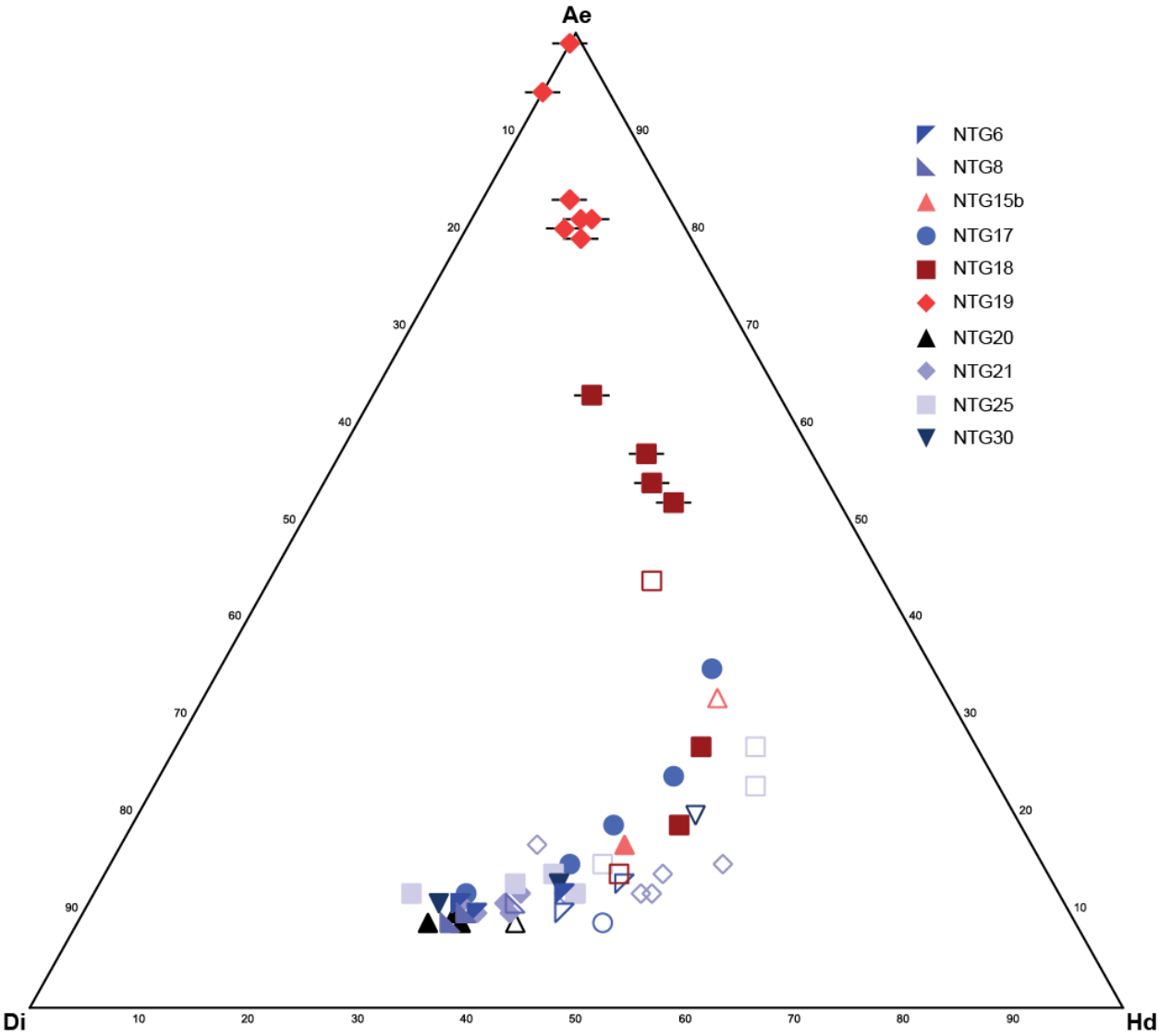

Figure 48: Clinopyroxene compositional end-members (Aegirine-Diopside-Hedenbergite) calculated from samples in Bjønnes (Table 2) showing differentiation in core-rim compositions. Filled and open symbols represent core and rim data respectively, whilst horizontal strikes represent secondary clinopyroxene. Eudialyte-bearing samples are highlighted by red symbols.

Another compositional feature of NTG19 is its elevated Ti content, with TiO_2 present up to 2.60 wt.% in NTG19-3. This is significantly greater than the highest total from any other sample, 1.14 wt.% in NTG20-3, or overall average of 0.76 wt.%. In high-Ti analyses from NTG19, $(Fe^{3+} + Fe^{2+} + Mn + Mg) > 1$, leaving the M1-site relatively unfilled. It can therefore be assumed that in this case Ti is incorporated into the M1-site via a coupled substitution with Na, in the form of $Ca^{2+}_{M2} + 2(Mg, Fe^{2+})_{M1} \rightarrow Na^{+}_{M2} + Ti^{4+}_{M1} + (Mg, Fe^{2+})_{M1}$ (*Nielsen, 1979*). NTG18 and NTG15 also contain slightly higher Ti than most samples and also have a relatively high aegirine component, suggesting that Ti was incorporated in the same way. A Tschermak substitution, in the form of $2Si^{4+}_{T} + (Mg, Fe^{2+})_{M1} \rightarrow 2Al^{3+}_{T} + Ti^{4+}_{M1}$ (*Nielsen, 1979*) may also have a minor influence on Ti incorporation throughout the samples.

Table 5: Composition (weight percent oxides) and formula calculations of pyroxenes from Bjønnes (C – core; R – rim; S – secondary).

Sample	NTG6-1	NTG6-2	NTG6-3	NTG6-4	NTG6-5	NTG8-1	NTG8-2	NTG8-3	NTG15b-1	NTG15b-2
C/R/S	R	C	C	R	C	C	C	R	R	C
n	4	2	2	3	2	4	4	1	3	3
SiO_2	50.1(3)	49.9(1)	51.3(2)	50.6(2)	51.0(1)	51.4(3)	51.2(2)	50.849	49.59(2)	50.0(2)
TiO_2	0.46(5)	0.674(2)	0.65(3)	0.55(3)	0.656(2)	0.60(1)	0.66(2)	0.533	0.76(1)	0.75(4)
ZrO_2	0.5(1)	0.45(7)	0.379(5)	0.46(2)	0.42(4)	0.34(3)	0.34(4)	0.450	0.88(2)	0.38(2)
Al_2O_3	0.68(4)	0.98(1)	1.077(8)	0.81(5)	0.935(8)	0.935(8)	1.02(3)	0.744	0.81(1)	0.97(5)
FeO	17.6(4)	15.8(1)	13.3(7)	15.70(6)	13.7(1)	13.4(1)	12.7(2)	14.608	21.7(3)	17.8(6)
MnO	0.93(2)	0.79(1)	0.68(3)	0.90(3)	0.78(1)	0.73(5)	0.73(4)	0.765	0.88(4)	0.78(1)
MgO	6.8(1)	7.526(8)	9.5(4)	8.05(9)	9.3(1)	9.53(5)	10.0(2)	8.475	3.31(4)	6.1(4)
CaO	20.60(7)	21.05(3)	21.61(6)	21.26(6)	21.65(7)	21.8(2)	22.0(1)	21.450	16.3(1)	20.5(2)
Na_2O	1.70(5)	1.54(4)	1.41(2)	1.32(3)	1.35(1)	1.32(1)	1.25(1)	1.451	4.29(9)	2.26(8)
Total	99.45	98.76	99.97	99.65	99.75	100.07	99.98	99.35	98.56	99.6
Structural formulas based on 4 cations and 12 negative charges										
Si	1.96	1.95	1.95	1.96	1.95	1.96	1.95	1.96	1.96	1.94
Ti	0.01	0.02	0.02	0.02	0.02	0.02	0.02	0.02	0.02	0.02
Zr	0.01	0.01	0.01	0.01	0.01	0.01	0.01	0.01	0.02	0.01
Al	0.03	0.05	0.05	0.04	0.04	0.04	0.05	0.03	0.04	0.04
Fe^{3+}	0.15	0.12	0.10	0.11	0.11	0.10	0.11	0.11	0.31	0.19
Fe^{2+}	0.43	0.39	0.32	0.40	0.32	0.32	0.30	0.36	0.41	0.39
Mn	0.03	0.03	0.02	0.03	0.03	0.02	0.02	0.03	0.03	0.03
Mg	0.39	0.44	0.54	0.46	0.53	0.54	0.57	0.49	0.20	0.36
Ca	0.86	0.88	0.88	0.88	0.89	0.89	0.90	0.89	0.69	0.85
Na	0.13	0.12	0.10	0.10	0.10	0.10	0.09	0.11	0.33	0.17
End-member calculations										
Ae	13	12	11	10	10	10	9	11	32	17
Di	39	45	55	46	54	55	57	50	21	37
Hd	48	43	34	44	36	35	34	39	47	46

Sample	NTG17-1	NTG17-2	NTG17-4	NTG17-5	NTG17-6	NTG17-7	NTG18-1	NTG18-2	NTG18-3	NTG18-4
C/R/S	C	C	R	C	C	C	C	R	S	S
n	9	3	6	2	2	2	4	1	4	2
SiO_2	51.4(3)	50.9(1)	51.0(3)	50.9(1)	50.7(1)	50.69(4)	50.1(2)	51.091	51.1(1)	51.2(3)
TiO_2	0.60(2)	0.57(3)	0.52(5)	0.48(4)	0.505(2)	0.21(9)	0.68(2)	0.621	0.9(1)	0.64(3)
ZrO_2	0.38(2)	0.66(2)	0.03(1)	0.06(1)	0.629(5)	0.3(1)	n.a.	n.a.	n.a.	n.a.
Al_2O_3	0.91(4)	0.73(1)	0.97(7)	0.82(6)	0.61(2)	0.15(6)	0.68(1)	0.727	0.83(2)	0.825(9)
FeO	13.3(3)	16.2(5)	16.6(5)	18.1(1)	20.23(5)	23.026(3)	19.3(2)	17.288	24.11(7)	23.707(6)
MnO	0.72(2)	0.90(5)	0.66(3)	0.682(9)	0.83(1)	1.47(4)	0.99(6)	0.891	0.65(4)	0.71(1)
MgO	9.3(1)	7.2(2)	7.2(4)	6.06(1)	4.83(8)	3.43(1)	5.0(2)	6.650	2.33(7)	2.45(7)
CaO	21.4(1)	20.4(3)	22.1(3)	19.723(8)	17.9(1)	15.7(1)	19.5(1)	20.681	10.53(9)	11.62(7)
Na_2O	1.62(3)	2.08(6)	1.28(8)	2.547(8)	3.37(7)	4.6(1)	2.5(1)	1.882	7.60(5)	6.94(5)
Total	99.63	99.67	100.38	99.39	99.63	99.52	98.86	99.83	98.00	98.08
Structural formulas based on 4 cations and 12 negative charges										
Si	1.96	1.97	1.97	1.98	1.98	1.98	1.97	1.98	1.99	2.00
Ti	0.02	0.02	0.02	0.01	0.01	0.01	0.02	0.02	0.03	0.02
Zr	0.01	0.01	0.00	0.00	0.01	0.01	-	-	-	-
Al	0.04	0.03	0.04	0.04	0.03	0.01	0.03	0.03	0.04	0.04
Fe^{3+}	0.11	0.14	0.09	0.17	0.23	0.36	0.18	0.12	0.51	0.46
Fe^{2+}	0.31	0.39	0.44	0.41	0.43	0.39	0.45	0.44	0.27	0.31
Mn	0.02	0.03	0.02	0.02	0.03	0.05	0.03	0.03	0.02	0.02
Mg	0.53	0.41	0.41	0.35	0.28	0.20	0.30	0.38	0.14	0.14
Ca	0.87	0.84	0.91	0.82	0.75	0.66	0.82	0.86	0.44	0.49
Na	0.12	0.16	0.10	0.19	0.25	0.35	0.19	0.14	0.57	0.53
End-member calculations										
Ae	12	15	9	19	24	35	19	14	57	52
Di	54	43	43	37	29	20	31	39	15	15
Hd	34	42	48	44	47	45	50	47	28	33

n.a.: not analysed

Table 5 continued.

Sample	NTG18-5	NTG18-6	NTG18-7	NTG18-8	NTG19-1	NTG19-2	NTG19-3	NTG19-5	NTG19-6	NTG19-7
C/R/S	S	C	R	S	S	S	S	S	S	S
n	5	1	1	1	16	1	2	9	2	2
SiO_2	51.2(2)	50.161	51.200	50.999	51.4(2)	50.954	51.7(2)	51.5(4)	51.31(3)	51.5(1)
TiO_2	0.7(1)	0.521	0.527	0.921	0.8(2)	0.876	2.60(7)	1.0(3)	1.88(5)	2.01(3)
ZrO_2	n.a.	n.a.	n.a.	n.a.	0.5(2)	0.681	0.5(1)	0.3(1)	0.34(2)	0.41(1)
Al_2O_3	0.86(2)	0.814	0.821	0.726	0.87(7)	1.355	1.0(1)	0.8(1)	0.7(1)	1.1(1)
FeO	24.0(3)	20.680	22.294	23.896	26.0(4)	26.113	26.8(2)	25.9(4)	24.98(1)	25.1(2)
MnO	0.66(6)	0.946	0.703	0.602	0.45(7)	0.510	0.074(7)	0.41(9)	0.8(1)	0.62(4)
MgO	2.58(9)	4.124	3.383	2.832	1.44(1)	1.999	0.417(4)	1.7(2)	1.60(2)	1.36(4)
CaO	11.3(2)	17.760	13.778	8.936	4.6(5)	1.437	0.16(5)	5.0(7)	5.3(4)	4.1(3)
Na_2O	7.29(4)	3.566	5.914	8.385	11.1(3)	12.017	13.92(3)	10.9(3)	10.9(3)	11.7(2)
Total	98.57	98.57	98.62	97.30	97.22	96.85	97.32	97.67	97.81	98.06
Structural formulas based on 4 cations and 12 negative charges										
Si	1.98	1.97	1.99	1.98	1.98	1.97	1.96	1.97	1.97	1.96
Ti	0.02	0.02	0.02	0.03	0.02	0.03	0.07	0.03	0.05	0.06
Zr	-	-	-	-	0.01	0.01	0.01	0.01	0.01	0.01
Al	0.04	0.04	0.04	0.03	0.04	0.06	0.05	0.04	0.03	0.05
Fe^{3+}	0.51	0.26	0.40	0.59	0.78	0.84	0.85	0.77	0.73	0.78
Fe^{2+}	0.27	0.42	0.32	0.19	0.05	0.00	0.00	0.06	0.07	0.02
Mn	0.02	0.03	0.02	0.02	0.01	0.02	0.00	0.01	0.03	0.02
Mg	0.15	0.24	0.20	0.16	0.08	0.12	0.02	0.10	0.09	0.08
Ca	0.47	0.75	0.57	0.37	0.19	0.06	0.01	0.21	0.22	0.17
Na	0.55	0.27	0.45	0.63	0.83	0.90	1.02	0.81	0.81	0.86
End-member calculations										
Ae	54	27	44	63	81	94	99	80	79	83
Di	16	25	21	17	9	6	1	11	10	9
Hd	30	48	35	20	10	0	0	9	11	8

Sample	NTG19-8	NTG19-9	NTG20-1	NTG20-2	NTG20-3	NTG20-4	NTG21-1	NTG21-2	NTG21-3	NTG21-4
C/R/S	S	S	C	R	C	C	R	R	C	C
n	2	1	7	2	2	2	4	13	12	2
SiO_2	51.53(6)	52.117	51.0(1)	50.87(8)	50.64(6)	51.2(1)	50.4(2)	50.6(2)	50.7(2)	50.76(2)
TiO_2	2.0(3)	0.549	0.67(5)	0.55(1)	1.14(3)	0.83(3)	0.57(3)	0.58(2)	0.59(2)	0.64(7)
ZrO_2	0.8(1)	0.218	0.33(3)	0.34(3)	0.381(7)	0.285(5)	0.37(4)	0.37(3)	0.37(3)	0.31(3)
Al_2O_3	0.87(5)	1.048	1.05(6)	0.84(1)	1.614(5)	1.403(2)	0.75(2)	0.89(4)	0.95(3)	1.06(1)
FeO	24.69(8)	26.138	13.0(2)	14.3(3)	12.84(4)	12.11(1)	17.0(3)	15.7(1)	14.3(3)	13.2(1)
MnO	0.71(5)	0.435	0.68(1)	0.76(2)	0.63(2)	0.665(6)	0.87(2)	0.80(4)	0.80(2)	0.711(4)
MgO	1.42(8)	1.375	9.9(1)	8.95(6)	9.69(1)	10.25(6)	6.8(1)	7.7(1)	8.7(2)	9.42(3)
CaO	4.51(8)	4.270	21.9(3)	21.7(2)	21.4(3)	22.05(6)	21.0(2)	21.5(1)	21.6(1)	21.94(6)
Na_2O	11.10(8)	11.374	1.16(6)	1.16(2)	1.38(1)	1.20(1)	1.62(4)	1.61(4)	1.4(1)	1.43(3)
Total	97.66	97.55	99.62	99.42	99.76	99.99	99.42	99.69	99.53	99.44
Structural formulas based on 4 cations and 12 negative charges										
Si	1.98	1.99	1.95	1.96	1.93	1.94	1.96	1.95	1.95	1.94
Ti	0.06	0.02	0.02	0.02	0.03	0.02	0.02	0.02	0.02	0.02
Zr	0.02	0.00	0.01	0.01	0.01	0.01	0.01	0.01	0.01	0.01
Al	0.04	0.05	0.05	0.04	0.07	0.06	0.03	0.04	0.04	0.05
Fe^{3+}	0.70	0.78	0.10	0.09	0.10	0.09	0.12	0.13	0.12	0.13
Fe^{2+}	0.09	0.05	0.31	0.37	0.31	0.29	0.44	0.37	0.34	0.29
Mn	0.02	0.01	0.02	0.02	0.02	0.02	0.03	0.03	0.03	0.02
Mg	0.08	0.08	0.56	0.51	0.55	0.58	0.40	0.44	0.50	0.54
Ca	0.19	0.17	0.89	0.89	0.88	0.90	0.88	0.89	0.89	0.90
Na	0.83	0.84	0.09	0.09	0.10	0.09	0.12	0.12	0.10	0.11
End-member calculations										
Ae	81	83	9	9	10	9	12	12	10	11
Di	8	9	56	51	56	59	38	45	51	55
Hd	11	8	35	40	34	32	50	43	39	34

n.a.: not analysed

Table 5 continued.

Sample	NTG21-5	NTG21-6	NTG21-7	NTG21-8	NTG21-9	NTG21-10	NTG21-11	NTG21-12	NTG25-1r
C/R/S	C	R	R	R	R	R	C	C	R
n	6	2	2	1	2	1	6	3	2
SiO_2	50.9(2)	49.3(3)	52.2(3)	50.063	49.0(1)	50.457	50.8(3)	50.8(2)	50.50(3)
TiO_2	0.59(1)	0.648(5)	0.51(3)	0.600	0.66(1)	0.539	0.58(3)	0.60(2)	0.608(9)
ZrO_2	0.35(5)	0.46(1)	0.43(3)	0.437	0.53(1)	0.375	0.40(1)	0.35(2)	0.47(2)
Al_2O_3	0.92(1)	0.92(4)	1.49(4)	0.728	0.95(2)	0.868	0.93(3)	0.97(1)	0.76(3)
FeO	14.7(3)	20.2(2)	15.1(1)	17.760	18.5(2)	16.004	14.3(3)	13.5(2)	17.2(1)
MnO	0.78(1)	0.91(2)	0.741(4)	0.937	0.893(5)	0.782	0.80(3)	0.79(4)	0.82(2)
MgO	8.3(2)	4.7(1)	7.61(1)	6.253	5.8(2)	7.450	8.8(2)	9.47(8)	6.8(2)
CaO	21.5(2)	20.0(1)	20.8(7)	20.676	20.5(1)	21.365	21.5(1)	21.6(1)	20.8(2)
Na_2O	1.56(1)	1.97(5)	2.32(2)	1.622	1.77(5)	1.538	1.46(6)	1.36(6)	1.969(2)
Total	99.68	99.17	101.4	99.08	98.61	99.36	99.7	99.51	100.05
Structural formulas based on 4 cations and 12 negative charges									
Si	1.96	1.95	1.97	1.97	1.94	1.96	1.95	1.94	1.95
Ti	0.02	0.02	0.01	0.02	0.02	0.02	0.02	0.02	0.02
Zr	0.01	0.01	0.01	0.01	0.01	0.01	0.01	0.01	0.01
Al	0.04	0.04	0.07	0.03	0.04	0.04	0.04	0.04	0.03
Fe^{3+}	0.12	0.15	0.13	0.11	0.17	0.12	0.13	0.13	0.17
Fe^{2+}	0.35	0.52	0.35	0.47	0.45	0.40	0.33	0.31	0.39
Mn	0.03	0.03	0.02	0.03	0.03	0.03	0.03	0.03	0.03
Mg	0.48	0.28	0.43	0.37	0.34	0.43	0.51	0.54	0.39
Ca	0.89	0.85	0.84	0.87	0.87	0.89	0.89	0.89	0.86
Na	0.12	0.15	0.17	0.12	0.14	0.12	0.11	0.10	0.15
End-member calculations									
Ae	12	15	17	12	14	12	11	10	15
Di	49	29	45	37	35	45	51	54	40
Hd	39	56	38	51	51	43	38	36	45

Sample	NTG25-2	NTG25-3	NTG25-4	NTG25-5	NTG25-6	NTG25-7	NTG30-1	NTG30-2	NTG30-3
C/R/S	R	R	C	C	C	C	R	C	C
n	2	6	2	2	2	2	9	5	5
SiO_2	49.51(6)	49.2(2)	51.01(3)	50.38(5)	50.6(1)	50.9(2)	50.0(2)	50.9(2)	51.3(3)
TiO_2	0.724(1)	0.75(4)	0.653(9)	0.567(3)	0.63(2)	0.72(1)	0.61(5)	0.56(2)	0.68(3)
ZrO_2	0.52(1)	1.13(7)	0.48(2)	0.48(4)	0.48(1)	0.49(3)	1.1(1)	0.52(3)	0.34(4)
Al_2O_3	0.729(6)	0.76(2)	0.817	0.80(2)	0.83(4)	1.03(2)	0.66(4)	0.76(4)	1.1(1)
FeO	22.28(2)	21.4(2)	14.8(3)	16.4(1)	15.8(4)	12.16(6)	19.8(4)	15.9(4)	12.6(6)
MnO	0.95(5)	1.04(4)	0.755(6)	0.870	0.826	0.74(6)	1.06(4)	0.82(3)	0.67(6)
MgO	3.20(3)	3.6(2)	8.4(3)	7.43(1)	7.7(2)	10.25(6)	4.7(3)	7.7(1)	9.9(4)
CaO	17.48(7)	18.3(2)	21.2(2)	21.4(1)	20.93(2)	21.793(8)	18.9(4)	21.0(1)	21.86(9)
Na_2O	3.51(4)	3.09(6)	1.77(5)	1.68(2)	1.8(1)	1.62(3)	2.673(3)	1.7(2)	1.5(1)
Total	98.94	99.25	99.85	100.03	99.6	99.75	99.62	99.94	99.95
Structural formulas based on 4 cations and 12 negative charges									
Si	1.96	1.95	1.96	1.94	1.95	1.93	1.97	1.96	1.95
Ti	0.02	0.02	0.02	0.02	0.02	0.02	0.02	0.02	0.02
Zr	0.01	0.02	0.01	0.01	0.01	0.01	0.02	0.01	0.01
Al	0.03	0.04	0.04	0.04	0.04	0.05	0.03	0.03	0.05
Fe^{3+}	0.26	0.24	0.14	0.16	0.15	0.16	0.18	0.13	0.12
Fe^{2+}	0.48	0.47	0.34	0.37	0.36	0.23	0.47	0.39	0.28
Mn	0.03	0.03	0.02	0.03	0.03	0.02	0.04	0.03	0.02
Mg	0.19	0.21	0.48	0.43	0.44	0.58	0.28	0.44	0.56
Ca	0.74	0.78	0.87	0.88	0.87	0.89	0.80	0.87	0.89
Na	0.27	0.24	0.13	0.13	0.14	0.12	0.20	0.13	0.11
End-member calculations									
Ae	27	23	13	12	14	12	20	13	11
Di	20	22	49	44	45	59	29	45	57
Hd	53	55	38	44	41	29	51	42	32

All samples show similar compositions with ranges that overlap with one another, with the exception of NTG19, which has a consistently greater aegirine component than all other analyses. The general trend appears to be curving along a path heading from diopside-dominant, increasing primarily in hedenbergite before curving in the direction of an increasing aegirine component, with NTG19 almost reaching a pure aegirine composition. Beyond this curve towards the aegirine end-member, the trend remains almost linear, showing an increasing aegirine component at the expense of diopside and hedenbergite components in consistent proportions.

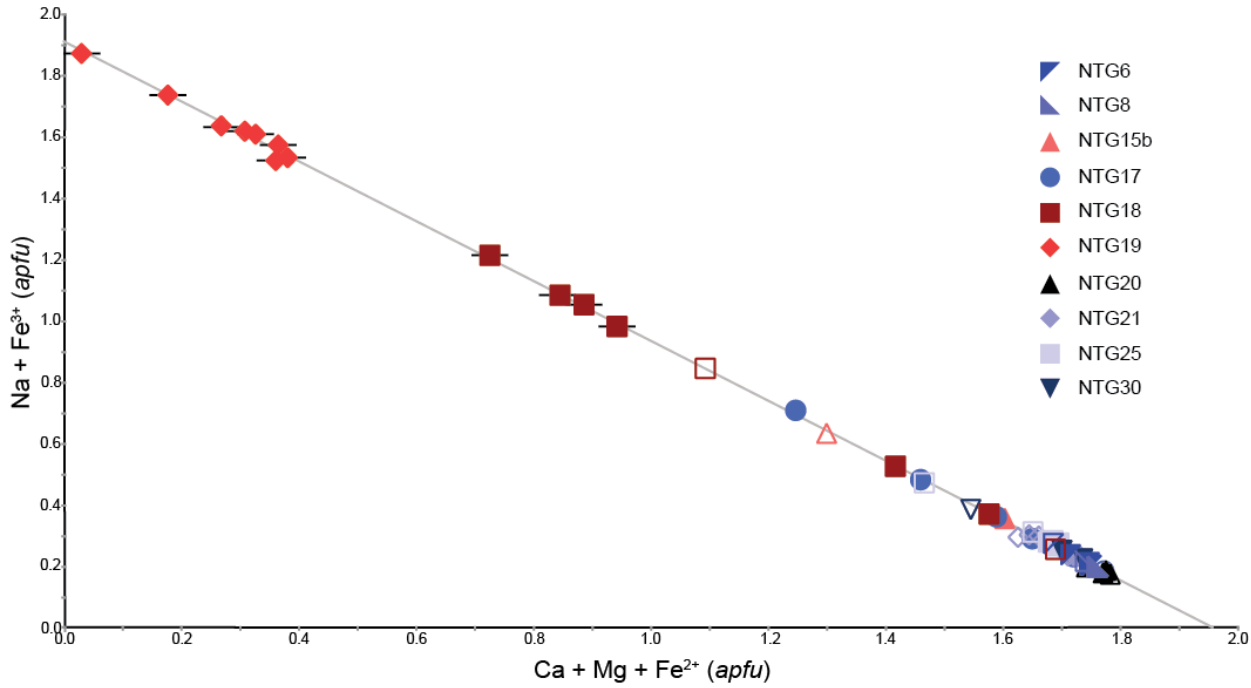

Figure 49: Graphical representation of the key substitution mechanisms within clinopyroxene from Bjønnes showing an increase in Na at the expense of Ca in the M2-site and Fe^{3+} at the expense of (Mg, Fe^{2+}) in the M1-site. The coupled substitution produces a strong linear trend that crosses the X- and Y-axes at just below 2.0, indicating that these elements fill up almost all of the M1- and M2-sites combined. Filled and open symbols represent core and rim data respectively, whilst horizontal strikes represent secondary clinopyroxene.

Concentrations of ZrO_2 generally range from 0.22 wt. % (NTG19-9) to 1.14 wt. % (NTG30-1), averaging 0.47 wt. %, however NTG17-4 and NTG17-5 contain exceptionally low Zr relative to other analyses. The Zr concentrations are quite standard and do not imply enrichment. They are also poorly constrained with no obvious controls on their distribution. In some analyses there appears to be a weak trend of increased Zr concentrations at zoned clinopyroxene rims, however this is largely diluted by random concentration variations. Incorporation of Zr into pyroxene was likely done through the replacement of Fe^{3+} from the aegirine component with Zr^{4+}, and Fe^{2+} (reduced fO_2) or Mg^{2+} (elevated fO_2) (*Andersen et al., 2011*).

Compositional zoning was common of all primary clinpyroxenes. The evolutionary trend from core to rim matches the larger evolutionary trend of clinopyroxene in the Bjønnes syenite, with cores being relatively diopsidic and rims showing increased hedenbergite and aegirine components. Internal compositional variations are usually shown by a smooth transition but can be irregular and locally quite sharp, possibly suggesting partial grain resorption during crystallisation (Figure 50).

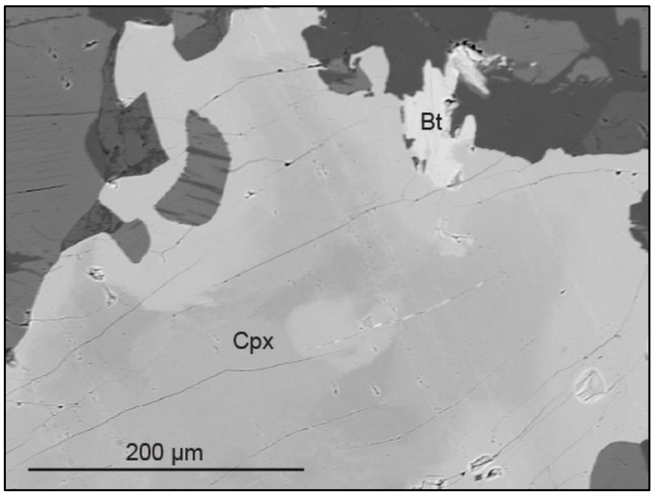

Figure 50: BSE image of a primary clinopyroxene (Cpx) from NTG25 showing characteristics of both regular and irregular zoning, generally progressing from a dark diopsidic composition to a lighter, more evolved composition.

Figure 51 shows the compositional variations throughout a zoned primary clinopyroxene analysed from NTG21, with 15 analyses taken from across its diameter. The components most strongly influenced by zoning are Fe and Mg, which show pronounced and almost opposite variation. They show a fairly consistent composition throughout most of the crystal, until around 50 µm from the edge of the grain, where compositional change begins sharply and continues at a consistent rate towards the rim. Other elemental variations occur to a lesser extent, with Na distribution showing strong correlations with Fe, whilst Al and Ca are depleted at the rim similar to Mg but are more irregularly distributed through the core. Differences in Na, Ca and Al occur on a significantly smaller scale than Fe and Mg, which may amplify random distribution and analytical uncertainty. Since Fe becomes more abundant than Mg towards the rim, and Na and Ca show comparatively little variation, the clinopyroxene evolution can be interpreted as a diopsidic core evolving into a hedenbergite-dominant composition towards the rim.

Zonation in NTG17 is quite different to other analysed samples. It is often much more patchy, irregular and less transitional. Many larger grains have a sharp zonation, suggesting some partial resorption of primitive clinopyroxene and most clinopyroxenes are overgrown and partially replaced by amphibole towards the rim. Around or within pyroxenes are smaller, more evolved pyroxenes with no significant internal variations in composition. Optically, these grains are grass green and appear to be associated with grass green clinopyroxene rims around paler cores, divided by a sharp zonation. This suggests that after partial resorption of primitive clinopyroxene, not only has more

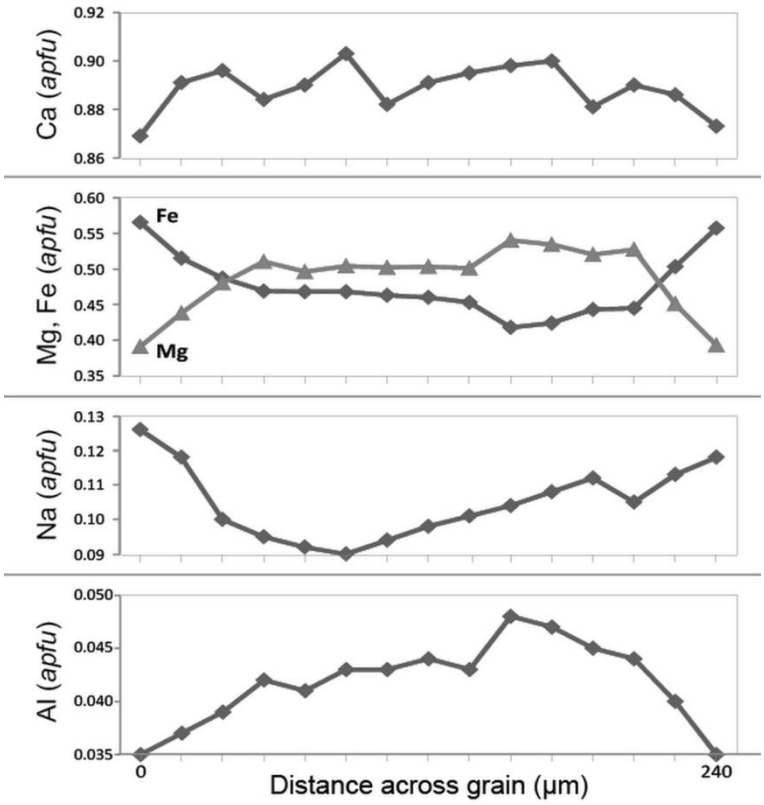

Figure 51: Selected elemental variations to display the rim-core-rim compositional zoning profile of a clinopyroxene from NTG21 showing the evolution from a diopsidic core composition to a hedenbergite-dominated rim composition. For compositional data of points see Appendix 5.

evolved clinopyroxene continued to grow, but new clinopyroxene grains have also nucleated. These are represented by NTG17-6 and NTG17-7, which have the highest aegirine component within NTG17.

An exception to the general zonation trend is seen from NTG17-5 (core) to NTG17-4 (rim), where the aegirine component drops by 10 % whilst Di/Hd remains fairly constant. The clinopyroxene analysed here is located within a large feldspar megacryst in a porphyritic syenite. Despite having a very different rim composition than would be expected, the core composition fits very well with the trend of NTG17 and other samples. The two analyses also show extremely low Zr concentrations of 0.02 – 0.06 wt. % ZrO_2. Due to the consistency of Zr distribution in clinopyroxenes across Bjønnes, including other parts of NTG17, this anomaly most likely represents a difference in either the very local surrounding melt or the behaviour of the pyroxene itself.

As seen from Figures 48 and 49, secondary clinopyroxene is most evolved. NTG18 provides a good example of evolution from core to rim to secondary, although NTG18-2 is unexpectedly low for a rim composition. It is represented by a single analysis so may be unreliable, although it does conform to the compositional trend of other analyses. Secondary clinopyroxene continues to evolve along the trend set by primary clinopyroxene.

3.2.3 Amphibole

Amphibole compositions and formulae can be found in Table 6. According to amphibole nomenclature (*Hawthorne et al., 2012*), amphiboles range from calcic Ti-rich hastingsite to sodic arfvedsonite subspecies, with most analyses falling under the intermediate sodic-calcic katophorite (ferri-, ferro-ferri-, Ti-rich ferro-ferri-, Ti-rich ferro-) subspecies. All amphibole analyses produce a tight trend from hastingsite to arfvedsonite as shown in Figure 52. Individual samples show fairly close groupings, indicating a relatively small compositional range within each grain and sample compared to the overall range of amphiboles across Bjønnes.

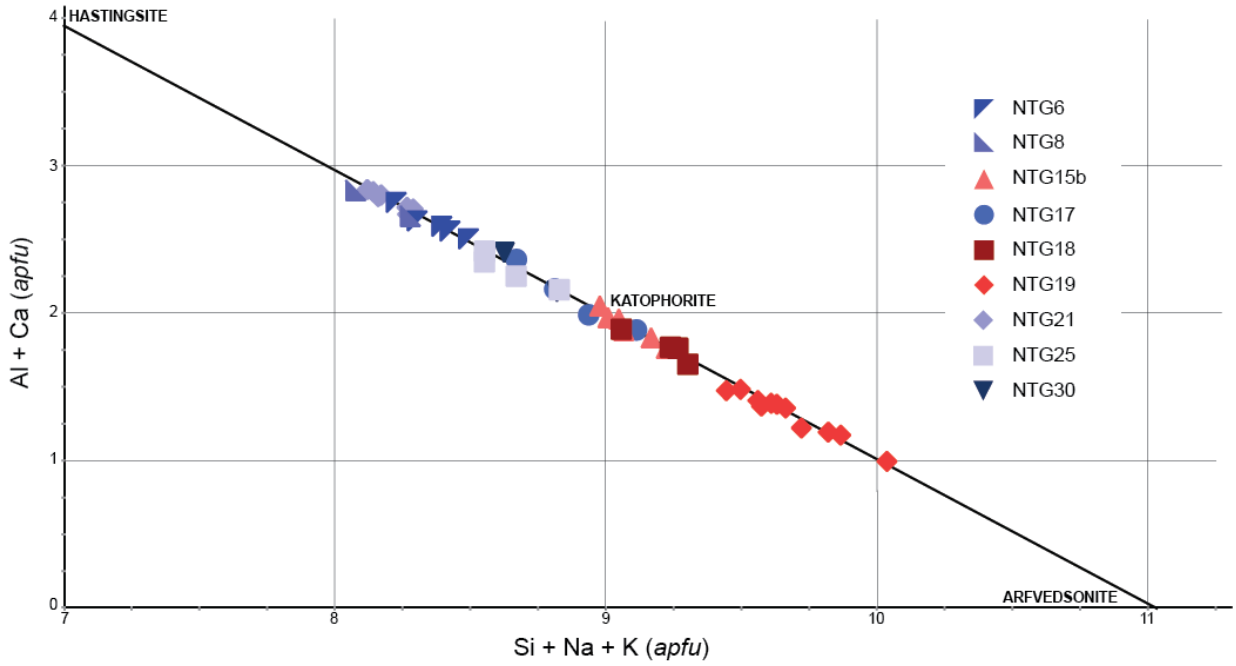

Figure 52: Representation of amphibole species based on chemical compositions showing a linear trend ranging from hastingsite to arfvedsonite. Red symbols indicate samples with eudialyte. These samples appear to have the most evolved amphibole compositions.

Amphiboles from eudialyte-bearing samples, shown in red in Figure 52, are generally the most compositionally evolved, much like the clinopyroxenes. There is an almost clear division around the point making pure katophorite composition, where amphiboles of eudialyte-bearing samples have compositions between katophorite and arfvedsonite, and other samples range from hastingsite to katophorite. This compositional division is supported by Figure 53.

The most sodic sample is NTG19, which has the broadest compositional range and contains the only analysed amphibole of arfvedsonite composition, NTG19-4. The more calcic hastingsite amphiboles are confined exclusively to NTG6, NTG8 and NTG21. The remaining samples represent katophorites, which appear to evolve from

ferro-katophorite (NTG30) to ferro-ferri-katophorite (NTG15b) moving towards an arfvedsonite composition (Figure 53).

The evolutionary trend of the amphiboles from calcic to sodic involves two primary substitution mechanisms. The first is $Ca^{2+}_{M4} + Al^{3+}_{M1-3} \rightarrow 2(Na^{+}, K^{+})_{A-M4} + Si^{4+}_{M1-3}$ (Figure 52). This assumes that all Al was present in the T-site, as was calculated for all analyses. The second substitution, shown in Figure 54 is Mg ↔ Fe, where Fe content generally increases consistently with Na, suggesting that the substitutions occurred simultaneously. A strong relationship between Fe and Mn suggests that Mn also substituted directly for Mg, albeit much less significant amounts. NTG19 and NTG18 stray from this trend, where analyses show greater contents of Na relative to their respective Fe content. The cause of this may be that the samples had a higher Fe^{3+}/Fe^{2+} ratio than any other sample. In the case these samples, a significantly higher proportion of the Fe-Mg substitution would have taken place through a coupled substitution with Na as $Ca^{2+}_{M4} + 2Mg^{2+}_{M1-3} \rightarrow Na^{+}_{A-M4} + Fe^{3+}_{M1-3} + Fe^{2+}_{M1-3}$, as opposed to the simple substitution $Mg^{2+} \rightarrow Fe^{2+}$.

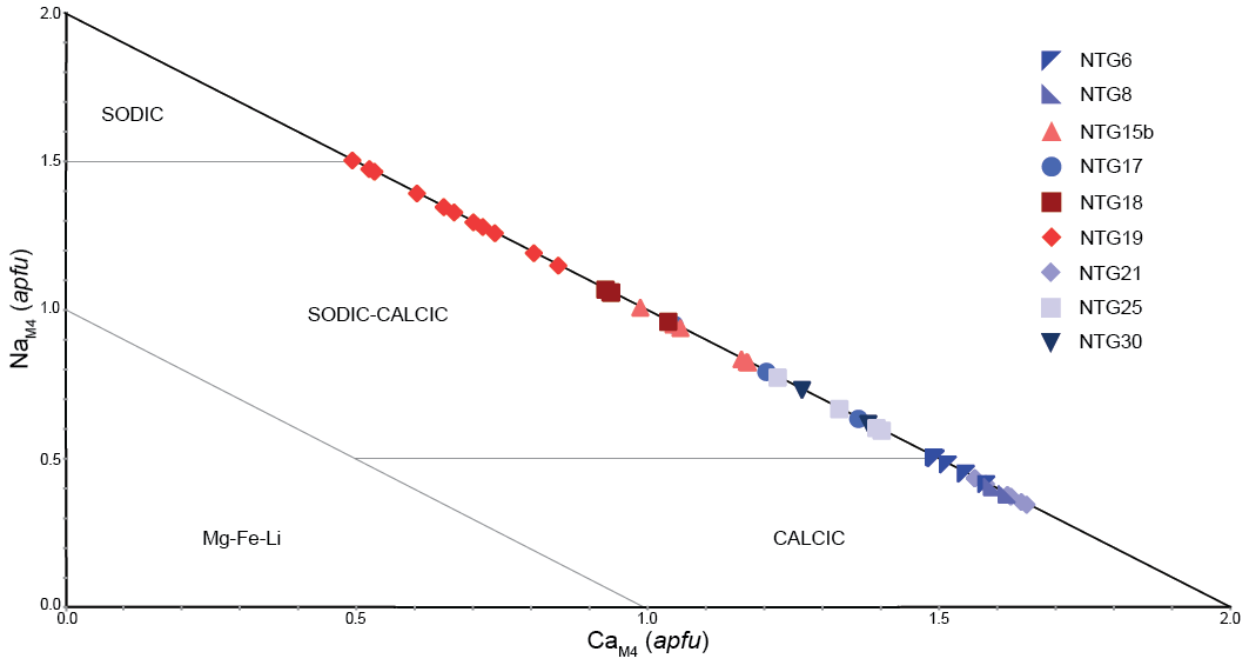

Figure 53: Representation of the M4-site substitution of Ca and Na in amphiboles, also showing classification between calcic and sodic. The analyses produce a linear trend intersecting the X- and Y-axes at 2.0, showing that Na and Ca occupy all of the M4-site. Red symbols indicate amphiboles from eudialyte-bearing samples. They show a greater collective range of composition than the remaining samples.

Amphiboles show no substantial evidence of zonation. In larger grains, such as the poikilitic amphiboles in NTG21, inconsistent internal variations occur throughout, most likely due to the size of the grains rather than due to evolving crystallising conditions during growth. Despite this, amphiboles in each sample produce a range of chemical compositions.

Table 6: Compositions (weight percent oxides) and formula calculations of amphiboles from Bjønnes.

Sample	NTG6-1	NTG6-2	NTG6-3	NTG6-4	NTG6-5	NTG8-1	NTG8-2	NTG15b-1	NTG15b-2	NTG15b-3	NTG15b-4	NTG15b-5	NTG15b-6	NTG17-1	NTG17-2
n	2	2	2	2	2	2	2	3	2	2	2	2	2	3	2
SiO_2	44.17(4)	44.73(7)	43.1(1)	43.440(2)	44.0(1)	43.9(2)	43.4(4)	44.8(1)	45.1(1)	44.12(9)	44.64(8)	44.49(8)	44.20(2)	44.5(1)	45.5(3)
TiO_2	2.99(8)	2.93(3)	3.40(2)	3.24(5)	2.735(5)	3.393(9)	3.04(6)	2.87(2)	2.68(3)	2.78(1)	2.90(4)	2.40(4)	3.08(5)	2.4(1)	2.40(7)
ZrO_2	0.494(1)	0.432(7)	0.424(2)	0.380(8)	0.50(1)	0.38(2)	0.40(2)	0.42(3)	0.39(1)	0.47(2)	0.412(2)	0.34(4)	0.51(1)	0.48(1)	0.44(1)
Al_2O_3	5.920(6)	5.61(5)	5.88(4)	6.44(7)	5.83(7)	6.78(3)	5.82(8)	4.386(9)	4.23(1)	4.55(4)	4.277(4)	4.1(1)	4.73(2)	5.25(6)	5.61(8)
FeO	20.18(8)	19.8(2)	20.65(9)	19.0(1)	21.7(2)	18.6(1)	19.47(4)	25.8(3)	25.7(1)	26.0(1)	25.92(6)	26.1(1)	25.6(1)	23.3(2)	18.05(7)
MnO	0.793(7)	0.79(1)	0.76(2)	0.748(6)	0.75(2)	0.663(5)	0.69(2)	1.09(4)	1.06(2)	1.041(2)	1.070(8)	1.01(1)	1.08(6)	1.00(3)	0.71(1)
MgO	8.07(2)	8.37(6)	7.700(8)	8.65(4)	7.31(4)	9.13(1)	8.6(1)	4.74(6)	4.724(3)	4.65(1)	4.64(4)	4.362(3)	4.50(6)	6.4(1)	10.0(1)
CaO	9.12(3)	9.01(1)	9.19(9)	9.50(8)	8.9(1)	9.8(1)	9.5(1)	6.84(8)	6.2(1)	6.16(6)	6.9(1)	5.7(2)	6.871(6)	7.17(7)	8.3(2)
Na_2O	4.08(5)	4.23(7)	3.95(3)	3.88(3)	4.07(3)	3.55(4)	3.846	5.11(9)	5.55(3)	5.63(8)	5.23(7)	5.48(1)	5.16(3)	4.99(4)	4.78(3)
K_2O	1.54(3)	1.52(1)	1.59(2)	1.500(6)	1.55(1)	1.46(1)	1.52(1)	1.679(5)	1.710(7)	1.742(9)	1.63(4)	1.76(1)	1.679(8)	1.58(1)	1.422(7)
Total	97.34	97.41	96.67	96.81	97.39	97.67	96.28	97.64	97.33	97.11	97.60	95.79	97.41	97.14	97.16
Structural formula based on 22 oxygens															
T-site															
Si	6.86	6.92	6.78	6.76	6.88	6.73	6.81	7.10	7.12	6.99	7.10	7.15	7.04	6.98	6.97
Al	1.08	1.02	1.09	1.18	1.07	1.23	1.08	0.82	0.79	0.85	0.80	0.79	0.89	0.97	1.01
Ti	0.06	0.06	0.13	0.06	0.04	0.04	0.12	0.09	0.09	0.17	0.10	0.06	0.07	0.05	0.02
Subtotal	8.00	8.00	8.00	8.00	8.00	8.00	8.00	8.00	8.00	8.00	8.00	8.00	8.00	8.00	8.00
M1-3-site															
Ti	0.29	0.29	0.28	0.32	0.28	0.35	0.24	0.26	0.23	0.17	0.25	0.23	0.30	0.23	0.26
Zr	0.04	0.03	0.03	0.03	0.04	0.03	0.03	0.03	0.03	0.04	0.03	0.03	0.04	0.04	0.03
Fe^{3+}							0.00	0.06	0.32	0.52		0.34		0.28	0.05
Mn^{2+}	0.10	0.10	0.10	0.10	0.10	0.09	0.09	0.15	0.14	0.14	0.14	0.14	0.15	0.13	0.09
Fe^{2+}	2.62	2.56	2.72	2.48	2.83	2.39	2.55	3.35	3.07	2.91	3.45	3.16	3.41	2.78	2.26
Mg	1.87	1.93	1.81	2.01	1.70	2.09	2.02	1.12	1.11	1.10	1.10	1.05	1.07	1.51	2.27
Subtotal	4.93	4.92	4.93	4.93	4.95	4.94	4.94	4.97	4.90	4.88	4.98	4.94	4.97	4.96	4.98
M4-site															
Ca	1.52	1.49	1.55	1.58	1.50	1.62	1.59	1.16	1.06	1.05	1.17	0.99	1.17	1.21	1.36
Na	0.48	0.51	0.45	0.42	0.50	0.38	0.41	0.84	0.94	0.96	0.83	1.01	0.83	0.80	0.64
Subtotal	2.00	2.00	2.00	2.00	2.00	2.00	2.00	2.00	2.00	2.00	2.00	2.00	2.00	2.00	2.00
A-site															
Na	0.75	0.76	0.75	0.76	0.73	0.68	0.76	0.73	0.76	0.77	0.79	0.69	0.77	0.72	0.78
K	0.31	0.30	0.32	0.30	0.31	0.29	0.30	0.34	0.35	0.35	0.33	0.36	0.34	0.32	0.28
Subtotal	1.05	1.06	1.07	1.05	1.04	0.96	1.07	1.07	1.10	1.12	1.12	1.06	1.11	1.04	1.06
O (non-W)	22.00	22.00	22.00	22.00	22.00	22.00	22.00	22.00	22.00	22.00	22.00	22.00	22.00	22.00	22.00
W-site															
OH, F, Cl	2.00	2.00	2.00	2.00	2.00	2.00	2.00	2.00	2.00	2.00	2.00	2.00	2.00	2.00	2.00

Table 6 continued.

Sample	NTG17-3	NTG17-4	NTG18-1	NTG18-2	NTG18-3	NTG18-4	NTG19-1	NTG19-2	NTG19-3	NTG19-4	NTG19-5	NTG19-6	NTG19-7	NTG19-8	NTG19-9
n	2	2	2	2	2	2	8	8	4	2	1	3	3	3	4
SiO_2	43.0(7)	44.8(1)	45.2(1)	45.46(7)	44.3(1)	45.2(1)	46.7(1)	45.8(4)	46.6(3)	47.8(1)	45.4	45.1(2)	45.48(5)	45.7(2)	46.4(4)
TiO_2	1.98(6)	1.89(5)	3.16(8)	2.96(1)	3.16(5)	2.66(8)	2.05(7)	2.60(9)	2.24(5)	1.80(4)	2.32	2.51(4)	2.53(3)	2.74(5)	2.22(4)
ZrO_2	0.45(4)	0.34(1)	n.a.	n.a.	n.a.	n.a.	0.26(4)	0.33(3)	0.2(1)	0.10(2)	0.41	0.28(1)	0.33(3)	0.38(4)	0.30(4)
Al_2O_3	5.05(4)	4.6(3)	4.53(2)	4.56(2)	4.65(4)	3.91(1)	3.24(9)	3.7(1)	3.59(6)	2.79(1)	3.78	3.65(4)	3.9(1)	3.67(5)	3.7(2)
FeO	27.52(1)	26.6(3)	24.69(6)	25.18(3)	25.6(1)	25.82(2)	26.4(2)	26.3(2)	26.3(1)	26.2(1)	27.1	26.8(1)	26.5(1)	27.00(6)	26.4(2)
MnO	1.44(2)	1.52(4)	1.00(3)	1.13(1)	1.11(1)	1.17(1)	1.22(8)	1.4(1)	1.17(3)	1.29(5)	1.24	1.26(3)	1.23(3)	1.26(3)	1.26(3)
MgO	3.78(6)	4.3(2)	5.174(3)	4.89(1)	4.79(4)	4.87(8)	4.6(1)	4.5(1)	4.68(6)	5.03(8)	4.31	4.38(4)	4.25(9)	4.20(7)	4.6(1)
CaO	6.09(4)	6.1(2)	5.5(1)	5.5(1)	6.1(3)	5.5(2)	3.6(2)	4.4(3)	3.1(2)	2.95(8)	3.15	4.7(2)	3.96(3)	4.1(1)	4.3(2)
Na_2O	5.45(5)	5.50(1)	5.58(7)	5.744(1)	5.51(2)	5.9(1)	7.0(1)	6.5(1)	7.21(7)	7.2(1)	7.0	6.3(1)	6.86(5)	6.66(4)	6.5(1)
K_2O	1.65(5)	1.57(1)	1.96(6)	1.77(1)	1.72(5)	1.71(2)	1.85(5)	1.79(2)	2.02(7)	2.042(3)	2.07	1.73(3)	1.88(3)	1.80(1)	1.82(9)
Total	96.45	97.15	96.90	97.19	97.00	96.79	96.93	97.27	97.11	97.22	96.80	96.80	96.97	97.62	97.49
Structural formula based on 22 oxygens															
T-site															
Si	6.90	7.10	7.13	7.15	7.02	7.15	7.32	7.20	7.28	7.44	7.15	7.15	7.16	7.18	7.26
Al	0.96	0.86	0.84	0.85	0.87	0.73	0.60	0.68	0.66	0.51	0.70	0.68	0.73	0.68	0.68
Ti	0.14	0.04	0.02		0.12	0.12	0.08	0.12	0.06	0.05	0.15	0.17	0.12	0.14	0.06
Subtotal	8.00	8.00	8.00	8.00	8.00	8.00	8.00	8.00	8.00	8.00	8.00	8.00	8.00	8.00	8.00
M1-3-site															
Ti	0.10	0.19	0.35	0.35	0.26	0.19	0.17	0.19	0.20	0.16	0.13	0.13	0.18	0.18	0.21
Zr	0.04	0.03	-	-	-	-	0.02	0.03	0.01	0.01	0.03	0.02	0.03	0.03	0.02
Fe^{3+}	0.72	0.44	0.25	0.25	0.38	0.49	0.72	0.60	0.82	0.76	0.95	0.67	0.78	0.64	0.57
Mn^{2+}	0.20	0.20	0.13	0.15	0.15	0.16	0.16	0.18	0.16	0.17	0.17	0.17	0.16	0.17	0.17
Fe^{2+}	2.97	3.09	3.01	3.06	3.00	2.92	2.75	2.86	2.62	2.65	2.62	2.88	2.72	2.90	2.89
Mg	0.90	1.01	1.22	1.15	1.13	1.15	1.09	1.05	1.09	1.17	1.01	1.03	1.00	0.98	1.08
Subtotal	4.92	4.95	4.96	4.96	4.93	4.91	4.90	4.91	4.89	4.91	4.90	4.90	4.86	4.91	4.94
M4-site															
Ca	1.05	1.04	0.94	0.93	1.04	0.94	0.60	0.74	0.52	0.49	0.53	0.81	0.67	0.70	0.72
Na	0.95	0.96	1.06	1.07	0.96	1.06	1.40	1.26	1.48	1.51	1.47	1.20	1.33	1.30	1.28
Subtotal	2.00	2.00	2.00	2.00	2.00	2.00	2.00	2.00	2.00	2.00	2.00	2.00	2.00	2.00	2.00
A-site															
Na	0.74	0.73	0.65	0.68	0.73	0.74	0.73	0.73	0.71	0.68	0.68	0.75	0.76	0.73	0.70
K	0.34	0.32	0.40	0.36	0.35	0.35	0.37	0.36	0.40	0.41	0.42	0.35	0.38	0.36	0.36
Subtotal	1.08	1.05	1.04	1.04	1.07	1.09	1.10	1.09	1.11	1.09	1.10	1.10	1.14	1.09	1.06
O (non-W)	22.00	22.00	22.00	22.00	22.00	22.00	22.00	22.00	22.00	22.00	22.00	22.00	22.00	22.00	22.00
W-site															
OH, F, Cl	2.00	2.00	2.00	2.00	2.00	2.00	2.00	2.00	2.00	2.00	2.00	2.00	2.00	2.00	2.00

n.a.: not analysed

Table 6 continued.

Sample	NTG19-10	NTG19-11	NTG21-1	NTG21-2	NTG21-3	NTG21-4	NTG21-5	NTG21-6	NTG21-7	NTG25-1	NTG25-2	NTG25-3	NTG25-4	NTG30-1	NTG30-2
n	2	2	4	4	3	6	2	3	3	2	2	2	2	2	3
SiO_2	46.1(2)	46.1(2)	43.21(7)	42.8(2)	42.2(4)	43.3(3)	43.4(2)	43.67(8)	43.14(8)	44.52(7)	44.3(3)	43.46(5)	43.60(6)	44.80(3)	44.8(2)
TiO_2	2.363	2.33(5)	3.4(1)	3.1(2)	3.14(3)	3.19(5)	3.274(7)	3.29(3)	3.32(3)	2.807	2.64(3)	3.108(7)	3.299(6)	2.75(8)	3.06(5)
ZrO_2	0.36(5)	0.28(4)	0.36(1)	0.37(5)	0.42(2)	0.41(3)	0.37(1)	0.46(4)	0.39(5)	0.41(4)	0.43(1)	0.47(3)	0.53(1)	0.406(4)	0.55(1)
Al_2O_3	3.89(3)	3.49(3)	6.07(5)	6.21(1)	6.42(5)	6.24(7)	6.55(6)	6.48(4)	6.51(8)	5.10(3)	5.21(5)	5.57(3)	5.04(2)	5.7(1)	4.82(3)
FeO	25.9(1)	26.14(6)	22.0(1)	21.86(4)	21.8(2)	20.68(1)	19.04(4)	20.1(1)	19.2(12)	22.1(3)	21.13(3)	24.12(7)	26.0(1)	21.924(8)	23.64(8)
MnO	1.21(1)	1.22(7)	0.82(1)	0.76(2)	0.771(8)	0.82(2)	0.750(8)	0.76(2)	0.69(1)	0.92(3)	0.95(2)	1.006(2)	1.037(4)	0.839(5)	1.00(4)
MgO	4.80(2)	4.74(7)	7.0(1)	6.90(4)	6.94(9)	7.71(4)	8.83(8)	8.25(1)	8.59(8)	7.41(6)	8.04(3)	5.48(1)	4.28(2)	7.34(4)	5.79(3)
CaO	3.875(9)	5.03(5)	9.32(7)	9.22(3)	9.7(1)	9.4(1)	9.76(4)	9.8(1)	9.85(7)	8.0(1)	8.41(5)	8.2(1)	7.16(7)	8.32(3)	7.51(6)
Na_2O	6.745(5)	6.23(2)	3.92(2)	3.93(6)	3.7(1)	3.94(4)	3.83(5)	3.75(3)	3.70(7)	4.778(5)	4.4(3)	4.37(3)	4.92(1)	4.62(3)	4.74(2)
K_2O	1.937(4)	1.71(1)	1.57(1)	1.61(3)	1.49(1)	1.55(2)	1.52(1)	1.52(1)	1.56(1)	1.61(1)	1.63(1)	1.59(2)	1.73(2)	1.55(2)	1.61(1)
Total	97.19	97.24	97.66	96.72	96.52	97.19	97.33	98.08	96.91	97.68	97.10	97.38	97.63	98.28	97.53
Structural formula based on 22 oxygens															
T-site															
Si	7.23	7.25	6.76	6.76	6.70	6.77	6.72	6.74	6.72	6.91	6.90	6.89	6.96	6.93	7.05
Al	0.72	0.65	1.12	1.16	1.20	1.15	1.20	1.18	1.20	0.93	0.96	1.04	0.95	1.05	0.89
Ti	0.06	0.11	0.12	0.08	0.11	0.09	0.08	0.08	0.09	0.16	0.15	0.07	0.10	0.02	0.06
Subtotal	8.00	8.00	8.00	8.00	8.00	8.00	8.00	8.00	8.00	8.00	8.00	8.00	8.00	8.00	8.00
M1-3-site															
Ti	0.22	0.17	0.29	0.29	0.27	0.29	0.30	0.30	0.30	0.17	0.16	0.30	0.30	0.30	0.31
Zr	0.03	0.02	0.03	0.03	0.03	0.03	0.03	0.04	0.03	0.03	0.03	0.04	0.04	0.03	0.04
Fe^{3+}	0.66	0.51				0.00				0.29	0.22				
Mn^{2+}	0.16	0.16	0.11	0.10	0.10	0.11	0.10	0.10	0.09	0.12	0.13	0.14	0.14	0.11	0.13
Fe^{2+}	2.73	2.93	2.87	2.89	2.89	2.69	2.47	2.59	2.50	2.59	2.53	3.20	3.48	2.84	3.11
Mg	1.12	1.11	1.63	1.63	1.64	1.80	2.04	1.90	2.00	1.72	1.87	1.29	1.02	1.69	1.36
Subtotal	4.92	4.91	4.93	4.93	4.94	4.92	4.93	4.92	4.91	4.91	4.94	4.96	4.97	4.97	4.95
M4-site															
Ca	0.65	0.85	1.56	1.56	1.65	1.58	1.62	1.63	1.64	1.33	1.40	1.39	1.22	1.38	1.27
Na	1.35	1.15	0.44	0.44	0.35	0.42	0.38	0.38	0.36	0.67	0.60	0.61	0.78	0.62	0.73
Subtotal	2.00	2.00	2.00	2.00	2.00	2.00	2.00	2.00	2.00	2.00	2.00	2.00	2.00	2.00	2.00
A-site															
Na	0.70	0.75	0.75	0.77	0.78	0.77	0.77	0.75	0.76	0.77	0.73	0.74	0.75	0.77	0.71
K	0.39	0.34	0.31	0.33	0.30	0.31	0.30	0.30	0.31	0.32	0.33	0.32	0.35	0.31	0.32
Subtotal	1.09	1.09	1.07	1.09	1.08	1.08	1.07	1.05	1.07	1.09	1.06	1.06	1.10	1.07	1.04
O (non-W)	22.00	22.00	22.00	22.00	22.00	22.00	22.00	22.00	22.00	22.00	22.00	22.00	22.00	22.00	22.00
W-site															
OH, F, Cl	2.00	2.00	2.00	2.00	2.00	2.00	2.00	2.00	2.00	2.00	2.00	2.00	2.00	2.00	2.00

Analysis of single amphibole of ferri-katophorite composition, NTG17-2, represents a lone compositional anomaly (Figure 54). It shows a high Na content relative to its low Fe-Mg ratio. The analyses represent a small isolated amphibole within a larger primary clinopyroxene. It may represent an apparent inclusion, actually representing an intergrowth or partial replacement observed from a 2D surface. NTG17-1 represents a katophorite rim around the clinopyroxene, however it is more conformable with the broadly linear trend. This suggests that NTG17-2 is a more primitive amphibole inclusion.

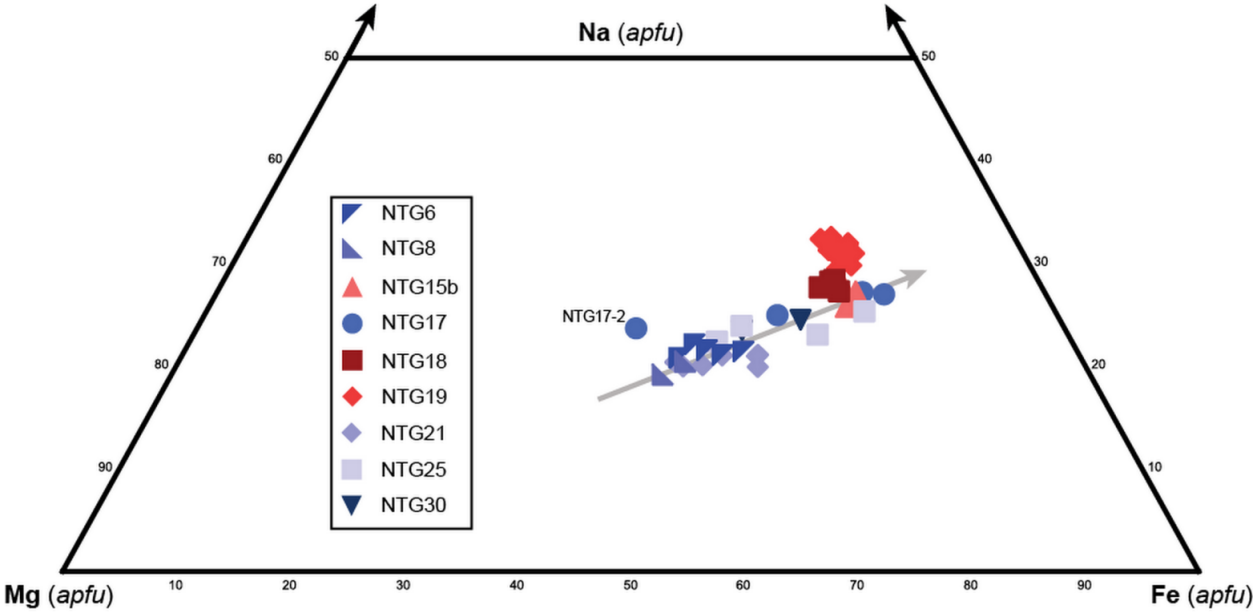

Figure 54: Molar Na-Mg-Fe ternary diagram showing compositional variations of amphiboles from Bjønnes. A broad linear trend line indicates the path of evolution. Anomalous NTG17-2 can be seen lying above this line, whilst NTG18 and NTG19 also form concentrated groups above the trend line. Analyses from eudialyte-bearing samples are highlighted by red symbols.

Many analyses are Ti-rich amphiboles (>0.3 Ti *apfu*), and in almost all analyses most of Ti was calculated to be sitting within the octahedral M1-3-sites. The primary substitution to assign Ti into the M1-3-sites is $(Mg, Fe, Mn)^{2+} \rightarrow Ti^{4+}$ and the charge balance is maintained by the substitution $2OH^{-} \rightarrow 2O^{2-}$ in the O3-site (*Hawthorne et al., 1998; Banno et al., 2009*), as shown in Figure 55. The distribution of Ti does not vary greatly between samples although the broad trend suggests that Ti content is greater in the more Ca- and Mg-rich amphiboles.

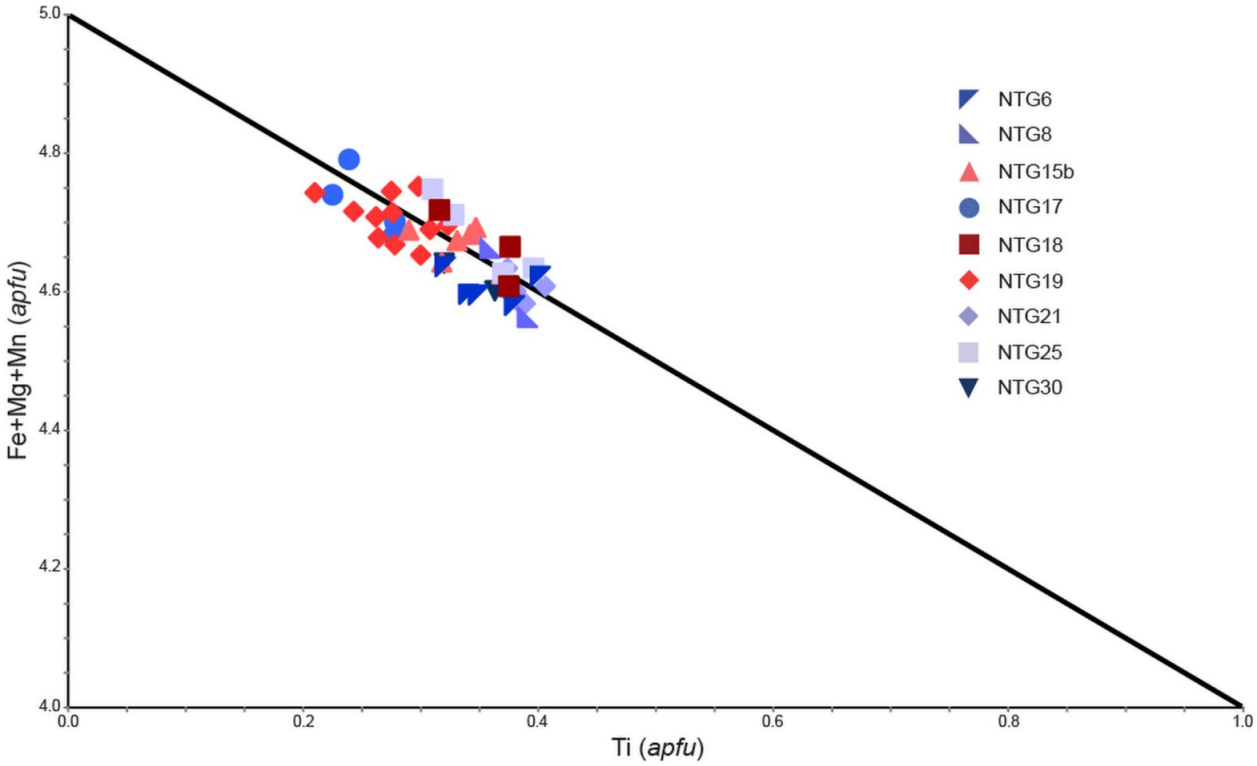

Figure 55: Compositions of amphiboles showing the substitution mechanism of Ti into the M1-3 sites in place of Fe^{2+}, Mg^{2+} and Mn^{2+}.

There is also a broadly linear relationship between Ti and Al, suggesting possible incorporation via a Tschermak substitution, incorporating Ti into the M1-3 sites and Al into the T-site. In more evolved samples, Ti and Al simultaneously decrease, suggesting a decreasing prominence of the Tschermak substitution and Ti and Al are removed by a substitution in the form $Ti^{4+}_{M1\text{-}3} + Al^{3+}_{T} \rightarrow Fe^{3+}_{M1}\text{-}3 + Si4^{+}_{T}$ (Figure 56).

The content of Zr in amphibole is low and its distribution is poorly constrained. It is assigned to the M1-3 sites like Ti. The lowest Zr contents are found in the most evolved amphiboles, such as those from NTG19. Similar to Ti, Zr content may decrease as a result of Fe^{3+} incorporation via a Tsckermak substitution as the system evolves. Another possibility could involve an A-site vacancy in the form $Na^{+}_{A} + Fe^{3+}_{M1\text{-}3} \leftrightarrow Zr^{4+}_{M1\text{-}3} + \square_{A}$ (*Andersen et al., 2011*). This may be possible since the A-site of more evolved amphiboles is generally fuller than other less evolved ones.

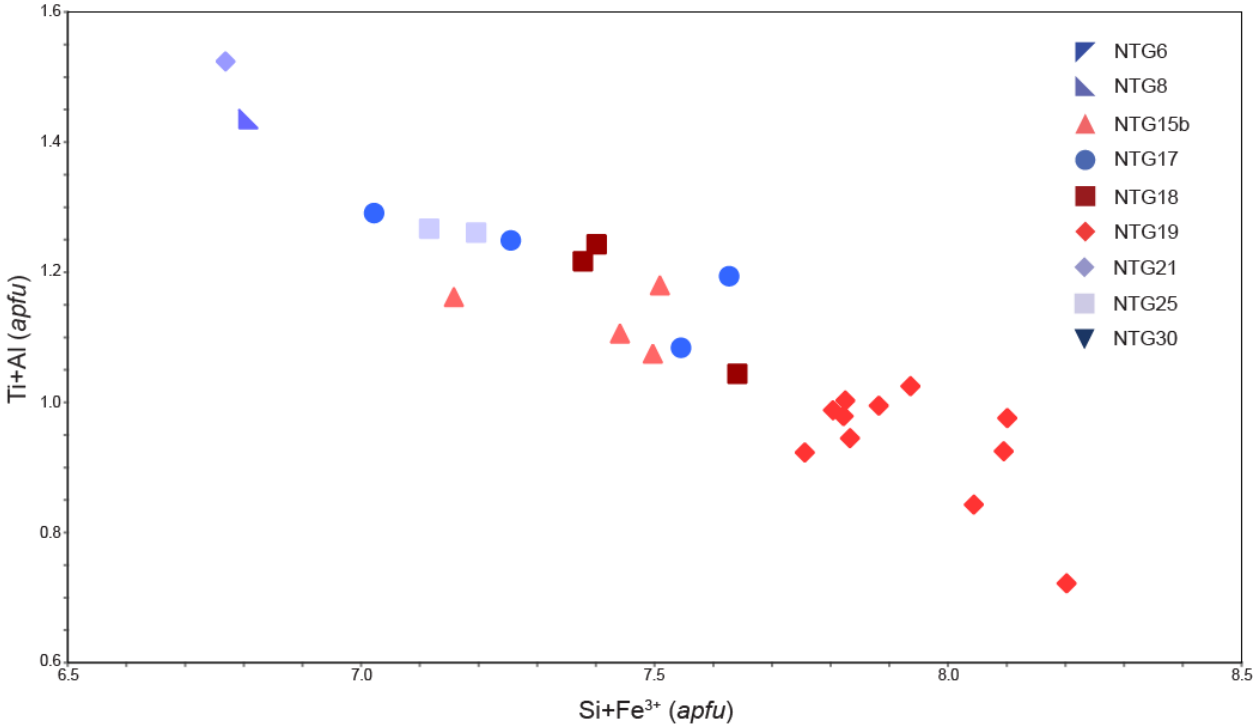

Figure 56: Binary diagram showing the increase of Si and Fe^{3+} in amphiboles at the expense of Ti and Al, indicating that a Tschermak component is responsible for some Ti and Al incorporation and that the substitution becomes less prominent as the system evolves. Only amphibole analyses that were calculated to contain Fe^{3+} have been included.

3.2.4 Biotite

Table 7 contains quantitative analyses of biotite from four samples showing compositions that can all be classified as annite (*Bailey, 1984*). The compositions are also supported by semi-quantitative EDS data from other samples which suggests that biotites throughout the Bjønnes syenite are similarly Fe-rich annites.

Internal compositional variations within samples were small in all cases, however variations between samples were detected. The greatest differences are observed in Ti, Fe and Mg content, which together occupy M-sites. There appears to be a controlling mechanism on Fe and Mg, where NTG17 and NTG21 have relatively high Fe and low Mg, whilst NTG6 and NTG19 have low Fe and high Mg. However, Ti appears to be controlled in a different manner, being relatively high in NTG6 and NTG21.

The trend of Ti compositions is similar to that observed in amphiboles, where NTG6 and NTG21 have significantly higher contents in both. However there appears to be no direct relationship in the trend between Fe and Mg content in biotites compared to pyroxenes and amphiboles. Instead, Ti increases as total Fe+Mg+Mn decreases, whilst Al also increases to a lesser extent than Ti. This suggests a combination of coupled substitutions to incorporate Ti into M-sites in the form of $2(Fe,Mg,Mn)^{2+}_{M} \leftrightarrow Ti^{4+}_{M} + \square_{M}$, and to a lesser extent the Tschermak substitution $(Fe,Mg,Mn)^{2+}_{M} + 2Si^{4+}_{T} \leftrightarrow Ti^{4+}_{M} + 2Al^{3+}_{T}$ (*Brigatti et al., 1991*).

Table 7: Composition (weight percent oxides) and formula calculations of biotites from Bjønnes.

Sample	NTG6	NTG17	NTG19	NTG21
n	3	3	16	3
SiO_2	36.5(4)	35.3(7)	37.4(8)	35.95(8)
TiO_2	6.3(7)	3.4(9)	3.3(2)	7.25(6)
Al_2O_3	10.7(1)	10.0(3)	9.9(3)	10.9(1)
FeO	25(1)	31(1)	25(1)	27.7(2)
MnO	0.41(8)	0.9(2)	1.5(1)	0.44(2)
MgO	7.7(6)	4.8(4)	8.3(9)	4.55(2)
CaO	0.02(1)	0.06(3)	0.07(6)	0.07(2)
Na_2O	0.24(2)	0.12(4)	0.1(1)	0.20(3)
K_2O	9.5(1)	9.35(6)	9.6(2)	9.37(3)
Total	96.12	94.94	95.29	96.42
Atomic ratios				
Mg#	0.26(4)	0.13(1)	0.25(3)	0.139(1)
Structural formulae calculated to 8 cations per formula unit				
Si	3.00	3.00	3.00	3.00
Ti	0.39	0.22	0.20	0.45
Al	1.04	1.01	0.94	1.07
Fe	1.70	2.21	1.67	1.93
Mn	0.03	0.07	0.11	0.03
Mg	0.94	0.61	0.99	0.57
Ca	0.00	0.01	0.01	0.01
Na	0.04	0.02	0.02	0.03
K	1.00	1.01	0.99	1.00
OH	2.00	2.00	2.00	2.00

Mg# shows molar atomic ratio presented as decimal fraction with propagated error.

3.2.5 Titanite

Quantitative analysis of titanite [$CaTiSiO_4(O,OH,F)$] was done on two samples, NTG17 and NTG19, and both show consistent chemical compositions (Table 8). Titanite from NTG17 was found at the core of an overgrowing pyroxene and appeared to have formed as a rim around small Fe-Ti oxides. Titanite from NTG19 is thought to be late-magmatic, filling a small interstitial space between amphibole and feldspar. The results are supported by semi-quantitative analyses from titanite from the same two samples, and NTG15b and NTG23. Contents of Ca and Ti between NTG17 and NTG19 vary. Significant differences are also seen in contents of minor components, in which NTG17 contains 0.8 wt. % more Al_2O_3 than NTG19, which in turn holds on average more Fe and Na. These variations are generally consistent with those seen in pyroxene and amphibole compositions of the corresponding samples.

Table 8: Composition (weight percent oxides) and formula calculations of titanites from Bjønnes.

Sample	NTG17	NTG17	NTG19	NTG19	NTG19
Analysis	43 / 1	44 / 1	93 / 2	94 / 2	95 / 2
SiO_2	29.92	30.32	29.96	29.87	29.80
TiO_2	37.47	37.92	38.31	38.27	38.90
ZrO_2	0.30	0.25	0.23	0.16	0.19
Al_2O_3	1.12	1.18	0.34	0.33	0.27
FeO	1.10	1.08	1.47	1.47	1.07
MnO	0.08	0.07	0.04	0.04	0.04
MgO	-	0.02	-	-	-
CaO	28.02	27.92	26.73	27.03	26.49
Na_2O	0.30	0.27	0.80	0.77	0.75
K_2O		0.01	0.06	0.03	0.03
Total	98.31	99.03	97.95	97.97	97.53
Structural formulae calculated to 3 cations per formula unit					
Si	0.98	0.99	0.99	0.99	0.99
Ti	0.93	0.93	0.95	0.95	0.97
Al	0.04	0.05	0.01	0.01	0.01
Fe	0.03	0.03	0.04	0.04	0.03
Ca	0.99	0.98	0.95	0.96	0.94
Na	0.02	0.02	0.05	0.05	0.05

Since Si content is consistent, these variables are likely the result of $Ti^{4+} \rightarrow Al^{3+}$, Fe^{3+}, coupled with $O^{2-} \rightarrow (Cl, F, OH)^-$ in the O_1-site (*Speer & Gibbs, 1976*), with Na substituting readily for Ca. Titanite in NTG15b was found to have traces of Nb and LREE's present. These would also substitute for Ti under the mechanism $2Ti^{4+} \rightarrow Al^{3+} + (Nb, Ta)^{5+}$ (*Janeczek, 1996*). From EDS analysis, HREE's and Y were not detected and are suspected to be less abundant since titanite in alkaline felsic systems generally has a greater affinity for LREE's (*Della Ventura et al., 1999*). Titanites hold a significant amount of F, as shown from semi-quantitative analysis.

3.2.6 Aenigmatite

Aenigmatite [$Na_4Fe^{2+}{}_{10}Ti_2Si_{12}O_{40}$] is present as a rock-forming mineral observed in five samples and was quantitatively analysed from two samples, NTG15b and NTG30 (Table 9). Both show very similar compositions and little evidence of zonation. They contain minor Mg and Mn components substituting for Fe, and a minor Ca component mostly substituting for Na in M-sites (*Grew et al., 2008*). Aenigmatite from NTG15b had higher Fe and Na contents than in NTG30, a difference also observed in clinopyroxene and amphibole compositions of the corresponding samples. In NTG30, the lower content of Fe was offset directly by a higher Mg content, with Mn content being consistent, however an increase in Ca to offset the lower Na contents was not observed. The content of Ti in NTG30 is also slightly higher.

Table 9: Composition (weight percent oxides) and formula calculations of aenigmatites from Bjønnes.

Sample	NTG15b	NTG30	NTG30	NTG30
Analysis	11/2	61/2	62/2	63/2
SiO_2	37.16	36.65	37.11	37.94
TiO_2	9.36	9.69	9.58	9.77
ZrO_2	0.10	0.12	0.05	0.04
Al_2O_3	3.01	2.98	2.92	2.96
FeO	39.27	37.75	37.58	37.87
MnO	1.55	1.65	1.60	1.62
MgO	0.95	1.64	1.60	1.71
CaO	2.16	2.01	2.05	2.18
Na_2O	6.35	6.03	6.09	6.07
Total	99.94	98.51	98.59	100.16
Structural formulae calculated to 28 cations per formula unit				
Si	10.62	10.61	10.71	10.79
Ti	2.01	2.11	2.08	2.09
Zr	0.02	0.02	0.01	0.01
Al	1.01	1.01	1.00	0.99
Fe	9.38	9.14	9.07	9.00
Mn	0.38	0.41	0.39	0.39
Mg	0.41	0.71	0.69	0.72
Ca	0.67	0.62	0.63	0.66
Na	3.52	3.38	3.41	3.35

Aenigmatite consistently contains around 3 wt. % Al_2O_3, which is unusually high. Analysed grains were large so this is not a result of contamination. Similarly high Al contents were described from some alkaline rock units in the Ilímaussaq complex by *Larsen (1977)*, where Al and Ca are incorporated through a coupled substitution $Na^{+}_{M} + Si^{4+}_{T} \rightarrow Ca^{2+}_{M} + Al^{3+}_{T}$. This would not account for all Al, however, since it is more abundant than Ca. Therefore the surplus Al is probably incorporated through $Fe^{2+}_{M} + Si^{4+}_{T} \rightarrow Fe^{3+}_{M} + Al^{3+}_{T}$ as coupled substitution (*Larsen, 1977*).

3.2.7 Zirconolite

Zirconolite [ideally $CaZrTi_2O_7$] was found as an accessory mineral in three samples, NTG6, NTG8 and NTG22 and were semi-quantitatively analysed using EDS. The dominant phase in all cases is $CaZrTi_2O_7$ although all samples contain other components. Analyses from NTG22 all contain a significant amount of REE's, notably Ce, Nd and Y, whilst also hosting high quantities of Nb, along with traces of Al. Samples NTG6 and NTG8 contained Ce but not Y and NTG8 also hold small amounts of Nd. Neither NTG6 nor NTG8 contain Nb, however both contain trace amounts of Th and U. In all samples, Fe is also a significant component. This compositional variation is most likely based around the coupled substitution $Ca^{2+} + 2Ti^{4+} \rightarrow (Fe^{2+}, Mn^{2+}) +$

REE^{3+} + Nb^{5+} (*Della Ventura et al., 2000*). More detailed analysis into the chemical variations between samples cannot be done with the semi-quantitative data available. Most zirconolite in the LPC is found in nepheline syenite pegmatites and is known as polymignite. This is a metamict variety of zirconolite, where internal radiation damage has left the mineral amorphous (*Larsen, 2010*). It is possible that zirconolite from the Bjønnes syenite is also metamict.

3.2.8 Eudialyte

Semi-quantitative data was collected from three samples, NTG15b, NTG19 and NTG23, for eudialyte [$Na_{15}Ca_6(Fe,Mn,Na)_3(Zr,Ti)_3(Si,Nb)_2Si_{24}O_{72}(O,OH,H_2O)_3(Cl,OH)_2$]. Figure 57 shows a typical EDS spectrum taken for eudialyte. Compositions are generally consistent between samples, showing a Na/Ca ratio ranging from 1.3 – 1.5. Similarly all samples are Fe-dominated with a Mn component, producing a Mn/Fe ratio of 0 – 0.3. Also, Cl is a prominent phase and its content is very consistent between samples. Very little variation between samples can be observed from EDS analysis however eudialyte in NTG15b appear to have a slightly higher Na content than other samples.

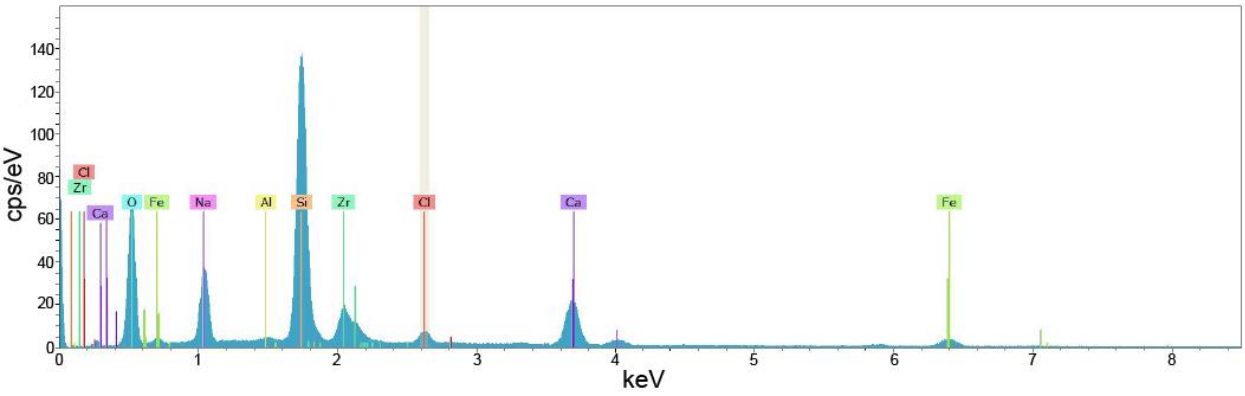

Figure 57: Typical EDS spectrum of unaltered eudialyte taken from NTG23.

Altered eudialyte was analysed from within and around the edge of eudialyte alteration zones. These eudialytes were observed to differ from primary eudialyte by having significantly higher Mn/Fe ratios (approx. 0.8) and lower Na/Ca ratios (approx. 1.0). They also show a much lower Cl content. If the eudialyte is indeed chemically altered and not secondary, it can be inferred that Na, Fe and Cl were stripped out preferentially during alteration, likely mobilised by a fluid.

3.2.9 Rosenbuschite

Several rosenbuschite [$Ca_6Zr_2Na_6(Zr,Ti)_2(Si_2O_7)_4(OF)_2F_4$] grains were analysed from NTG19 using EDS. Mineral compositions vary slightly between analyses, with Na/Ca ratios ranging from 0.5 – 0.8 and Ti/Zr ratios of 0.1 – 0.5. In some analyses Nb was detected and Zr was in turn depleted, with all analyses showing consistent totals of Zr + Ti + Nb. Analyses containing Nb also appeared to have less F content than observed elsewhere. This relationship appears to be related through an unknown substitution mechanism. It has been speculated that a coupled substitution of $Zr^{4+} + F^- \leftrightarrow Nb^{5+} + O^{2-}$ could take place in wöhlerite, another F-bearing Zr-silicate mineral (*Biagioni et al., 2012*), although this may not apply to rosenbuschite.

3.2.10 Catapleiite

Catapleiite [$Na_2ZrSi_3O_9 \cdot 2(H_2O)$] was semi-quantitatively analysed from NTG15b and NTG19. Compositional variations are mostly confined to Na and Ca, where Na/Ca ratios range from approximately 1.0 – 2.0, a product of the substitution $2Na^+ \leftrightarrow Ca^{2+}$. Small amounts of Al and Fe were also detected in some analyses, most likely substituting for Si (*Deer et al., 1997*).

3.2.11 Apatite

Apatite [$Ca_5(PO_4)_3(F,Cl,OH)$] is a common accessory mineral found in all samples. Semi-quantitative analysis of seven samples was used to categorise all analyses as fluorapatite based on consistent F content. Compositional variations between samples were difficult to distinguish using EDS.

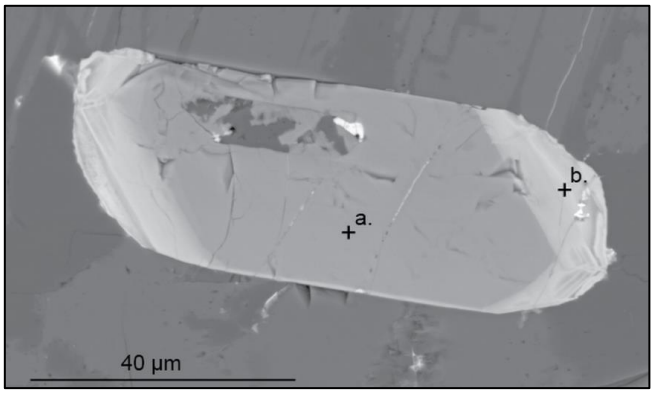

Figure 58: EDS image of a zoned apatite grain (NTG30) showing a core (a.) with little impurities and a rim (b.) with relatively high concentrations of Si and REE's.

Some apatites show a chemical zonation, which is not common but occurrs in a variety of samples. An example is shown in Figure 58. The rims of these zoned apatite show an elevated Si-content and also contained LREE's, notably Ce, La and Nd. Some high-Si, REE-bearing apatites also appear to show elevated Na-content, although variations are generally too low to distinguish a trend from EDS data. Analysed rims of zoned apatites in NTG30 also showed traces of Th.

The substitution $Ca^{2+} + P^{5+} \rightarrow REE^{3+} + Si^{4+}$ was probably the main mechanism for the compositional zoning, whilst the substitution $2Ca^{2+} \rightarrow Na^{+} + REE^{3+}$ may have also been in effect (*Rønsbo, 1989*).

3.2.12 Monazite-(Ce)

Monazite [$(Ce,La,Nd,Th)PO_4$] was found as a minor accessory mineral in NTG17. Over 50 % of the REE mol. content is Ce, whilst La and Nd also make up significantly amounts. Compared to apatite from the same sample, Si content is lower. A significant amount of Fe was also detected.

3.2.13 Britholite-(Ce)

Britholite [$(Ca,LREE,Th)_5(SiO_4,PO_4)_3(OH,F)$] was found as an accessory mineral in NTG25 and analysed using EDS. It consists of high quantities of Ce and Si, classifying the mineral as britholite-(Ce). Significant proportions of Ca and also La are present, although Y was not detected in any samples. P and Al are both present in high proportions, and in some analyses Th was also detected. Analyses showed immeasurably low amounts of F.

A REE silicate mineral believed to be britholite, but unconfirmed, was found in several eudialyte alteration assemblages using EDS. The REE component of the mineral is mostly Ce and La, with some Nd in lower amounts. The mineral contains no Ca or P, although F is present. Quantitative analysis is needed to confirm the identity of this mineral. The small size of minerals in these alteration assemblages also poses issues such as contamination of EDS spectra from neighbouring grains.

3.2.14 Pyrochlore

Pyrochlore [$(Na,Ca)_2Nb_2(O,OH,F)_7$] was found as an accessory mineral in a variety of samples. The B-site is dominated by Nb in every analysis, with Ti being a major component in most. The ratio of Ti/Nb ranges from 0 – 0.7. Other minor constituents in the B-site include Ta, Zr, Si, Al and Fe^{3+} (*Atencio et al., 2010*), of which none were detected in all analyses. Ratios of Na/Ca show a range from 0.1 – 1.0. Other constituents are Y, Ce, Nd, Th, U and Fe^{2+}, which likely sit in the same site (*Atencio et al., 2010*). Analyses typically show elevated amounts of F, although this has some variability. In general, most of the analysed minerals can be classified as fluorocalciopyrochlore (*Christy & Atencio, 2013*). However, quantitative compositional data and x-ray analyses are required to fully characterise the pyrochlore group.

In NTG15b, some analyses showed Y and Ce present in relatively high enough quantities to be considered major components. They are also absent of F. No Ti is present in the B-site also, although Ti in general is relatively less abundant in pyrochlore analyses from NTG15b.

3.2.15 REE Carbonates

A variety of REE carbonate minerals were analysed via EDS from NTG15b, NTG19, NTG23, NTG25 and NTG30. All analyses show Ce as the dominant REE component with Ce/ΣREE approximately ranging from 0.5 – 0.7. Another prominent REE is La, which is present in all analyses. Key components in the minerals are Ce, Ca, C and F. Contents of these elements vary to produce compositions generally ranging between synchisite-(Ce) [$CaCe(CO_3)_2F$], hydroxlsynchisite-(Ce) [$Ca(Ce,La)(CO_3)_2(OH)$], parasite [$CaCe_2(CO_3)_3F_2$] and bastnäsite-(Ce) [$CeCO_3F$], and possibly with calcioancylite-(Ce) [$(Ce,Ca,Sr)CO_3(OH,H_2O)$] component since some analyses contain Sr, albeit relatively low amounts. As carbon cannot be accurately measured using EDS the exact species of these carbonate minerals cannot be confirmed.

3.2.16 Thorite

Thorite [$ThSiO_4$] was analysed by EDS in NTG19, NTG23 and NTG25 as an accessory mineral. In all analyses Si has a higher content than Th, suggesting that impurities are substituting preferentially for Th. The most abundant of which is Ca, whilst Al was also present in fairly significant amounts, along with traces of U. Some analyses also detected small amounts of F.

3.2.17 UKM1

UKM1 is an unidentified Ti-silicate mineral analysed from NTG19 (Figure 59). It contains roughly equal proportions of Ti and Ca + REE's, with Si content approximately double. Other components in the mineral include Al, Fe and Th and their content varies between grains. In some grains no Fe was detected. The main REE component was Ce in all analyses, with Nd the only other detected REE. Zoning was observed in many grains but not well constrained. The mineral was analysed using EDS and it was not possible to positively identify from semi-quantitative data. It could possibly be a rinkite-group mineral.

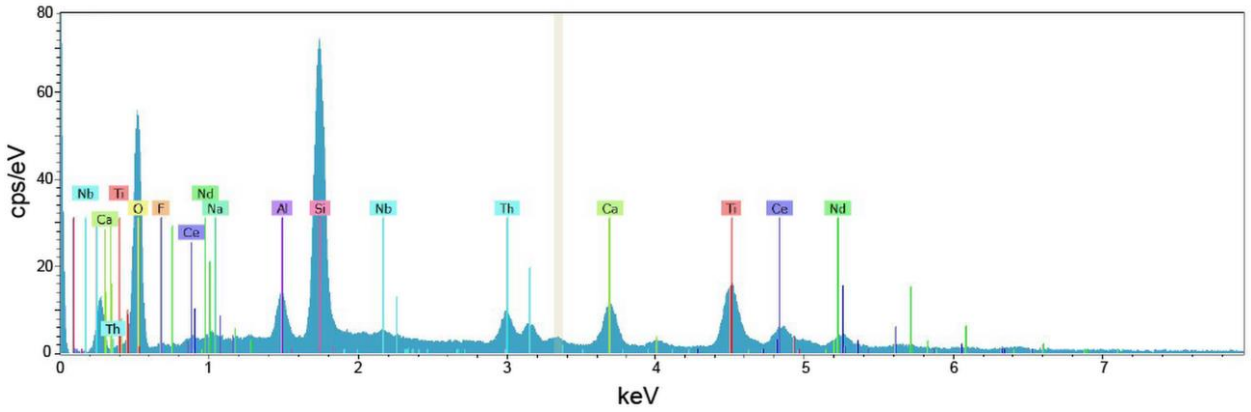

Figure 59: Typical EDS spectrum of UKM1 taken from NTG19.

3.2.18 UKM2

UKM2 is another unidentified mineral analysed using EDS from NTG19 (Figure 60). It is an F-bearing silicate containing both Ti and Zr, where Ti is more abundant. Other major components include Ca and Na, whilst minor yet consistent proportions of Al, K and Mn were detected in each analysis. There is a possible relationship between the proportions of Ca and Ti, which are the two most abundant components. As with UKM1 it was not possible to positively identify the mineral from semi-quantitative data.

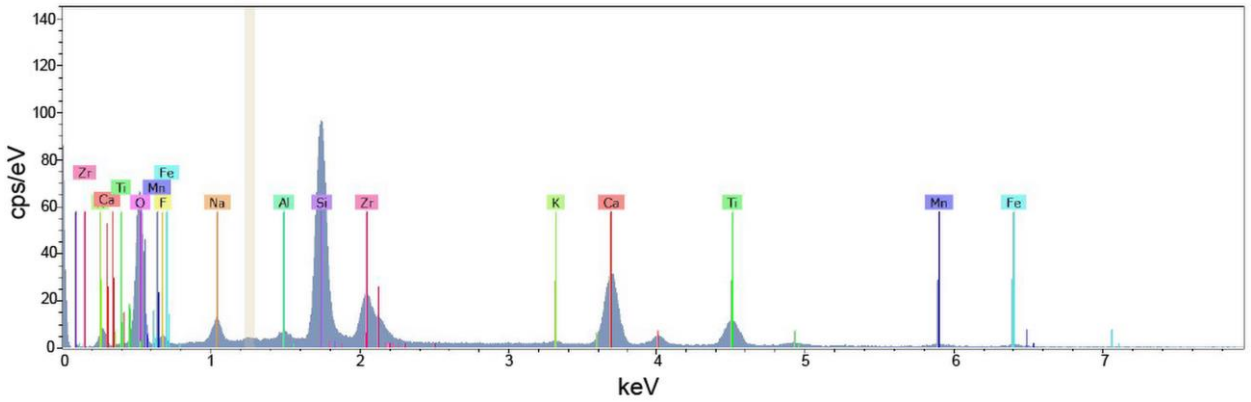

Figure 60: Typical EDS spectrum of UKM2 taken from NTG19.

4. Discussion

4.1 Timing of emplacement

Field relationships between the Bjønnes syenite and surrounding larvikite show that the Bjønnes syenite was injected into larvikite and must therefore post-date the emplacement of RS VI larvikite. Nepheline syenite dykes intrude into larvikite, sourced from the pluton. Rounded larvikite xenoliths are found commonly within the outer margins of the pluton in transitional zones.

The mylonite-like texture formed locally within larvikite along the contact of the Bjønnes syenite is evidence of intense plastic deformation in the form of shearing. This texture is found mostly along the contact between larvikite and syenite, or larvikite and pegmatite. The LPC is thought to have been emplaced in the upper crust (*Neumann, 1980*). Even with a high geotherm that would be expected in a rift system, pressure and temperature conditions would not be high enough to accommodate plastic deformation, which is mostly associated with the middle-lower crust (*Fossen, 2010*).

Plastic deformation of larvikite could therefore not have occurred in cold, crystalline conditions. Consequently the larvikite must still have been hot, possibly not fully crystallised, at the time of deformation. Since deformation appears to be confined to areas around the Bjønnes syenite, its emplacement can be considered as the cause of deformation. It can be concluded that the Bjønnes syenite most likely intruded into hot larvikite and emplacement of the Bjønnes syenite occurred shortly after the larvikite of RS VI.

This is supported by other observed field relationships between larvikite and syenite. For example, the lack of chilled or baked margins at contacts implies no major temperature difference between the units. Partial assimilation of larvikite in the nepheline syenite hints at small amounts of magma mixing, either of two partially liquid components interacting, or through partial remelting of larvikite. Partial remelting is the most likely cause, since assimilation occurs mostly at points where larvikite locally has high surface area/volume ratio. This model resembles a model produced by *Andersen (1984)* to describe the transition zone between larvikite and intruding nordmarkite (syenite) in the Sande Cauldron in the Oslo rift.

Plastic deformation often follows the perimeter of a larvikite block suggesting dragging forces have acted upon the surface of the larvikite. Extensive flow textures typical of the surrounding syenite suggest that the syenite magma was being pushed

against the larvikite wall rock during intrusion. It is likely that larvikite blocks were plucked away from the main body of larvikite by the friction of the Bjønnes syenite being ejected. Their partly rounded shape may suggest that the wall rock was not completely solid, or that partial assimilation of blocks occurred at corners.

Petersen (1978) describes the presence of chilled margins at the contacts between certain ring sections in the LPC. Of the examples mentioned, chilled margins were observed North of Tvedalen at the contact of RS VI and RS VII. This would suggest that the larvikite of RS VI had enough time to cool before emplacement of RS VII. This therefore implies that the Bjønnes syenite was emplaced before RS VII, assuming that it intruded hot larvikite.

4.2 Internal evolution of the Bjønnes syenite

4.2.1 Textural variations

There appears to be a broadly concentric textural evolution of the Bjønnes syenite, from trachytoid in the outer regions, progressing inwards through equigranular to a gneissic centre. The transitional nature of texture changes in the Bjønnes syenite suggests that emplacement occurred as a single event. Contacts between slightly different nepheline syenite bodies can be seen throughout the Bjønnes syenite, particularly in the trachytoid regions. Despite this, the different rock units appear to have been emplaced and crystallised simultaneously.

The Bjønnes syenite is very heterogeneous, often showing intricate mixing and mingling of numerous layers and flows of nepheline syenite, most likely emplaced in numerous short pulses over a short period of time. Large modal mineral variability of nepheline for example, occurs over very short distances is characteristic of the whole area. It could be a result of nepheline accumulation in the melt that may have been unevenly distributed.

The outer domains of the Bjønnes syenite show the development of a trachytoid texture. This texture is not observed in Tvedalen and appears to be confined to the margins of the Bjønnes syenite. It is most likely the development of a marginal foliation in the Bjønnes syenite as a result of differential motion across the wall rock contact upon emplacement (*Winter, 2010*). Petrographically, trachytoid Bjønnes syenite is distinctly different from foyaites in Lågendalen and their similar trachytoid texture appears to be coincidental. The trachytoid texture that defines the foyaites persists throughout intrusions, rather than being confined to their margins.

The majority of exposure of the Bjønnes syenite shows a gneissic texture. It

typically forms bands that are texturally and mineralogically divergent. The texture has a major influence on the development of mafic minerals, typically dividing bands dominated by small clinopyroxene from bands dominated by large poikilitic amphibole. The development of magmatic foliation or banding is usually representative of deformation during crystallisation (*Paterson et al., 1998*).

The viscous magma would have crystallised whilst under directed pressure or movement as a result of a deformation mechanism. Intracrystalline deformation at a hypersolidus state would have caused the development of grain-supported alignment and flow textures (*Paterson et al., 1998; Rosenberg, 2001*), which are present throughout the majority of the Bjønnes syenite to an extent. Grains may have crystallised along an elongated path whilst under strain, creating a foliated or lineated appearance (*Paterson et al., 1998*) however grains showed no further evidence of internal strain deformation once crystallised.

Alternating mafic and felsic bands are seen in locations where gneissic texture has developed most strongly, for example around NTG15, and minerals have been stretched. The texture produces a lineation in cross-section, displaying the most common features of the gneissic syenite, being the segregation of clinopyroxene-dominated bands and poikilitic amphibole-dominated bands. Between these domains felsic material remains roughly constant in its composition and appearance. One minor exception observed in NTG25 showed a reduced grain size in felsic minerals within the clinopyroxene domain compared to felsic minerals in amphibole-rich domains, but this was the only apparent difference. It is unclear what controls cause this division.

A key factor in their differentiation could be water content. Amphibole typically contains 2 – 3 wt. % H_2O, whereas clinopyroxene is anhydrous. Dividing partially crystalline melts into relatively wet and dry bands could therefore have an influence on the ability of amphibole to crystallise. Also, by concentrating water content, amphibole and biotite, both water-bearing minerals, could form in greater quantity and also grow as larger single crystals due to increased diffusivity of molecules in the melt. The mechanics behind this are unknown.

It may also be possible that the bands were magmatically separated through gravitational differentiation and rhythmic magmatic layering that coincides with the principle direction of deformation. This would also help to explain the development of similar, yet less prominent textures in the nepheline syenite dykes in Tvedalen.

A likely deformation mechanism is a fault zone, especially given the shallow depth of emplacement and geological setting. In this instance faulting must occur only

in the early stages of crystallisation since there is little evidence of brittle deformation. Magmatic fabrics preserve only the last increments of strain (*Paterson et al., 1998*), suggesting that deformation occurred at high temperatures and the melt crystallised freely afterwards (*Rosenberg, 2001*). Magmatic fabrics rarely record deformation resulting from plutonic ascent or emplacement so the process of deformation via internal stresses is highly unlikely (*Paterson et al., 1998*).

Several prominent NNE-SSW striking lineaments throughout the LPC run parallel to rift-related fractures elsewhere in the Vestfold graben of the Oslo rift (*Petersen, 1978; Larsen et al., 2008*). One of these highlighted by *Petersen (1978)* strikes along the East coast of the Bjønnes peninsula, extending South through the Langesundsfjord. This gives rise to the most likely theory that rift-related faulting caused deformation of the Bjønnes syenite. It is plausible that if tectonic activity occurred during crystallisation, then faulting may have influenced the initial emplacement of the Bjønnes syenite.

4.2.2 Alkalinity and textural distribution

The most alkaline samples are found within the gneissic syenite. All eudialyte-bearing samples were also confined to gneissic syenite. Trachytoid NTG8 has the lowest alkalinity whilst equigranular NTG6 and NTG20 also have relatively low alkalinity. It appears that alkalinity generally increases towards the centre of the Bjønnes syenite.

It is possible that zoning of the pluton is a result of multiple stages of emplacement. If emplacement occurred in a series of stages, it would be expected that the outer units would have the highest alkalinity since they would have formed from the lowest fraction of partial melting of the source, and been pushed outwards by later intruding batches of melt.

To explain the increase in alkalinity towards the core, one possibility could be the fractionation of a single source melt before upwelling and emplacement either as a single continuous event or as several stages. In this case a fractionation mechanism would be required to allow the most alkaline melts to be emplaced last.

4.2.3 Evolution of paragenesis

The increase in alkalinity in the Bjønnes syenite leads to changes in mineralogy and petrogenesis, which can be divided into three assemblages. A total of four samples from Bjønnes were peralkaline and contained agpaitic mineral assemblages. Three of those (NTG15, NTG18 and NTG 23) are eudialyte syenites. These are used to construct the mineral paragenesis of the agpaitic group (Figure 61). NTG19 and

NTG33, which do not have geochemical data, also fit into this group and are expected to be peralkaline.

The fourth peralkaline sample, NTG30, does not contain eudialyte or any other complex Zr-silicates. Zircon is the dominant Zr-bearing mineral. Despite this, it does contain a significant amount of aenigmatite, a complex Ti-silicate. The sample shows a miaskitic Zr-bearing mineral assemblage and agpaitic Ti-bearing mineral assemblage, and has an alkalinity index of just 1.001. NTG30 seemingly represents a transitional stage between miaskitic and agpaitic, where agpaitic Ti-silicates have become stable before agpaitic Zr-silicates as alkalinity increases. In Figure 61, the Zr assemblage is classed as part of the evolved miaskitic group and the Ti-assemblage is part of the agpaitic group.

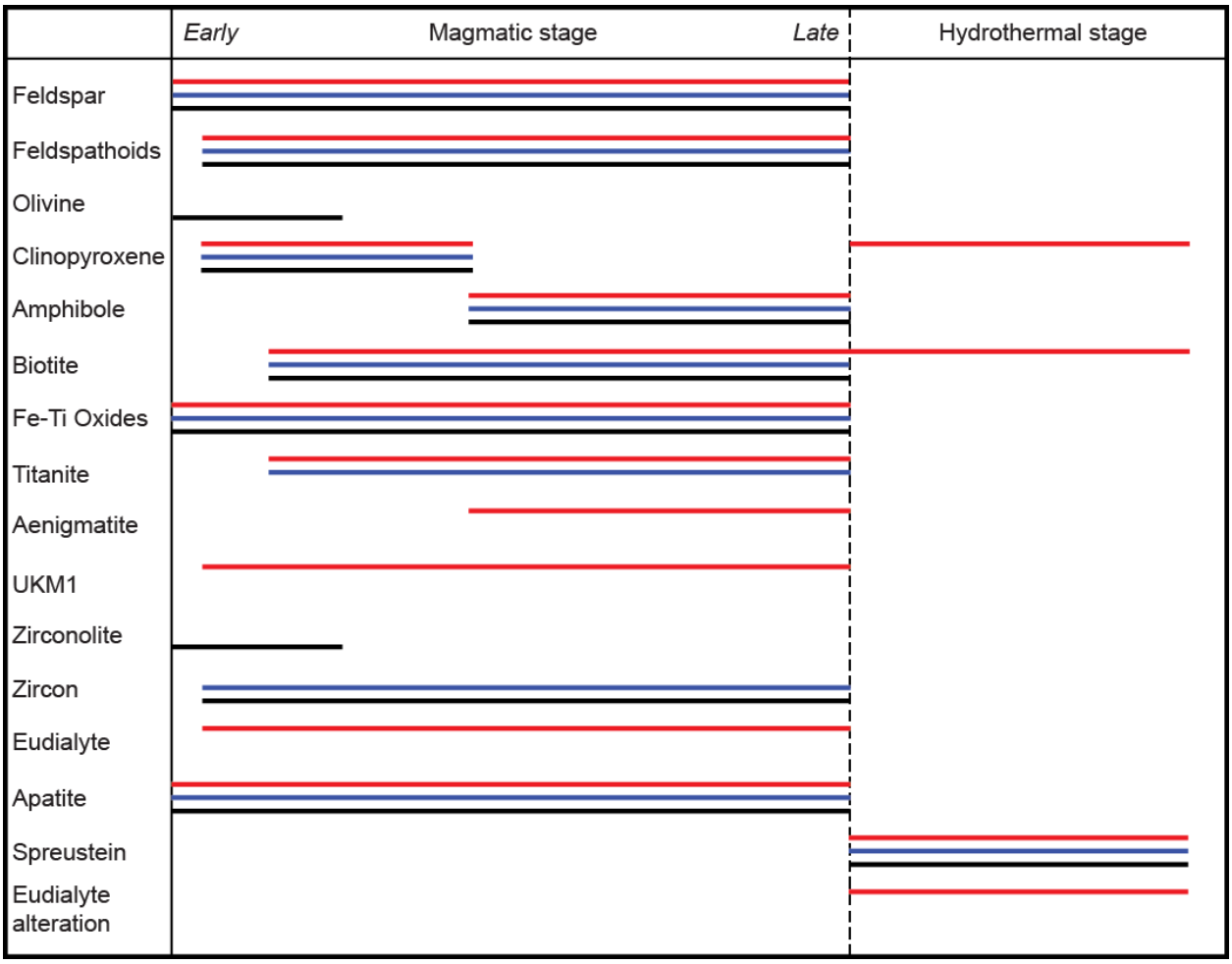

Figure 61: Three generalised paragentic sequences from the Bjønnes syenite showing the comparison between mineralogy and alkalinity from low-evolved miaskitic (black), to highly-evolved miaskitic (blue), to agpaitic (red).

The samples from Bjønnes with the lowest alkalinity index, excluding NTG17, (NTG6 and NTG8) also have distinct miaskitic mineralogy. NTG22 has a comparably low alkalinity index and would also fit into this group, although it should be remembered

that it represents a nepheline syenite dyke outside of the main pluton. NTG7 also has a comparable mineralogy but has not been geochemically analysed. This group contains olivine and zirconolite, relatively little amphibole and no titanite.

The remaining samples fit into an intermediate, more evolved miaskitic group, where samples are approaching peralkaline conditions. These samples remain miaskitic but have evolved beyond the formation of olivine and zirconolite, which either no longer form or are resorbed back into melt during early stages of crystallisation. Figure 61 shows schematic parageneses for these three groups.

The distribution of Zr is mostly confined within zircon, zirconolite or eudialyte, with each sample having a single dominant Zr-bearing mineral. Zircon was the most widespread Zr-bearing mineral, found in most miaskitic samples, including zirconolite-bearing samples. Zircon was found to be unstable in eudialyte-bearing samples but is present as the main Zr-bearing mineral in NTG30, which also contains agpaitic mineral aenigmatite.

Zirconolite is found in samples with the lowest peralkalinity. It is the only mineral present to assign sites to both Zr and Ti. It is found in nepheline syenite pegmatites in the LPC and as a rare accessory mineral in larvikite (var. polymignite) but is notably absent or very rare in nepheline syenite pegmatites in Tvedalen and the Langesundsfjord (*Larsen, 2010*). Zirconolite is also found in other alkaline complexes such as Khibina, Kola peninsula, Russia, where it is associated only with miaskitic mineral assemblages including Fe-Ti oxides, titanite and zircon (*Yakovenchuk et al., 2005*).

The distribution of Ti also differed depending on petrogenesis. In miaskitic samples, Ti was mostly spread between ilmenite and titanite (mostly secondary). Ilmenite is present to some extent in all samples and is the main Ti-bearing mineral in the lowest alkalinity samples, which do not contain any titanite. Titanite is found in most other samples, both miaskitic and agpaitic. One sample that contains no titanite is NTG21 despite a moderate alkalinity, and Ti is most likely stored in ilmenite, like in less alkaline samples.

In the Bjønnes syenite, primary titanite exists only in peralkaline samples, both as skeletal prisms or interstitial material. This is contradictory to the popular definition that titanite is a miaskitic mineral (*Sørensen, 1997*). Despite this, titanite is known to occur in agpaitic rocks of some complexes such as Khibina, Russia (*Khomyakov, 1995; Yakovenchuk et al., 2005*). Primary titanite occurs in all nepheline syenite dykes from Tvedalen, with the exception of NTG29, and also in foyaites, all of which are miaskitic.

Ti distribution in agpaitic samples is therefore more complex. All samples contain both ilmenite and titanite (primary and secondary), but also contain complex Ti-silicate minerals typical of an agpaitic assemblage. In NTG15, NTG23 and NTG30, aenigmatite is the dominant Ti-bearing mineral. Aenigmatite has been found in pegmatites from the LPC but this appears to be the first occurrence of aenigmatite found within a main rock unit in the LPC. In NTG19 and perhaps NTG18 and NTG33, aenigmatite is absent and Ti is instead taken up in part by UKM1. In NTG19 small quantities of rosenbuschite also incorporate Ti.

4.2.4 Zr and Ti incorporation in mafic minerals

Electron microprobe analysis showed an average of 0.45 wt. % and 0.39 wt. % ZrO_2 in clinopyroxene and amphibole respectively. There were no observed relationships between Zr content in these minerals, and alkalinity or total Zr content of their corresponding whole rock samples. These mafic minerals appear to have no significant role in the distribution of Zr throughout evolution of the system. Therefore a combination of factors including fO_2, a_{H2O}, a_{SiO2} and a_{Nds} have been such as to prevent Zr uptake in clinopyroxene and amphibole, as is seen in other alkaline complexes like the Mt Gibraltar microsyenite, Australia, for example (*Andersen et al., 2011*). *Nds* refers to a sodium disilicate component $Na_2Si_2O_5$.

Clinopyroxene incorporates more Ti as its aegirine component increases and is incorporated into the M1-site via a coupled substitution with Na. This relationship is typical of pyroxenes in alkaline complexes, such as those in the Gardar province, Greenland (*Marks et al., 2004* and references within). This infers that there are constraints on the crystallisation of clinopyroxene preventing the incorporation of Zr but not Ti as a_{Nds} increases.

Calcic amphiboles contain more Ti than sodic amphiboles and Ti content decreases as Fe^{3+} becomes increasingly incorporated (Figure 54). The initial mechanism of Ti incorporation is most likely a combination of a Tschermak substitution and a coupled substitution with O^{2-}. Similar to clinopyroxene, Ti content is affected as alkalinity increases, with *fO2* likely a major factor. However Zr, which possibly shows a minor decrease as alkalinity increases, is not incorporated into amphibole to the extent of Ti and its distribution is poorly constrained.

4.2.5 Evolution of mafic mineral chemistry

Clinopyroxene shows a single evolutionary compositional trend beginning with a primitive diopsidic composition and increasing in Na and Fe to an almost pure aegirine composition. A limited range of this evolution can be seen internally within samples, for example through zoning. Zonation in almost all cases shows an increase in Na and Fe content towards the rim, reflecting the direction of melt evolution during crystallisation. The compositional range within samples follows the larger-scale trend between different samples suggesting that initial melt compositions vary across Bjønnes. A single evolutionary trend suggests the melting of a single, largely homogeneous source with a stable magmatic oxidation state. Another factor that seemingly influences clinopyroxene evolution paths is Na/Ca ratio of the melt or fluid that the clinopyroxene crystallises from (*Marks et al., 2008a*).

Both primary and secondary clinopyroxene occur on the same evolutionary path. Secondary clinopyroxene is believed to have crystallised from late- to post-magmatic fluids. To evolve along the same trend as primary magmatic clinopyroxene, it can be assumed that the responsible fluids were from residual magma, essentially in a closed system without the percolation of external fluids.

Secondary clinopyroxene consistently has a higher aegirine component than primary clinopyroxene analyses, shown by the compositional distribution of NTG18 (Figure 48). In NTG19, secondary clinopyroxene approaches a pure aegirine composition. Secondary aegirine replacement of amphibole is a fairly common feature of agpaitic systems, observed in other complexes such as Puklen, Greenland (*Marks et al., 2003*), and Tamazeght, Morocco (*Marks et al., 2008a*). In the Tamazeght complex, primary clinopyroxene is replaced by magmatic amphibole, which is further replaced by hydrothermal secondary clinopyroxene (*Marks et al., 2008a*), very similar to the trend observed in the Bjønnes syenite.

Amphibole compositions demonstrate a comparable trend to clinopyroxene, from calcic hastingsite to sodic arfvedsonite. The arrangement of samples along this trend is largely in agreement with clinopyroxene. Since clinopyroxene and amphibole compositions reflect the same chemical evolution it can be assumed that compositional variations are dependent on the melt rather than the mineral. The continuation of evolutions also suggests that the melt remained chemically undisturbed during crystallisation. Samples tend to have a short compositional range with the exception of NTG17, discussed further later on.

One compositional difference observed in the amphiboles was the relatively high Na contents of NTG18 and NTG19 compared to other samples, which create a strong linear trend in Figure 54. This is because of an elevated Na content in The B-site relative to other samples. They are the only samples that consistently have higher Na than Ca content in the M4-site. This is caused by an elevated oxidation state. NTG15, for example, has a similar total Fe content to NTG19 but mostly in the form of Fe^{2+}, whereas NTG19 has a significant Fe^{3+} proportion. This allows Na^{+} to substitute for Ca^{2+} in a coupled substitution by raising the oxidation state of Fe. This suggests that NTG18 and NTG19 may have crystallised in a more oxidised environment which coincides with the increasing aegirine components observed from clinopyroxene data.

From the outlined parageneses in Figure 62, a correlation can be made between mafic mineral chemistry and evolution. The most primitive, calcic samples, such as NTG8 and NTG22 coincide with the less-evolved miaskitic petrogenesis, whilst the most Na- and Fe- rich mafic minerals are found in samples of agpaitic paragenesis, like NTG18.

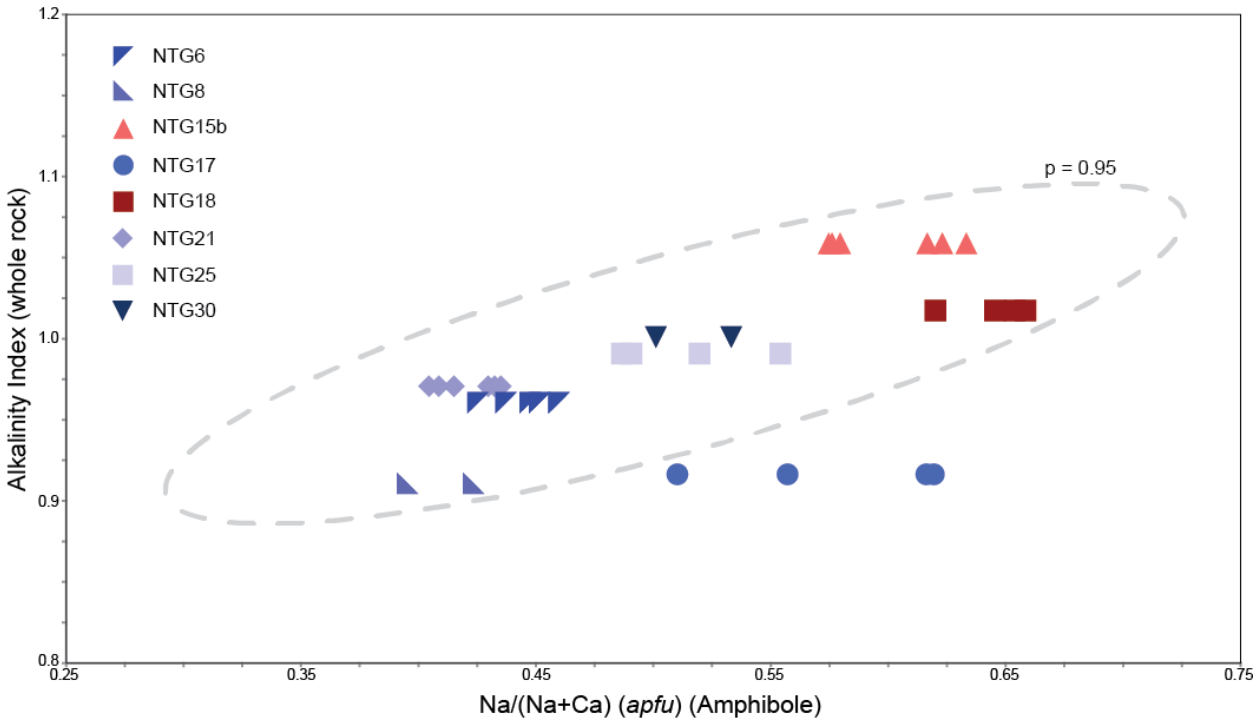

Figure 62: A plot of alkalinity against Na/(Na+Ca) values for amphiboles to show the positive relationship between them. The Mahanalobis eclipse depicts the area of which a reproduced analysis from these samples would have a 95 % (2σ) chance of plotting within. Notably all four analyses from NTG17 sit outside of this ellipse.

Figure 62 shows alkalinity index plotted against calculated Na/(Na+Ca) values for amphibole. The internal compositional ranges obscure the data slightly but a clear linear relationship can be observed showing an increase in Na with alkalinity. One

exception is NTG17, which is discussed later. A similar yet less defined trend is also observed for clinopyroxene.

4.2.6 Eudialyte syenite

Eudialyte is found as a rock-forming mineral in some samples from the Bjønnes syenite. Those that have been geochemically analysed all have alkalinity indexes above 1.0. Therefore under modern definitions, these samples are agpaitic. This is the first known discovery of a truly agpaitic rock found in Norway apart from some nepheline syenite pegmatites in the LPC.

The distribution of eudialyte syenite is confined towards the central gneissic region of the pluton and occurs in small areas. Eudialyte syenites NTG15 and NTG23 are surrounded by zircon-bearing miaskitic syenite over short distances. Missing outcrops showing any transition zones raise the possibility of fault controls, where eudialyte syenite may have been thrust up or down alongside miaskitic syenite from an agpaitic domain of the pluton, differentiated on a large scale. Subvertical slickenlines of an E-W trending fault plane were found between NTG15 and NTG25 although eudialyte had already seemingly disappeared before the fault. Overall there is little evidence to support this theory.

Other possibilities include localised increases in alkalinity, either through fractionated emplacement, or through magmatic heterogeneity. Another possibility is that truly agpaitic melts may have become immiscible from surrounding miaskitic melts, concentrating in small areas. The formation of eudialyte required high a_{HCl} suggesting that these agpaitic melts would be fluid-rich. This would allow for the formation of abnormally large mafic minerals and eudialyte crystals. It could also explain the formation of the small eudialyte pockets, where small pockets of agpaitic melts have exsolved from the surrounding miaskitic melts. Alternatively, these may have formed as pegmatite pockets at a later magmatic stage from fluid-rich residual melts.

In the Tamazeght alkaline complex, Morocco, there is a similar distribution of eudialyte-bearing nepheline syenite, occurring within spatially restricted areas several tens of square metres in size and surrounded by miaskitic nepheline syenites (*Marks et al., 2008b*). The eudialyte-bearing syenites are thought to be the most evolved areas in their unit, like in the Bjønnes syenite. The Tamazeght complex is believed to be the product of melting of a heterogeneous source, leading to the formation of a diverse suite of alkaline rocks (*Marks et al., 2008a*).

Figure 63 shows the relationship between P_2O_5 and total REE content between samples. The strong positive linear trend produced by the majority of samples suggests that apatite has a major influence on the distribution of REE's in Bjønnes and Tvedalen. Foyaites may follow a different trend but the number of analyses is too limited to make data conclusive. Two notable exceptions are NTG15 and NTG23, both eudialyte syenite samples, which have extremely high REE contents and moderate P_2O_5 content relative to other samples. It appears that eudialyte has also been a major contributor in REE distribution. NTG15 and NTG23 are relatively enriched in HREE's relative to other samples and this may suggest that eudialyte preferentially incorporates HREE's. NTG18, however, remains on the P_2O_5-ΣREE trend. Eudialyte in NTG18 is therefore likely to be REE-poor.

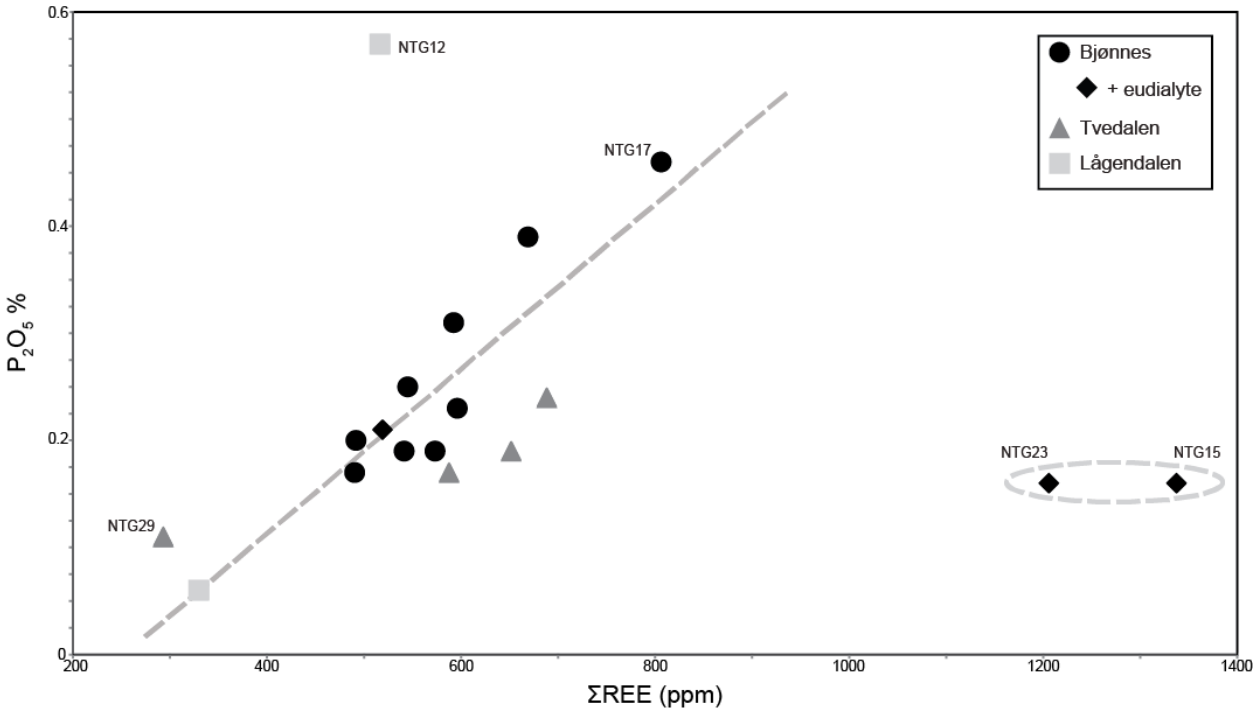

Figure 63: A plot of geochemical data showing P_2O_5 against the sum REE total. The roughly linear trend indicates that P_2O_5, of which the vast amount is found in apatite, has a strong affinity for REE's. The two outlying eudialyte-bearing samples show abnormally high REE content, indicating that eudialyte is also influential on REE content.

NTG15 and NTG23 are very similar in mineralogy and geochemistry, and due to their close proximity, may be a part of the same eudialyte syenite unit. NTG18, however, shows major differences in trace element compositions. Coupled with nearby NTG19, they also show a further evolved mafic mineral chemistry and share a different mineralogy. Notable mineralogical differences include the presence of aenigmatite (NTG15 and NTG23 only) and secondary clinopyroxene (NTG18 and NTG19 only). Despite this they have a comparable alkalinity index. This suggests that two varieties of

eudialyte may be present in the Bjønnes syenite, where individual eudialyte syenite zones have formed under different conditions.

4.2.7 Eudialyte alteration

Late- to post-magmatic alteration of eudialyte was observed in all eudialyte syenite samples. Within nepheline syenite pegmatites at Sagåsen (Tvedalen), a very similar alteration of eudialyte-group minerals (EGM) is seen (*Larsen, 2001; Larsen et al., 2005*). Masses of composed of finely crystalline aegirine, zircon, pyrochlore and fluorite occur in outer rims and crosscutting veins of EGM masses. Astrophyllite was also found in completely altered EGM assemblages in Sagåsen (*Larsen et al., 2005*), but was not observed in extensive alteration assemblages from the Bjønnes syenite. Instead, secondary titanite was found near altered eudialyte in contact with biotite. Catapleiite was identified as an alteration product of eudialyte in nepheline syenite pegmatites at Bjørndalen (*Larsen, 2001*), similar to occurrences in NTG15.

Such similar alteration within the same complex is most likely the result of the same processes. The fact that alteration occurs along fractures through EGM's in Sagåsen suggests that the alteration process involves pervasive fluids. In Bjønnes, the extent of alteration depends on the interface with the neighbouring minerals. It is likely that fluids were preferentially penetrating along the most accessible planes within the rock. Therefore eudialyte in contact with biotite was seen to be most extensively altered because biotite is easily penetrable by fluids along its excellent cleavage planes.

The simultaneous alteration of two minerals, eudialyte (reaction 1) and nepheline (reaction 2) were observed in Figure 43 and are shown below. Reaction 1 shows the reaction of eudialyte to form aegirine, zircon and fluorite. In this case fluorite is the dominant Ca-bearing product although it should be noted that calcite can also occur in greater quantities and for the purpose of this reaction is interchangeable. Reaction 2 shows the reaction of nepheline to products sodalite and K-feldspar.

Reaction 1:

$$\underset{Eud}{Na_{15}Ca_6Fe_3SiZr_3Si_{25}O_{73}(O,OH,H_2O)_3(Cl,OH)_2} + 12F^- \rightarrow \underset{Aeg}{3NaFe^{3+}Si_2O_6} + \underset{Zrn}{3ZrSiO_4} + \underset{Fl}{6CaF_2} + 12Na^+ + 17Si^{4+} + 43O^{2-} + 2Cl^-$$

Reaction 2:

$$\underset{Ne}{Na_4KAl_5Si_5O_{20}} + Si^{4+} + Cl^- \rightarrow \underset{Sod}{Na_4Si_3Al_3O_{12}Cl} + \underset{Kfs}{KAlSi_3O_8} + Al^{3+}$$

In reaction 1, significant amounts of F need to be added to the system in order to produce fluorite, and also CO_3 to form calcite and REE carbonates. It should also be noted that precipitation of secondary catapleiite found in NTG15 requires H_2O levels above or close to its saturation point (*Andersen et al., 2010*). The reaction is not closed and Na, Si, O and Cl are all released. Product Na, Si and O from this reaction can also be considered as a sodium disilicate component *Nds*, written as $6Na_2Si_2O_5 + 5Si^{4+} + O^{2-}$

In reaction 2, additional Si and Cl are required as reactants. These are both released as products from reaction 1, linking the two reactions together where reaction 1 appears initiate a metasomatic process. Reaction 2 releases a small excess of Al. No F or CO_3 is released in this reaction to explain its influx into reaction 1, meaning that they must have been introduced by fluids. It is probable that product Na, Si and Al was removed from the assemblage by these fluids. No zeolites were found around these alteration zones.

Nielsen (1979) described a reaction of nepheline in the presence of an *Nds* component and Cl, both products released from reaction 1. The products of this reaction are albite and brine, shown below.

$$\underset{Ne}{NaAlSiO_4} + \underset{Nds}{Na_2Si_2O_5} + 2HCl \rightarrow \underset{Ab}{NaAlSi_3O_8} + \underset{brine}{2NaCl + H_2O}$$

In this example, K is not considered as a major component in nepheline, as seen in reaction 2. Albite as a product is not observed but K-feldspar is, suggesting that the K component has been preferentially involved in the reaction. *Ferguson (1978)* describes another reaction observed from nepheline syenites where nepheline reacts with late-stage brine-rich fluids to form sodalite.

$$\underset{Ne}{3NaAlSiO_4} + \underset{brine}{NaCl} \rightarrow \underset{Sod}{Na_4Al_3Si_3O_{12}Cl}$$

This suggests that reaction 2 may actually represent two separate reactions, where K-feldspar has formed at the interface of eudialyte and the subsequent products have caused further alteration of nepheline to sodalite. This explains why K-feldspar forms

closest to eudialyte, with sodalite formed further within nepheline crystals.

In hydrothermal environments rich in F, H_2O and CO_3, Zr, Nb and REE's become more soluble and therefore easily mobilised (*Piilonen et al., 2012 and references within*). It is highly likely that fluids enriched in F, H_2O and CO_3, probably post-magmatic in nature, circulated through the rocks and caused the alteration of eudialyte by mobilising HFSE (high field strength elements). In eudialyte alteration assemblages without a nepheline interface, Cl-bearing minerals are not produced and Cl is most likely removed from the system in fluids. Therefore it is likely that Cl acts as a catalyst of nepheline alteration, remaining within the system in sodalite.

Figure 64 shows EDS elemental maps of Ca, Cl, F, Fe, Na, Nb and Zr from a eudialyte and nepheline alteration zone from NTG19 (see Figure 43 for annotations). It must be noted that EDS peaks may overlap and misrepresent data, for example Nb and Zr leading to the overrepresentation of Nb. The retention of Cl within sodalite can be seen clearly, along with its absence in any eudialyte alteration products.

Secondary pyrochlore is present in small amounts. The source of Nb is likely in the single Si-site in eudialyte, which can hold either Si or Nb. As seen in the Nb element map, pyrochlore is a minor phase, suggesting that Nb is present in small amount in eudialyte.

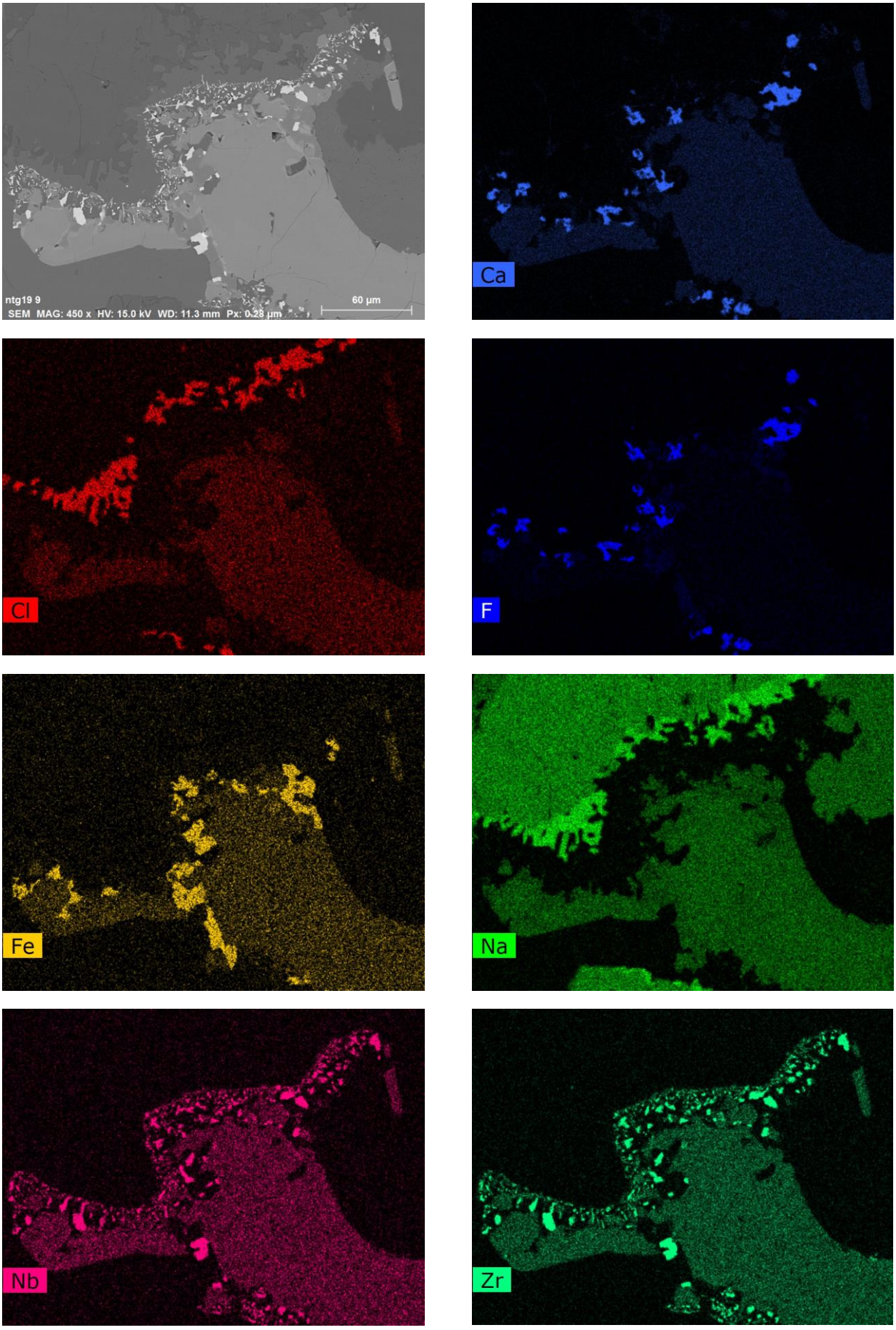

Figure 64: Selection of EDS elemental maps showing the redistribution of elements during alteration of eudialyte and nepheline (see Figure 43 for annotations and further details).

4.2.8 The roles of Cl and F

Sodalite was found in many samples from all three study areas, usually in small amounts. It was also found to coexist with zircons in many cases. In some samples such as NTG24, larger zircons were often seen in close proximity to sodalite. The presence of sodalite shows that Cl content must have been significant, even in relatively low alkalinity samples, allowing Cl to be precipitated. Despite this, zircon remains stable and does not form eudialyte in the presence of Cl until peralkaline conditions. NTG26b and NTG30 have alkalinity indexes of 1.01 and 1.00 respectively, and contain both zircon and sodalite. Sodalite by itself does not indicate an agpaitic system. In a sodalite-saturated system, the stability of zircon or eudialyte depends mostly on a_{Nds}, with eudialyte becoming stable at higher a_{Nds} (*Andersen et al., 2010*). The formation of eudialyte in agpaitic samples requires a high a_{HCl} to form preferentially over other agpaitic F-bearing Zr-silicate phases, along with high peralkalinity (*Andersen et al., 2010*).

In terms of its magmatic role, F does not appear to have a great influence. Small quantities are found in titanite, whilst apatite is the only other common F-bearing mineral. Minute amounts of pyrochlore and REE-carbonates also contain F. An exception to this is NTG19 which contains a small amount of rosenbuschite and fluorite, whilst UKM1 also contains a small quantity of F.

The lack of F-bearing Zr-silicates or magmatic fluorite is interesting since wöhlerite, for example, was commonly found in pegmatites on Bjønnes. These F-bearing Zr-silicates are commonly seen as intermediate Zr phases between zircon and eudialyte and their absence suggests that a_{HF} is significantly below fluorite saturation (*Andersen et al., 2010*).

Despite this, F appears to have a greater role in the hydrothermal stage, as seen by its influx in eudialyte alteration assemblages. The presence of F-bearing Zr-silicates in pegmatites suggests that F remained mostly in the melt and was mobilised mostly into late-stage pegmatite formation and post-magmatic fluids.

4.2.9 Oxygen fugacity

Throughout the Bjønnes syenite, biotite can be seen mantling Fe-Ti oxides. This is a feature observed in all major rock types in the LPC and elsewhere in the Oslo rift. The reaction between the minerals and its control on internal fO_2 is discussed by *Carmichael et al. (1974)*, where annite is formed from the following reaction between magnetite and K-feldspar.

$$\underset{Mag}{Fe^{2+}Fe^{3+}{}_2O_4} + \underset{Kfs}{KAlSi_3O_8} + H_2O = \underset{Bt\ (Ann)}{KFe_3AlSi_3O_{10}(OH)_2} + \frac{1}{2}O_2$$

Whilst this is not a true univariant oxygen buffer curve due to the activity of water, *fO₂* will be largely controlled whilst biotite and Fe-Ti oxides remain stable (*Andersen et al., 2010*).

Biotite begins to crystallise later than Fe-Ti oxides. Biotite is still considered to form relatively early and is commonly found intergrowing with primary clinopyroxene, or being overgrown by amphibole. This boundary must have been crossed at some stage of magmatic crystallisation and petrographic relationships suggest that it may have occurred fairly early.

The presence of aenigmatite in peralkaline samples suggests a reaction of Fe-Ti oxides (Ti-magnetite) with a peralkaline silica-undersaturated melt and is constrained within a 'no-oxide' field (*Carmichael et al., 1974; Marsh, 1975*). Aenigmatite overgrows and presumably replaces Fe-Ti oxides. In most peralkaline samples clinopyroxene is rare however in NTG30, aenigmatite seemingly replaces clinopyroxene when association with Fe-Ti oxides. This indicates the crossing of the upper stability field of the 'no oxide' field, from aegirine-ilmenite to aenigmatite-*Nds*. This corresponds to the following reaction (*Carmichael et al., 1974*).

$$\underset{Ilm}{FeTiO_3} + 4Na\underset{Aeg}{Fe^{3+}Si_2O_6} = \underset{Aen}{Na_2Fe^{2+}{}_5TiSi_6O_{20}} + \underset{Nds}{Na_2Si_2O_5} + O_2$$

The precipitation of amphiboles reaching arfvedsonite compositions also requires conditions below the FMQ-buffer (*Marks et al., 2003*). The replacement of clinopyroxene by amphibole during the intermediate stages of crystallisation indicates reducing *fO₂* conditions where amphibole acts as a sink for Fe^{2+} from clinopyroxene. It is defined by the aegirine-arfvedsonite stability fields, which have a flat slope in *fO₂* – T space relative to other buffer curves. This corresponds to the following reaction (*Andersen et al., 2016*).

$$5Na\underset{Aeg}{Fe^{3+}Si_2O_6} + H_2O = \underset{Arf}{NaNa_2(Fe^{2+}{}_4Fe^{3+})Si_8O_{22}(OH)_2} + \underset{Nds}{Na_2Si_2O_5} + O_2$$

The reactions suggest that the Bjønnes syenite crystallised under slightly reducing conditions, much like the larvikites and nepheline syenite pegmatites, where

fO_2 was buffered to maintain stability of biotite and Fe-Ti oxides (*Neumann, 1976; Andersen et al., 2010*).

Hydrothermal minerals from the Bjønnes syenite include aegirine and haematite, where Fe exists in a trivalent state, representing an increased oxidation state in post-magmatic fluids. This increase in fO_2 is supported by the replacement of sodic amphibole by sodic clinopyroxene, transitioning from arfvedsonite to aegirine stability fields (*Carmichael et al., 1974*).

4.2.10 Porphyritic syenite (NTG17)

Porphyritic syenite makes up a minor textural component of the Bjønnes syenite and is represented in analysis by NTG17. The chemical evolutionary trends of clinopyroxene and amphibole from NTG17 range from some of the least evolved to some of the most evolved, relative to other samples from Bjønnes. Despite mafic minerals showing well-evolved chemistry, whole rock alkalinity is relatively low. Figure 62 shows whole rock alkalinity index plotted against calculated Na/(Na+Ca) values for amphibole. A Mahalanobis contour ellipse (p=0.95) has been plotted using ioGas software. It shows that all four amphibole analyses taken from NTG17 lie outside the prediction ellipse and are therefore anomalous to the general trend.

The mineral chemistry of NTG17 is slightly unusual in that it creates several data points that lie away from general trends, caused by analyses of clinopyroxene and amphibole from within the feldspar megacrysts. These analyses are relatively calcic and give the sample a larger compositional range than other samples. These analyses also stray from evolutionary trends, where a clinopyroxene analysis can be seen with an unexpectedly low aegirine component (Figure 48) and an amphibole analysis shows unusually low Fe content (Figure 54). This suggests that Fe is not being incorporated into mafic minerals situated within feldspar megacrysts in the same manner as is typical in the Bjønnes syenite, with Mg contents remaining relatively high.

Since petrography and mineral chemistry of mafic minerals outside of the feldspar megacrysts appear to comply with observations and data from other samples, it is more likely that mineral compositions are as expected, and therefore whole rock alkalinity is unusually low. The minor presence of secondary clinopyroxene is also associated with samples with higher alkalinity. This may be explained by the significant presence of feldspar megacrysts that define the texture. As a result of these megacrysts, feldspar content is much higher than in other samples. Consequently they have affected the whole rock geochemistry. Despite this, SiO_2 content coincides with

the majority of other samples from Bjønnes.

The appearance of the feldspar megacrysts is very similar to those found in surrounding larvikite. The origin of these megacrysts is unknown but their appearance and the texture of the rock suggests that they have originated from the larvikite or larvikite source. They could have simply crystallised within the syenite in the same way as those in larvikite, meaning low alkalinity was the result of other factors. This is possible since the megacrysts appear to have crystallised contemporaneously with other early-magmatic minerals, at least to some extent. NTG17 also shows a strong negative Eu-anomaly consistent with other samples from the Bjønnes syenite, as well as having a similarly low Sr content. Accumulated feldspars would likely dilute this anomaly. This suggests that the feldspars are phenocrysts, rather than accumulated larvikite xenocrysts.

To have originated directly from larvikite, one possibility is that larvikite blocks were assimilated in the nepheline syenite and feldspar megacrysts became incorporated within the syenite. One problem with this is that porphyritic syenite was found far from larvikite wall rock, meaning blocks would have needed to be transported towards central areas of the pluton before assimilating. This explanation also does not account for the lack of other megacrystic minerals, for example nepheline, which is typically much larger in surrounding larvikite.

The ternary feldspars of larvikites formed after emplacement of magma into the upper crust at low fluid pressures, as a result of resorption of plagioclase (*Neumann, 1980* and references within). NTG17 has relatively high P_2O_5 content, similar to that of larvikites. The megacrysts may have resulted from a separate pulse of magma that had accumulated feldspars and apatite through fractionation processes in the source. Alternatively, fractionation of larvikites continued after emplacement in the upper crust (*Neumann, 1980*) and a similar process may have occurred to form the porphyritic syenites. However the apparent lack of controls on its distribution makes this unlikely.

Despite contrasting evidence, the feldspar megacrysts are most likely phenocrysts that have crystallised from the Bjønnes syenite melt. Their poorly defined grain boundaries on a small scale indicate that they have crystallised simultaneously with other surrounding minerals. Mafic mineral inclusions with slightly unusual mineral chemistry were most likely segregated from the surrounding melt during crystallisation, influencing their chemistry. It is unclear why these phenocrysts form, and why they are restricted to small areas of the Bjønnes syenite.

4.3 Nepheline syenite dykes

Geochemical data from NTG16b, NTG26a and NTG26b is very consistent with the bulk of samples from the Bjønnes syenite. Petrographically, these samples are also very similar to those from Bjønnes, with NTG26a and NTG26b displaying gneissic texture. They show miaskitic mineral assemblages similar to NTG24 or NTG30 for example.

Despite their similarities, NTG29 has a distinctly different geochemistry. It is the only sample to classify as peraluminous, has the highest SiO_2 content and the lowest Fe_2O_3 + MgO content of any geochemically analysed sample. Similarly, it also has relatively high Al_2O_3 and K_2O contents but the lowest totals of TiO_2, P_2O_5 and CaO of any analysed sample. Petrographically it is somewhat different, with few mafic minerals, mostly clinopyroxene and interstitial Fe-Ti oxides. Feldspars consist mostly of homogeneous microcline and albite, rather than being predominantly perthitic. NTG29 also has the lowest ΣREE content and an unusually small negative Eu anomaly. Other samples from Tvedalen and Bjønnes share strong negative Eu anomalies.

Another nepheline syenite dyke, NTG22, also shows geochemical and petrographical differences, although to a lesser extent. Similarly it has an unusually high SiO_2 content, but also high Fe_2O_3 + MgO content and the lowest Al_2O_3 content of all analyses. It is relatively fine-grained and contains very little amphibole.

From this small pool of samples it is unclear if the nepheline syenite dykes in Tvedalen and the Langesundsfjord are related to the Bjønnes syenite. Observations of more dykes in the field also show some dykes that are texturally very similar in appearance to the Bjønnes syenite, whilst others appear significantly different. No immediate spatial trend linking different types together was observed.

There is, however, the possibility that at least some of the dykes are related to Bjønnes. With the exception of NTG29, analysed nepheline syenite dykes are extremely similar to the Bjønnes syenite and there is a probable connection between the Bjønnes syenite and at least some of the nepheline syenite dykes in Tvedalen.

It may be possible that the Tvedalen and Langesundsfjord dykes are offshoots from the main Bjønnes syenite pluton, intruding into surrounding larvikite, similar to what is suggested by *Dahlgren (2010)*. One issue is that the nepheline syenite dykes in Tvedalen are generally coarser than the Bjønnes syenite. An explanation for this could be that the Bjønnes syenite is close to the western margin of the LPC, almost bordering cold Palaeozoic sediments, which could have encouraged increased cooling rates. Meanwhile the dykes intruding eastwards in Tvedalen and islands of the

Langesundsfjord are moving further into the LPC. With the assumption that the Bjønnes syenite intrudes hot larvikite, the dykes would not be chilled by the surrounding wall rock and would cool slowly alongside the larvikite, resulting in a slower cooling event than that experienced by the Bjønnes syenite.

It is also feasible that the nepheline syenite dykes do not originate from the Bjønnes syenite but originate from their own source or sources. In this scenario, one or several similar yet smaller sources would lead to the emplacement of the nepheline syenite dykes in a manner much like that of the Bjønnes syenite. This would allow for the formation of nepheline syenites resembling the Bjønnes syenite and would also account for nepheline syenites such as NTG29, which are not so similar. However, based on similarities in geochemistry, mineral chemistry and textures between the Bjønnes syenite and the nepheline syenite dykes, another source would need to be very similar in origin and evolution to the Bjønnes syenite.

4.3.1 Evidence for timing

Nepheline syenite dykes in Tvedalen show a complex, often intricate relationship with pegmatites. This relationship is cogenetic, with substantial evidence of both marginally predating one another and showing alternating phases of emplacement. Pegmatites typically form from fluid-rich residual melts at a late-magmatic stage. If the pegmatites originate from surrounding larvikite, this implies that the nepheline syenite dykes were emplaced during the latter stages of larvikite crystallisation, which is highly comparable to the apparent age of the Bjønnes syenite.

4.3.2 Source of the nepheline syenite pegmatites

Due to their relationship with the nepheline syenite dykes, it has been speculated that pegmatites in Tvedalen and the surrounding areas originate from the Bjønnes syenite (*Dahlgren, 2010*). Despite a possible link between nepheline syenite dykes and the Bjønnes syenite, no genetic relationship could be found between the pegmatites and the nepheline syenite dykes or Bjønnes syenite. Similar nepheline syenite pegmatites occur as far East as RS III (*Øyvind Sunde, pers. comm.*), meaning that the pegmatites most likely originate from larvikite, but the origin of the pegmatites is still unknown.

Pegmatites within the Bjønnes syenite were seemingly less common than in Tvedalen. It is unlikely that such high volumes of residual melt could be forced out of the Bjønnes syenite to such distances. NTG29 for example was collected over 6 km

East of the Bjønnes peninsula. It is feasible that the Bjønnes syenite is more expansive below the surface and spreads further East, with nepheline syenite dykes and/or pegmatites intruding upwards. This is speculative however, with no real supporting evidence.

4.4 The Bjønnes syenite as part of the LPC

4.4.1 Comparing geochemistry

Figure 65 plots the alkalinity index of rocks from across the LPC against their Mg# and compares them to data from *Neumann (1980)*. Each rock type is roughly divided into its own domain, displaying a linear trend of decreasing alkalinity as Mg# increases. Three subparallel trend lines have been plotted with arrows showing the direction of evolution. The upper trend is defined by lardalites and foyaites. The middle trend is mostly defined by larvikites from RS IV – VI, and possibly RS III. The lower trend is defined by larvikites from RS II, VII and VIII. Some of the larvikite data may be anomalous, as discussed by *Neumann (1980)*.

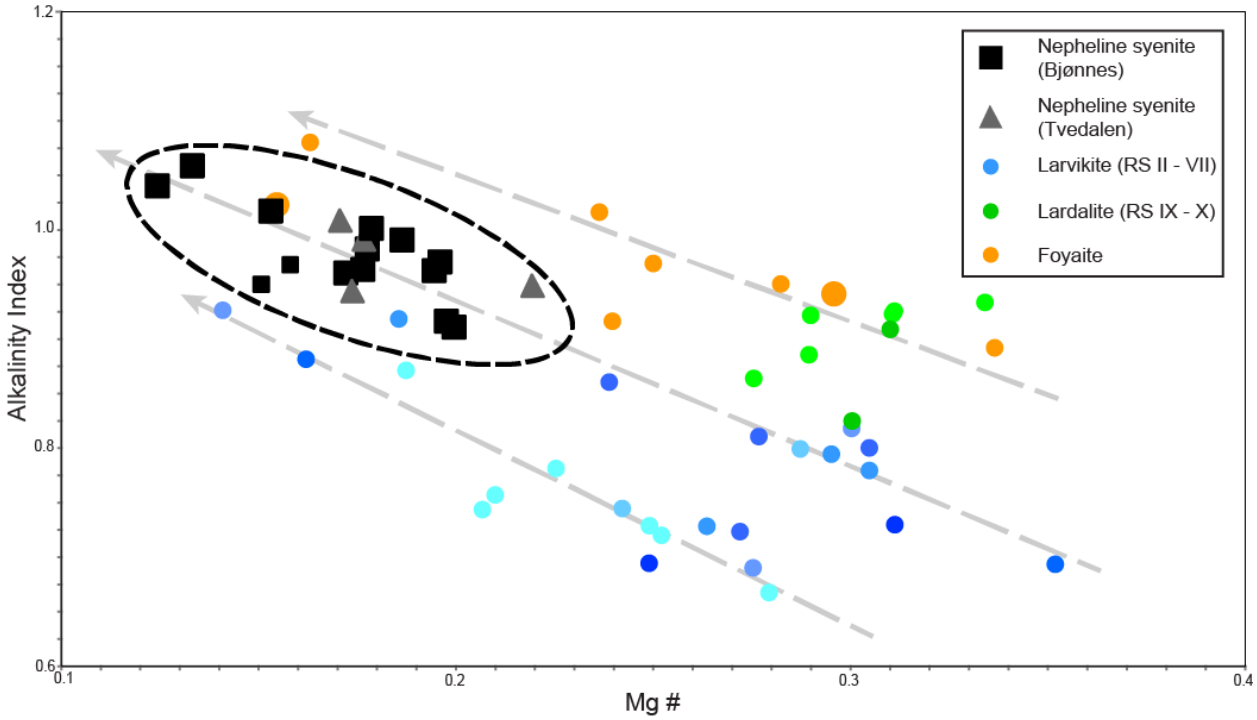

Figure 65: Alkalinity plotted against Mg# for different rock types across Bjønnes showing a generally decreasing Mg# as alkalinity increases along a series of trends (modified from *Neumann, 1980*). Individual ring sections of larvikite and lardalite are represented by colours ranging from light (earlier ring sections) to dark (later ring sections). Larger spots represent data collected during this study. The trends have been plotted as dashed grey lines indicating direction of evolution.

The nepheline syenites from Bjønnes and Tvedalen are very similar, highlighted by an ellipse. They create a well-defined, distinct domain that appears to continue

along the trend seen in the larvikites of RS IV – VI. This is interesting considering that the nepheline syenites are confined within RS VI. Also, this diagram shows that the evolution of larvikites does not follow a single, consistent trend, and the geochemistry of RS VII and VIII is more comparable with RS II than RS VI. Foyaites increase in alkalinity along the same trend as less evolved lardalites, much like the trend of nepheline syenites and larvikites. The difference is that these rocks have systematically higher Mg#'s at a given Al. It is interesting that even though foyaites have a similar alkalinity to the Bjønnes syenite, they do not exhibit agpaitic mineralogy. The presence of sodalite suggests a high a_{HCl} so there must be other preventing factors.

Figure 66 shows a plot of P_2O_5 against TiO_2 for rocks throughout the LPC incorporating data from *Neumann (1980)*, plotted in the same manner as Figure 65 above. A positive linear correlation parallel to the equiline (1:1) can be observed, creating a trend including larvikites and lardalites. The nepheline syenites of Bjønnes and Tvedalen create a similar trend but with a lower gradient. It is not clear if the foyaites follow the trend of the larvikites and lardalites, or the trend of the nepheline syenites.

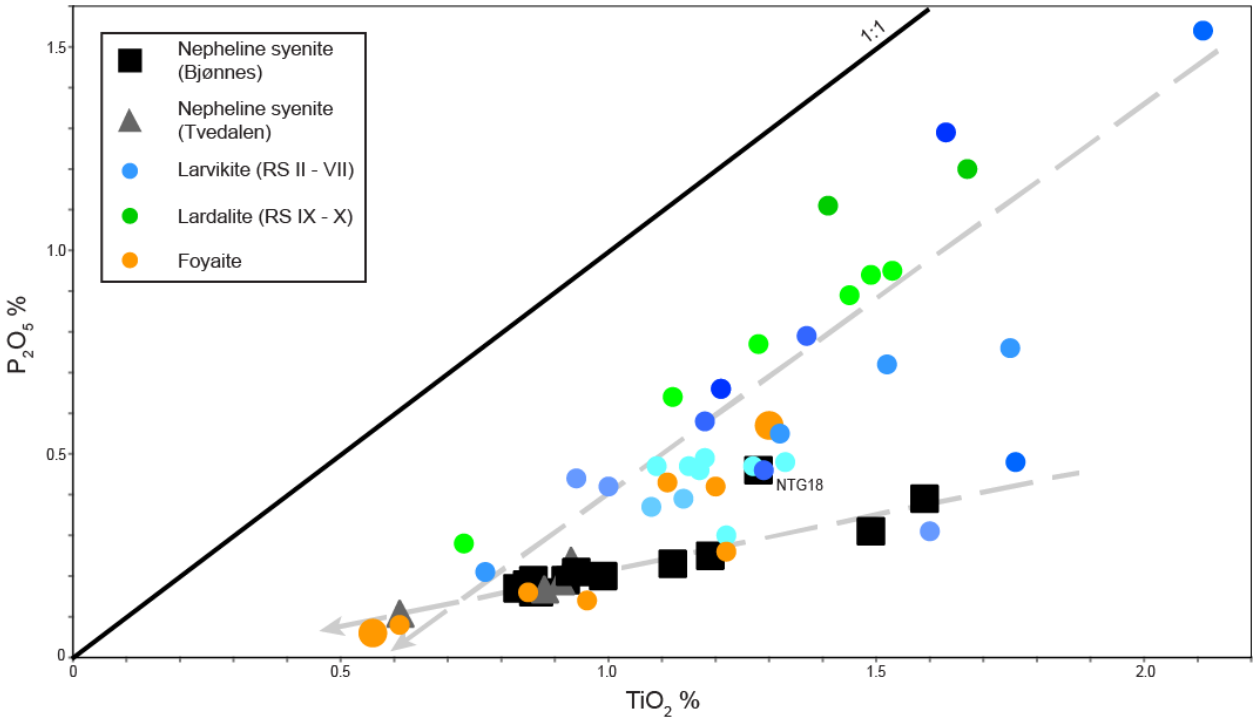

Figure 66: Whole rock P_2O_5 content plotted against TiO_2 content for rocks throughout the LPC incorporating data from *Neumann (1980)* showing the nepheline syenites having been relatively depleted in P_2O_5. Individual ring sections of larvikite and lardalite are represented by colours ranging from light (earlier ring sections) to dark (later ring sections). Larger spots represent data collected during this study. The equiline is marked 1:1 and trends have been plotted as dashed grey lines indicating direction of evolution.

It is common in magmatic systems that TiO_2 content decreases with differentiation (*Pitcher, 1997*) as early magmatic crystallisation of Fe-Ti oxides commences (*Ferrara & Treuil, 1974*). In alkaline systems this is observed in Ilímaussaq, for example, however the opposite is true in Lovozero (*Ferguson, 1970*). Figure 66 shows that TiO_2 decreases systematically with differentiation in the LPC. Internally this is also true of the Bjønnes syenite, where TiO_2 decreases as alkalinity increases. Apatite occupies the vast majority of P_2O_5 in magmatic systems and it typically decreases in concentration as differentiation occurs (*Pitcher, 1997*). As seen in samples from throughout the LPC, apatite crystallises very early and it has been suggested by *Neumann (1980)* that it is involved in melt fractionation.

The two distinct trends of nepheline syenite, and larvikites and lardalites suggest that P_2O_5 has been relatively depleted from the source of the nepheline syenites relative to the source of the larvikites and lardalites. This implies that the process of apatite fractionation has occurred, inferring that apatite crystallised at an early stage. This is supported by observations from the thin sections of all analysed samples. The apparent lack of TiO_2 depletion seemingly suggests that Fe-Ti oxides have not been fractionated to the extent of apatite or feldspar. It is possible that TiO_2 may have also been depleted but to a lesser extent than P_2O_5. It is interesting that NTG17, containing what are believed to be larvikite feldspar megacrysts, does not fit the trend of the nepheline syenites and fits better into the larvikite trend. It was suggested that feldspar accumulation relative to other nepheline syenite samples may have occurred and these data suggest that apatite may also have been relatively accumulated.

Figure 67 shows the contents of Sr against Rb in rocks throughout the LPC, incorporating trace-element geochemical data from *Neumann (1980)*. Relatively, Sr is a more compatible element than Rb. Strontium is divalent and has a similar ionic radius with Ca^{2+}, allowing it to be incorporated into Ca-bearing minerals such as plagioclase and clinopyroxene. The more incompatible Rb^+ has the same valence and a similar ionic radius to K^+, mostly partitioned into micas and K-feldspar.

As shown by Figure 67, the nepheline syenites from Bjønnes and Tvedalen show very similar Sr/Rb ratios. They show a clear enrichment in Rb relative to the rest of the LPC and have a low Sr content. A curve shows a general exponential trend of decreasing Sr and increasing Rb. Larvikites and lardalites, with no clear distinction between individual ring sections, are enriched in Sr and have low Rb contents. Foyaites follow the trend from the larvikites and lardalites, showing low Sr and moderate Rb contents.

From this trend, it can be assumed that both foyaites and nepheline syenites have originated from fractionated sources, where Sr had already been preferentially removed relative to Rb, presumably by a previous episode of melting. The enrichment of Rb in nepheline syenites relative to foyaites suggests that the nephelines syenites are more evolved, where concentration of Rb has increased through the preferential removal and subsequent dilution of more compatible elements during fractionation.

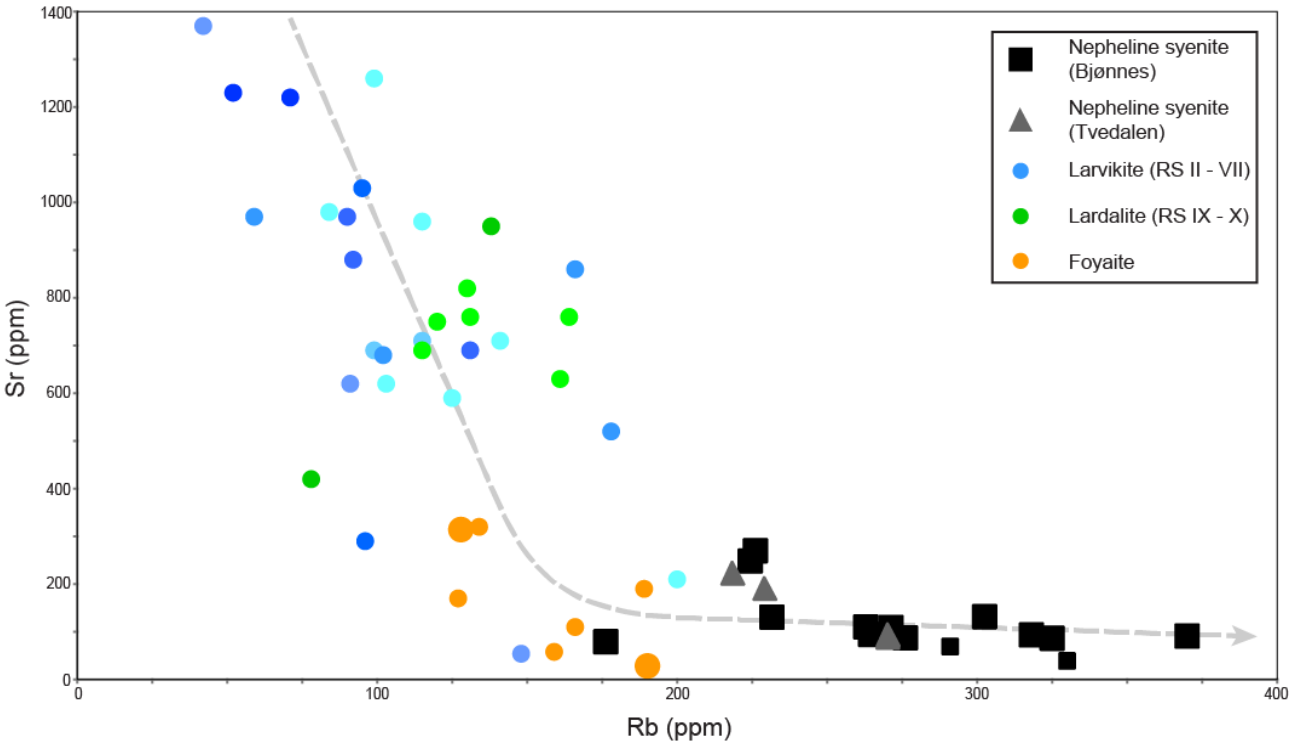

Figure 67: Trace element geochemical data plotting relatively compatible Sr against incompatible Rb for rocks throughout the LPC incorporating data from *Neumann (1980)*. Individual ring sections of larvikite and lardalite are represented by colours ranging from light (earlier ring sections) to dark (later ring sections). The larger spots represent data collected during this study. A trend line has been plotted indicating direction of evolution.

Figure 68 shows a series of binary relationships between incompatible trace elements in rocks throughout the LPC incorporating trace-element geochemical data from *Neumann (1980)*. The format of the figure is the same as used previously throughout this chapter. Black lines represent equilines grey lines highlight trends in the data. Data of all rocks excluding the nepheline syenites produce single, strong linear trends. In Figures 68B (Hf vs. Th), 68C (La vs. Th) and 68F (U vs. Ta), the trends fall either on or parallel to the respective equiline.

The nepheline syenites follow the trends set by the other rock units in Figures 68A (Hf vs. Rb), 68C (La vs. Th), 68E (Th vs. U) and 68F (U vs. Ta), however in Figure 68D (Rb vs. Ta) the nepheline syenites concentrate in a well-defined, Ta-depleted group away from this trend. In Figure 68B (Hf vs. Th) the nepheline syenites appear to be split, with some samples following the common trend and others following a different,

Hf-enriched trend. In five of six diagrams, eudialyte-bearing NTG15 and NTG23 sit as outliers expressing relatively enriched Ta, Hf and La contents. Opposing this, NTG18 is relatively depleted in Ta and Hf relative to other samples.

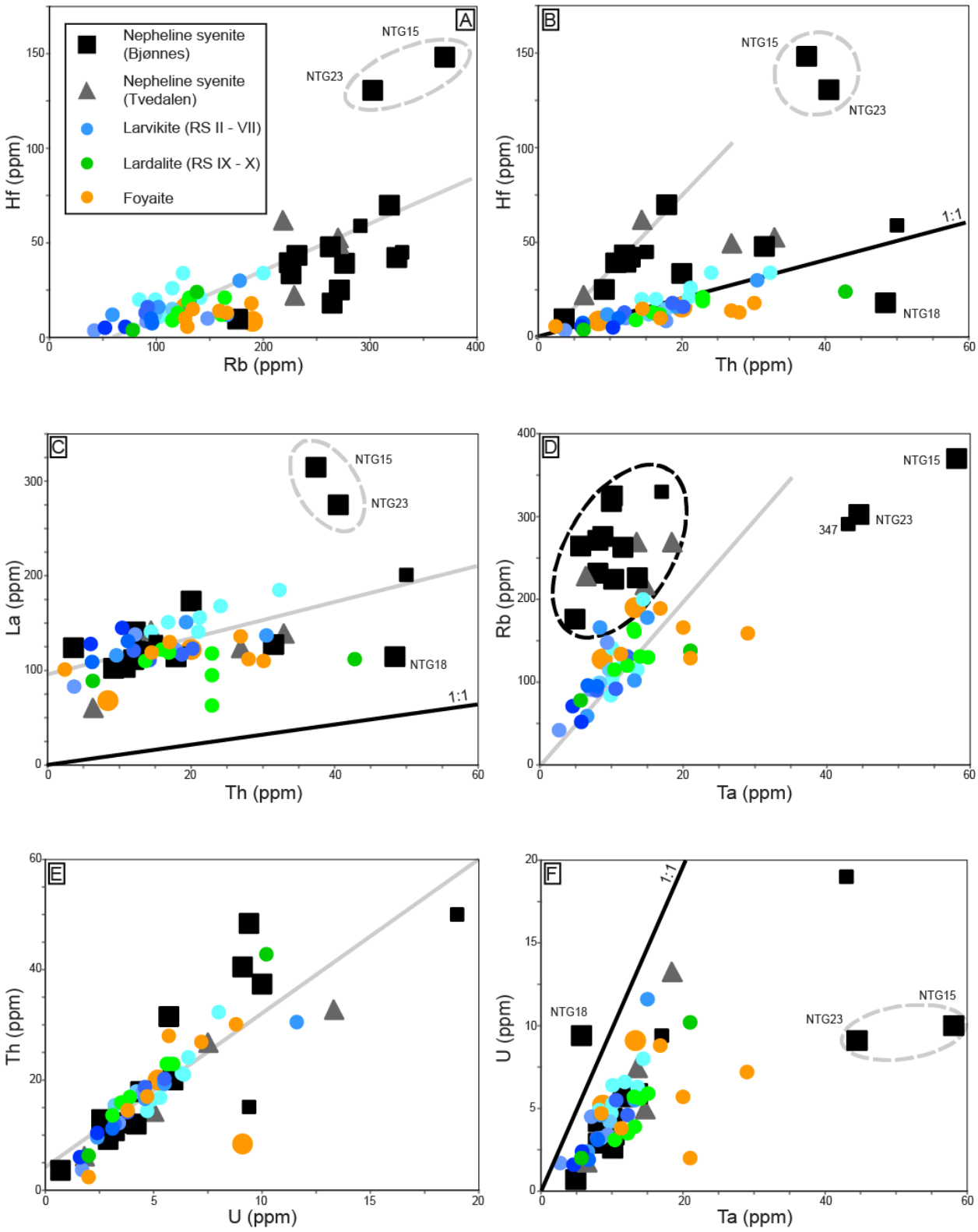

Figure 68: A series of incompatible trace element plots for rocks throughout the LPC incorporating data from *Neumann (1980)*. Individual ring sections of larvikite and lardalite are represented by colours ranging from light (earlier ring sections) to dark (later ring sections). Larger spots represent data collected during this study. The equiline is marked 1:1 and trends have been plotted as dashed grey lines indicating direction of evolution.

The seven elements plotted in these diagrams are incompatible high field strength elements (HFSE). The ratios of incompatible trace elements do not change greatly through processes of partial melting or fractionation in a magmatic system (Ferrara & Treuil, 1974), implying that trace element ratios observed in magmatic rocks reflect those of its source. The consistency of ratios in larvikites, lardalites and foyaites in all examples therefore seems to reflect derivation from melts of a single homogeneous source, as concluded by *Neumann (1980)*.

The nepheline syenites however are more ambiguous. Despite deviating trends, particularly for Ta and Th, the nepheline syenites mostly coincide with trend of other rocks of the LPC and can be assumed to originate from the same source. The effects of periodical melt replenishment and subsequent magma mixing are not accounted for when considering trace element ratios and this was likely a factor in the emplacement of the LPC, making incompatible trace element data somewhat unreliable (*Neumann, 1980; Rollinson, 1993*).

Figure 69 shows the REE distribution of rocks in the LPC. Each line shows the average REE content of an individual rock type by combining data from Table 3 with data from *Neumann (1980)*.

Nepheline syenites from Bjønnes and Tvedalen show very similar, distinct patterns. One key feature is the presence of a strong negative Eu anomaly. In comparison, larvikites have weak positive to negative Eu anomalies and lardalites show weakly positive Eu anomalies. Foyaites show a negative Eu anomaly but not nearly as strong as the nepheline syenites. Unlike other REE's, Eu can exist in both a trivalent and bivalent state and Eu^{2+} has a comparable ionic radius to Ca^{2+}, making it compatible in plagioclase and also K-feldspar (*Rollinson, 1993*). Therefore a negative Eu anomaly suggests fractionation of feldspars in the system, where feldspars have been removed or accumulated elsewhere. This seemingly adds weight to the argument that the nepheline syenites and possibly foyaites were formed from a more fractionated melt source.

The nepheline syenites are consistently enriched in both LREE's and HREE's relative to other rock types, most notably foyaites. This distinction is most profound in distribution of HREE's. The HREE's of the nepheline syenites produce a trough-shaped pattern. Petrographic mixing calculations by *Neumann (1980)* suggest that the fractionation of apatite may be responsible for the removal of middle REE's from the melt, developing weak trough patterns in the most evolved larvikite samples, 'ditroites' (Bjønnes syenite) and nepheline syenite pegmatites. Titanite partitions REE's in a

similar manner to apatite (*Rollinson, 1993*) and may also have had an influence. Both nepheline syenites and foyaites have low P_2O_5 contents relative to larvikites and lardalites, which support the theory of apatite fractionation.

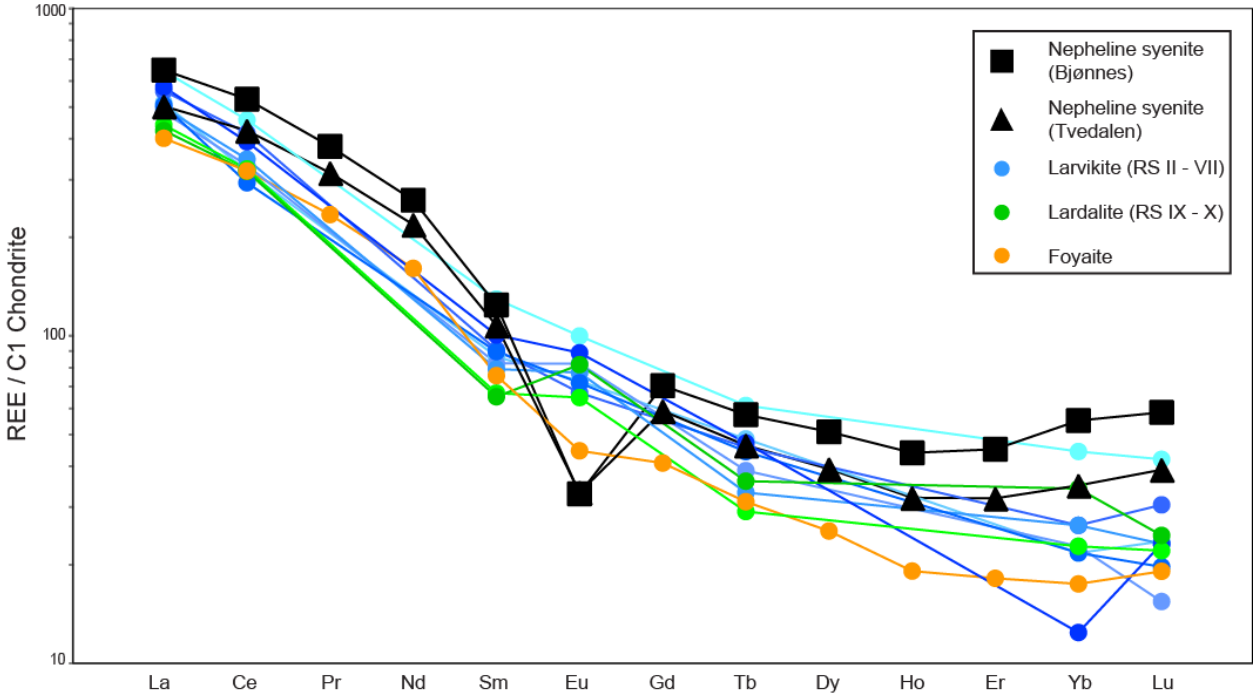

Figure 69: REE spider diagram normalised to C1 chondrite (*McDonough & Sun, 1995*) showing the average REE content of analysed each unit of the stated rock types from the LPC incorporating data from *Neumann (1980)*. Individual ring sections of larvikite and lardalite are represented by colours ranging from light (earlier ring sections) to dark (later ring sections).

4.4.2 Evolution of mineral chemistry

Figure 70 shows a ternary aegirine-diopside-hedenbergite plot of clinopyroxene end-member proportions from across the LPC including data from nepheline syenite pegmatites. End-member proportions of analyses from other studies were recalculated to enable a direct comparison.

Most nepheline syenite pegmatites roughly follow the evolutionary trend of the clinopyroxenes of the Bjønnes syenite, which was discussed previously. The pegmatites are more commonly dominated by an aegirine component, suggesting that they are highly evolved, as would be expected based on their mineralogy and formation from late-stage melts. Although pegmatites group well together, there is a slight distinction between 'T-type' (Tvedalen) and 'L-type' (Langesundsfjord) pegmatites (*Piilonen et al., 2013*), which have been linked to the Bjønnes syenite previously (*Dahlgren, 2010*). Generally amphiboles of 'T-type' pegmatites are found to the hedenbergite-enriched side of the trend line, implying slightly lower oxidised conditions, whereas 'L-type' pegmatites are generally found to the hedenbergite-depleted side,

implying more oxidised conditions. Due to compositional ranges it can be assumed that both formed under similar conditions to the clinopyroxenes of the Bjønnes syenite. Other pegmatite types are also included in Figure 70 and are discussed in *Piilonen et al. (2013)*.

Lardalites and larvikites are similarly primitive, showing the most diopsidic compositions. Both appear to fit well as a primitive extension to the trend Bjønnes syenite trend, suggesting that the Bjønnes syenite could have evolved from a similar melt composition as both rock types. Data on larvikites and lardalites are limited, however, and there is no indication as to whether clinopyroxenes in these rocks would continue to evolve along this trend.

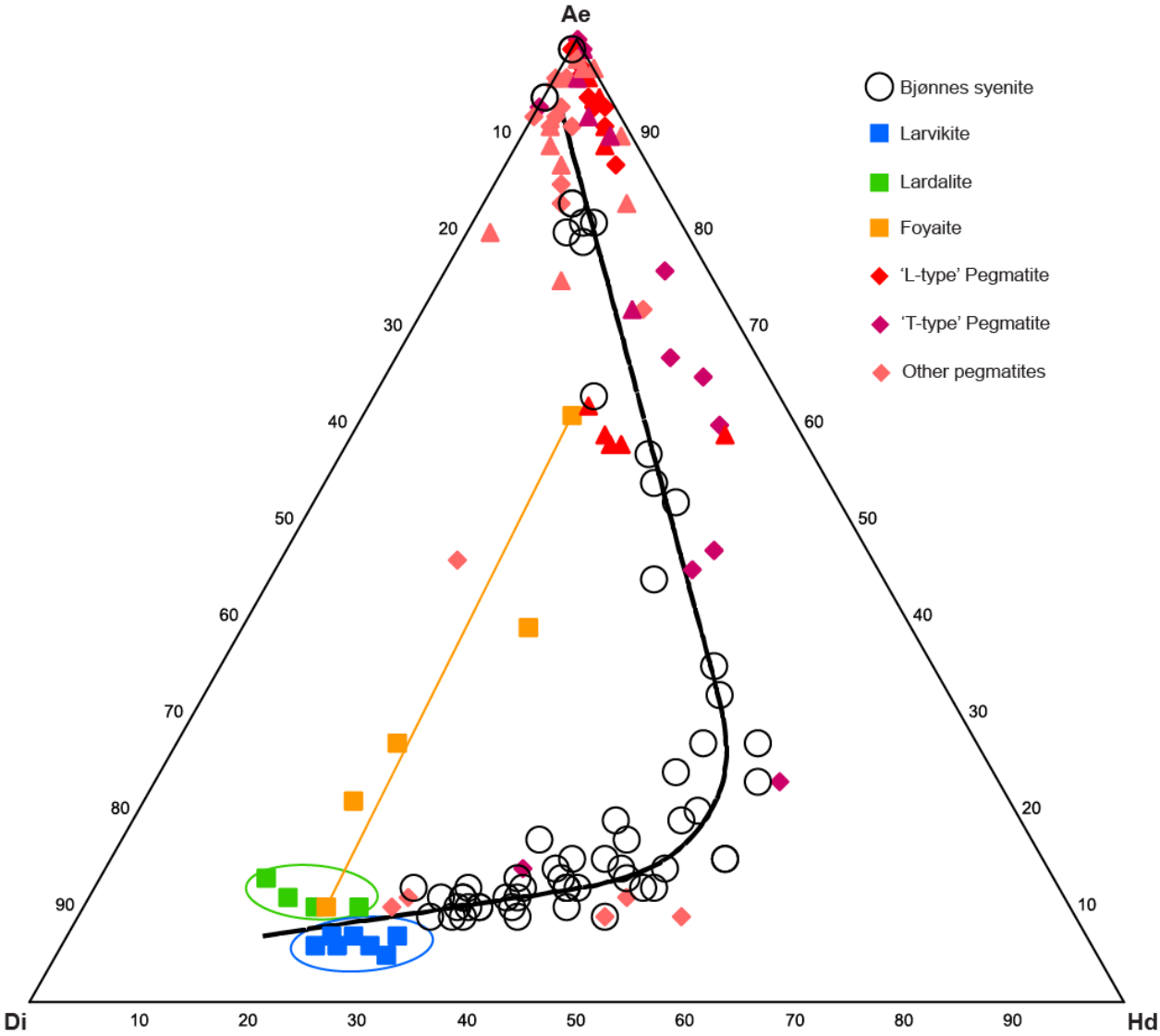

Figure 70: Ternary aegirine-diopside-hedenbergite plot of clinopyroxene end-member proportions from units across the LPC (triangles from *Larsen & Raade, 1997;* diamonds from *Piilonen et al., 2013*), larvikites, lardalites and foyaites (*Neumann, 1976*).

Foyaites also have limited mineral chemistry data available but they appear to develop a much different trend. They do not appear to increase in hedenbergite component as they evolve, suggesting that the crystallising conditions were more oxidised relative to other rocks of the LPC. This would lead to incorporation of Fe^{3+} in higher quantities than Fe^{2+}, leading to the replacement of Ca^{2+} by Na^{+}, bypassing the hedenbergite component. This would indicate that formation of foyaites occurs in much more oxidised conditions to the Bjønnes syenite.

Figure 71 shows a Na-Mg-Fe ternary plot of amphiboles from the same rock types, including data from larvikites, lardalites and foyaites (*Neumann, 1976*), nepheline syenite pegmatites (*Piilonen et al., 2013*). The data seems to show that the amphiboles of the Bjønnes syenite become relatively sodic as Fe increases, compared to larvikite and most of the nepheline syenite pegmatites. Some pegmatites do appear to follow the trend more closely, especially as more primitive compositions. As the Fe/Mg ratio increases, these rocks maintain consistent amounts of Na, possibly increasing very slightly. In the Bjønnes syenite, however, Na clearly increases throughout its evolution.

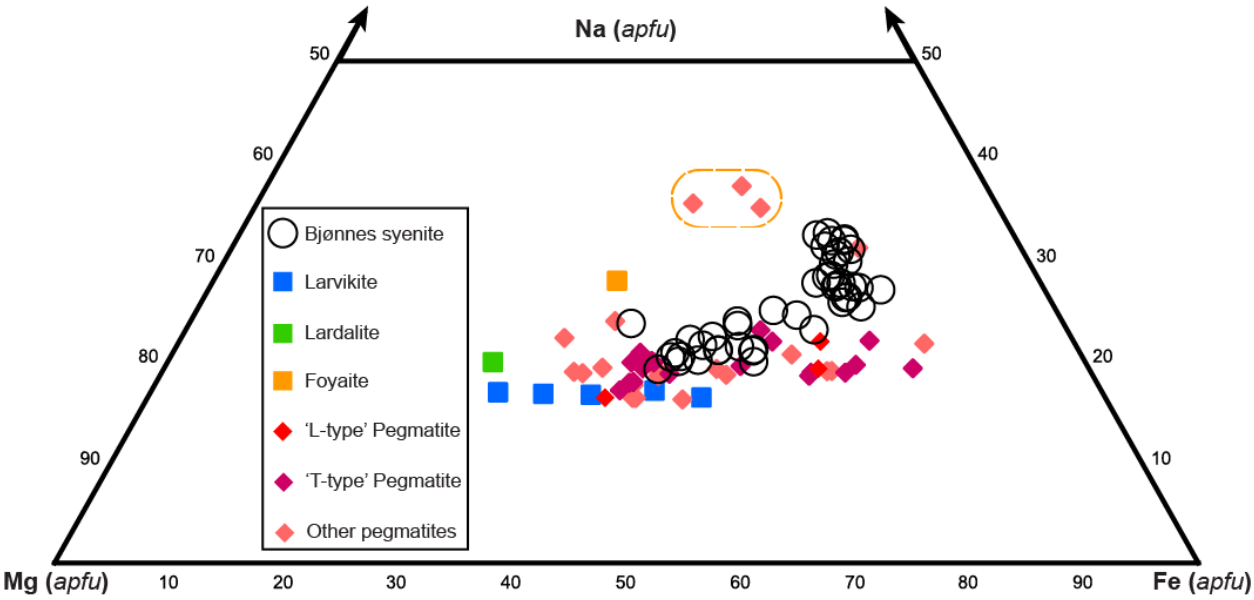

Figure 71: Ternary Na-Mg-Fe plot of amphibole *apfu* proportions from units across the LPC incorporating data from *Neumann (1976)* (squares) and *Piilonen et al. (2013)* (diamonds).

Unlike the clinopyroxenes, there appears to be a difference in the evolution of amphiboles from nepheline syenite pegmatites and those from the Bjønnes syenite. Many of the pegmatites seemingly follow a less sodic trend that may extend from larvikite analyses but more larvikite data is required to make justified conclusions. Amphiboles from 'T-type' pegmatites are generally more comparable to those from the

Bjønnes syenite, particularly in primitive compositions but the Na component is apparently lower in the most evolved compositions. Similarly 'L-type' pegmatites follow the same trend although data is limited. It appears that amphiboles from these pegmatites, and most other analysed pegmatites, are more similar to larvikite in composition.

Lardalites and foyaites are underrepresented in the data so no definitive conclusions can be made. The three nepheline syenite pegmatite analyses with the highest Na content were sampled from Bratthagen, in Lågendalen, and clearly do not relate to other nepheline syenites in this data. The analyses of lardalite, foyaite, and pegmatites from Lågendalen line up along a linear path and could represent a separate evolutionary trend. Of course much more data would be needed to give more substantial support to this. However the trend would suggest incorporation of Na at an almost equal rate to Fe, implying highly oxidised conditions, and would be similar to the clinopyroxene evolutionary trend of foyaite. The mafic mineral chemistry of the foyaites suggests more oxidising crystallising conditions than the Bjønnes syenite.

Biotite both from Bjønnes and nepheline syenite dykes in Tvedalen is classified as annite by their compositions. Annite analysed from Bjønnes have a generally higher Mg-content and subsequently lower Fe-content than those analysed from nepheline syenite pegmatites across the LPC by *Larsen (1998)*. In comparison, annite from the Bjønnes syenite has a molar Mg# ranging from 0.22 to 0.37, with an average of 0.29, whereas annites from nepheline syenite pegmatites have a Mg# range of 0.13 to 0.32, averaging 0.18. This is expected since the nepheline syenite pegmatites are thought to be the most evolved rock in the western LPC, possibly evolved from the Bjønnes syenite. The increase in Fe-content in more evolved rocks is a trend also observed in clinopyroxene, amphibole and whole rock compositions from Bjønnes and the LPC.

The annites analysed from the nepheline syenite pegmatites of the LPC show a trend of increasing Mg# towards the East of the complex (*Larsen, 1998*), moving further away from the Bjønnes syenite near the Western margin. The annites from Bjønnes also contain more Ti and less Al, probably related through the substitution $3Ti^{4+} + \square \leftrightarrow 2Al^{3+} + 2Fe^{3+}$. The content of K in annite from Bjønnes is also consistently higher.

4.4.3 Emplacement of the Bjønnes syenite

Trace element data indicated that the Bjønnes syenite was most likely formed from the same relatively homogeneous alkali-to-transitional basalt source (*Neumann, 1980*). Deviations in the distribution of certain trace elements such as Ta and Th is

likely due to replenishment of melt from continued partial melting of the source and consequent magma mixing (*Neumann, 1980*). These factors are common in felsic systems and make trace element ratios somewhat unreliable. The shifting centre of magmatic activity throughout emplacement of the LPC (*Petersen, 1978*) also implies that magma is being replenished throughout this migration.

The depletion of elements such as P, Sr and Eu in the Bjønnes syenite can be accounted for by fractionation and removal of feldspar and apatite. Major element compositions of the Bjønnes syenite show an evolutionary trend that appears to continue along the same trend as comparatively less evolved larvikites, particularly from RS IV – VI. There is little observable difference between the geochemistry and mineral chemistry of larvikite and lardalite, and lardalite is probably underrepresented overall. It is plausible that the Bjønnes syenite could be related to either rock type.

Incompatible trace element data and REE patterns indicate that foyaites also originate from a fractionated source melt and appear to represent an intermediate phase between larvikite and lardalite, and the strongly fractionated Bjønnes syenite. However mineral chemistry data for the foyaites indicate much more oxidised crystallising conditions. The origin of the foyaites is unclear and they are not believed to be related to lardalites (*Neumann, 1976; Petersen, 1978*).

Two possible theories can be examined from this information. Firstly, the Bjønnes syenite may represent residual fractionated melts from the LPC as a whole, emplaced after the ten ring sections. Secondly, the Bjønnes syenite was emplaced from residual melts of RS VI, emplaced by a different mechanism than the traditional ring sections.

The first theory would suggest that the Bjønnes syenite and perhaps the foyaites in Lågendalen were emplaced as the last plutonic stages of the LPC. They would represent residual felsic melts from the source of both the larvikites and the later lardalites. Both the Bjønnes syenite and foyaites lack a ring structure, are finer grained than their host rocks, and are also more alkaline and indicated a degree of fractionation. If they represent similar residual melts, they must be isolated from one another to account for different crystallising conditions.

By the time that the lardalites were being emplaced, the centre of magmatic activity had migrated significantly north of the location of the Bjønnes syenite. Therefore later emplacement of the Bjønnes syenite would require a shift in magmatic activity back to the West of the LPC. If the Bjønnes syenite were considered to be the last stage of a fractionated melt from the LPC, the ring sections of the LPC would be

expected to show more progressive evolutionary trends in geochemistry and mineral chemistry, evolving towards those of the Bjønnes syenite. However there is very little difference in mafic mineral chemistry between larvikites and lardalites, which would be expected to show more evolved compositions. The geochemistry of the ring sections does not show a consistent, progressive evolution (Figure 65).

The second theory would correlate better with evidence from field relationships suggesting that the timing of emplacement of the Bjønnes syenite is constrained between RS VI and RS VII, intruding hot larvikite. It would suggest that residual felsic melt left behind by RS VI was somehow emplaced before further fractionation took place to give rise to RS VII. Figure 65 shows nepheline syenites from Bjønnes and Tvedalen continuing along the same evolutionary path as RS VI larvikite.

Neumann (1980) discusses that fractionation of an intermediate melt occurred during quiet tectonic periods, allowing melts to differentiate into light felsic and dense cumulates, where the lighter felsic melts would rise once they reached a low enough density to penetrate the crust and be emplaced as ring sections. The Bjønnes syenite was not emplaced as a traditional ring section, suggesting that other factors may have influenced its emplacement. Tectonic activity may have allowed residual felsic melts from RS VI to rise through the crust. Faulting would reduce overburdening pressure and provide a route to through the crust for a relatively small amount of melt that may not have the mass to penetrate through the crust like the more voluminous ring sections.

By assuming a single magma chamber source, this would require extensive replenishment and/or fractionation of melt from the source in order to emplace RS VII. It is likely that multiple magma chambers from the same source existed to create the LPC, as opposed to a single large magma chamber (*Neumann, 1980*). This is thought to be the case in the development of many plutons (*Glazner et al., 2004; Kelley & Barton, 2008*). Applying this model, the relatively small size of the Bjønnes syenite may suggest that it originates from one of numerous magma chambers. This may also explain discrepancies in some incompatible trace element ratios.

4.5 Comparisons to other alkaline complexes

Agpaitic rocks can be divided into five categories based on their mineral assemblages; low agpaitic, medium agpaitic, highly agpaitic and hyperagpaitic. The agpaitic rocks of the Bjønnes syenite are low agpaitic (*Khomyakov, 1995*). This coincides with the low alkalinity of the Bjønnes syenite relative to other alkaline complexes with higher agpaitic mineralogy. Hyperagpaitic lujavrites from Ilímaussaq, for example, have alkalinity indexes of 1.55 – 1.69, whilst the lujavrites of Lovozero have an alkalinity index of 1.43 (*Sørensen, 1997* and references within). A closer comparison would be nepheline syenites of the McGerrigle complex, which has miaskitic to low agpaitic mineral assemblages and alkalinity indexes ranging from 0.96 – 1.09, although mineral assemblages are somewhat different to the Bjønnes syenite (*Wallace et al., 1990*).

Marks et al. (2011) discuss two trends observed between different Ti- and Zr-bearing mineral assemblages from a variety of alkaline complexes. It is proposed that these assemblages are directly related to the parental magmas. Geochemical data from rocks from the Gardar province, Greenland (including Ilímaussaq, Grønnedal-Ika and Puklen), show strongly negative Eu-anomalies, inferring extensive plagioclase fractionation and depleting the parental melts in Ca. The parental source rock is thought to be basalt of high Al_2O_3/CaO proportions at the base of the crust. Alternatively, rocks from the Tamazeght complex and the Kola province (including Khibina and Lovozero) originated from a nephelinitic source and did not undergo plagioclase fractionation prior to formation and assumed parental melts were much less aluminous. This resulted in no depletion of Ca from their source, allowing the formation of Ca-rich minerals (*Sørensen, 1997; Marks et al., 2011* and references within). The Pilanesberg complex, South Africa, also originated from a nephelinitic source and has a comparable mineralogy to the alkaline complexes of the Kola province (*Andersen et al., 2016*).

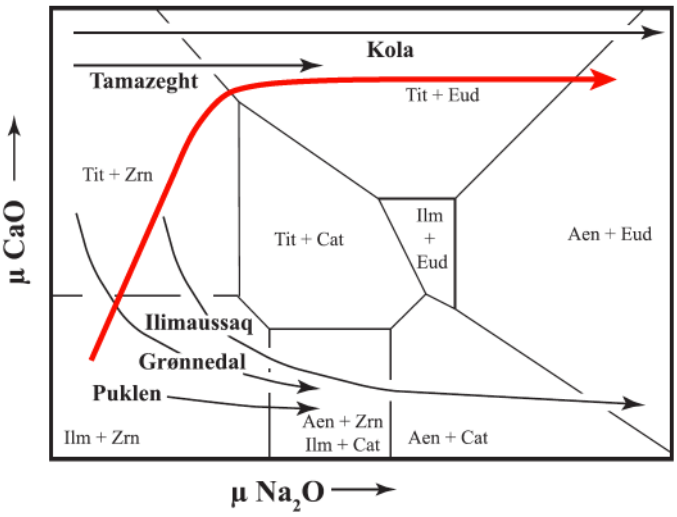

Figure 72: Evolutionary trends of Ti- and Zr-bearing mineral assemblages in different alkaline complexes compared to that observed from the Bjønnes syenite (red) (modified from *Marks et al., 2011*).

The LPC is thought to originate from an alkali basaltic source (*Neumann, 1980*), similar to the Gardar province. Figure 72 shows the Ti- and Zr-bearing mineral assemblages of these complexes, where μCaO has been schematically plotted against μNa_2O (in this scenario μX is equivalent to $\log a_x$). A clear division can be made from complexes depleted and not depleted in Ca. The path of the Bjønnes syenite, plotted in red, does not follow this trend. The strong depletion of plagioclase from the parental melt is similar to those of the Gardar province and the Bjønnes syenite initially shows similarly low-Ca miaskitic assemblages. However rather than continuing to develop low-Ca minerals, the agpaitic mineral assemblages become calcic and follow the same trend observed from Tamazeght and Kola.

It must also be mentioned that this phase diagram does not contain a zirconolite phase. Zirconolite was found to be stable with zircon and Fe-Ti oxides in the most primitive samples from Bjønnes. It contains Ca, Ti and Zr, which would theoretically increase the starting μCaO of the Bjønnes syenite. Figure 72 is also controlled by other parameters which may not apply to the Bjønnes syenite. For example a_{HCl} is believed to be relatively high and a_{H2O} is thought to be low, which would increase eudialyte stability and decrease catapleiite stability respectively.

Figures 73 and 74 compare the chemical evolutionary paths of clinopyroxene and amphibole respectively from the Bjønnes syenite with those of a selection of other alkaline complexes. Both clinopyroxene and amphibole evolutionary trends are comparable to those from Grønnedal-Ika. Amphibole from Bjønnes has a greater compositional range that coincides with a trend from Ilímaussaq, running parallel to the trend of Grønnedal-Ika.

Nepheline syenites in the Grønnedal-Ika complex are silica-undersaturated and formed from magmas produced by fractional crystallisation of a largely homogeneous and uncontaminated mantle source (*Marks et al., 2004*). This genesis is very similar to the emplacement of the LPC, as described by *Neumann (1980)*. Furthermore, the Gardar province represents the development of a failed rift system, much like the Oslo rift. Its various alkaline complexes formed under differing degrees of crustal contamination and clinopyroxene trends indicate that Grønnedal-Ika crystallised under relatively oxidised conditions (*Marks et al., 2004*).

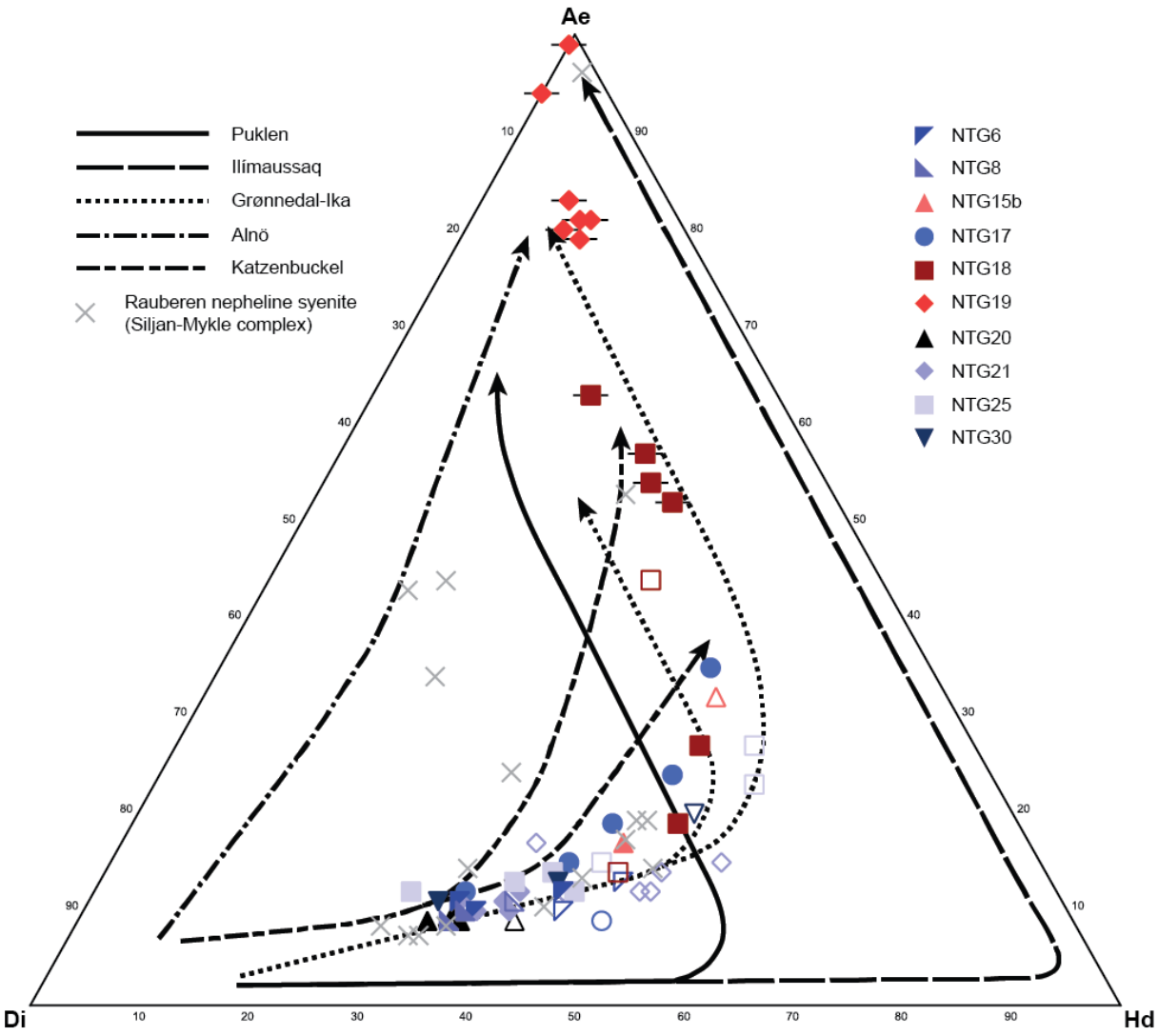

Figure 73: Ternary aegirine-diopside-hedenbergite plot of clinopyroxene end-member proportions comparing the Bjønnes syenite to a variety of other alkaline complexes including data from *Marks et al. (2004)* and references within, *Piilonen et al. (2013)* and references within and *Andersen & Sørensen (1993)*.

Clinopyroxene data has been included in Figure 73 from the Rauberen nepheline syenite from the Siljan-Mykle complex, a neighbouring larvikitic complex immediately North of the LPC (*Andersen & Sørensen, 1993*). The clinopyroxene of the Rauberen nepheline syenite are rather anomalous, with a grey colour and much higher Al_2O_3 content than any other clinopyroxenes from the Oslo rift (*Neumann, 1976; Andersen & Sørensen, 1993*). Many of the clinopyroxenes of the Rauberen nepheline syenite also show a similar trend to the Bjønnes syenite, extending through into the larvikite composition field in the most primitive analyses. They also display a similar range, reaching almost pure aegirine compositions. These clinopyroxenes are discussed in detail by *Andersen & Sørensen (1993)*.

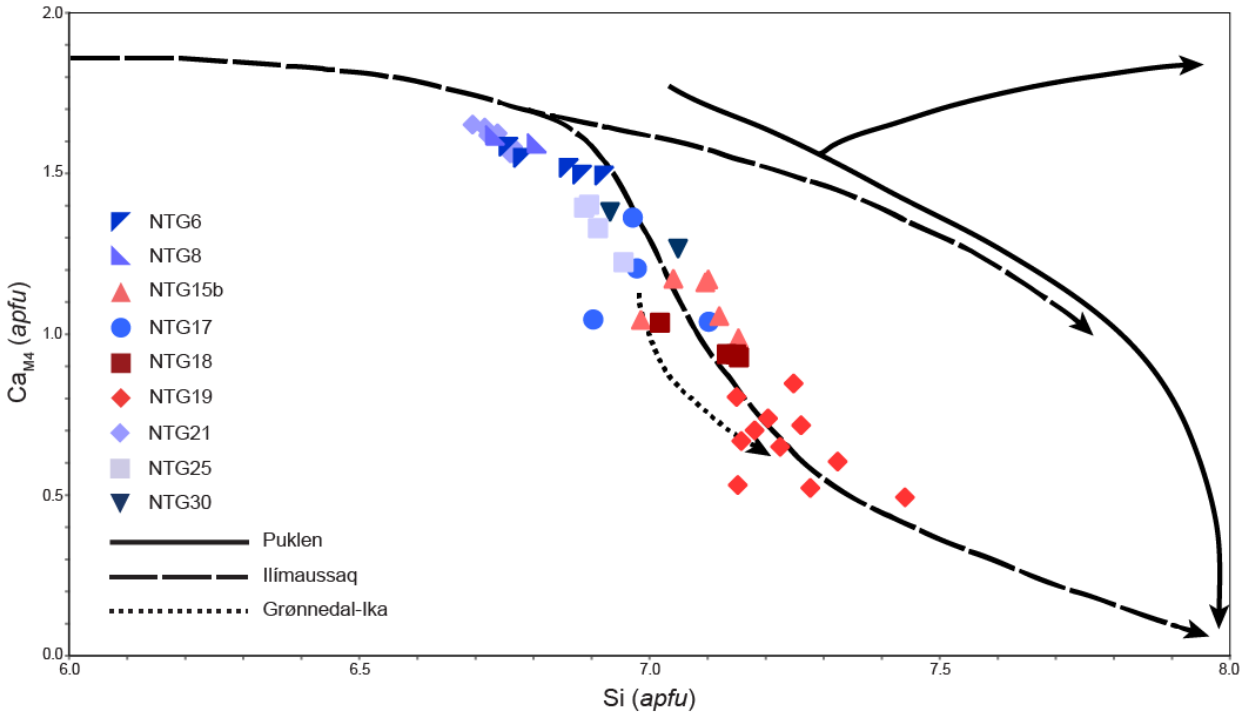

Figure 74: Major element compositional plot of amphiboles comparing those from Bjønnes against trends observed in other alkaline complexes (modified from *Marks et al., 2011*).

4.6 Resource potential

Apatite has a major effect on REE content (Figure 63) but is present only in small quantities with no concentrated distribution. Eudialyte, a non-conventional REE source, also has a strong influence of REE's and in much more abundant and concentrated in certain parts of the Bjønnes syenite, such as the locality of NTG15 and NTG23. High concentrations of eudialyte are required to reach ore potential due to its generally low total REE content (*Stark et al., 2017*). To examine ore potential, the eudialyte must be characterised by quantitative analysis. Eudialyte is investigated as a potential resource in the Norra Kärr complex, Sweden, and tested samples have a REE concentration of around 4 % for example (*Stark et al., 2017*). Eudialyte is also exploited in other alkaline complexes such as Lovozero (*Zakharov et al., 2011*), and creates a world-class potential ore deposit in Ilímaussaq (*Borst et al., 2014*).

One major downfall of the Bjønnes syenite is that eudialyte was found to be spatially restricted, severely limiting ore potential unless larger expanses of eudialyte syenite exist below the surface, for example. Alteration may also present an issue, possibly affecting recovery and complicating processing methods (*Zakharov et al., 2011; Borst et al., 2014*). However ore elements (Zr-Nb-REE) appear to have been largely retained despite alteration.

It is also important to note that NTG18, unlike NTG15 and NTG23, does not appear to show a strong affinity for REE's. In the Norra Kärr complex, three EGM varieties were distinguished with different affinities for REE's (*Sjöqvist et al., 2013*). There is evidence to suggest that more than one eudialyte group is present.

5. Conclusions

The Bjønnes syenite is a texturally zoned, medium grained nepheline syenite intrusion within RS VI larvikite of the LPC. The majority of the intrusion displays a gneissic texture that is developed most strongly towards the core of the intrusion, caused by syn-magmatic deformation as a result of rift-related faulting.

Agpaitic mineralogy in the LPC was previously believed to be confined to nepheline syenite pegmatites. However, the Bjønnes syenite locally transitions into agpaitic nepheline syenite, containing rock-forming minerals such as eudialyte and aenigmatite. Agpaitic minerals only occur in peralkaline rocks. The transition between miaskitic and agpaitic is variable, with samples containing eudialyte and titanite, and another containing zircon and aenigmatite, suggesting that further controls beyond alkalinity influenced the formation of Zr- and Ti-bearing minerals.

Titanium content in clinopyroxene and amphibole is partly controlled by alkalinity, however zirconium is only incorporated in small amounts and its behaviour is not well constrained. Clinopyroxene evolution follows a single trend that fits trends of larvikite and nepheline syenite pegmatites hosted within larvikite. Compositions range from diopsidic to almost pure aegirine. Amphibole compositions follow a similar trend, ranging from hastingsite to arfvedsonite. Whilst amphibole shows little evidence of chemical zonation, primary clinopyroxene evolves from diopsidic cores, increasing in hedenbergite and aegirine components. Secondary clinopyroxene replaces primary amphibole as a post-magmatic hydrothermal phase and shows the most evolved clinopyroxene compositions.

The Bjønnes syenite intruded into hot larvikite, resulting in local plastic deformation and partial assimilation in a complex transitional contact zone. The timing of emplacement of the Bjønnes syenite can be constrained between the timing of RS VI and RS VII larvikite emplacement. The Bjønnes syenite probably originated from the same heterogeneous basaltic source as larvikites and lardalites. Trace element ratios showed some variability, as is expected in highly evolved felsic systems, and most trace elemnt ratio trends were consistent with other rock units from the LPC. Consistently strong negative Eu anomalies and low contents of elements such as Sr and P relative to surrounding LPC rock units suggest that extensive fractionation of a source melt occurred, leading to the removal of plagioclase and apatite. Therefore the Bjønnes syenite most likely originates from a melt source that underwent extensive fractionation,

leading to the emplacement of RS VI larvikite. This is supported by major element geochemistry, where the Bjønnes syenite typically shows more evolved compositions along a similar trend.

Nepheline syenite dykes in Tvedalen generally show strong textural and geochemical similarities to the Bjønnes syenite. They intrude larvikite at approximately the same time as nepheline syenite pegmatite formation. Assuming that the pegmatites originate from larvikite, this would suggest that the nepheline syenite dykes intruded at the late stages of larvikite RS VI crystallisation, much like the Bjønnes syenite. Evidence suggests that at least some of the nepheline syenite dykes are likely to be related to the Bjønnes syenite.

Foyaites from Lågendalen showed major differences in mineralogy, mafic mineral chemistry and geochemistry to the Bjønnes syenite and other rock units from the LPC, and appears to show no relationship to them. They crystallised under much more oxidised conditions and despite their high alkalinity, do not exhibit agpaitic mineralogy.

5.1 Further research

Before this project, very little has been written about the Bjønnes syenite, meaning that there are many potential options to conduct further research in the area.

- As previously mentioned, the quantitative characterisation of eudialyte would give an insight into the distribution of REE's and other HFS elements.
- The whole rock characterisation of Cl and F. The analysis of F and Cl would help to understand their role in the miaskitic-agpaitic transition.
- Dating of the Bjønnes syenite (e.g. U-Pb dating) would give chronological constraints on its timing of emplacement relative to other units of the LPC.
- A radiogenic isotope study (e.g. Sm-Nd, Pb-Pb) of the Bjønnes syenite to see if the source is indeed the same as the other rock units of the LPC.

There are also many possibilities for further research to be done in the LPC.

- An assessment of the structural geology of the LPC could provide insights into a number of processes, possibly including the emplacement of the Bjønnes syenite.
- A study focusing on the geology of RS IX and X would help to further understand the process of their evolution as current data is scarce. Foyaites also appear to show significant internal variations, despite currently being treated as a single undifferentiated unit.

References

Andersen, T. (1984). Hybridization between larvikite and nordmarkite in the Oslo region, S.E. Norway: A case study from the Sande Cauldron central pluton. *Norsk Geologisk Tidsskrift* **64**, 221 – 233.

Andersen, T. & Sørensen, H. (1993). Crystallization and metasomatism of nepheline syenite xenoliths in quartz-bearing intrusive rocks in the Permian Oslo rift, SE Norway. *Norsk Geologisk Tidsskrift* **73**, 250 – 266.

Andersen, T., Erambert, M., Larsen, A.O., & Selbekk, R.S. (2010). Petrology of nepheline syenites pegmatites in the Oslo Rift, Norway: Zirconium silicate mineral assemblages as indicators of alkalinity and volatile fugacity in mildly agpaitic magma. *Journal of Petrology* **51,** 2303 – 2325.

Andersen, T., Carr, P & Erambert, M. (2011). Late-magmatic assemblages with siderite and zirconian pyroxene and amphibole in the anorogenic Mt Gibraltar microsyenite, New South Wales, Australia, and their petrological implications. *Lithos* **151**, 46 – 56.

Andersen, T., Elburg, M. & Erambert, M. (2016). The miaskitic-to-agpaitic transition in peralkaline nepheline syenite (white foyaite) from the Pilanesberg Complex, South Africa. *Chemical Geology*, http://dx.doi.org/10.1016/j.chemgeo.2016.08.020.

Atencio, D., Andrade, M.B., Christy, A.G., Gieré, R. & Kartashov, P.M. (2010). The pyrochlore supergroup of minerals: nomenclature. *The Canadian Mineralogist* **48**, 673 – 698.

Bailey, S. W. (1984). Classification and structures of the micas. In: Bailey, S. W. (ed.), *Micas*. *Reviews in Mineralogy and Geochemistry* **13**, 1 – 12.

Banno, Y., Miyawaki, R., Matsubara, S., Sato, E., Nakai, I., Matsuo, G.-I. & Yamada, S. (2009). Potassic-ferropargasite, a new member of the amphibole group, from Kabutoichib, Mie Prefecture, central Japan. *Journal of Mineralogical and Petrological Sciences* **104**, 374 – 382.

Biagioni, C., Merlino, S., Parodi, G. C. / Perchiazzi, N. (2012). Crystal chemistry of minerals of the wöhlerite group from the Los Archipelago, Guinea. *The Canadian Mineralogist* **50**, 593 – 609.

Bollingberg, H. J., Ure, A. M., Sørensen, I. & Leonardsen, E. S. (1983). Geochemistry of some eudialyte-eucolite specimens and a coexisting catapleite from Langesund, Norway. *Tschermaks Mineralogische und Petrografische Mitteilungen* **32**, 153 – 169.

Borst, A., Waight, T., Smit, M., Friis, H. & Nielsen, T. (2014). Alteration of eudialyte and implications for the REE, Zr and Nb resources of the layered kakortokites in the Ilímaussaq intrusion, South West Greenland. *European Rare Earth Resources Conference (ERES2014)* **1**,

325 – 332.

Brady, J. & Perkins, D. (2015). Pyroxene and Mica Spreadsheets. *Web reference link*: http://serc.carleton.edu/research_education/equilibria/mineralformulaerecalculation.html

Brigatt, M. F., Galli, E. & Poppi, L. (1991). Effect of Ti substitution in biotite-*1M* crystal chemistry. *American Mineralogist* **76**, 1174 – 1183.

Brøgger, W. C. (1890). Die Mineralien der Syenitpegmatitgänge der südnorwegischen Augit- und Nephelinsyenite. *Zeitschrift für Krystallographie* **16**, 1 – 235; 1 – 663.

Brøgger, W. C. (1898). Die Eruptivgesteine des Kristianiagebietes III. Das ganggefolge des Laurdalits. *Skr. Videnskabs-selskabet, I. Mat. Naturv.* **6**, 1 – 377.

Carmichael, I. S. E., Turner, F. J., Verhoogen, J. (1974). *Igneous Petrology*. New York: McGraw-Hill Book Company, 739 p.

Christy, A. G. & Atencio, D. (2013). Clarification of status of species in the pyrochlore supergroup. *Mineralogical Magazine* **77** (1), 13 – 20.

Corfu, F. & Dahlgren, S. (2007). Pervoskite U-Pb ages and the Pb isotopic composition of alkaline volcanism initiating the Permo Carboniferous Oslo Rift. *Earth and Planetary Science Letters* **265**, 256 – 269.

Dahlgren, S. (2010). The Larvik Plutonic Complex: The larvikite and nepheline syenite plutons and their pegmatites. In: Larsen, A. O. (ed.), *The Langesundsfjord. History, Geology, Pegmatites, Minerals*. Salzhemmerdorf, Germany: Bode, pp. 26 – 37.

Deer, W. A., Howie, R. A. & Zussman, J. (1997). *Rock Forming Minerals Vol. 1b: Disilicates and Ring Silicates (2nd edition).* London: The Geological Society, 631 p.

Della Ventura, G., Bellatreccia, F. & Williams, C. T. (1999). Zr- and LREE-rich titanite from Tre Croci, Vico volcanic complex (Latium, Italy). *Mineralogical Magazine* **63** (1), 123 – 130.

Della Ventura, G., Bellatreccia, F. & Williams, C. T. (2000). Zirconolite with significant *REE*ZrNb(Mn,Fe)O_7 from a xenolith of the Laacher See eruptive center, Eifel volcanic region, Germany. *The Canadian Mineralogist* **38**, 57 – 65.

Ferguson, A. K. (1978). The occurrence of ramsayite, titan-låvenite and a fluorine-rich eucolite in a nepheline syenite inclusion from Tenerife, Canary Islands. *Contributions to Mineralogy and Petrology* **66**, 15 – 20.

Ferguson, J. (1970). The differentiation of agpaitic magmas; the Ilímaussaq intrusion, south Greenland. *The Canadian Mineralogist* **10** (3), 335 – 349.

Ferrara, G. & Treuil, M. (1974). Petrological implications of trace element and Sr isotope distributions in basalt-pantellerite series. *Bull. Volcan*. **38**, 548 – 574.
Fossen, H. (2010). *Structural Geology*. Cambridge: Cambridge University Press, 463 p.

Frost, B. R. & Frost, C. D. (2008). A geochemical classification for feldspathic igneous rocks. *Journal of Petrology* **49**, 1955 – 1969.

Glazner, A. F., Bartley, J. M., Coleman, D. S., Gray, W. & Taylor, R. Z. (2004). Are plutons formed over millions of years by amalgamation from small magma chambers? *GSA Today* **14** (4/5), 4 – 11.

Grew, E. S., Hålenius, U. & Pasero, M. (2008). The crystal-chemistry of aenigmatite revisited: electron microprobe data, structure refinement and Mössbauer spectroscopy of aenigmatite from Vesterøya (Norway). *European Journal of Mineralogy* **20**, 983 – 991.

Hawthorne, F.C., Oberti, R. & Zanetti, A. (1998). The role of Ti in hydrogen-deficient amphiboles: sodic-calcic and sodic amphiboles from Coyote Peak, California. *The Canadian Mineralogist* **36**, 1253 – 1265.

Hawthorne, F.C., Oberti, R., Harlow, G.E., Mareschi, W.V., Martin, R.F., Schumacher, J.C., & Welch, M.D. (2012). Nomenclature of the amphibole supergroup. *American Mineralogist* **97,** 2031 – 2048.

Janeczek, J. (1996). Nb-, Ta- and Sn-rich titanite and its alteration in pegmatites from Zolkiewka, Poland. *Neues Jahrbuch für Mineralogie, Moatshefte* **10**, 459 – 469.

Kelley, D. F. & Barton, D. (2008). Pressures of crystallization of Icelandic magmas. *Journal of Petrology* **49** (3), 465 – 492.

Khomyakov, A. P. (1995). Mineralogy of Hyperagpaitic Alkaline Rocks. Oxford: Oxford Scientific Publications, Clarendon Press, 222 p.

Larsen, A. O. (1995). Identiteten til de sorte amfibolene fra Oslofeltets syenittpegmatitter. *Norsk Bergverksmuseum Skriftserie* **9**, 27 – 34.

Larsen, A. O. (1998). Identiteten til sorte glimmere i biotittserien fra syenittpegmatitter i Langesundsfjordområdet. *Norsk Bergverksmuseum Skriftserie* **14**, 5 – 8.

Larsen, A. O. (2001). Chemical composition of catapleiites from the syenite pegmatites in the Larvik plutonic complex, Norway. *Norsk Bergverksmuseum Skriftserie* **18**, 5 – 9.

Larsen, A. O. (2010). *The Langesundsfjord. History, Geology, Pegmatites, Minerals*. Salzhemmerdorf, Germany: Bode, 239 p.

Larsen, A. O. & Raade, G. (1997). Pyroksener fra Oslofeltets syenittpegmatitter.

Bergverksmuseets Skriftserie **12**, 16 – 21.

Larsen, A. O., Åsheim, A. & Gault, R. A. (2005). Minerals of the eudialyte group from the Sagåsen larvikite quarry, Porsgrunn, Norway. *Bergverksmuseets Skriftserie* **30**, 58 – 62.

Larsen, B.T. & Sundvoll, B. (1984). The Oslo Graben: A Passive High Volcanicity Continental Rift. EOS 65, no 45, 1084.

Larsen, B. T., Olaussen, S. & Heeremans, M. (2008). The Permo-Carboniferous Oslo Rift through six stages and 65 million years. *Episodes* **31** (1), 52 – 58.

Larsen, L. M. (1977). Aenigmatites from the Ilímaussaq intrusion, south Greenland: chemistry and petrological implications. *Lithos* **10**, 257 – 270.

Le Maitre, R. W. (ed.) (2002). *Igneous Rocks: A Classification and Glossary of Terms (2nd edition)*. Cambridge: Cambridge University Press, 236 p.

Locock, A. J. (2014). An Excel spreadsheet to classify chemical analyses of amphiboles following the IMA 2012 recommendations. *Computers & Geosciences* **62**, 1 – 11.

Marks, M. A. W., Vennemann, T., Siebel, W. & Markl, G. (2003). Quantification of magmatic and hydrothermal processes in a peralkaline syenite – alkali granite complex based on textures, phase equilibria, and stable and radiogenic isotopes. *Journal of Petrology* **44** (7), 1247 – 1280.

Marks, M. A. W., Halama, R., Wenzel, T. & Markl, G. (2004). Trace element variations in clinopyroxene and amphibole from alkaline to peralkaline syenites and granites: implications for mineral-melt trace-element partitioning. *Chemical Geology* **211**, 185 – 215.

Marks, M.A.W., Schilling, J., Coulson, I.M., Wenzel, T. & Markl, G., (2008a). The alkaline–peralkaline Tamazeght complex, High Atlas Mountains, Morocco: mineral chemistry and petrological constraints for derivation from a compositionally heterogeneous mantle source. *Journal of Petrology* **49**, 1097–1131.

Marks, M. A. W., Coulson, I. M., Schilling, J., Jacob, D. E., Schmitt, A. K & Markl, G., (2008b). The effect of titanite and other HFSE-rich mineral (Ti-bearing andradite, zircon, eudialyte) fractionation on the geochemical evolution of silicate melts. *Chemical geology* **257**, 153 – 172.

Marks, M.A.W., Hettmann, K., Schilling, J., Frost, B.R. & Markl, G. (2011). The mineralogical diversity of alkaline igneous rocks: critical factors for the transition from miaskitic to agpaitic phase assemblages. *Journal of Petrology* **52**, 439 – 455.

Marsh, J. S. (1975). Aenigmatite stability in silica-undersaturated rocks. *Contributions to Mineralogy and Petrography* **50**, 135 – 144.

McDonough, W. F. & Sun, S.-S. (1995). Composition of the Earth. *Chemical Geology* **120**, 223

– 253.

Middlemost, E. A. K. (1994). Naming materials in magma/igneous rock system. *Earth Science Review* **37**, 215 – 224.

Murad, E. (2006). Mineralogy of aegirine from Låven Island, Langesundsfjorden, southern Norway. *Norwegian Journal of Geology* **86,** 435 – 438.

Neumann, E.-R. (1976). Compositional relations among pyroxenes, amphiboles and other mafic phases in the Oslo Region plutonic rocks. *Lithos* **9**, 85 – 109.

Neumann, E.-R. (1980). Petrogenesis of the Oslo Region larvikites and associated rocks. *Journal of Petrology* **21**, 498 – 531.

Neumann, E.-R., Wilson, M., Heeremans, M., Spencer, E. A., Obst, K., Timmerman, M. J. & Kirstein, L. (2004). Carboniferous-Permian rifting and magmatism in southern Scandinavia and northern Germany: a review. In: Wilson, M., Neumann, E.-R., Davies, G. R., Timmerman, M. J., Heeremans, M. & Larsen, B. T. (eds) *Permo-Carboniferous Magmatism and Rifting in Europe*. *Geological Society, London, Special Publications* **223**, 11 – 40.

Nielsen, T. F. D. (1979). The occurrence and formation of Ti-aegirines in peralkaline syenites. *Contributions to Mineralogy and Petrology* **69**, 235 – 244.

Oftedahl, C. (1960). Permian rocks and structures of the Oslo region. In: O. Holtedahl (Editor), Geology of Norway. *Norges geologiske undersøkelse Bulletin* **208**, 298 – 343.

Oftedahl, C. & Petersen, J.S. (1978). Southern part of the Oslo Rift. *Norges geologiske undersøkelse Bulletin* **337**, 163 – 182.

Paterson, S. R., Fowler Jr, T. K., Schmidt, K. L., Yoshinobu, A. S., Yuan, E. S. & Miller, R. B. (1998). Interpreting magmatic fabric patterns in plutons. *Lithos* **44**, 53 – 82.

Pedersen, T. & van der Beek, P. (1994). Extension and magmatism in the Oslo rift, southeast Norway: No sign of a mantle plume. *Earth and Planetary Science Letters* **123**, 317 – 329.

Pedersen, L.E., Heaman, L.M. & Holm, P.M. (1995). Further constraints on the temporal evolution of the Oslo Rift from precise U-Pb zircon dating in the Siljan-Skrim area. *Lithos* **34**, 301 – 315.

Petersen, J. S. (1978). Structure of the larvikite-lardalite complex, Oslo Region, Norway, and its evolution. *Geologisches Rundschau* **67**, 330 – 342.

Piilonen, P.C., McDonald, A.M., Poirier, G., Rowe, R., Larsen, A.O., & Dahlgren, S. (2012). Magmatic and hydrothermal zircon from alkaline pegmatites in the Larvik Plutonic Complex, Oslo rift valley, Norway – implications for petrogenesis from trace-element geochemistry. *Mineralogical Magazine* **76,** 649 – 672.

Piilonen, P. C., McDonald, A. M., Poirier, G., Rowe, R. & Larsen, A. O. (2013). Mafic minerals of the alkaline pegmatites in the Larvik Plutonic Complex, Oslo Rift, Southern Norway. *The Canadian Mineralogist* **50**, 735 – 770.

Pitcher, W. S. (1997). *The Nature and Origin of Granite (2nd edition)*. London: Chapman & Hall, 358 p.

Pouchou, J. L. & Pichoir, F. (1984). A new model for quantitative X-ray microanalysis: application to the analysis of homogeneous samples. *Récherche Aerospatiale* **3**, 13 – 38.

Raade, G. (1973). Distributions of radioactive elements in the plutonic rocks of the Oslo region. Unpublished thesis, University of Oslo, 125 p.

Ramberg, I. B. (1976). Gravity interpretation of the Oslo graben and associated igneous rocks. *Norges geologiske undersøkelse Bulletin* **337**, 55 – 73.

Rämö, O. T. & Andersen, T. (2011). Magmatic evolution of the Permo-Carboniferous Oslo rift: U-Pb- and Lu-Hf-in-zircon evidence from the 299-289 Ma Larvik plutonic complex. *American Geophysical Union, Fall Meeting 2011,* abstract #V12B-02.

Reguir, E. P., Chakmouradian, A. R., Pisiak, L., Halden, N. M., Yang, P., Xu, C., Kynicky, J. & Couëslan, C. G. (2012). Trace-element composition and zoning in clinopyroxene- and amphibole-group minerals: Implications for element partitioning and evolution of carbonitites. *Lithos* **128-131**, 27 – 45.

Rollinson, H. R. (1993). *Using geochemical data: evaluation, presentation, interpretation*. Harlow: Longman Scientific & Technical, 352 p.

Rønsbo, J. G. (1989). Coupled substitutions involving REEs and Na and Si in apatites in alkaline rocks from the Ilímaussaq intrusion, South Greenland, and the petrological implications. *American Mineralogist* **74**, 896 – 901.

Rosenberg, C. L. (2001). Deformation of partially molten granite: a review and comparison of experimental and natural case studies. *International Journal of Earth Sciences* **90**, 60 – 76.

Sæbø, P. C. (1965). Contributions to the mineralogy of Norway. I. The first occurrence of the rare mineral barylite, $Be_2BaSi_2O_7$, in Norway. II. Note on the new occurrence of chrysoberyl in Norway. III. The first occurrence of ramsayite, $Na_2Ti_2Si_2O_9$, in Norway. Unpublished thesis, University of Oslo, 38 p.

Schilling, J., Wu, F.-Y., McCammon, C., Wenzel, T., Marks, M. A. W., Pfaff, K., Jacob, D., E. & Markl, G. (2011). The compositional variability of eudialyte-group minerals. *Mineralogical Magazine* **75** (1), 87 – 115.

Sjöqvist, A. S. L., Cornell, D. H., Andersen, T., Erambert, M., Ek, M. & Leijd, M. (2013). Three compositional varieties of rare-earth element ore: eudialyte-group minerals from the Norra Kärr alkaline complex, Southern Sweden. *Minerals* **3**, 94 – 120.

Sørensen, H. (1992). Agpaitic nepheline syenites: a potential source of rare elements. *Applied Geochemistry* **7**, 417 – 427.

Sørensen, H. (1997). The agpaitic rocks – an overview. *Mineralogical Magazine* **61**, 485 – 498.

Speer, J. A. & Gibbs, G. V. (1976). The crystal structure of synthetic titanite, $CaTiOSiO_4$, and the domain textures of natural titanites. *American Mineralogist* **61**, 238 – 247.

Stark, T., Silin, I. & Wotruba, H. (2017). Mineral processing of eudialyte ore from Norra Kärr. *Journal of Sustainable Metallurgy* **3**, 32 – 38.

Strunz, H. & Nickel, E. H. (2001). *Strunz Mineralogical Tables (9th edition)*. Stuttgart: Schweizerbart, 870 p.

Ussing, N. V. (1912). Geology of the country around Julianehaab, Greenland. *Meddelelser om Grønland* **38**, 1 – 376.

Wallace, G. M., Whalen, J. B. & Martin, R. F. (1990). Agpaitic and miaskitic nepheline syenites of the McGerrigle plutonic complex, Gaspé, Quebec: an unusual petrological association. *Canadian Mineralogist* **28**, 251 – 266.

Watson, E. B. & Harrison, M. T. (1983). Zircon saturation revisited: temperature and composition effects in a variety of crustal magma types. *Earth and Planetary Science Letters* **64**, 295 – 304.

Whitney, D. L. & Evans, B. W. (2010). Abbreviations for names of rock-forming minerals. *American Mineralogist* **95**, 185 – 187.

Winter, J. D. (2010). *Principles of Igneous and Metamorphic Petrology (2nd edition)*. New York: Prentice Hall, 702p.

Yakovenchuk, V. N., Ivanyuk, G., Pakhomovsky, Y. & Men'shikov, Y. (2005): *Khibiny*. Apatity & London: Laplandia Minerals in association with the Mineral. Soc. of GB & Ireland, 468 p.

Zakharov, V. I., Maiorov, D. V., Alishkin, A. R. & Matveev, V. A. (2011). Causes of insufficient recovery of zirconium during acidic processing of Lovozero eudialyte concentrate. *Russian Journal of Non-Ferrous Metals* **52** (5), 423 – 428.

Web references

http://www.earth.google.com/
Google earth V 7.1.1.1580.

https://www.mindat.org/

http://serc.carleton.edu/research_education/equilibria/mineralformulaerecalculation.html
Spreadsheets created and uploaded by Brady, J. & Perkins, D. (2015).